A tale of two surveys: searching for extrasolar planets from Australia and Antarctica

Author:
Christiansen, Jessie Leigh

Publication Date:
2007

DOI:
https://doi.org/10.26190/unsworks/6610

1226704

PLEASE TYPE

THE UNIVERSITY OF NEW SOUTH WALES
Thesis/Dissertation Sheet

Surname or Family name: Christiansen

First name: Jessie

Other name/s: Leigh

Abbreviation for degree as given in the University calendar: PhD

School: Physics

Faculty: Science

Title: A Tale of Two Surveys: Searching for Extrasolar Planets from Australia and Antarctica

Abstract 350 words maximum: (PLEASE TYPE)

The transit method of detecting extrasolar planets relies on the small periodic changes in the brightness of the planet's host star as the planet orbits between the observer and the star. Transiting planets are extremely useful discoveries due to the significant gain in information that can be obtained on the planet and its host star than extrasolar planets discovered with other methods. The field of transiting planets has matured rapidly in the last 5 years, particularly in the area of wide-field surveys. This thesis describes the results of two such surveys.

The Vulcan South Antarctic Planet Finder was designed to exploit the conditions at the South Pole, which are ideal for a transit survey. Several hardware failures resulted in the acquisition of only a small amount of corrupted data on a single field.

The University of New South Wales Extrasolar Planet Search is an ongoing transit survey using the 0.5-m Automated Patrol Telescope at Siding Spring Observatory, Australia. 25 fields were observed for 1–4 months each between 2004 October and 2007 May. Light curves were constructed for ~ 87, 000 stars down to $I = 14^{th}$ magnitude, and from these 23 planet candidates were identified. Ten candidates were eliminated using higher spatial resolution archived images and online catalogue data. Eight were followed up with higher spatial resolution imaging and/or medium resolution spectroscopy and were determined to be eclipsing binaries. Five candidates remain that require additional observation to determine their nature. No planets have been confirmed in this data set thus far.

The large sets of high precision light curves generated by transit surveys hold significant potential for additional data-mining. To demonstrate this, a variable star catalogue was compiled from the full data set. A total of 850 variable stars were identified, with 659 new discoveries. In the course of compiling this catalogue, the first example of a high-amplitude Scuti star in an eclipsing binary was identified. This represented the first opportunity for a dynamical mass measurement of a high-amplitude Scuti star, and the system was studied comprehensively.

Declaration relating to disposition of project thesis/dissertation

FOR OFFICE USE ONLY

Date of completion of requirements for Award: 12/5/08

THIS SHEET IS TO BE GLUED TO THE INSIDE FRONT COVER OF THE THESIS

A Tale of Two Surveys: Searching for Extrasolar Planets from Australia and Antarctica

by

Jessie L. Christiansen

A thesis submitted in satisfaction of
the requirements for the degree of

Doctor of Philosophy

in the Faculty of Science.

18th of December, 2007

THE UNIVERSITY OF
NEW SOUTH WALES

SYDNEY · AUSTRALIA

Statement of Originality

I hereby declare that this submission is my own work and to the best of my knowledge it contains no materials previously published or written by another person, nor material which to a substantial extent has been accepted for the award of any other degree or diploma at UNSW or any other educational institution, except where due acknowledgement is made in the thesis. Any contribution made to the research by others, with whom I have worked at UNSW or elsewhere, is explicitly acknowledged in the thesis.

I also declare that the intellectual content of this thesis is the product of my own work, except to the extent that assistance from others in the project's design and conception or in style, presentation and linguistic expression is acknowledged.

COPYRIGHT STATEMENT

AUTHENTICITY STATEMENT

Abstract

The transit method of detecting extrasolar planets relies on the small periodic changes in the brightness of the planet's host star as the planet orbits between the observer and the star. Transiting planets are extremely useful discoveries due to the significant gain in information that can be obtained on the planet and its host star than extrasolar planets discovered with other methods. The field of transiting planets has matured rapidly in the last 5 years, particularly in the area of wide-field surveys. This thesis describes the results of two such surveys.

The Vulcan South Antarctic Planet Finder was designed to exploit the conditions at the South Pole, which are ideal for a transit survey. Several hardware failures resulted in the acquisition of only a small amount of corrupted data on a single field.

The University of New South Wales Extrasolar Planet Search is an ongoing transit survey using the 0.5-m Automated Patrol Telescope at Siding Spring Observatory, Australia. 25 fields were observed for 1–4 months each between 2004 October and 2007 May. Light curves were constructed for $\sim 87,000$ stars down to $I = 14^{\text{th}}$ magnitude, and from these 23 planet candidates were identified. Ten candidates were eliminated using higher spatial resolution archived images and online catalogue data. Eight were followed up with higher spatial resolution imaging and/or medium resolution spectroscopy and were determined to be eclipsing binaries. Five candidates remain that require additional observation to determine their nature. No planets have been confirmed in this data set thus far.

The large sets of high precision light curves generated by transit surveys hold significant potential for additional data-mining. To demonstrate this, a variable star catalogue was compiled from the full data set. A total of 850 variable stars were identified, with 659 new discoveries. In the course of compiling this catalogue, the first example of a high-amplitude δ Scuti star in an eclipsing binary was identified. This represented the first opportunity for a dynamical mass measurement of a high-amplitude δ Scuti star, and the system was studied comprehensively.

Contents

List of Tables

List of Figures

Acknowledgements

I would firstly like to acknowledge and gratefully thank my supervisor, Michael Ashley. From the very beginning you have been wonderfully encouraging and enthusiastic, and over the last four years you have worked hard to nurture and develop my ideas and my skills. Thank you very much for all the opportunities you have given me and for helping to make my thesis an extremely rewarding experience.

In the same vein, I would like to thank the rest of the planet group, especially Marton Hidas and John Webb, for the invigorating discussions and constant stream of optimism when the dearth of discoveries was beginning to weigh more heavily. Thanks also to John Storey and the Antarctic group for much of the same during the Vulcan South project. And not to forget the rest of the department, especially my fellow students, for providing such an interesting and stimulating environment in which to toss around ideas or to supply appropriate distraction when required.

I have been very fortunate to have received funding assistance from various sources while undertaking my thesis, without which I could not have achieved much of the following work. Many thanks to the Australian government for providing me with the Australian Postgraduate Award, and the University of New South Wales for an additional Antarctic top-up scholarship. Thanks also go to the Astronomical Society of Australia, NASA Ames Research Centre, US National Science Foundation, and the organisers of the Protostars & Planets V conference, IAU Colloquium 200 and Transiting Extrasolar Planet Workshop for travel grants. On my travels I was hosted by the Institute of Astronomy at Cambridge University and the SETI Institute, and I am very grateful for these opportunities.

Thank you to everyone who has helped convert the seven A4 account books full of notes into this work you are reading now. To Michael Murphy, for providing his comprehensive thesis template; to Mikaela Bowmar, for volunteering to be the only non-astrophysicist to read the entirety of this thesis for much-appreciated proofreading and, more importantly, providing the essential service of keeping me sane during the last few years; to John Webb for additional proofreading even when pressed for time; and to Kelly Papadopoulos for going through it all at the same time and always knowing what to say.

Thank you also to all my friends and family for supporting me throughout this occasionally chaotic time. Special thanks to the CC girls for all the distractions and discussions and laughter and tears, and for being there 24/7. It would be impossible to thank everyone that has helped to get to me this day, but I am indebted to every one of you.

Finally, my mum. I don't know what to say, so: thank you for everything, and I love you. That should cover it.

Preface

This thesis contains the standard use of the first person plural. However, besides the major contributions from my collaborators listed below and additional minor contributions acknowledged throughout the thesis, the work presented herein is my own. Where the results of this work have been published is also detailed below.

Section 2-1 of Chapter 2 is based on the Christiansen et al. (2006) conference proceedings.

Chapter 3 describes the University of New South Wales Extrasolar Planet Search, as conducted from 2004 October to 2007 May. The survey proper was initiated in 2001 and Marton Hidas has written a comprehensive thesis on the establishment of the survey procedures, including a thorough investigation of the many factors contributing to the photometric precision, and the experimentation which led to the adoption of aperture photometry. By late 2004, most of the survey structure described in Chapter 3, including the complete data reduction pipeline, was already in place and the candidate wishes to acknowledge Marton's contribution and refer the interested reader to his thesis.

Chapter 6 is comprised of a paper submitted to the Monthly Notices of the Royal Astronomical Society in 2007 December. The paper is included in its entirety, except where text and tables presented elsewhere in the thesis are removed where indicated to avoid repetition. The catalogue of variable stars was extracted from the full data set of light curves, cross-identified with existing catalogues, and assigned preliminary periods and classifications by the candidate. The periods were refined and classifications confirmed by Aliz Derekas. The subset of binaries potentially containing low-mass components was defined by the candidate, and the three subsets of potential low mass-ratio binaries, binaries containing pre-main-sequence components and RR Lyrae stars exhibiting the Blazhko-effect were defined by Aliz Derekas and Laszlo Kiss. Martin Thompson and the candidate worked together to convert the data to a Virtual Observatory-compliant format.

The first part of Chapter 7 is comprised of a paper in its entirety published in the Monthly Notices of the Royal Astronomical Society (Christiansen et al. 2007).

The direction of this paper was developed in close collaboration with Aliz Derekas and Laszlo Kiss. Michael Ashley and John Webb contributed valuable suggestions during the analysis and writing stages. All of the observing, data reduction and analysis in this paper was performed by the candidate except in the following cases:
(1) The original observations over 29 nights on the Automated Patrol Telescope were performed by the five rostered observers—the candidate, Michael Ashley, Marton Hidas, John Webb and Duane Hamacher—as part of the University of New South Wales Extrasolar Planet Search.
(2) The data obtained from the 40-inch telescope as part of the follow up were observed by Duane Hamacher and reduced by the candidate.
The second part of Chapter 7 is comprised of supplementary data and additional explanations of the techniques and programs used in the paper.

Chapter 1

Introduction

1-1 Extrasolar planets

> There are countless suns and countless earths all rotating around their suns in exactly the same way as the seven planets of our system. We see only the suns because they are the largest bodies and are luminous, but their planets remain invisible to us because they are smaller and non-luminous. The countless worlds in the universe are no worse and no less inhabited than our Earth. —*Giordano Bruno, 1584*

Prior to 1992, the possibility of planets orbiting around other stars was merely conjecture. In the four hundred years since the time of Italian philosopher Giordano Bruno, the idea had at least evolved from heretical speculation to a well-accepted hypothesis, but there remained no proof, no confirmed detections of such a phenomenon. It was not known whether the formation of the planets in our Solar System was a rare occurrence, or in fact quite common. However, the search for these extrasolar planets motivated the development of new observing techniques and algorithms to overcome the difficulties inherent in their detection, succinctly stated by Bruno. As a result, since the first extrasolar planetary system was confirmed in 1992, discoveries have been accumulating at an increasing rate for the last 15 years; the total now stands at over 260 extrasolar planets[1]. These discoveries have painted

[1] 268 as of 14 December, 2007. This total is increasing daily and the numbers presented in this

a picture quite different to expectations, and progress in the field has been rapid and exciting.

1-1.1 Definition

The International Astronomical Union formed a Working Group on Extrasolar Planets in 1999. Part of their charge was establishing the following definition of extrasolar planets (Boss et al. 2007):

1. Objects with true masses below the limiting mass for thermonuclear fusion of deuterium (currently calculated to be 13 Jupiter masses for objects of solar metallicity) that orbit stars or stellar remnants are "planets" (no matter how they formed). The minimum mass/size required for an extrasolar object to be considered a planet should be the same as that used in the Solar System[2].
2. Sub-stellar objects with true masses above the limiting mass for thermonuclear fusion of deuterium are "brown dwarfs", no matter how they formed nor where they are located.
3. Free-floating objects in young star clusters with masses below the limiting mass for thermonuclear fusion of deuterium are not "planets", but are "sub-brown dwarfs" (or whatever name is most appropriate).

This definition explicitly ignores the formation process for the bodies under consideration—objects that are found orbiting at distances that would preclude them from having formed in the protostellar disk are named planets, but objects that were formed in a protostellar disk and later ejected are not. It also results in the scenario of two identical objects in different locations having different titles, as in the case of the free-floating "sub-brown dwarfs" that were originally "planets".

thesis will become rapidly out of date; the most recent totals are available on-line at The Extrasolar Planets Encyclopedia: http://exoplanet.eu

[2]This minimum mass was determined at the 2006 International Astronomical Union General Assembly in Prague to be the smallest mass for which self-gravity could overcome the rigid body forces and force the body into hydrostatic equilibrium, having a nearly round shape.

A thorough discussion of the formation and evolution of planetary systems is beyond the scope of this work, however the interested reader is directed to Klahr et al. (2006) for a comprehensive recent volume summarising our current understanding of the fundamental processes.

1-1.2 Motivation for study

The original groundwork for theories describing planetary formation and evolution was established with a sample size of one—our Solar System. These theories were inevitably geared to replicate what we knew: the formation of small, rocky inner planets and large, gaseous outer planets, existing in nearly circular, coplanar orbits. However well these theories worked for reproducing the Solar System, their applicability to other systems could not be assessed until these systems could be found and characterised. Indeed, the first 268 extrasolar planets demonstrate distributions in mass, orbital distance and eccentricity that were not predicted by previous theories (see Section 1-3). This in turn has raised new questions regarding:

- formation scenarios for the surprising variety of system configurations dissimilar to our Solar System,
- evolution and migration processes for systems where the observed configuration is evidently not the original configuration, and
- distribution of extrasolar planets with stellar metallicity and mass.

In order to address these issues, we need to continue to characterise the population of extrasolar planets that is accessible to discovery. The dependence of extrasolar planets on the stellar parameters of mass and metallicity needs to be more fully explored and explained. The variety of environments in which a planetary system can form, such as in multiple star systems or in clusters, must be examined, and the effect of the environment on the system parameters determined, if any. New regimes of planetary size, mass and orbital distance will have to be explored to provide more comprehensive tests of theoretical predictions, requiring further development of detection techniques to continue probing the lower limits of detection.

From a purely anthropic point of view, there is an additional area of interest pertaining to the existence of Earth-like planets, particularly in habitable zones around stars, i.e. where the surface temperature of the planet would sustain liquid water. By characterising the population of extrasolar planets as comprehensively as possible, we can better understand the frequency of Earth-like planets and the orbits they might typically inhabit.

1-2 Methods for detection

The majority of the methods that are used to detect extrasolar planets rely on indirect means, typically by measuring the effect the planet has on different properties of its host star. The history, implementation, discoveries and myriad opportunities for further study offered by each method are fascinating, but would require significant space to recount; for the methods that were not employed in this work, only a summary is included here and readers are referred to a detailed review by Perryman et al. (2005) and the sources cited below for additional information.

1-2.1 Pulsar timing variations

The first discovery of an extrasolar planetary system in 1992 was entirely serendipitous; the team was not searching for planets, but studying the millisecond radio pulsar PSR1257+12. They found periodic departures in the pulse times-of-arrival which could be fit by two periods of 66.6 and 98.2 days, and determined these to have been caused by the reflex motion of the pulsar due to the orbital motion of two planet-sized bodies with minimum masses of 3.4 $M_\oplus$ and 2.8 $M_\oplus$[3], orbiting at 0.47 AU and 0.36 AU respectively (Wolszczan & Frail 1992). This method can be used to derive the planet's orbital period, orbital distance, eccentricity, inclination and mass (Konacki et al. 2003).

Due to the precision of the pulse times-of-arrival, this technique could potentially be used to detect objects with masses smaller than the Moon ($< 0.01\ M_\oplus$)

[3] 1 $M_\oplus$ = 1 Earth mass = 0.0031 $M_{\rm Jup}$

(Wolszczan & Frail 1992; Perryman 2000). However, it has a limited applicability, being restricted to a small number of objects. Additionally, these objects are in a quite evolved phase, and thus the information that can be gleaned about the planetary formation and distribution scenarios will be significantly different than for the majority of planets that are found around main sequence stars. There are, however, further studies being performed (Bryden et al. 2006), including the exotic possibility of discovering quark planets around pulsars (Liu et al. 2007). The total number of planets detected around pulsars currently stands at five, in three separate planetary systems.

1-2.2 Radial velocity variations

The radial velocity method of detection relies on the Doppler effect on the spectral lines of a star, produced by the reflex motion of the star due to orbiting planet/s. The first success with this method was the discovery by Latham et al. (1989) of a large ($\sim 10\ M_{\rm Jup}$) planet around a "normal" solar-type star (as compared to a pulsar), which was later revealed to be a member of a wide binary system (Patience et al. 2002). The radial velocity method also led to the discovery of the first sub-Jupiter mass planet by Mayor & Queloz (1995). It has been the most successful method of detection by a considerable margin, having discovered $\sim$ 95% of the extrasolar planets known to date (O'Toole et al. 2007). This method returns the planet's orbital period, orbital distance, and eccentricity, but only a lower limit on the mass ($m$sin$i$), due to a degeneracy with the inclination.

The radial velocity method requires very high precision spectroscopic measurements in order to measure the small shifts in stellar spectral lines due to the presence of orbiting planets. For example, the reflex motion of the Sun due to the orbit of Jupiter is only 13 ms^{-1}. When this accuracy was initially achieved, the obvious selection bias that the largest planets in the closest orbits would create the largest, and most easily detectable, radial velocity variations, uncovered an unexpected new population of extrasolar planets—Jupiter-sized gas giants orbiting their host stars at distances closer than Mercury's orbit in our own Solar System ($<$ 0.1 AU). These have been coined "hot Jupiters" due to their inferred surface temperature and size.

As the achievable spectroscopic precision of teams dedicated to radial velocity surveys (for instance the HARPS planet search (Bonfils et al. 2007) and the Carnegie & California Planet Search (O'Toole et al. 2007; Wright et al. 2007)) has continued to improve down to a level of $\sim 1 - 3$ m s^{-1}, the lower mass limit on detectable planets has decreased to the point that the latest discoveries are now being coined "super-Earths", with masses down to 5 $M_\oplus$ (Udry et al. 2007). A total of nearly 2500 solar-type stars (FGKM dwarfs) have been observed by the various teams and thus far over 250 planets have been detected, including 25 multiple-planet systems.

1-2.3 Gravitational lensing detections

Gravitational microlensing occurs when a foreground object, or "lens", passes close to or across the line of sight to a background illumination source. This gravitational lens acts in the same way as an optical lens, bending the light from the background source and creating a well-known symmetric light curve profile in time series photometry. If the foreground object is in fact a double lens, composed of a star and a planet, the light curve profile will display characteristic differences. This method can be used to detect planets in the mass range of gas giants (with profile deviations on the order of a few days) down to terrestrial-mass planets (a few hours) (Bennett & Rhie 1996) and possibly below (Beaulieu et al. 2006). From the light curve profile, the mass ratio and separation of the two objects in the lens can be determined. Assuming a main sequence primary, the mass of the planetary companion and the orbital period can be inferred. The first detection was made in 2004 (Bond et al. 2004), and a total of four planets have been detected with this method.

1-2.4 Direct imaging

Direct imaging is, as the name suggests, a direct method for detecting extrasolar planets. Imaging is made very difficult by the large dynamic range between the planet and its substantially brighter host star. However, by targeting fainter stars (K dwarfs to brown dwarfs) with adaptive optics in the infrared, where gas giant planets emit a significant fraction of their radiation, this contrast can be reduced to the point where large planets ($> 5\ M_{\mathrm{Jup}}$) at wide separations (>5 AU) have been detected. The mass of the planet can be inferred from its infrared colours. The projected separation between the planet and host star is directly measured. The first detection was obtained by Chauvin et al. (2004), who imaged a small red object ~ 55 AU from a $\sim 25\ M_{\mathrm{Jup}}$ brown dwarf, deriving a mass of $5 \pm 2\ M_{\mathrm{Jup}}$. Four planets have been detected via direct imaging in total, although the three more recent discoveries are borderline planet/brown dwarf candidates (Neuhäuser et al. 2005; Chauvin et al. 2005; Biller et al. 2006).

Direct imaging is also the focus of several planned space missions, using two different approaches to reduce the contrast between the planet and host star. NASA's Terrestrial Planet Finder Coronagraph will mask out the light from the host star and the diffracted light from the edges of the telescope (Traub et al. 2006). The second instrument in NASA's complementary suite of space observatories, the Terrestrial Planet Finder Interferometer, will combine light from multiple telescopes to null the light from the host star (Beichman et al. 2006). The European Space Agency has a similar interferometry space mission for direct imaging of extrasolar planets called Darwin (Kaltenegger & Fridlund 2005). All three missions are expected to be able to obtain images of Earth-like planets.

1-2.5 Astrometric variations

Astrometry involves precise determinations of stellar positions on the sky. The astrometry method of planet detection involves detecting the periodic movements or "wobbles" in a star's position on the sky due to the orbital motion of planet/s orbiting in or near the plane perpendicular to the line of sight. Radio astrometry can achieve better than 100 microarcsecond accuracy in positioning, which is sufficient to detect planets of mass $\sim 1\ M_{\mathrm{Jup}}$ at 1 AU in orbit around low-mass stars (Bower et al. 2007). In conjunction with spectroscopic measurements to determine the parameters of the host star, this method can be used to determine the planet's orbital period, orbital distance, and eccentricity. As for the radial velocity method, only a lower limit on the mass ($m\sin i$) can be obtained, due to a degeneracy with the inclination. However, if radial velocity and astrometric variations can be fitted simultaneously, the inclination and thus the mass of the companion can be determined (Benedict et al. 2002; Bean et al. 2007), making the measurement of astrometric variations extremely useful for extrasolar planets detected with the radial velocity method. Detection of astrometric variations has not produced confirmed discoveries of any extrasolar planets as yet, however, several groups are concentrating their efforts on overcoming the current challenges and improving the achievable astrometric accuracy (Bower et al. 2007; Lanza et al. 2008).

1-2.6 Transit detections

The transit detection method is the technique employed by the two surveys that are the subject of this work. For extrasolar planets in randomly inclined orbits, the probability that they will transit in front of their host stars is governed by the ratio of the stellar radius to the semi-major axis of the orbit of the planet. In our solar system, this probability on the order of 1% for Jupiter; for hot Jupiters with much shorter periods and therefore smaller orbits, this probability can be as high as 17% (Bouchy et al. 2004). For gas giants, the transits cause a periodic dimming in the total brightness of the star of up to a few per cent, depending on the relative sizes of the host star and transiting body. The resultant characteristic light curve shape is shown in Figure 1.1, and high precision time series photometry is required to detect these shallow transits.

The transit method was first suggested by Rosenblatt (1971), and later refined by Borucki & Summers (1984) and Borucki et al. (1995). The first transiting planet, HD 209458 b, was discovered in 1999 (Henry et al. 2000; Charbonneau et al. 2000), and there are currently 34 known transiting planets, with no multiple-planet systems detected to date.

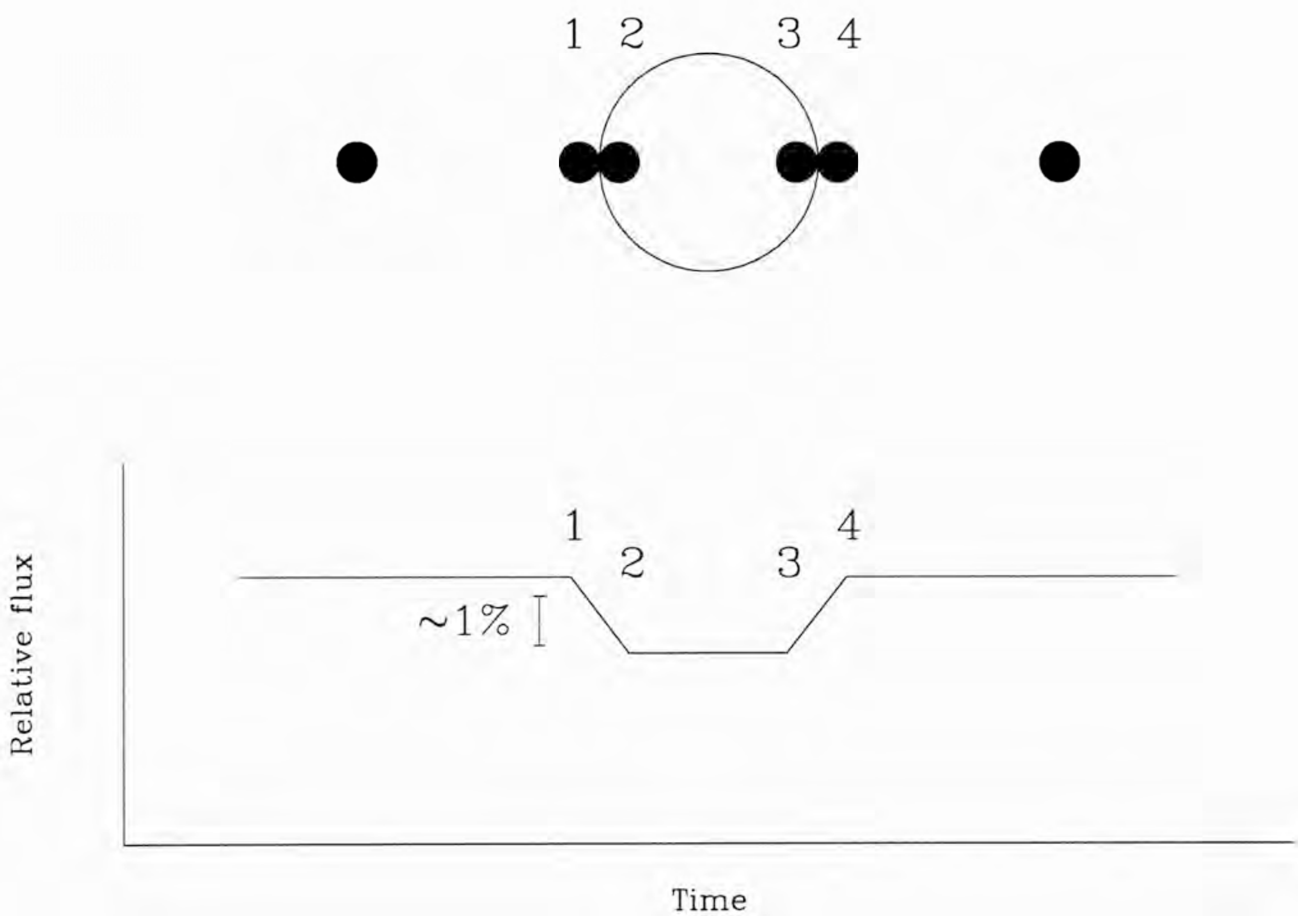

Figure 1.1. A simplified characteristic light curve of a transiting extrasolar planet. The numbers 1–4 indicate the points of first, second, third and fourth contact between the projected surfaces of the planet and the host star. Limb darkening effects have been neglected; these produce a slightly more rounded bottom to the transit that is deepest in the centre.

1-2.6.1 Advantages of the transit technique

As a result of the dual requirements of the planetary orbit having a favourable geometric alignment requirement, and of observing the planet during the small fraction of time in each orbit when it is transiting its host star, there is a lower probability of detecting any given planet with the transit method than the radial velocity method. However, one can use large-format CCDs and telescopes with a wide field of view to monitor tens of thousands of stars simultaneously, which swings the probability back in favour of the transit method. Moreover, these instruments can be quite small ($\sim$ 10–20 cm) and constructed from relatively inexpensive commercially available hardware (Alonso et al. 2004; Pollacco et al. 2006). The telescopes can also be dedicated solely to planet detection, in contrast to the methods previously described which must typically compete for time allocation on facilities at the national or international level. The motivation for performing transit surveys is the significant gain in information about extrasolar planets that can be gained by identifying and investigating transiting planets.

The transit method can be used to find the planet's orbital period, orbital distance, inclination and radius, and in conjunction with radial velocity measurements can be used to break the $m\sin i$ degeneracy to return the true mass and a measure of the mean density of the planet. Transiting planets are the *only* planets for which the values for mass, radius and mean density can be accurately derived. These are extremely important constraints for testing models of planetary composition and structure. Analysing the density of known transiting planets reveals a large range of possibilities, from values considerably less dense than can be theoretically reproduced, to planets with large dense cores and possible icy mantles (see Section 1-3.2.4). For ground-based transit surveys, the current lower limit on size is $\sim 0.4\ R_{\mathrm{Jup}}$, however with the launch of the *COROT* satellite (Costes et al. 2004; Aigrain et al. 2007) and the planned space mission *Kepler* (Jenkins et al. 2007) the aim is to observe Earth-sized rocky planets in transit in the near future.

Transiting planets also offer extensive scope for further investigations. These include:

- examining the composition of the atmosphere of the planet, using high precision transmission spectroscopy during the transit (Charbonneau et al. 2002), including the evaporating atmospheres of hot Jupiters (Vidal-Madjar et al. 2003, 2004),

- directly measuring the infrared emission from the planets with the infrared space telescope *Spitzer*, by detecting secondary eclipses (Charbonneau et al. 2005),

- obtaining higher precision light curves of the planet during the transit to search for signs of moons (Doyle & Deeg 2004) or rings (Barnes & Fortney 2004),

- monitoring the host star for transits of additional planets, as there is a significant probability that if there are multiple planets in the system their orbits will be coplanar; this can be extended to search for terrestrial planets that may be found in the habitable zones outwards in orbit of hot Jupiters (Raymond et al. 2004),

- using long-term observations to infer the presence of additional planets in the system down to Earth-mass planets due to transit timing variations (Agol et al. 2005; Holman & Murray 2005),

- observing the Rossiter-McLaughlin effect (described in Section 7-8) to examine the alignment of the orbital and spin axes of the planet, which can in turn constrain the possible formation and evolution scenarios (Winn et al. 2007), and

- amassing a large data set of high precision light curves, which can be explored for a wealth of secondary science, including microlensing events, variable stars and eclipsing binary systems with low-mass components.

Transit surveys can also be tailored to investigate specific environments, including open clusters (von Braun et al. 2005; Mochejska et al. 2005; Hartman et al. 2007), globular clusters (Weldrake et al. 2005, 2007) and the Galactic bulge (Sahu et al. 2006; Gould et al. 2006). By constraining the survey target parameters, such as age and metallicty, to within a certain range, more rigorous investigations of the dependence of the frequency of extrasolar planets on these parameters can be undertaken. In contrast, radial velocity surveys are presently volume-limited to the solar neighbourhood ($\sim$ 200 pc).

1-2.6.2 Disadvantages of the transit technique

The primary disadvantage of transit surveys is the variety and frequency of astrophysical and instrumental signals that can mimic a planetary transit event. The instrumental false positives are discussed further in Section 1-2.6.5; here we concentrate on the astrophysical false positives. The wide range of stellar systems that most commonly display periodic, shallow transits were classified by Brown (2003) as:

- MPU: a transiting planet system, composed of a main sequence primary star and a planetary companion, observed with an unblended light curve,
- MSU: an eclipsing binary, composed of a main sequence primary star and a main sequence secondary star, observed with an unblended light curve,
- MSDF: a blended eclipsing binary, composed of a main sequence primary star and a main sequence secondary star, observed with the light curve diluted by a foreground object,
- MSDT: a blended eclipsing binary, as for MSDF, but observed with the light curve diluted by a bound triple star, and
- GSU: an eclipsing binary, composed of a giant primary star and a main sequence secondary star, with an unblended light curve.

With simulations, Brown (2003) showed that ratio of astrophysical false positives to real planets was about 10 to 1, with MSU systems being the primary source of imposters. This was confirmed observationally by Pont et al. (2005), who found that transits by planet-sized dwarfs at the bottom of the main sequence formed the majority of the false positives.

Although several techniques for rejecting the false positives have been developed (Seager & Mallén-Ornelas 2003; Tingley 2004; Hoekstra et al. 2005), the precision with which transit surveys can typically parametrize transit light curves is insufficient for a rigorous analysis, and even with careful pre-selection the lowest ratio of false positives to real planets that has been achieved is 5 to 1 (Collier Cameron et al. 2007b).

The implication of this high false positive rate is that many good quality transit candidates must be obtained for the return of a few real transiting planets. Eliminating the false positives typically requires follow up observations on much larger facilities (described further in Chapter 5), and the cost is expensive in terms of instrument time and data analysis. However, the scientific return when a transiting planet is identified is sufficient to justify weeding through the plethora of false positives, and as the achievable precision of transit surveys increases, our ability to reduce this number will also improve.

1-2.6.3 The different strategies employed for transit searches

Horne (2003) showed that the predicted planet catch from a transit survey scales with the survey volume $\theta^2 d^{3/2}$, where θ^2 is the solid angle (or field of view of the telescope) out to a distance of d. The implication of this dependence is that 10-cm telescopes with wide fields of view can compete with 4-m telescopes with narrow fields of view, albeit observing different targets. Horne (2003) also provided a summary of the transit surveys that were operational or in planning stages at the time[4] which fall into two general categories: surveys that used dedicated small aperture telescopes or networks of telescopes ($<$ 50-cm) and had wide fields of view ($>$ 1 square degree); or surveys that were awarded blocks of time on larger aperture telescopes ($>$ 1-m) and had significantly smaller fields of view (typically $<$ 0.6 square degrees).

The Optical Gravitational Lensing Experiment (OGLE) is the survey from the

[4]An updated version of this table can be found at `http://star-www.st-and.ac.uk/ kdh1/transits/table.html`

latter category that has achieved significant success, having discovered 6 transiting planets. The survey uses a 1.3-m telescope imaging a 0.59 deg^2 field of view and probing a depth of $\sim$ 3500 pc, significantly further than the 300–700 pc reached by the smaller aperture surveys (Pont & Bouchy 2006). However, the disadvantage of such a deep survey is that the faintness of the targets ($V \sim 15 - 18$) restricts the possibilities for follow-up investigations with other instruments (see Section 1-2.6.1). For example, atmospheric spectroscopy requires brighter targets than this.

The two surveys that are the focus of this work have smaller apertures and larger fields of view, targeting the brighter stars that offer the largest scope for further investigations. The remainder of this section will focus on the expectations, issues and discoveries pertaining to wide-field surveys.

1-2.6.4 Predictions and initial results for wide-field surveys

The first planet that was identified as transiting its host star, HD 209458 b, had been previously identified with radial velocity measurements. The transits were detected with a 10-cm telescope as part of the STARE wide-field survey for transiting planets (Charbonneau et al. 2000). The transits of HD 209458 b were 1.6% deep, and the relative ease with which they were detected led to a optimistic wave of wide-field transit surveys being established, without due consideration for the difficulties inherent in producing high precision photometry over wide fields of view (Bakos et al. 2004).

After the success of HD 209458 b, the initial results were disappointing. Brown (2003) used the abundance of hot Jupiters derived from radial velocity surveys to calculate an expected frequency of 0.4 transiting planets for every 10,000 stars, with realistic stellar population models and distributions to take into account the blending and dilution of the transit signal by additional sources close to the line of sight. This analysis demonstrated that part of the difficulty arose in acquiring photometry on a sufficient number of solar- and late-type main sequence stars, found in largest numbers towards the Galactic plane, without introducing a prohibitive degree of blending with background sources.

However, although the ingredients for the predictions seemed well-constrained, wide-field surveys were not producing confirmed detections of extrasolar planets (Latham 2003; Bakos et al. 2004; Kane et al. 2005), and by 2003 HD 209458 b remained the only transiting planet to have been detected. Finally the first discovery of a transiting extrasolar planet in a wide field survey was made in 2004 by the Trans-Atlantic Exoplanet Survey (TrES) Network of 10-cm telescopes (Alonso et al. 2004), but this discovery stood anomalously alone. Eventually attention turned to the final ingredient in the predictions—the detection threshold above which transiting planets were expected to be detected—and the next significant burst of progress in the field was made.

1-2.6.5 Recognising systematics and subsequent success

The initial predictions for transit survey yields (Horne 2003; Brown 2003) were based on the premise that sky noise, a predominately white noise source (having approximately equal power across all frequencies), was the noise limit. When calculating the strength of a signal (such as a transit signal) in the presence of white noise, the errors on each data point are assumed to be uncorrelated. For a transit depth d, the significance S_d of a detection can be expressed as:

$$S_d = \frac{d}{\sigma_0} n^{\frac{1}{2}} \tag{1.1}$$

where σ_0 is the individual measurement uncertainty, which is assumed to be the same for all measurements, and n is the number of in-transit data points (Pont et al. 2006). In order to generate the planet catch predictions, transiting light curves with detection statistics above some level of significance (typically $S_d > 10$) were assumed to be detected.

However, in practice, the noise in high precision time series photometry was found to have a significant low frequency component, known as red noise. The resulting noise in the light curve is therefore a superposition of white noise and red noise (also known as pink noise). These three colours of noise are demonstrated in Figure 1.2, reproduced from Pont et al. (2006). The top panel shows purely white noise, the

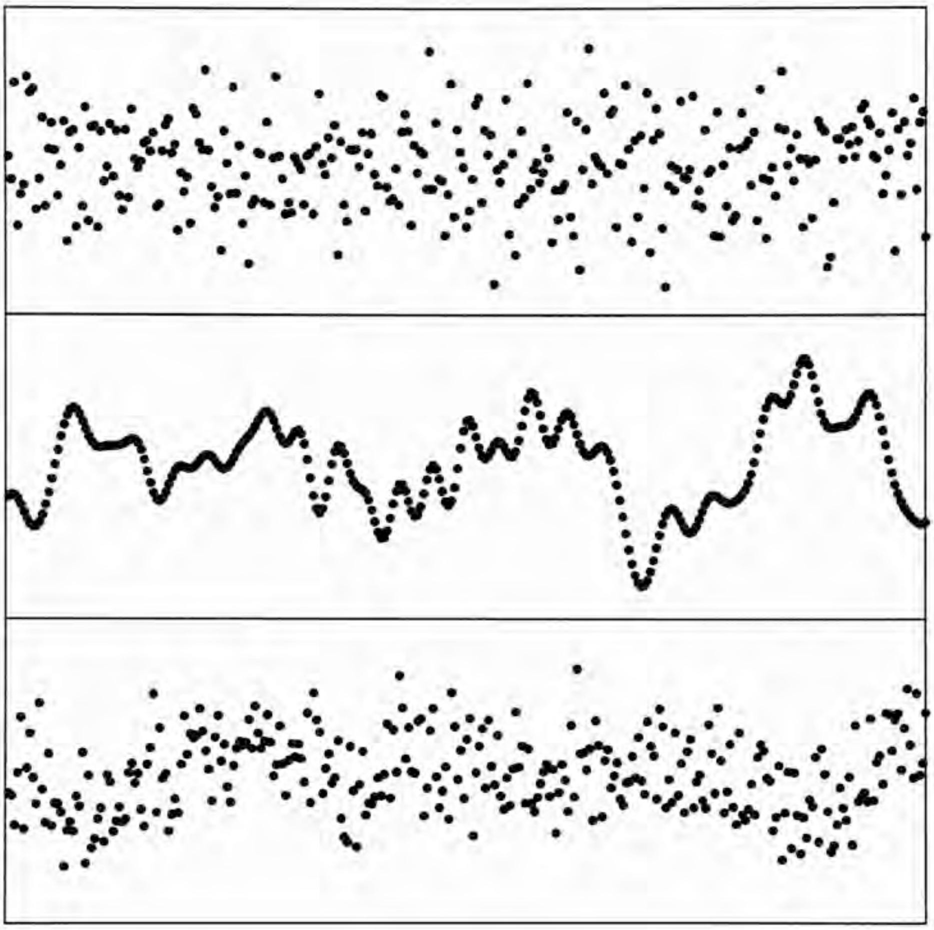

Figure 1.2. Comparison of white, red and pink noise, from Pont et al. (2006), fig. 2. The top panel is purely white noise, the middle panel is purely red noise, and the bottom panel shows pink noise, a combination of the two. The dispersion is the same in each case.

middle panel shows purely red noise, and the bottom panel shows a combination of the two. Each panel has the same dispersion (the average distance of each data point from the mean of all data points is the same in each case); only the frequency of the noise is changed. The implication of this is that errors on each data point are not uncorrelated and in fact are covariant. In the literature, this additional source of noise has been referred to as red noise, covariant noise, and due to the fact that it effects many stars across wide fields of view in a similar manner, systematic noise or just systematics. In this work we will use the latter terminology.

There have been many sources suggested to explain the presence of systematics in the light curves, including: colour-dependent airmass variations, changing atmospheric conditions on scales smaller than the field of view, telescope tracking errors, flat-field errors, and focus changes. These can often vary on timescales of a few hours, similar to the duration of a typical transit signal. Several of these possibilities are discussed further in Section 4-3.

Pont et al. (2005) showed that systematics were the dominant obstacle to detecting transits in brighter stars, and that there was a minimum, or "floor", level of noise that could be reached in the presence of systematics, regardless of the individual photometric errors. This minimum noise level, in conjunction with correlated errors, affects the detection threshold above which transiting planets can be found. If adjacent data points are correlated, increasing the number of points observed in-transit will obviously not increase the detection statistic S_d to the same extent as if the data points were uncorrelated. The real detection threshold may be up to twice as high in the presence of systematics (Pont et al. 2005).

In order to compensate for the effects of systematics on the detection threshold, the number of in-transit data points must be increased, requiring a significantly longer observing baseline than was originally deemed necessary. Brown (2003) used 38 nights for their simulations, which contained no systematics, and Mallén-Ornelas et al. (2003) found that merely 20 nights of observations on each field would be the optimum length of time for maximising the planet catch. Smith et al. (2006) re-calculated the predictions of Brown (2003), this time including the effects of systematics, and found that in order to reproduce the detection rate of 0.4 planets in 10,000 stars, the observing baseline needed to be increased from 38 nights to 80–130 nights.

Another response to the presence of systematics was the development of several algorithms for post-processing of the light curves, to remove the systematics as much as possible after the fact. These algorithms are discussed in detail in Sections 4-3.3 and 8-2.1; in brief they are:

- the trend-filtering algorithm of Kovács et al. (2005): each light curve is reconstructed from linear combinations of a randomly selected template set of light curves, and the reconstruction subtracted from the original light curve; any sys-

Table 1.1. A summary of the characteristics of successful wide-field surveys. For each survey, the number and diameter of the telescopes used, the size of the fields of view, the spatial resolution, the faint magnitude limit and the number of planets detected is given. [a]Pollacco et al. (2006); [b]Bakos et al. (2004); [c]Alonso et al. (2004); [d]McCullough et al. (2005). †These experiments have instruments spaced longitudinally to increase the continuous phase coverage.

Survey	No.	Size (cm)	Field (square deg)	Resolution ($''$ pixel^{-1})	Magnitude limit	Planets
SuperWASP[a]	8	20	482	13.7	$V < 11.5$	5
HATnet[b]†	6	11	67	14	$I < 12$	6
TrES[c]†	3	10	36	11	$V < 12$	4
XO[d]	2	20	49	25	$V < 12$	3

tematics that are common to the target light curve and the template subset are removed, and any signals unique to the target light curve that cannot be reproduced with the template subset remain behind, and

- the systematic removal algorithm (SYSREM) of Tamuz et al. (2005): the residuals in each light curve are solved for ensemble linear trends that are subsequently removed; the process is repeated for a user-specific number of iterations.

With the evolution in observing strategies to compensate for the systematics, and the implementation of algorithms to reduce their effects in the post-processing stage, wide-field surveys finally began to produce discoveries of transiting planets; 5 discoveries were made in 2006, and a further 12 discoveries thus far in 2007. The parameters of the surveys that have successfully detected planets are given in Table 1.1. The gross physical characteristics of the transiting planets and host stars are discussed in the next section.

1-3 The emerging picture of extrasolar planets

Now that the number of known extrasolar planets has reached over 260, inferences about the statistical properties of the planets and planet host stars can begin to take shape. Although the selection effects of the different detection methods will remain a significant influence on the results, the parameter space for both planet and host star properties is rapidly expanding. The majority of the conclusions drawn below are based on the $\sim$ 2500 or so FGKM dwarfs that have been studied by radial velocity surveys, around which over 250 planets have been found, including 34 transiting planets.

1-3.1 Planet frequency

For the subset of FGKM dwarfs observed by the California & Carnegie Planet Search, Marcy et al. (2005b) found that 1.2% harboured hot Jupiters in close orbits ($<$ 0.1 AU) and that 6.6% were orbited by gas giants within 5 AU. Using a flat extrapolation beyond 5 AU, they predicted that 12% of solar-type stars would host gas giants out to 20 AU, beyond which the protostellar disc density is thought to be too low to support the formation of Jupiter-mass planets. Patel et al. (2007) found for the same sample that an additional 6% of stars displayed long-period ($>$ 10 years) curvature in their radial velocity signatures that was indicative of low-mass companion/s orbiting at wider separations.

Using Monte Carlo simulations to account for survey completeness, Naef et al. (2005) estimated from the ELODIE radial velocity search results that 0.7$\pm$0.5% of stars would be orbited by planets $> 0.5\ M_{\rm Jup}$ in close orbits and 7.3$\pm$1.5% by planets within 5 AU, in good agreement with the Marcy et al. (2005b) findings.

Of the planetary systems that have been detected, 25 ($\sim$ 10%) are multi-planetary systems, with well-defined masses and orbits. Nine of these systems show mean-motion resonances between the orbiting planets, typically a 2:1 resonance, (e.g. Gliese 876 (Laughlin et al. 2005), HD 128311 (Sándor & Kley 2006)). This indicates that the planets have migrated into their current traps from their original orbits, further constraining migration theory and models. The observed fraction of multi-planet systems represents a lower limit on the true fraction, and is a function of the current sensitivity of the detection methods.

Extrasolar planets have also been found orbiting in multiple-star systems. In fact, over 30 of the 268 known planets are orbiting one of the members of a double- or multiple-star system (Udry & Santos 2007). Although gravitational collapse and core accretion theories predicted that planet formation would be unlikely in binaries separated by less than 50 AU (Nelson 2000), several planets have been found in close binary systems separated by < 20 AU (Udry & Santos 2007).

1-3.2 Planet properties

1-3.2.1 Orbits and periods

Figure 1.3 shows the distribution of extrasolar planet semi-major axes out to 10 AU (updated from Butler et al. (2006), fig. 7). Beyond 3 AU the coverage by radial velocity surveys is incomplete, however from 0.3–3.0 AU there is a marked increase in the distribution of orbital distances.

There is a pile-up of planets around 0.05 AU, where for FGKM dwarfs hot Jupiters are typically orbiting with periods of ~ 3 days. As previously mentioned, the presence of gas giant planets in such short-period orbits was unexpected, and caused significant upheaval in planetary formation and migration theories. The previous assumption was that these planets, which would have to form at significantly larger distances from the host star in order to acquire such a significant mass, would continue to orbit at the distance at which they were formed. The excess of planets in 3 day orbits indicates that either the processes mediating the planetary migration cease at this proximity to the host star, or the braking mechanism slowing the planet's descent into the star stops at this point (Butler et al. 2006).

One of the outcomes of the eventual success of the transit surveys was the discovery of another population of hot Jupiters in even shorter (~ 1 day) orbits, coined "very hot Jupiters". This is undoubtedly due to the selection bias of the particular detection method—shorter periods mean smaller semi-major axes, increasing the probability that a planet will transit, and will also result in a higher number of transits being observed. This result was still surprising, however, as radial velocity surveys are also more sensitive to shorter periods, and had placed a lower limit of ~ 2.5 d on hot Jupiter orbital periods (Udry et al. 2007). As radial velocity survey

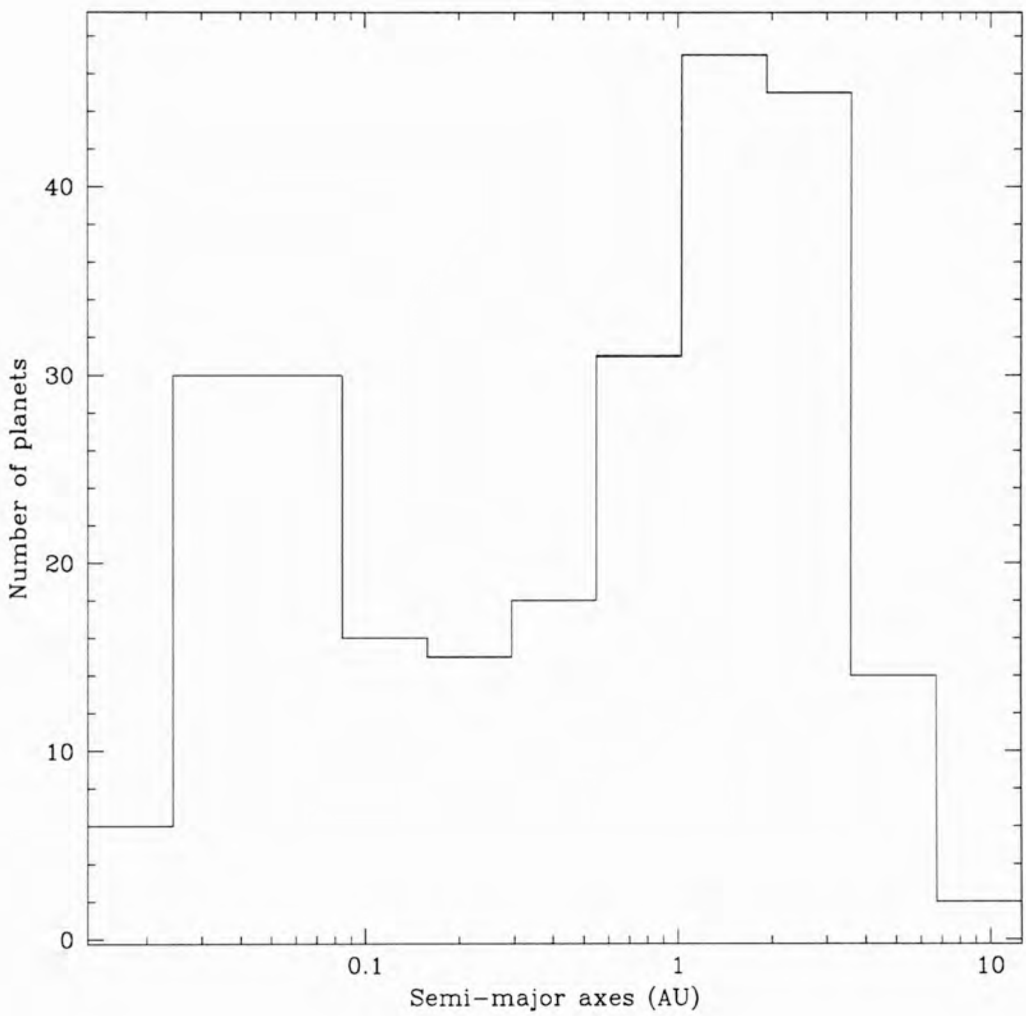

Figure 1.3. Distribution of extrasolar planet semi-major axes, updated from Butler et al. (2006), fig. 7.

completeness has increased, planets with periods from 2–3 days have been detected and it appears there is no underlying discrepancy between the distribution of periods in this range detected by transit and radial velocity surveys (O'Donovan et al. 2007). Taking the relative selection biases of the detection methods into account, Gaudi et al. (2005) determined that very hot Jupiters are 10–20% as frequent as hot Jupiters.

There is, however, an apparent real dearth of orbits in the range $\sim 0.02-0.03$ AU, which has remained consistent as the total numbers of detected planets have increased.

1-3.2.2 Eccentricities

Another unexpected result from radial velocity surveys is the large range in eccentricities that has emerged. Prior to 1995, the paradigm for gas giant planets was that they would be found in predominately circular orbits. For planets within 0.1 AU this is nearly always true, due to tidal circularisation, however beyond 0.3 AU there is an even distribution between $0 < e < 0.8$ (see, for example, fig. 10 of Butler et al. (2006)). With non-circular orbits comprising the majority of eccentricities out to 3 AU, planetary evolution theories typically invoke perturbative processes such as the gravitational interaction of planet/esimals (Chatterjee et al. 2007; Ford & Rasio 2007) or the mean-motion resonance of bodies with periods that are integer multiples of each other (Thommes et al. 2007) to explain the distribution. The implications of gas giants in close-in eccentric orbits for terrestrial planets in habitable zones include the possibility of induced eccentricities (Adams & Laughlin 2006), jeopardising the annual stability of liquid water.

1-3.2.3 Planet mass distribution

The majority of the extrasolar planets found to date are gas giants, with masses of the order of Jupiter's mass. However, in the last few years lighter, potentially rocky, planets have been found (Udry et al. 2006, 2007), and there are now over 20 planets detected with Neptune-range ($\sim$ 0.05–0.1 $M_{\rm Jup}$) masses. Figure 1.4 shows the distribution of minimum masses, updated from Butler et al. (2006), fig. 6. The distribution can be fit approximately with the power law $dN/dM \propto M^{-1.16}$, with the number of planets $> 3\ M_{\rm Jup}$ falling off rapidly with increasing mass. Since the observational selection bias is towards heavier planets, this effect will be magnified as the radial velocity surveys continue to probe lower planetary mass regimes (Butler et al. 2006).

This bias also provides evidence for the "brown dwarf desert", a paucity of sub-stellar companions with masses from 13–80 $M_{\rm Jup}$, where the bimodal distributions of planet and stellar masses meet (Grether & Lineweaver 2006). This suggests the possibility that the planetary and stellar systems are formed via different physical mechanisms.

A naïve extrapolation of the historical rate at which the lower limit on planet masses (see fig. 1 of Udry & Santos (2007)), leads us to expect detections of Earth-mass planets by 2010.

1-3.2.4 Density and composition

Due to the increase in the number of known transiting planets, the mean densities and inferred compositions of extrasolar planets can begin to be explored. These results have also challenged theoretical predictions, with several planets having larger radii, and correspondingly lower densities, than could be accounted for in earlier models (e.g. HD 209458 b (Charbonneau et al. 2000) and TrES-4 (Mandushev et al. 2007)). At the other extreme, high density planets with larger cores (such as HD 149026 b (Sato et al. 2005) and the example of Gliese 436 b, detailed below) have begun to broach the gas giant/icy planet divide (Gillon et al. 2007).

The Neptune-mass planet Gliese 436 b was recently discovered to be transiting, and was found to have a density of 1.7 $\mathrm{gcm^{-3}}$ (Gillon et al. 2007). This suggests a iron/silicate core, a water ice envelope, and a significant atmosphere of H and He (Gillon et al. 2007), although the relative radii of each component is not well constrained (Adams et al. 2007). Determining densities and compositions of extrasolar planets also helps to constrain models of migration and evolution; using the same

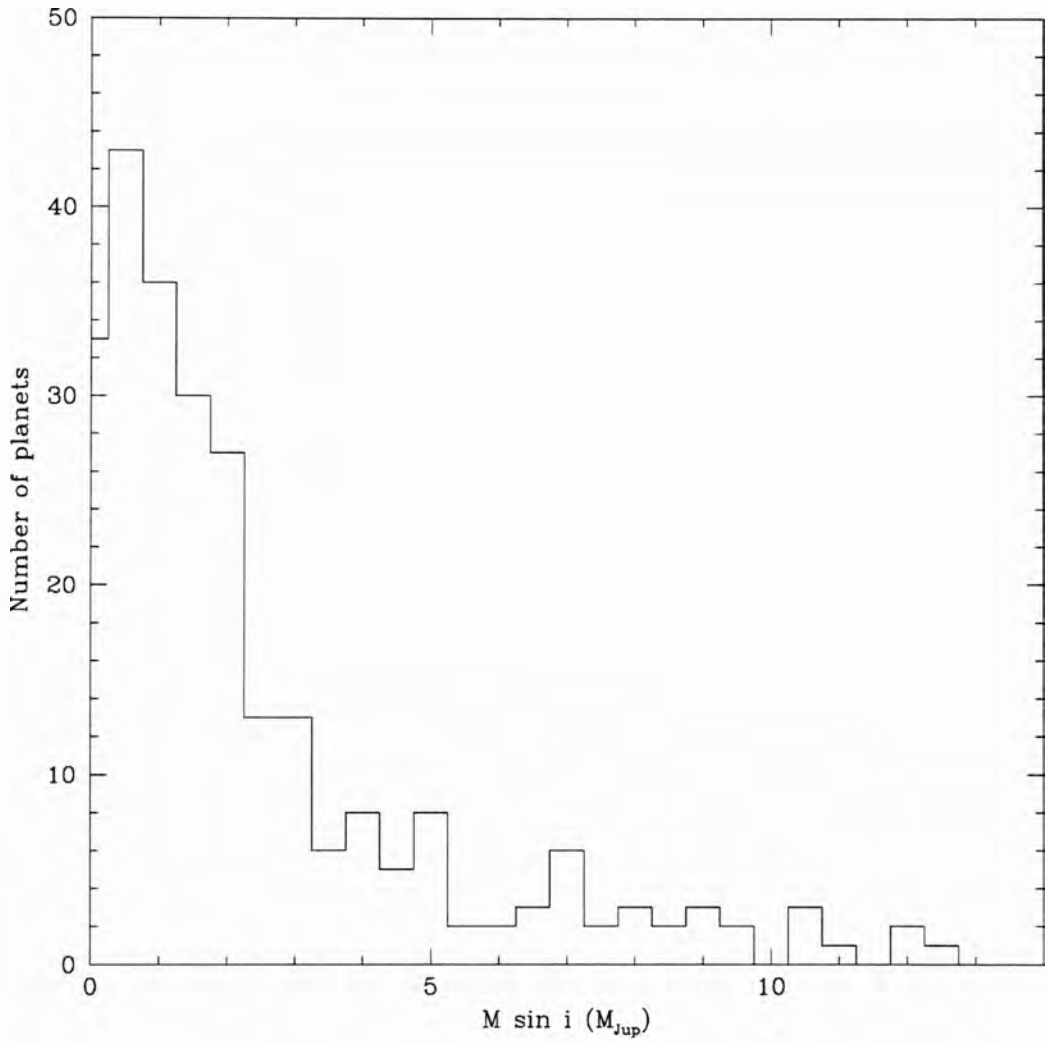

Figure 1.4. Distribution of extrasolar planet minimum, updated from Butler et al. (2006), fig. 6.

example, the presence of a substantial amount of water ice in Gliese 436 b, which is orbiting at a distance of 0.03 AU, indicates that this planet must have formed beyond the "snow line" of the protoplanetary disc, where water can condense, and then migrated to its current location (Gillon et al. 2007b).

1-3.3 Stellar host properties

1-3.3.1 Stellar mass

As radial velocity surveys widen the stellar mass range of their target stars, the emerging trend is for hot Jupiters to be more common around heavier stars, with a frequency of $\sim 8\%$ for 1.5–2.5 $M_\odot$ stars (Johnson et al. 2007), $\sim 6\%$ for solar-type stars $\sim 1\ M_\odot$ (Marcy et al. 2005b), and $< 2\%$ for 0.1–0.6 $M_\odot$ M dwarfs (Bonfils et al. 2007). Additionally, the planets that have been found orbiting low-mass stars are of significantly lower mass on average (Bonfils et al. 2007), as predicted by core accretion theory (e.g. Ida & Lin (2005)).

1-3.3.2 Stellar metallicity

The metallicity of the host star strongly influences the probability of the star hosting a gas giant planet: the more metal-rich the star, the higher the chances of harbouring a Jupiter-mass planet (see for example fig. 9 of Udry & Santos (2007)). An analysis by Fischer & Valenti (2005) showed that while only 3% of stars with $-0.5 <$ [Fe/H] < 0.0 host gas giants, they are found orbiting 25% of stars with [Fe/H] > 0.3. This dependence has not been found for lower mass planets, where the stellar metallicity distribution appears to be flat (Udry et al. 2006).

Although the numbers are small, there is a trend for planets with cores of higher mass to be found orbiting more metal-rich stars (Burrows et al. 2007).

1-4 The Vulcan South Antarctic Planet Finder

Part I of this thesis focuses on the Vulcan South Antarctic Planet Finder. This project was a wide-field transit survey based at the South Pole. It was a collaboration between the NASA Ames Research Center, the SETI Institute, the Center for Imaging Science at the Rochester Institute of Technology, and the University of New South Wales, and represented the next step for the Vulcan wide-field transit survey undertaken at the Lick Observatory in California (Borucki et al. 2001). Chapter 2 presents a justification of the choice of the South Pole, an ideal site for transit surveys. The instrument design is described, and the proposed data handling procedures outlined. Several hardware problems curtailed the scientific output of the Vulcan South project; these are discussed and several possible solutions proposed.

1-5 The University of New South Wales Extrasolar Planet Search

The University of New South Wales Extrasolar Planet Search is a wide-field transit survey that has been undertaken by the University of New South Wales since 2001. The survey uses the 0.5-m Automated Patrol Telescope (APT) owned by the university and installed at Siding Spring Observatory, Australia, with a wide-field CCD camera covering $2^{\circ}\times3^{\circ}$. A large-scale observing project was required to take advantage of the robotic nature of the telescope, the southern observing site and the large field of view. A number of wide-field transit surveys had been established by 2001 (see table 3 of Horne (2003)) with small aperture telescopes ($<$ 20 cm), to complement the deeper surveys being undertaken with larger aperture telescopes ($>$ 1 m), and there was an obvious niche for a telescope of the order of size of the APT. The advantage of being the largest clear aperture telescope in the wide-field transit survey category could be exploited in one of two ways: either the same magnitude range could be explored as the smaller aperture projects, with an increased time sampling due to the increased collecting area; or a deeper magnitude limit could be reached, allowing us to open up a new window in parameter space between the shallow, wide-field surveys ($V > 12$) and the deep, narrow surveys ($14 > V > 18$).

1-5.1 2001–2004

The commissioning, testing and initial results of the survey are comprehensively described by Marton Hidas in his thesis entitled "A Search for Transiting Extrasolar Planets with the Automated Patrol Telescope". The primary goal of this period was to establish that the photometric precision required for detecting shallow planet transits could be consistently achieved using the available hardware. This entailed a complete characterisation of the potential sources of photometric noise, discussed further in Section 3-2. A comparison of the two common techniques for producing high precision time series photometry—aperture photometry and point-spread function (PSF) fitting—was performed on a subset of the initial data, and aperture photometry was found to give the best results. As a result, a robust data reduction pipeline based on aperture photometry was constructed, described in Section 3-3.

In order to verify that the required photometric precision was being achieved, the known transiting planet host HD 209458 was observed during two predicted transit times. The data were reduced using the aperture photometry pipeline and, with a photometric precision of 3 mmag, clearly showed the two transit events. The data are shown in Figure 1.5, reproduced from fig. 3.1 of the thesis described above. It has been fit with the best model of Brown et al. (2001), with two additional models indicating fits with $\pm$ 10% of the planetary radius.

After this confirmation of the performance of the instrument and data reduction pipeline, observations began on the first sets of target fields for the transit survey. The initial observing strategy was to observe adjacent fields in sets of four, observing each field once in every cycle of four images, in order to maximise the number of observed stars. During this early observing phase, several hardware problems were identified and mitigated, including issues with the shutter and the CCD mounting, and much of the automation of the observing procedure was put into place (see Section 3-1).

Two sets of four target fields were observed with sufficient precision down to $V = 13$ and adequate phase coverage to allow analysis for transit candidates. These fields included one centred on the open cluster NGC6633, and one on the open

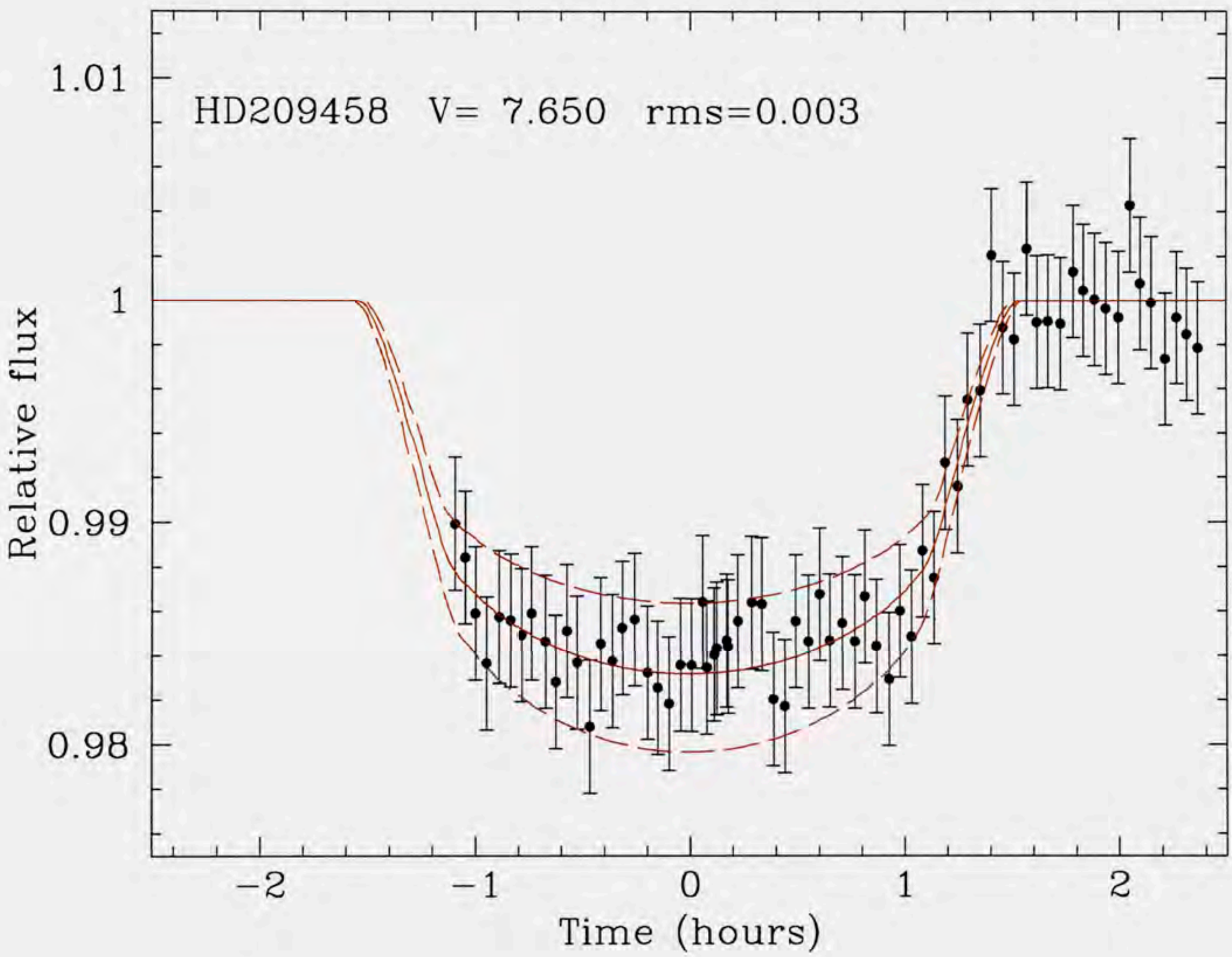

Figure 1.5. Early APT observations of two transits of HD 209458 b, reproduced from fig. 3.1 of Marton Hidas' thesis. It has been fit with the model of Brown et al. (2001) (solid line), with two additional models indicating fits with the planetary radius ± 10% (dashed lines).

cluster NGC3532. Seven candidates were identified across the 8 fields; these were subsequently identified as eclipsing binary systems. One candidate was found to be a detached eclipsing binary system of two K7V dwarfs, which was investigated more thoroughly due to the scientific interest in deriving the absolute parameters (e.g. radii) of low-mass stars (Young et al. 2006). Additionally, the field centred on NGC6633 was searched for variable stars and 49 light curves were identified. The majority of the results from the period 2001–2004 are presented in Hidas et al. (2005).

1-5.2 Simulations

In order to improve the observing strategy, a series of Monte Carlo simulations of potential transit detection rates was performed, described in full detail in Hidas et al. (2005). In the simulations, fake star fields were realistically recreated using the luminosity function for the Solar neighbourhood, allowing for an exponential decrease with scale height above the Galactic plane; these fields were then sampled using the spatial resolution of the APT. Planets were randomly distributed in period and inclination around the stars, and for a particular set of observational parameters, the probability of detecting at least two transits for each planet was assessed.

The parameters that were varied included observation bandpass (V or I), Galactic latitude, time-sampling of the fields, number of nights of observations obtained, and the number of hours of observations obtained each night. The results of these simulations defined our initial observing strategy, outlined in Section 3-4; in brief, the highest planet detection rate would be achieved by observing two fields in parallel in the I-band, for a minimum of 15–20 nights and 8–10 hours per night, between Galactic latitudes of 15°–45°. Figure 1.6 is reproduced from fig. 6.7 of the aforementioned thesis, and shows the turnover in the expected planetary yield at 20 nights for the observing strategy outlined above.

Based on this observing strategy and the assumption that 10 fields per year would be observed, the University of New South Wales Extrasolar Planet Search was predicted to yield 2–3 planet discoveries per year.

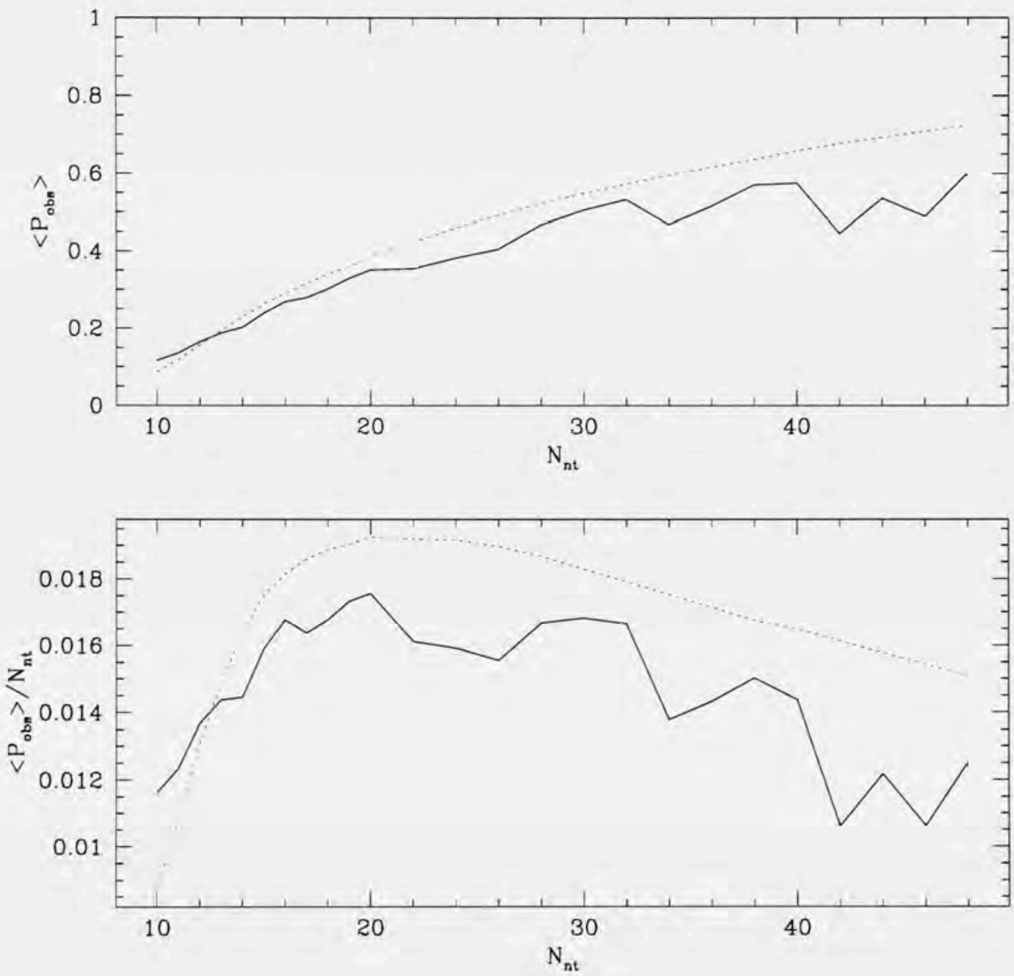

Figure 1.6. The length of an observing run resulting in the most efficient planet detection rate can be measured by $< \mathrm{P_{obs}} > /N_{\mathrm{nt}}$ (Mallén-Ornelas et al. 2003), where $\mathrm{P_{obs}}$ is, in this case, the probability of observing at least two complete transits averaged over the period range 1–9 d (sampled logarithmically), and for each night of observations covering ~ 8 hours. The top panel shows the average $\mathrm{P_{obs}}$ as a function of the total number of nights in an observing run. The bottom panel shows the turnover in efficiency beyond 20 nights, after which point the planet detection rate is increased by moving on to a new field.

1-5.3 This work

Part II of this thesis describes the University of New South Wales Extrasolar Planet Search in the period 2004 October to 2007 May. The aims of the project during this period were four-fold:

1. To build on the platform of the previous work and perform an efficient and sustained transit survey, compiling a large data set of time series photometry on tens of thousands of stars.

2. To extract the highest quality transit candidates from the data and to perform the further analysis required to determine the true nature of the observed systems.

3. To continually monitor the performance of the survey, identifying areas of improvement from the instrument design to the post-processing of the data, and to explore and implement solutions where possible.

4. To explore the additional science that could be performed with the final data set of high precision light curves, thereby increasing the scientific output of the survey.

Chapter 3 outlines the survey design, including the telescope, CCD camera and observing procedures. The photometric precision required for detecting transiting hot Jupiters is assessed with respect to the limiting noise factors inherent in the instrument design and observing site. The data reduction pipeline is described, and the survey strategy based on the simulations described previously is outlined.

Chapter 4 summarises the data that were collected during this period, and demonstrates the initial photometric precision that was achieved. The effect of systematics on the data, introduced in Section 1-2.6.5, is discussed. Several methods for alleviating the systematics are introduced and tested, and the final photometric precision is presented. The procedures and criteria for selecting transit candidates from the final data set are described, and a summary of the results given.

The results of the primary science driver for this project—analysis of transiting hot Jupiter candidates—are presented in Chapter 5. Initially, the candidates are assessed using available on-line catalogue information and higher spatial resolution archive images. The candidates that are not eliminated at this stage require additional follow up observations to be performed; the instruments and procedures used for these observations are described. The results for each candidate followed up are presented and discussed. Finally a list of the remaining candidates that have not had their status confirmed thus far is given.

One of the obvious byproducts of a transit survey that is of high scientific interest are well-sampled variable star light curves. Using the full data set, a variable star catalogue of 850 light curves was compiled, and is presented in Chapter 6. The procedures for extracting the variable light curves from the data set and calculating periods where appropriate are described. Several potentially interesting subsets of light curves from the catalogue are identified.

In the course of compiling the variable star catalogue, we discovered the first high-amplitude δ Scuti star to be found in an eclipsing binary system. This system was explored in significant detail, and the results are presented in Chapter 7. Radial velocity data were obtained, and fit simultaneously with the original light curve to give the absolute parameters of the two components of the system. This is the first time these parameters have been derived for a high-amplitude .

Finally, the conclusions of the survey with respect to the potential for detecting transiting extrasolar planets are discussed in Chapter 8. Solutions for some of the main issues identified during the period covered in this work are proposed. These include both software and hardware upgrades, to be performed before the next stage of the University of New South Wales Extrasolar Planet Search begins.

Part I

Vulcan South—Antarctic Planet Finder

Chapter 2

Project summary

The Vulcan South—Antarctic Planet Finder project was a collaborative effort between several teams to conduct a wide-field transit survey at the South Pole. The principal collaborators were the NASA Ames Research Center, the SETI Institute, the Center for Imaging Science at the Rochester Institute of Technology, the University of New South Wales and the Australian National University. The initial funding for this project was granted by the National Science Foundation for the three years 2003–2005.

This project represented the next phase of the Vulcan Camera Project, a wide-field transit survey undertaken at the Lick Observatory in California from 1998 to 2002. This survey used a small 10-cm telescope with a 4k $\times$4k CCD camera to observe a field of view of 49 square degrees (Borucki et al. 2001). Given the increasingly large number of groups undertaking transit searches at various locations, including space and multi-site campaigns, and the emergence of the Antarctic plateau as a prime astronomical observing site (see Section 2-1), the decision was made to propose Vulcan South—a reincarnation of the original project, with the same CCD camera housed in a new 20-cm photometer, to be based at the South Pole.

This chapter describes the short history of the Vulcan South project at the South Pole, from the installation of the hardware in 2004 January to its dismantling in 2005 December. A justification of the choice of the South Pole observing site is presented. The instrument design is described, and the data handling procedures that were designed to ensure maximum reliability and recovery of data outlined. The project was unfortunately afflicted by several hardware failures; one failure, in the analog-to-digital unit converter of the CCD camera, resulted in corruption of most of the images. Possible mitigation and correction strategies are discussed.

2-1 Advantages of the South Pole

The various motivations for choosing the South Pole as the site for this project can be loosely divided into two categories: astronomical and logistical.

The US Amundsen-Scott South Pole Station is a permanent base at the geographic South Pole, shown in Figure 2.1, at an altitude of 2850 m. It is occupied year round, and the personnel include science and technical staff who monitor and run the scientific experiments at the base. Prior to Vulcan South, astrophysics was already well established at the South Pole, with several large projects operating successfully, including millimetre (VIPER, Peterson et al. (2000)), infrared (SPIREX, Fowler et al. (1998)) and high energy astrophysics (AMANDA, Halzen (1998)) experiments.

The University of New South Wales had previously completed a rigorous optical/IR site-testing campaign at the South Pole (Ashley et al. 1996; Storey 1998; Phillips et al. 1999). After the success of the various experiments to characterise the site (several results are discussed in Sections 2-1.1 and 2-1.2) and the installation of key infrastructure (described in Section 2-1.5), the momentum and interest had gathered, and the time was ripe for an optical science experiment, as opposed to site testing.

The advantages for astronomical observations provided by a site on the Antarctic plateau are explained in detail in a number of places (Burton et al. 1994; Ashley et al. 2004). In comparison to many other sites, including those on the Antarctic plateau, the South Pole is in fact the ideal site for a wide-field extrasolar planet transit survey. The advantages of the site are summarised below, and compared with two of

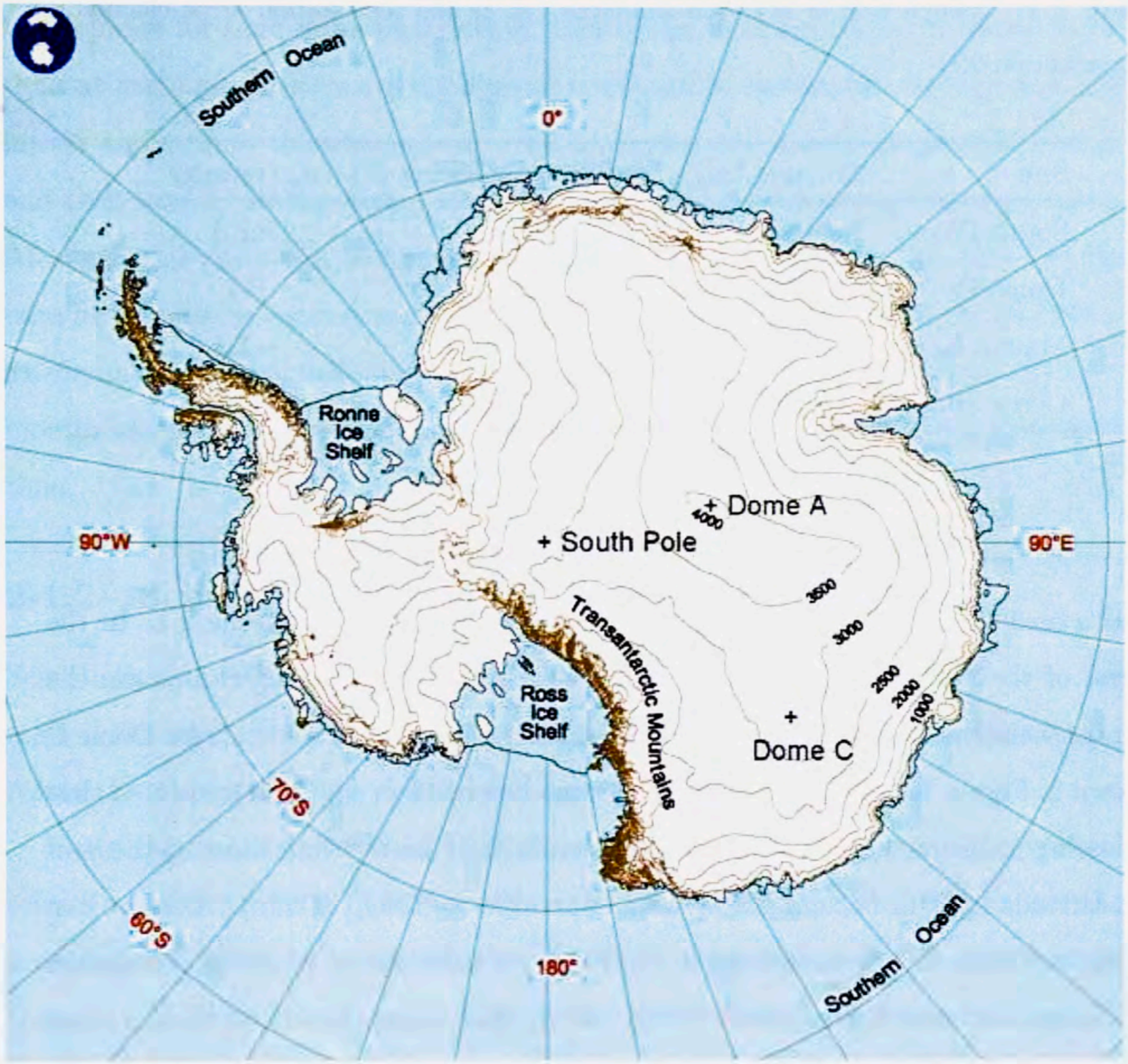

Figure 2.1. Antarctic plateau observing sites. (Australian Antarctic Data Centre)

the best representative mid-latitude sites, Mauna Kea (Hawaii) and Cerro Tololo (Chile), and also Dome C (Antarctica), an exceptional Antarctic plateau site.

2-1.1 Seeing

The possibility of exceptional seeing conditions on the Antarctic plateau has been postulated for well over a decade (Gillingham 1991; Burton et al. 1994). Seeing is a measure of the resolution we can obtain when observing a point source of light through the refractive index perturbations of the Earth's atmosphere. The extremely cold and dry atmosphere located above the Antarctic plateau is noted for producing

Table 2.1. Comparison of site characteristics. σ_s is the scintillation error calculated from equation 2.1.

Site	Altitude (m)	Median total seeing ($''$)	σ_s (mmag)
South Pole	2850	1.6	<1.3
Dome C	3250	0.27	0.4
Mauna Kea	4200	0.51	~1.3
Cerro Tololo	2200	0.95	1.5

the stable, low turbulence conditions required to achieve the best seeing.

The median seeing value for each of the four sites is given in Table 2.1. In the course of the University of New South Wales Antarctic site-testing campaign, the average seeing measurements were measured for the South Pole and also for Dome C (shown in Figure 2.1), at an altitude of 3260 m. Lawrence et al. (2004) reported that the seeing measurements at Dome C were significantly better than those at the best mid-latitude sites in Mauna Kea (Hawaii) and Cerro Tololo (Chile). The median seeing at Dome C was measured at $0.27''$ above an altitude of 30 m, compared to Mauna Kea and Cerro Tololo where the median seeing has been measured as $0.51''$ (Tokovinin et al. 2003) and $0.95''$ (Tokovinin et al. 2005) respectively. However the median seeing at the South Pole is $1.6''$ (Marks et al. 1999), which is substantially worse than the mid-latitude sites. This is due to the presence of a significantly turbulent boundary layer from 0–220m—above this height the median seeing drops to $0.32''$ (Marks et al. 1999).

Although the seeing measurements at the South Pole are high, Vulcan South was a wide-field project, with corresponding large pixels of $\sim 9''$ that are not sampling the seeing. Hence, improvement in the mean seeing would not translate into improved photometry. In fact, having the broader point spread function (PSF) provided by the relatively poor seeing would decrease the noise contribution from intra-pixel variations (Toyozumi & Ashley 2005).

Finally, it is variations in the seeing which contribute most significantly to photometric noise for time series photometry. One of the foremost causes of seeing variations at mid-latitude sites are the diurnal temperature variations—the sun rises and injects energy into the atmosphere, creating turbulence and increasing the seeing, and then sets. Over the night as the atmosphere cools, the seeing decreases again. Although this effect can be largely corrected for, the systematics introduced to the data in the process are non-negligible. However, during winter, the season for optical astronomy at the South Pole, this variation is largely removed as the sun sets for 6 months at a time. This creates an extremely stable atmosphere for long periods of time.

2-1.2 Scintillation

Scintillation can also contribute to the photometric noise. As the light from the stars is distorted by the atmosphere, the intensity of the light can fluctuate rapidly. Again, a stable atmosphere is the best way to decrease this source of noise.

Using the method described by Kenyon et al. (2006), one can use the vertical refractive index profile ($C_n^2(h)$, where h is the height above the site) to calculate the scintillation error, σ_s. The contribution to the photometric noise from scintillation at Dome C and Cerro Tololo can be derived using the Vulcan South survey parameters. The turbulence profile information required for the calculation is incomplete for the Mauna Kea and South Pole sites, however educated guesses can be made as to their values relative to Dome C and Cerro Tololo.

For Vulcan South, the exposure time (60 seconds) was much larger than the scintillation timescale, and therefore the scintillation error σ_s at the zenith is given by:

$$\sigma_s = S_3 D^{-2/3} t^{-1/2} \tag{2.1}$$

where D is the telescope aperture and t is the exposure time. The speed of the turbulence layer is $V_\perp(h)$, and S_3 is given by

$$S_3 = \left[10.7 \int_0^\infty \frac{C_n^2(h) h^2}{V_\perp(h)} dh\right]^{1/2} \tag{2.2}$$

Using the values for S_3 measured at Dome C and Cerro Tololo, the scintillation noise can be derived as 0.4 mmag and 1.5 mmag respectively, for D = 0.2 m and t = 60 seconds.

Mauna Kea is reported to have similar optical turbulence profiles to the Chilean site Cerro Pachon, nearby to Cerro Tololo (Tokovinin et al. 2005). The scintillation error at Cerro Pachon can be derived in the same manner described above as 1.3 mmag.

At the South Pole, as described in the previous section, the turbulence in the atmosphere is largely confined to a boundary layer up to 220m. Above this height, the atmosphere is exceptionally clear and stable. Since the scintillation error increases with h^2 (equation 2.1), it is dominated by the contributions from the higher levels in the atmosphere (4–16 km). Therefore we can assume that the scintillation error at the South Pole will be significantly better than the mid-latitude sites, given the stability of the upper atmosphere. Table 2.1 summarises the scintillation error contributions from the four sites.

For stars brighter than $R = 10$, the 1.5 mmag scintillation at Cerro Tololo is above the Poisson noise level expected for Vulcan South exposure times, and scintillation would therefore contribute to the total noise, and decrease the chances of detecting low amplitude transits. However, the 0.4 mmag value at Dome C is below the Poisson noise level, and therefore is a negligible source of error. As a measure of the level of significance, 1.5 mmag is the depth of a Neptune-sized object transiting a solar-type star. In order to detect these objects at the temperate sites, more transits would have to be observed in order to increase the S/N of the signal. Increasing the times spent on each field decreases the total number of observable fields, and as a result decreases the overall potential planet yield of the telescope.

2-1.3 Airmass variations

As indicated in Section 1-2.6.5, removing systematics from transit survey data has been recognised as a significant issue. One source of systematic noise is airmass variations—atmospheric extinction affecting the photometry of the stars as they rise and set. Variations in the airmass will cause variations in the noise contributions from seeing and scintillation, discussed in the previous sections, introducing an additional source of noise.

At the geographic South Pole, the celestial South Pole (CSP) is at a constant declination of $-90°$. The airmass through which the stars are seen remains constant throughout the year for each star, as they maintain a constant distance from the CSP at the zenith.

Although this constancy removes airmass variations as a source of photometric noise, it does reduce the total amount of sky accessible from the South Pole. However, the Galactic plane is high in the sky at all times, providing a large scope for target fields with large numbers of stars. Additionally, the constant airmass eliminates differential refraction and field rotation as potential sources of error. The constancy of the declination of the stars at the South Pole also alleviated a hardware failure described in Section 2-5.1.

2-1.4 Phase coverage

The amount of time required to observe a given field and maximise the number of planets found will depend on the achievable phase coverage: the most efficient phase coverage will result in the most efficient field coverage. Given a desired level of phase coverage, the number of fields observable per year at each of the four sites can be calculated.

Using the number of dark hours (defined as when the sun is more than 18° below the horizon) at each site, and the published figures for numbers of photometric nights, we can derive the final number of usable hours. These data are given in Table 2.2. Photometric nights at the mid-latitude sites are defined as completely cloudless nights. Although the mid-latitude sites have more true dark time, the exceptionally cloudless skies above Dome C puts the number of usable hours at this site between Cerro Tololo and Mauna Kea. Although the bright phases of the Moon were not included in this calculation, they will be less significant at the Antarctic sites as the maximum elevation of the Moon is far below the zenith for both sites.

Table 2.2. Usable dark time at potential transit survey sites. [a]Ortolani, S. (2003). [b]Osmer & Wood (1984). [c]Lawrence et al. (2007). [d]Travouillon et al. (2003).

Site	Dark hours	Photometric nights	Usable Hours
South Pole	1959	45%[a]	882
Dome C	1792	96%[b]	1720
Mauna Kea	3390	45%[c]	1526
Cerro Tololo	3312	60%[d]	1987

To simulate the cloud-affected dark time, an appropriate number of randomly selected 24-hour periods were removed from the dark time. At the South Pole, this would translate to 24 continuous hours being removed. At the mid-latitude sites, this could translate to three continuous eight-hour nights. The phase coverage of transit periods from 1–4 days is then calculated using the remaining dark time. Figure 2.2 shows the number of fields that could be surveyed at each of the four sites given a specified detection rate of 75% (hollow) and 90% (solid). A detection is defined as having observed at least two transits, partial or full.

The surprising result from this calculation is that although the South Pole has a lower number of usable dark hours by a factor of almost 2, the fact that they come in much longer continuous blocks than at the mid-latitude sites means the required phase coverage can be achieved rapidly, with 9 fields covered at the 90% detection level, compared to 7 fields at Dome C, 6 at Cerro Tololo and 5 at Mauna Kea. Dome C is also assisted by longer periods of dark time, with as good as or better field coverage as Cerro Tololo, and significantly better field coverage than Mauna Kea.

2-1.5 Infrastructure

Once the advantages of excellent astronomical conditions and phase coverage offered by an Antarctic plateau site became apparent, the South Pole had the clear advantage over other possible locations due to the significant level of infrastructure and

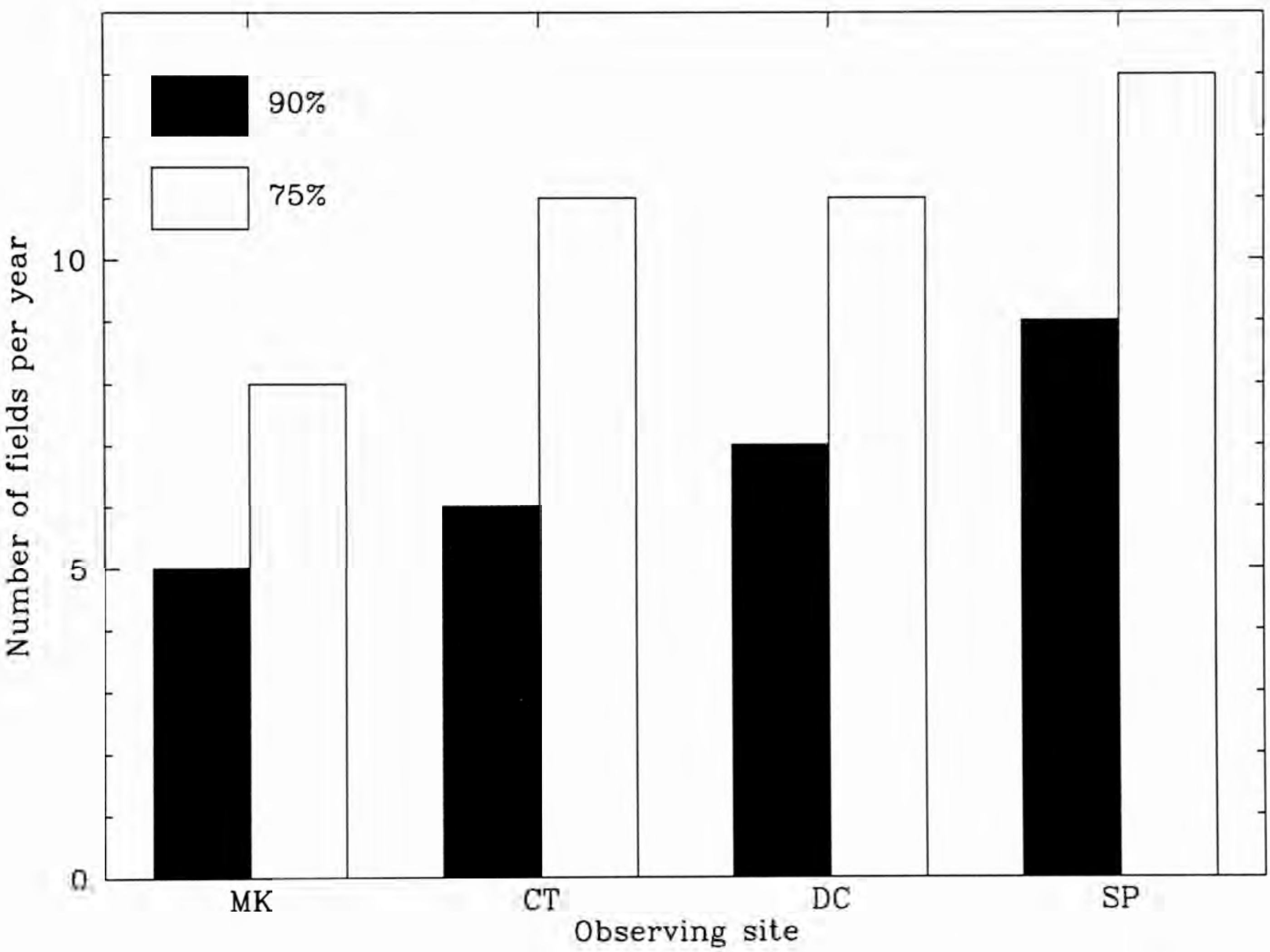

Figure 2.2. The number of fields observable at each of the four sites. Sufficient phase coverage must be achieved for each field such that there is a 75% (solid) to 90% (hollow) detection rate of at least three transit events, with periods of 1–4 days.

logistical support that was already in place.

The US Amundsen-Scott South Pole Station is manned year round by science, technical and support staff. This includes an ever-increasing number of winterover personnel who can perform limited on-site repairs as required during the months when the site is effectively sealed off from additional support. The station has sufficient power and network capabilities to execute, monitor and maintain a remotely operated project like Vulcan South.

Many of the hardware and software requirements for a project of this scale had already been put into place over the previous six years during the extensive site-testing campaign completed by the University of New South Wales and the Australian National University. These included a fully functioning autonomous site-testing laboratory, the tower and mount for the telescope, the computers and software required to run these components, and an Iridium communications link for data transfer, which are described in more detail in Sections 2-3 and 2-4.

2-2 Proposed observing strategy

In order to maximise the chances of detecting planetary transits, the following observing strategy was proposed. The Besançon Observatory Galactic stellar population models (Robin et al. 2003) would be used to select appropriate fields in or near the Galactic plane with a significant number of later-type spectral stars (F0–M5 dwarfs). The coordinates of the first five proposed fields and the numbers of dwarfs in each are given in Table 2-2. Each field would be observed continuously until sufficient phase coverage between periods of 1–4 days had been achieved for a $\sim 90\%$ detection rate (see Section 2-1.4). Flat field frames were to be obtained during the long evening and morning twilight periods, and bias and dark frames to be obtained at regular intervals during the scheduled observing.

The filter chosen was a single custom filter with a central wavelength of $\lambda =$ 675 nm and a FWHM of 30 nm. There were several motivations for this choice: to avoid the bright 630.0 and 636.4 nm OI auroral lines and the night sky lines longward

Table 2.3. Proposed Vulcan South target fields. Each field is 7°×7°. The numbers of F0–M5 dwarfs are taken from the Besançon Observatory Galactic models down to $R = 13$.

Field	l	b	Constellation	F0–M5 dwarfs
1	285	-20	Carina	7100
2	285	-10	Carina	9300
3	285	0	Carina	10700
4	300	-10	Musca	9400
5	300	0	Crux	10700

of 720 nm (Dempsey et al. 2005); to increase the contribution to the photometry of the smaller late spectral type targets relative to larger stars; and to balance these requirements with the quantum efficiency of the CCD, which is 0.35 in the red. The throughput of this filter is shown in Figure 2.3.

The eventual aim was for automated observing, with daily status reports containing the pertinent system status information to be emailed to the team members. However, due to various setbacks this was never fully implemented.

2-3 Instrument design

The basic Vulcan South system consisted of a small optical photometer contained within an hermetically sealed shell and controlled via an external equipment shelter (EES), both of which were constructed by our collaborators at NASA Ames. The photometer and shell were mounted on the two-axis Generic Mount (GMount), which sits with the EES atop the 7.5 m Gtower. They were powered and controlled externally by the nearby Automated Astrophysical Site Testing Observatory (AASTO). The photometer was installed at the South Pole with the pre-existing GMount and AASTO facilities in 2004 January.

2-3.1 Photometer

The Vulcan South photometer was based around a fast (f/1.5) 20-cm refractor illuminating a large format CCD camera. The fast lens was chosen to obtain the large focal plane of 50 mm, producing the wide field of view onto the CCD of 49 square

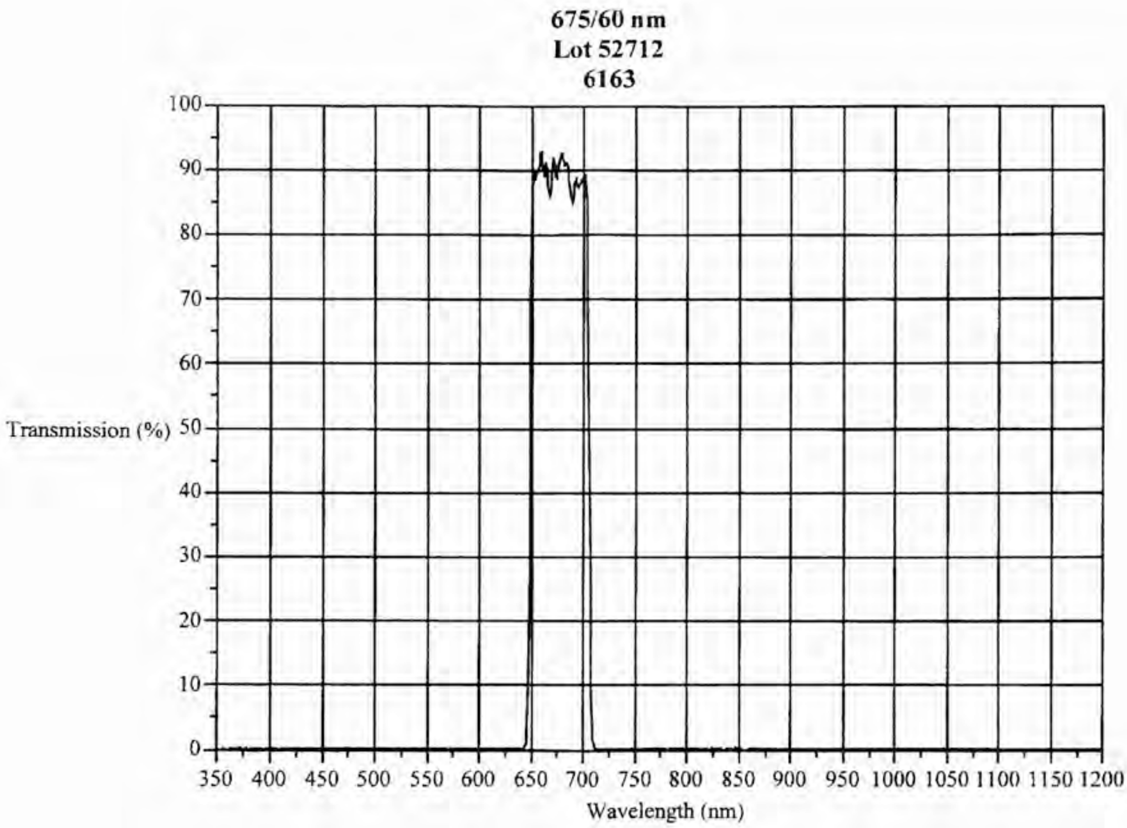

Figure 2.3. Vulcan South optical filter throughput.

degrees. Thermal testing was undertaken at NASA Ames and the lens was found to operate well down to a temperature of $-30°$C.

The CCD camera was supplied by the Rochester Institute of Technology, and consists of a Roper PXL Camera and a front-side illuminated Kodak 16800 CCD. The CCD has 4096×4096 pixels of 9 μm, which can be read out in 16 seconds. With the field of view, this results in a relatively low spatial resolution of $9.7''$ pixel^{-1}. Previously this camera served in the Vulcan Camera Project at Lick Observatory (Borucki et al. 2001).

The photometer, CCD camera and filter are mounted on a temperature-controlled optical bench to maintain focus. The bench is mounted inside a reinforced, cylindrical, insulated shell, to provide temperature control and protection from the weather. At the front of the shell is a coated 25 cm diameter optical window, which is heated to keep it clear of ice. The presence of ice is detected through scattering of light from an LED. The photometer is shown without the exterior shell in Figure 2.4, with the CCD camera visible at the right of the figure.

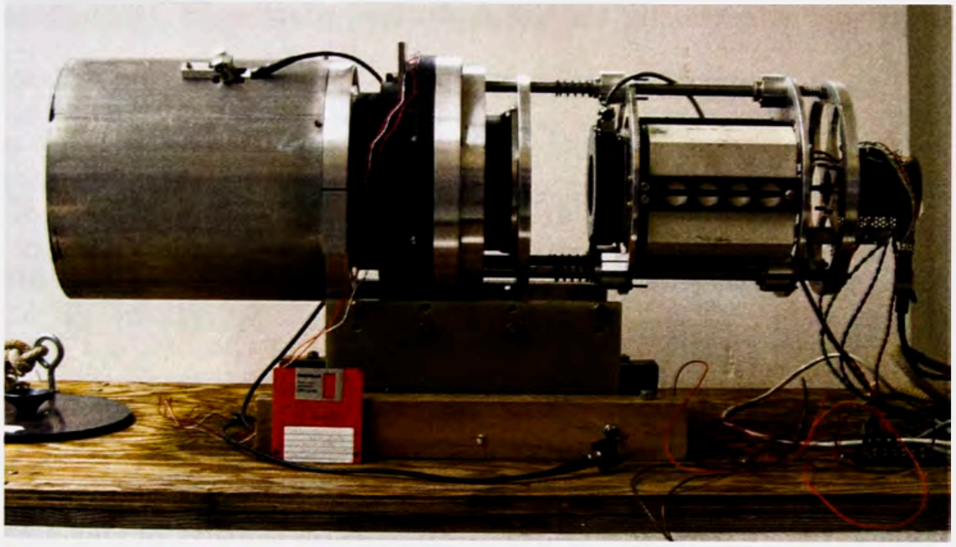

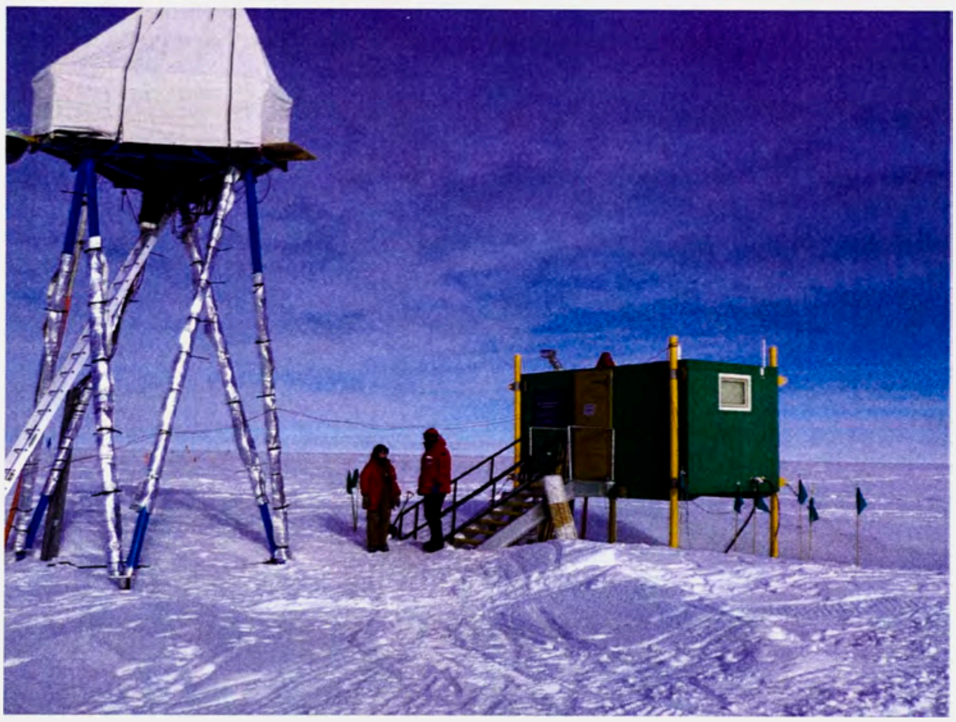

Figure 2.4. The Vulcan South hardware. The top image shows the photometer, without its hermetically sealed shell, with the CCD camera to the right. The bottom image shows the AASTO on the right and the Gtower on the left. In the centre are our summer and winterover technicians, Brenda Everitt (left) and Dana Hrubes (right). The tent has been installed on the Gtower for re-installation of the repaired camera.

2-3.2 AASTO

The Automated Astrophysical Site-Testing Observatory (AASTO) is a small, self-contained, portable laboratory. It was commissioned from Lockheed by the University of New South Wales and the Australian National University for the purposes of remote astrophysical site-testing on the Antarctic plateau in 1996 (Storey et al. 1996) and was officially opened in January 1997. The design is based on the Automated Geophysical Observatory, half of dozen of which were already operating successfully on the Antarctic plateau at the time. It was built as part of the first phase of the extensive site-testing campaign being undertaken by the University of New South Wales (Storey 1998), and is shown installed at the South Pole in Figure 2.4.

The primary considerations in the design and implementation of the AASTO and its suite of site-testing instruments were that they be reliable, operate autonomously, require very little power, and have negligible impact on the surrounding environment. For Vulcan South the power restrictions were relaxed as the AASTO was drawing from station power, in contrast to previous years when it was self-powered by thermoelectric generators (Storey 1998)

The AASTO supported several successful site-testing instruments, operating for nearly nine years until it was decommissioned in 2005 December. Prior to Vulcan South, these included an automated weather station, near- and mid-infrared sky monitors (NISM and MISM) (Storey et al. 1999), a sonic radar (SODAR) experiment (Travouillon et al. 2003), a fibre-fed spectrometer (AFOS) for detecting aurora and sky lines (Dempsey et al. 2004), a submillimetre sky monitor (SUMMIT), and a differential image-motion monitor (ADIMM) (Dopita et al. 1996).

For the Vulcan South project, the AASTO served the primary purpose of providing a benign environment in which to house and supply power for the control computers, uninterrupted power supply (UPS) systems, hard drive arrays, Iridium phone, and various monitoring systems. However, the hard limit on the length of the cables from the CCD camera housed at the rear of the photometer on the tower meant that not all control computers could be housed in the AASTO, necessitating the development of the External Equipment Shelter (EES), installed atop the Gtower with the photometer.

2-3.3 External Equipment Shelter

The External Equipment Shelter (EES) was a large, insulated Zarges K470 case, which was mounted beside the GMount. It contained most of the CCD camera electronics, including the control and power box and a focus control unit. Also included were an additional computer for control, a network switch and a KVM (Keyboard, Video, Mouse) over IP unit for convenient control of the computer, and various instruments for monitoring the conditions of the EES and of the photometer (D. Caldwell et al., in preparation).

2-3.4 GMount and Gtower

The photometer is mounted at the top of the 7.5 m Gtower, which is adjacent to the AASTO (on the left in Figure 2.4). The pointing of the photometer is controlled and driven by the Generic Mount (GMount), an altitude-azimuth mount with a single counterbalanced strut. The alt-az design was chosen due to its low power requirements, since it can be approximated by an equatorial mount so close to the South Pole, and therefore the amount of power required to drive the altitude axis is very low. Additional reasons were the ease of deployment, and the lower wind resistance compared to other designs that were considered, including gimbal and self-adjusting polar (Dopita et al. 1996). The mount is designed to be as insensitive to temperature variations as possible, and as such the axis encoding is through an inductosyn transducer mounted on each of the two axes. The failure of one of these transducers and the resulting impact on the project is described further in Section 2-5.

2-4 Proposed data acquisition and handling procedures

The software development was designed with the eventual goal of autonomous operations for several months at a time, with minimal onsite intervention. A LabVIEW platform was constructed by a private contractor to perform the following tasks:

- to control the camera operations and auxiliary hardware, with immediate reporting of errors to team members via email; this included monitoring the temperature controllers inside the photometer, at the photometer window and inside the EES and maintaining a specified set-point temperature with appropriate voltages; pointing control of the GMount through the separate GMount computer, and frost detection via a short feedback test with an LED illuminating the front window before each exposure,

- to implement observing scripts facilitating autonomous acquisition and storage of star field images and calibration frames; the images were to be stored in the standard FITS format, compressed, and archived in round-robin fashion in a set of external hard drives, so that the failure in any one drive would merely results in a small loss in time sampling,

- to provide an interface through which remote observers could change the observing scripts, modify the system configuration, issue immediate commands in place of scripts, and update the source code,

- to deliver daily status reports via email to team members, including: hourly temperature readings from inside the photometer and the EES; image data for any acquired images, with the image name, time of acquisition, exposure time, size, CCD temperature, and possibly rudimentary pixel statistics; a log of the GMount pointing commands; a record of the frost detection results and voltages; and any additional out-of-routine commands such as focus runs or power cycling occurrences, and

- to provide diagnostic tools for testing various aspects of the instrument and software systems.

The two computers that controlled the photometer and data storage were connected to each other and the South Pole intranet via an ethernet connection. The connectivity beyond the South Pole network is limited to a few hours per day when the satellites are above the horizon, and there is a strict bandwidth limitation. Therefore, given the expected rate of data collation (1–2 images every five minutes) and the size of each image (32 MB), it would not have been feasible to return the data for analysis in real time over the internet connection. It was determined that at the end of each winter observing season, the hard drives would be physically shipped out to the team members for analysis and replaced with new drives.

The data were to have nominally been reduced with the pre-existing Vulcan Camera Project data processing pipeline. This customised pipeline is described in Borucki et al. (2001) and relies on differential relative photometry; in brief the steps were as follows:

- correction of each individual image with calibration frames (dark and flat frames) and for CCD non-linearity,
- registration of each image with respect to a chosen reference frame via point-spread function (PSF) fitting of the brightest stars for centroiding, then a second-order coordinate transformation,
- PSF-fitting for each star in the transformed frame, including correction for energetic particle hits ("cosmic rays"),
- extinction correction via ensemble fitting of the brightest non-variable stars, and
- dividing the extinction-corrected flux by the average of the extinction-corrected comparison stars.

This pipeline was demonstrated to achieve better than 1% hourly precision in the magnitude range $V \sim 9 - 12$ with the data obtained at the Lick Observatory (Borucki et al. 2001).

2-5 Instrument performance

2-5.1 GMount

When the hardware was initially installed at the South Pole in 2004 January, an attempt was made to fix an intermittent fault in the GMount that had been noticed previously. The fault was that the altitude axis would lose knowledge of its position, slewing into the limit switch, and several pre-amplifiers were replaced in the hopes of solving the problem, which could thereafter not be reproduced. The system was left operating but inactive until twilight and observations began in 2004 April. The fault returned almost immediately and soon after became permanent—the altitude axis could not be used.

The winterover technician performed a slew of diagnostic tests, and the fault was eventually isolated to the rotor in the inductosyn transducer encoder on the altitude axis. This was a custom-made part and no spares were available; additionally it was not feasible to perform the repair on top of the 7.5 m tower in the winter months, and the temperature was below that at which the machinery required to lift the mount off the tower and into a warm laboratory could run. Therefore a repair was not deemed possible. A software patch was devised by the team which allowed the system to operate in azimuth-only mode, with the altitude axis left in a fixed position. The repeatability of setting this position after any movement of the altitude axis was found to be $\sim 0.1^{\circ}$ using either a mechanical post or a digital level.

2-5.2 CCD camera problems

When observations recommenced in 2004 June, it was discovered that the the CCD camera had failed. Another series of diagnostic tests tracked the source to a serial clock board on the camera head. The manufacturer indicated that the problem could be a known fault with a double Schottky diode on the board, however a replacement diode was not available on the station. Again, the repairs were deemed too risky for the personnel and equipment to be undertaken during the winter. Observations were halted for the remainder of the observing season. The camera was subsequently removed and shipped back to the US for repair in 2004 November.

In 2005 January, a team of four people comprised of the candidate and Colin Bonner from the University of New South Wales, and Doug Caldwell and Fred Witteborn from the NASA Ames Research Centre were deployed to the South Pole for two weeks. During this time the camera was reinstalled in the photometer, the software systems were upgraded and reconfigured, and the GMount was aligned and tested in the new azimuth-only mode.

Calibration frames were obtained during twilight in 2005 April, however by the time scheduled observations of the star fields began in 2005 May, a new camera fault had occurred: the 14-bit analogue-to-digital unit (ADU) converter had acquired "stuck" bits. When reading out an image, each pixel can have a value between 0 (all bits set to 0) and 16383 (all bits set to 1). However, bits 0 (pixel value of 1), 1 (pixel value of 2), 2 (pixel value of 4), 6 (pixel value of 64) and 10 (pixel value of 1024) were all stuck at either 0 (bits 0 and 2) or 1 (bits 1, 6 and 10). The data that resulted were of the quality shown in Figure 2.5; this is a 100×100 pixel cut-out of the centre of a raw image. The problem was thought to be in the ADU converter daughter board, and despite considerable effort it was not possible to repair.

Bits 0, 1 and 2 contributed pixel values that were below the level of Poisson noise expected for even the faintest stars, and so could be ignored; bits 6 and 10 on the other hand were a significant problem. Several ideas were explored to try and correct the data.[1]

2-5.2.1 Varying the exposure time

The flux in each pixel can be approximated by $f_1 = i * t_1 + b$, where f_1 is the total flux measured by the ADU converter, i is the incident flux per second on the pixel, t_1 is the exposure time in seconds and b is the bias level. If you increase the exposure time by some factor, for example by doubling it to $t_2 = 2 * t_1$, the new flux in the same pixel should be $f_2 = i * t_2 + b$. It should therefore be possible to determine

[1]Much of the discussion and initial testing of the possible solutions took place during the candidate's one week visit to the NASA Ames Research Center in 2005 October.

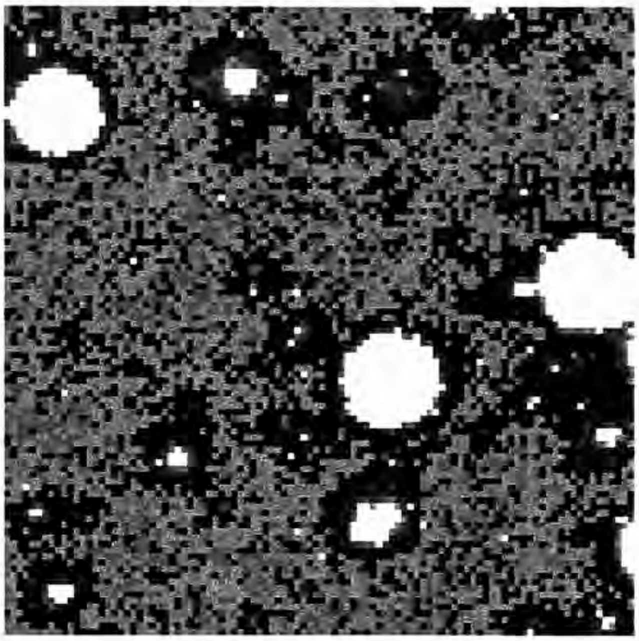

Figure 2.5. 100×100 pixel cut-out sample of corrupted data. The image contrast has been stretched to highlight the differences caused by the stuck bits; only the centres of a few stars are actually saturated.

the true values of the stuck bits and solve for the correct fluxes by using the ratio of the exposure times. Regarding bit 10, there are four possible resulting scenarios:

- the bits should be turned on in both exposures, therefore $t_2/t_1 = (f_2 - b)/(f_1 - b)$,
- the bit should only be turned on in the second exposure, therefore $t_2/t_1 = (f_2 - b)/(f_1 - b - 1024)$,
- the bit should only be turned on in the first exposure, therefore $t_2/t_1 = (f_2 - b - 1024)/(f_1 - b)$, and
- the bits should be turned off in both exposures, therefore $t_2/t_2 = (f_2 - b - 1024)/(f_1 - b - 1024)$.

However, in the presence of Poisson noise, especially in the brightest stars, the additional stuck bit 6, and the absence of accurate pointing to keep the incident flux on the same position on the CCD, simulations indicated that this method would not reach the level of reliability for the extraction of precision photometry.

2-5.2.2 PSF-fitting

One possibility was that if enough corrupted images were registered into the same frame and stacked together, it might be possible to extract the stellar PSF, which could then be used on the individual images to identify pixels that were incorrect. Unfortunately stacking the images typically exacerbated the problem rather than alleviating it, and additionally the PSF varied considerably across the wide field of view, adding another layer of complexity to the problem.

2-5.2.3 Local pixel cleaning

By taking each pixel on a case-by-case basis, it is possible to compare the pixel value to its surrounding 8 neighbour pixels, and determine to some extent which pixels should have bit 10 set to zero. For instance, if in a set of 9 pixels, the values are 4154, 4195, 4282, 4239, 5301, 5366, 5256, 5392 and 5409, the latter 5 pixels most likely need to have bit 10 set to zero, since they are all ~ 1024 greater than the first four. By completing multiple passes of the image and taking into account the flat-field pixel-to-pixel variations, a relatively "clean" image can be produced; if several of these cleaned images are stacked together, one can form a master image which reliably identifies the state of bit 10. An example of a stack of 9 cleaned image is shown in Figure 2.6, which is an obvious improvement on Figure 2.5. The degradation in quality around the edges is due to the smaller number of neighbour pixels with which each pixel can be compared. However, this method is far less effective for cleaning bit 6, which is a problem for the fainter stars in the field.

Ideally, a master image of the entire field would be generated. Then the master image would be inverse-flat-fielded and scaled to each individual image, which could then be corrected on a pixel-by-pixel basis. How this would effect transit detection is an important question. If each pixel is being corrected back to some "ideal" value, but in reality the pixel value is varying, variability above some threshold will be lost. If we take the upper limit on a potential planetary transit detection as a 5% change in flux, then for the brightest unsaturated pixels this is ~ 800 counts. This is less than the unit correction level of 1024, but approaching the line between an obvious

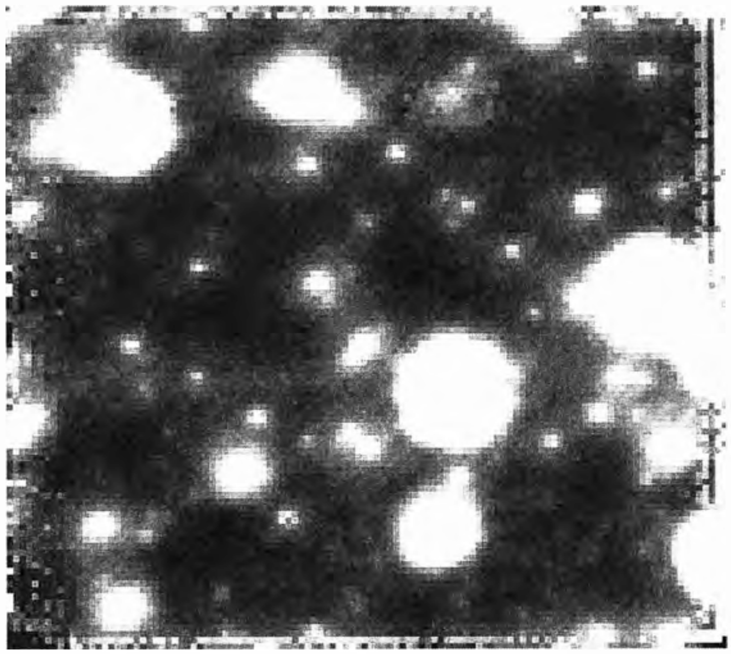

Figure 2.6. 100×100 pixel cut-out sample of cleaned data.

correction and a more complex situation. For the majority of stars, which are below the level of saturation, variations due to transit-like events should be preserved.

2-6 Data analysis

Approximately 2 months of the corrupted data were obtained from 2005 June to 2005 August on Field 2 (see Table 2-2). These data were shipped back to the US in 2005 December for analysis. Funding for the project was not renewed, and the instrument was removed from the site at the same time. It was suspected that even with the local pixel cleaning method, the problem of bit 6, the errors introduced by the lack of accurate pointing, and the relatively short duration and sporadic nature of the final data set, any photometry extraction would fail to meet the precision required for the detection of transiting planets. Combined with the lack of funded personnel time on this project, the data are currently stored with no immediate plans for further analysis.

2-7 Conclusion

The Vulcan South—Antarctic Planet Finder project represented the next technical phase in optical astronomy at the South Pole after the site-testing campaign was completed. The challenge of installing, testing and repairing a new system designed to run virtually autonomously for the next nine months in under two weeks each summer proved daunting. The failure of three separate components was critical to the outcome of the project. Although all possible means of resurrecting the project were explored, and much appreciation in this respect must go to our winterover technician for both seasons, Dana Hrubes, for the considerable effort that he put into diagnosing the problems in difficult conditions and investigating every possibility for on-site repair, a lack of science results from the first two years' observing resulted in a lack of additional funding to repair the mount and the camera. However, the quality of the South Pole as a site for transit surveys, or indeed other surveys requiring high precision time series photometry, is undiminished, and we hope to see this potential exploited in the near future.

Part II

The UNSW Extrasolar Planet Transit Search

Chapter 3

Survey design

The University of New South Wales Extrasolar Planet Transit Search is a wide-field optical imaging survey, with the primary science driver of detecting transiting hot Jupiters. Given the technical difficulty that this poses, it is critical to optimise the survey design and strategy, and to be able to fold in modifications and improvements as they are identified.

This chapter describes the survey design during the period 2004 October to 2007 May, following on from the period 2001–2004 discussed in Section 1-5.1. Section 3-1 describes the telescope set-up and observation procedures. Section 3-2 details the photometric precision required of the survey in order to detect the low-amplitude transit signals. The factors limiting our ability to achieve this precision are discussed, drawing on the results of the 2001–2004 period. Section 3-3 details our customised data reduction pipeline, and Section 3-4 describes the survey strategy we developed to maximise our transit detection rate.

3-1 The Automated Patrol Telescope

The Automated Patrol Telescope (APT) is a fully robotic telescope situated at Siding Spring Observatory, Australia. The telescope is owned and operated by the University of New South Wales and is dedicated to this transit survey. It was originally a Baker-Nunn satellite tracking camera, based in Woomera, Australia in the 1960's, then moved to a site near Canberra, and finally donated to the University of New South Wales by the Smithsonian Institute in 1987. It was then modified and shipped to the present site at Siding Spring Observatory. It is housed in a small detached building on-site, shown in the top panel of Figure 3.1. The roll-off roof provides access to most of the sky, with software limits of -70°S and +30°N, and a hardware limit ±6 hours either side of the meridian. The telescope has a clear aperture of 0.5-m, which is the largest of the wide-field transit surveys (see Table 1.1).

Modifications to the telescope continue to be made as the survey highlights potential improvements. One of the recommendations of the 2001–2004 findings was to increase the hour angle software limit from ±4 hours to allow for up to 10 hours per night on a target field at an airmass of < 2, as this was predicted to increase the transit detection rate by 50%. This modification was made in 2005 November, by introducing a zenith distance limit, which allowed the hour angle limit to be increased to ±6 hours.

Another change was the addition of a hood surrounding the lens cap at the top of the telescope in 2006 November. This was designed to decrease the amount of moonlight making its way into the telescope: analysis had shown that the times of moon-rise and moon-set were correlated with significant undesirable signals in our measured photometry. The lens hood is shown in the bottom panel of Figure 3.1.

3-1.1 Optical design

The telescope has an f/1 focal ratio and a 0.78-m spherical primary mirror. The original Baker-Nunn optical design utilised a curved focal plane, and did not allow the insertion of a filter. As described in Carter et al. (1992), the original three-element lens was modified to give a flat focal plane of 5° diameter with the use of a filter. There are five filters available, including Johnson *BVRI* and a clear filter.

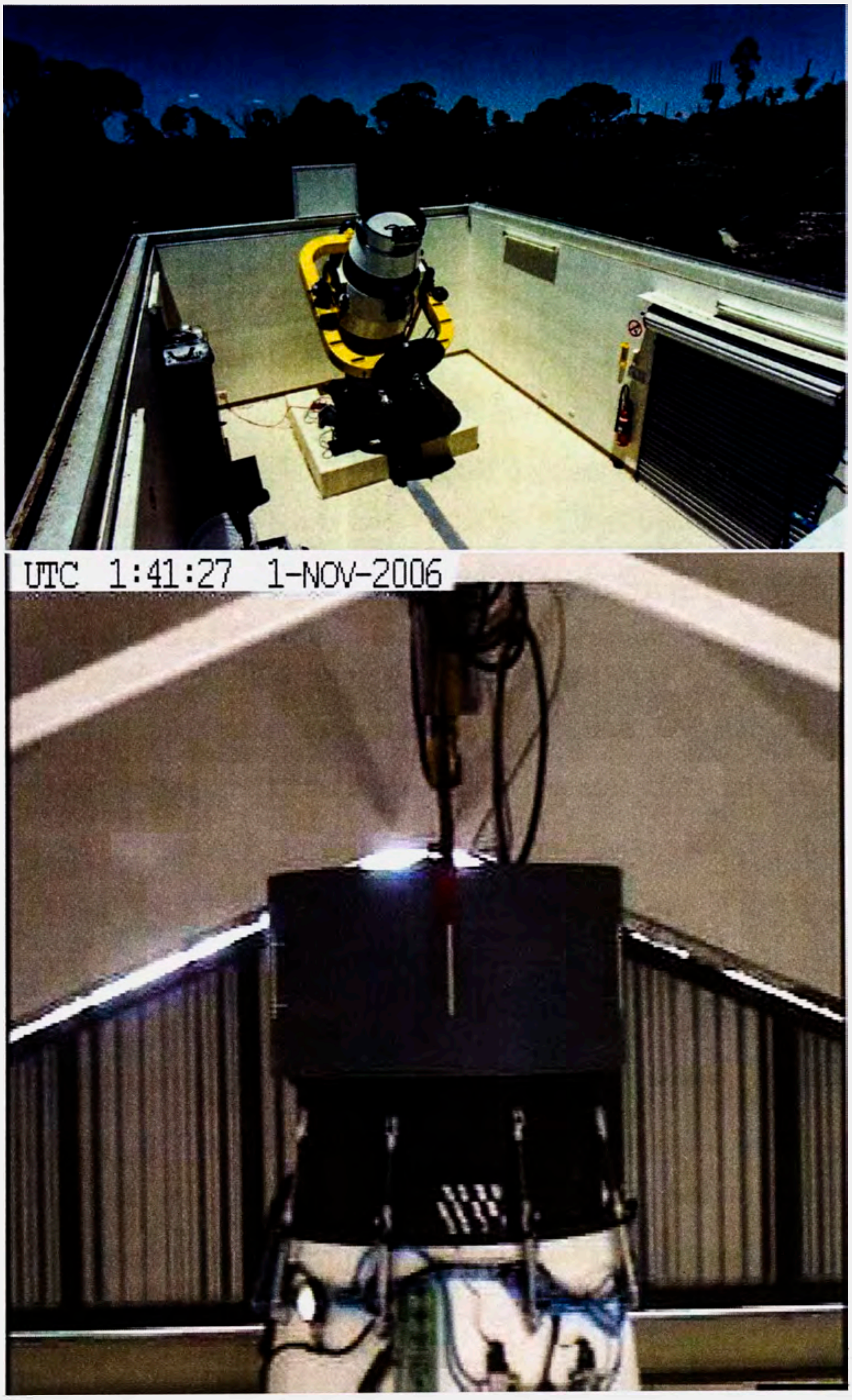

Figure 3.1. The Automated Patrol Telescope. The top panel shows the telescope with the roof retracted (Photo: Michael Ashley). The bottom panel shows the hood that was added to reduce scattered moonlight, taken with the colour web-camera.

3-1.2 CCD

The charge-coupled device (CCD) camera used for this survey is a Wright Instruments EEV (English electric valve) CCD05-20 chip. The layout of the chip is 770 columns $\times$ 1152 rows of pixels, and the data are typically read out with an additional 30 columns of overscan region. The pixels are 22.5 μm on each side, providing a spatial resolution of 9.43 arcsec pixel^{-1}. This gives a field of view of 3° E-W $\times$ 2° N-S.

A new CCD camera giving a $7 \times 7°$ field of view has been built for this project and we expect it to be installed in 2008. This camera and the implications for the project are discussed further in Section 8-2.2

3-1.3 Remote operation

The survey is designed to be carried out remotely—i.e. without a dedicated observer on-site. There is a single PC running Linux that controls the telescope operations—the telescope itself, the CCD camera, the shutter, and the building status (for example lights on or off, roof open or closed). Observing is generally performed via remote log-in to this PC and the execution of various shell scripts, unless an available observer is on-site for other reasons. Observations are scheduled for each night when the weather is clear and the moon is not full.

On a typical night, there will be two rostered observers—one to observe from dusk to midnight, and one from midnight to dawn. Initially, the weather is assessed using the all-sky camera installed near the APT building for this purpose, and also data downloaded from the weather stations installed on the nearby Australian National University 2.3-m telescope and 3.9-m Anglo Australian Telescope. If the weather is clear, the first observer will log in to the PC, open the roof, start the telescope and run the script for obtaining evening twilight flat frames. Once the sky is dark enough this script automatically stops, and the observer will start the script to observe the scheduled field/s. After this point the observing itself is almost completely automated and the primary role of the rostered observer is to monitor the small amount of status information that is returned and also the weather and humidity conditions. The telescope can continue operations up to 95% humidity due to a small amount of dry air that is injected after each exposure between the lens and the large air-tight pneumatic lens cap. The second observer will take over the monitoring at midnight and, if the weather permits, allow the scripts to automatically switch over to morning twilight scripts at dawn. The scripts automatically stop when the sky becomes too bright, at which point the observer shuts down the telescope, closes the roof, and runs a few housekeeping scripts. A log is kept each night of the rostered observers, the fields that were observed, the general weather conditions, and any problems that were encountered.

It is extremely important with remote observing to ensure that fail-safes are in place for different scenarios. As a result, while the telescope is operational a crontab safety script monitors various pieces of information, and if for example the internet connection to the control PC is disconnected, and therefore the remote observer has no access to the telescope, the script will automatically close the roof. This will also occur if the control PC loses connection with the 2.3-m weather station, or indeed if either of the 2.3-m or 3.9-m domes close, although in these latter cases the script can be overridden by the observer. There are also two web-cameras located within the telescope enclosure, one pannable colour camera and one fixed infrared camera, associated with incandescent and infrared lamps respectively, giving the observer the means to visually ascertain the status of the roof and of the telescope. Finally, there is generally an on-site technician who is on-call to close the roof and shut-down the telescope as a last resort.

3-2 Photometric precision requirements and limitations

As described in Section 1-2.6.2, transit surveys are a numbers game. Hot Jupiters have a low ($\sim 10\%$) geometric probability of transiting their host stars, and observing windows dictated by diurnal and seasonal constraints decrease the opportunities to detect these transits in the numbers required for a concrete detection. In order to maximise the detection statistics, surveys must aim to observe tens of thousands of stars with an extremely high photometric precision. For clarity, we are using *photometric precision* to describe the repeatability of the magnitude measured for a single star, and we use the root-mean-square (rms) of the residuals of a star's magnitude to its mean magnitude as a measure of this:

$$\sigma_{\mathrm{rms}} = \sqrt{\frac{1}{N}\sum_{i=1}^{N}(I_i - \bar{I})^2} \tag{3.1}$$

here N is the number of observations, I_i is the magnitude of the ith observation and $\bar{I}$ is the mean I-band magnitude over all observations.

Recalling that the depth of a Jupiter-sized planet around a solar-type star is ~ 10 mmag, we need to achieve an rms magnitude variation smaller than this. Given this basic requirement and our desire to utilise our large aperture advantage over other wide-field surveys, we are aiming to achieve a photometric precision of less than 10 mmag for stars with magnitudes $8 > I > 12$, and less than 50 mmag for stars with magnitudes $12 > I > 14$.

The photometric precision we can realistically achieve is limited by a number of sources of noise. In his thesis describing the establishment and initial phases of this survey in the period 2001–2004, Marton Hidas performed a rigorous characterisation of these sources using simulated APT images and the interested reader is referred to his thesis for a full discussion.[1] The calculations for the Poisson noise and scintillation contributions are updated here to reflect the change of filter from Johnson V to Johnson I, and the results are summarised below.

3-2.1 Poisson noise

Poisson noise is the statistical noise inherent in the fact that the flux impinging on a CCD is composed of a discrete number of photons. For simple aperture photometry the rms magnitude variation is given by:

[1] `http://www.library.unsw.edu.au/~thesis/adt-NUN/public/adt-NUN20060118.110819/index.html`

$$\sigma_{\mathrm{P}} = \frac{a}{f}\sqrt{\frac{f+s}{g}} \tag{3.2}$$

where f is the flux and s is the sky in the photometry aperture in analogue-to-digital unit (ADU) counts, g is the gain in electrons per ADU, and $a = 2.5/\ln 10$. To assess the contribution to our error budget of 10 mmag, we can use a typical 60-s frame in the I-band. This corresponds to a zero-point of $I \sim 22$ (the apparent magnitude of a star that would cause 1 ADU of flux to be detected at zero airmass), a gain of 8 e-/ADU, a dark time sky count of $\sim$ 2000 ADU and the relation $m = z - 2.5\log f$. For stars of 8$^{\mathrm{th}}$ magnitude we find $\sigma_{\mathrm{P}} = 0.6$ mmag, and for stars of 14$^{\mathrm{th}}$ magnitude we find $\sigma_{\mathrm{P}} = 4.2$ mmag, compared to $\sigma_{\mathrm{P}} = 0.5$ mmag and $\sigma_{\mathrm{P}} = 3.1$ mmag respectively in the V-band. The increase is due to the sky background which is considerably higher in the I-band.

3-2.2 Atmospheric effects

- Scintillation: As described in Section 2-1.2, this is the noise due to the fluctuations in intensity caused by atmospheric distortion. There is inadequate atmospheric turbulence profile data available for Siding Spring Observatory for a rigorous analysis of the scintillation error such as the type undertaken in Section 2-1.2, however we can use the rough approximation of Kjeldsen & Frandsen (1992) as follows:

$$\sigma_{\mathrm{scint}} = 0.09 D^{-2/3} \chi^{3/2} \Delta t^{-1/2} e^{-h/8} \tag{3.3}$$

  where D is the telescope aperture in centimetres, χ is the average airmass, Δt is the exposure time in seconds and h is the altitude of the observatory in kilometres. For typical 60-s I-band exposures and the telescope parameters described above (D = 50-cm, χ = 1.5, h = 1.15-km) we find a magnitude-independent error of $\sigma_{\mathrm{scint}} = 1.4$ mmag (compared to $\sigma_{\mathrm{scint}} = 0.9$ mmag in the V-band with longer exposures of 150-s).

- Seeing: The seeing at Siding Spring Observatory has a median of $1.2''$ (Wood et al. 1995), but can vary from $1''$–$4''$ over a night. Given the size of our pixels is 9.43 arcsec pixel^{-1} and the effective point-spread function of our stellar profiles is ~ 1.5 pixels (see Section 3-2.3), or $\sim 15''$, the noise contribution due to this variation was assumed to be significantly less than the Poisson noise limit.

- Differential extinction and transparency: Another atmospheric effect is differential extinction across the wide field of view with changing airmass, and changing transparency in the presence of thin cloud. Although we can correct for this effect on large scales by comparing measurements of a large number of stars across the field, on smaller scales (both spatially and temporally) this effect becomes more difficult to remove due to a smaller number of comparison observations. On poor quality nights this effect can be as large as 5–10 mmag. Differential extinction also contains a colour-dependent term, whereby stars of different temperatures are affected to a slightly different extent by the extinction. Since we are using a filter, it is only the slope of the stellar spectrum across the bandpass that causes the residual colour effect, and it has been measured as being no larger than 2 mmag for the colour variation expected in our fields.

- Image distortion: As the airmass of an image changes through the night, the relative position of a star on the chip in will change due to atmospheric refraction—the higher the airmass, the higher in the sky the star appears to be relative to its true position. Additionally, the image is found to rotate slightly over the night, by ~ 4 arcmin in 8 hours, which may be due to polar misalignment. As a result of these effects it is not possible to put every star in exactly the same place on the CCD chip for every observation, which increases the errors due to the CCD effects listed below.

3-2.3 CCD effects

- Undersampled pixels: The wide-field nature of the survey results in low spatial resolution imaging—the image scale of our CCD is 9.43 arcsec pixel^{-1}, considerably larger than the median seeing of Siding Spring Observatory of $\sim 1.2''$. Toyozumi & Ashley (2005) measured the instrumental point-spread function (iPSF) of our CCD as ~ 0.7 pixels—this is the full-width half maximum (FWHM) of a single star focussed onto the CCD. The effective point-spread function (ePSF) produced by the convolution of the CCD sampling and the iPSF is ~ 1.1 pixels. For a star centred on a pixel, 52% of the flux from the star falls within that pixel; single stars are therefore sampled by very few pixels. The lack of detailed spatial information on the distribution of the flux increases the difficulty of accurate centroiding and also of fitting a stellar point-spread function (PSF), one of the more commonly used methods of extracting high precision photometry. Another disadvantage is that the undersampled pixels cover a larger area on the sky, and the Poisson noise in the sky background increases the total noise in each pixel. We have found that due to the crowding effects of multiple stars in nearby pixels and a background of faint stars the sky background can change quite rapidly over small scales, which increases the significance of the error introduced by undersampled pixels. The problem of sky background subtraction is discussed in more detail in Sections 3-3.4 and 4-3.1. Finally, due to the narrow PSF concentrating most of flux from a star onto a small number of pixels, the pixels will saturate faster than if the same flux were spread over many more pixels. This limits the achievable signal to noise (S/N) ratio of a star relative to additive noise sources in the pixels, such as readout noise.

- Intra-pixel sensitivity variations: Another result of undersampled pixels is the increased significance of intra-pixel sensitivity variations—changes in the flux registered by a pixel given the position within the pixel on which the light falls. This effect was measured by Toyozumi & Ashley (2005) for our CCD chip as causing a $\pm 2.5\%$ flux variation the I-band across a single pixel. In order to overcome this, a new observing technique was developed and tested during the period 2001–2004, which involved rapidly rastering the telescope back and forth over the area of a single pixel during each exposure. While this has the effect of broadening the ePSF to ~ 1.5 pixels, it also significantly decreases the intra-pixel sensitivity variations to 0.5 mmag. Note that simply defocussing the telescope is not sufficient to achieve the same effect, since a defocussed image does not have a smooth profile.

- Flat-fielding: Flat-fielding for wide fields of view is a critical challenge. Vignetting, both geometrical and optical, can be corrected for, but the residual errors will be proportional to the amount of correction which is necessary. Due to the fast focal ratio, it is usually not feasible to perform dome flats. However, sky flats will show significant intrinsic gradients over the several degrees in the field of view, and median combining of the time-dependent gradients becomes problematic, tending to select out a single slope. Our procedure to deal with these problems is outlined in Section 3-3.3. Importantly, flat fields derived from twilight or dome flats are not truly representative of the real performance of the telescope, since each pixel includes scattered light from all possible sources on the sky.

- Blending: Blending of stellar profiles is typical for wide-field surveys where multiple stars are imaged by a small number of pixels. For time-series photometry, if this blending is constant in time it will not reduce the measurable photometric precision, however any transit signals that are present will be diluted due to the flux contribution from the surrounding stars. It also affects centroiding and astrometry, and increases the errors in the local sky background calculations. If the blending is not constant in time due to FWHM variations over the night, then this can introduce correlated errors in the data. This concept is explored further in Section 4-3.

The possible sources of error that were considered and found to contribute a negligible amount to the photometric precision were: cosmic ray noise; small variations in the PSF across the field of view; tracking errors; and charge transfer inefficiency, readout noise, dark current and non-linearity in the CCD.

3-3 Data reduction pipeline

3-3.1 Aperture photometry vs. PSF-fitting

Many projects have been achieving high precision photometry through the use of point-spread function (PSF) fitting—finding an accurate count of the flux by fitting either analytical or semi-empirical profiles to the sources in the image. This is especially useful in images with blended sources, since each individual source can be reconstructed with its own PSF and the blend is thus disentangled. However, with significant undersampling, where each stellar profile is only sampled by a few pixels, there is not enough information about the profile for a precise fit to be made; the errors introduced by a mismatch between the observed and modeled PSF in this case are not negligible, especially for the brightest stars (Kjeldsen & Frandsen 1992).

One alternative is aperture photometry—placing an aperture of some size and shape over sources in the image and counting up the flux contained within, occasionally with some weighting scheme based on the flux in each pixel. This method has its own disadvantages—in order to measure at least a representative amount of flux from a source, the apertures typically need to have a large size on the sky, especially for undersampled pixels. This increases the contribution of sky background noise to the total noise level. Another problem is blended sources; aperture photometry does not offer a simple way of disentangling which flux is from the source being measured and which is not.

However, for bright sources above the sky, it can be shown that aperture photometry converges to the equivalent result that would be obtained with well-defined PSF-fitting (Kjeldsen & Frandsen 1992; Irwin 1997). In practice, given the additional error introduced by a mismatch in the PSF-fitting, aperture photometry can out-perform PSF-fitting (Hartman et al. 2005).

Given these arguments, and the results of some preliminary testing in the 2001–2004 period, a simple and robust automated pipeline based on aperture photometry was constructed for this survey.[2] Two of the more successful wide-field transit

[2]The pipeline was designed and implemented primarily by Marton Hidas, Mike Irwin and

surveys (SuperWASP and HAT) also use aperture photometry.

A third method, image subtraction, is becoming increasingly common and has recently been shown to out-perform both aperture photometry and PSF-fitting (Montalto et al. 2007), although the pixels were not undersampled in this case. This possibility is discussed further in Section 8-2.3.

3-3.2 On-site processing and data handling

After each image is obtained by the telescope, a small astrometry program is run on the hundred or so Tycho-2 stars (Høg et al. 2000) that are typically present, and a world coordinate system (WCS) transformation between pixel and celestial coordinates accurate to within ~ 0.2 pixel is written to the image header. During the observing this is used to correct the telescope pointing. At the end of each night the data are stored locally on the telescope control PC, including an automatically generated log file containing the metadata for each file, and the observer's log described previously.

Data are generally downloaded to the main processing computer in blocks of several nights using a fast internet connection. Backup data are couriered from Siding Spring Observatory to Sydney on hard disk drives.

3-3.3 Initial processing stages

The initial stages of the pipeline were adapted from the Isaac Newton Telescope Wide Field Survey data processing toolkit, developed by Irwin & Lewis (2001). These steps include: de-biassing, using a single number taken from the overscan region; trimming; non-linearity corrections taken from an empirical look-up table; flat-fielding; and gain correction.

As mentioned earlier, flat-field correction can be a significant source of error and therefore must be handled correctly. We typically generate a master flat-field from the best quality twilight and morning sky flats taken during an observing run, some 50–100 frames. Instead of median combining, we take the average of the central

---

Michael Ashley.

70% of values for each pixel. Generating the master flat-field is the first of only two interactive steps in this otherwise entirely automated pipeline, and needs to be done only once for each observing run.

3-3.4 Sky background calculation

After the initial processing, the sky background is calculated on the first pass through the image. The typical process of defining the sky value by using an annulus around each object is not practical in this situation due to the level of blending in our fields.

As an alternative, the entire field is divided into blocks of size 64×64 pixels, which seems to be the optimal size for following real variations while still giving a robust error estimate. For each block, a histogram of the pixel intensities is generated and a Gaussian fit to the core of the histogram ($\pm 1\sigma$ of the peak) is performed. Only the core is used for the fit because the pixels containing additional flux from stars will skew the histogram to higher values. An array of sky values is thus created, one for each block, which can then be interpolated to any point in the original field to give the local sky background value.

During the course of the survey we noticed that this method of calculating the sky background did not seem to cope well if there were residual slopes in the field after flat-fielding due, for example, to changing moonlight illumination. This could be because the presence of a slope in a single block of pixels will broaden the pixel intensity histogram and reduce the accuracy of the Gaussian fit (M. Irwin, private communication). A simple way to address this may be to fit and remove a slope from each image after flat-fielding; this is explored further in Section 4-3.1.

3-3.5 Catalogue generation

On the second pass through the image, the object catalogue is generated. This step is also taken from the Irwin & Lewis (2001) toolkit. Pixels are flagged if they are brighter than a certain level above the sky background (in our case 4σ, where σ is the sky background noise), and when four or more such pixels are connected they are recorded as an object. Individual peaks within groups of flagged pixels are recorded as isolated sources in an attempt to deal with the blending, however given the degree of the undersampling in our images this has not been of much use.

A master catalogue is generated from a combined master frame. Approximately 10 consecutive low-airmass images with very small image-to-image shifts from a clear night are stacked together to create a master frame. This frame is deeper than a typical image and should also have more accurate centroiding of the sources, which was a potential problem for undersampled pixels. This is the second of the two interactive steps and needs to be performed once per field per observing run.

Once the catalogues have been generated for each image, the linear transformations between the image catalogues and the master catalogue are calculated using:

$$x' = ax + by + c; y' = dy + ex + f \tag{3.4}$$

where $a, \ldots, f$ are constants for each image catalogue.

Using these transformations the master catalogue is then transformed into each of the individual image reference frames, resulting in a final identical catalogue co-located onto each image. Using the thousands of objects in each frame for this process gives us a placement accuracy of within ~ 0.01 of a pixel.

3-3.6 Aperture photometry

Simple unweighted aperture photometry is then performed, with fluxes summed over a fixed circular aperture of radius three pixels (i.e., a diameter of nearly 1 arcminute). Intensity contributions from pixels on the boundary of the aperture are calculated exactly using analytical integration over the area of the pixel contained within the aperture. Any pixels on the boundary with counts higher than 20,000 ADU are generally due to blending or bleeding from saturated pixels and therefore the total sum in the aperture is set to zero and that data point is discarded. Values are also automatically calculated for apertures of radius 1.5, $3\sqrt{2}$, 6 and $6\sqrt{2}$ pixels.

3-3.7 Image-to-image correction

Temporally- and spatially-dependent effects such as extinction cause variations in the measured fluxes from image-to-image over a single night. We calibrate the images to correct for this using a subset of the brightest stars (roughly magnitudes 9–11). For each of the reference stars, the mean magnitude over the night is calculated. Then for each image, the difference between each star and its mean magnitude is calculated. The set of residuals $\Delta m_{i,s}$, for the ith image and the sth star, are then fit with the following function:

$$\Delta m_{i,s} = a_i + b_i x + c_i y + d_i xy + e_i y^2 \tag{3.5}$$

where $a_i, \ldots, e_i$ are the constants for the ith image. The second order term along the longer y axis is necessary as the airmass varies most along this axis. The fit is subtracted from individual stars, and any stars which vary wildly from this fit (i.e., which still have high rms magnitude variations after the fit is subtracted) are rejected, and the fit is performed again. In this way we can exclude variable and poorly-measured stars from the calibration. The process is iterated until the fit converges, typically after 4–7 iterations. After this point the fit is applied to all stars, and the individual images are then reassessed. If the median rms of the magnitude residuals for the reference stars is > 12 mmag, the image is removed from the calibration, and the process is repeated without it.

As a final step, the magnitude zero-point is set by using the hundred or so Tycho-2 stars present in each field. The Tycho-2 magnitudes are converted to I-band magnitudes using an approximate $(V - I)$ to $(B - V)$ correlation for main-sequence stars (Cox 2000); we expect the accuracy of the zero-point to be ≤ 0.1 mag. However since we are interested in precise *relative* photometry, as compared to absolute photometry, this does not decrease our photometric precision.

3-4 Survey strategy

After the simulations of the 2001–2004 period, we initially started with the following strategy:

- Time spent on each field: From simulations, the optimal length of time to observe each field was determined to be a minimum of 20 nights with 8 hours of observations per night, or a minimum of 15 nights if 10 hours per night was achieved. Therefore we used 20 nights as our minimum achievable target—taking into consideration time lost to inclement weather and moon phase (several days are lost around the full moon due to intolerably high sky background), we expected to spend up to two months on each field.

- Field selection: We chose to alternate between two neighbouring fields—with 60-s exposures and time lost to slewing and readout time this would give us a cadence of ~ 15 images hour^{-1} for each field. In order to balance the opposing requirements of maximising the number of stars, particularly main sequence dwarfs, in the fields and minimising the crowding we aimed for fields lying within the Galactic latitudes of $15° \leq b \leq 25°$ when this region was reachable. We additionally tried to choose the most southerly fields (above the limit of $-70°$S), in order to keep the airmass as constant as possible over the night.

- Filter selection: As described in Section 1-5.2, the recommendation was to observe in the Johnson I filter. This had the advantages of increasing the contribution of the smaller, redder stars around which a planet transit will be deeper, while allowing for shorter exposures due to the higher quantum efficiency of the CCD in the I-band. This change was implemented in 2004 October. Note that our CCD, being front-illuminated, is not affected by fringing, which would otherwise be a problem in the I-band.

3-4.1 The impact of systematics

After using this strategy for 23 months, we determined that it was not ideal for transit detection. The presence of strong correlated noise signals in our data (explained in further detail in Section 4-3) reduced the efficiency with which we could detect low-signal transits. Therefore from 2006 September we updated the strategy to require observing a single field for as long as it was possible to obtain a minimum of $\sim 3-4$ hours per night on the field, typically 3 months, continuing with the initial placement criteria of Galactic latitude and southerly declination.

Using the predictions from the 2001–2004 period, and the hardware, software and strategy described above, we expected to detect 2–3 transiting planets per year. The data we obtained and the transit candidates we identified are described in the following chapters.

Chapter 4

Data and preliminary analysis

Given the daunting statistics implicit in the detection of transiting hot Jupiters, it is inevitable that the teams searching for them will amass equally daunting amounts of data. Section 4-1 describes the observations that were obtained in the course of the University of New South Wales Extrasolar Planet Search in the period 2004 October and 2007 May. In Section 4-2 our initial level of precision is assessed. The problem of systematics is explored in Section 4-3, and an improved level of precision for the light curves is presented in Section 4-4. The procedures for selecting transit candidates from these light curves are described in Sections 4-5.

4-1 Observations

The raw survey data were obtained with the Automated Patrol Telescope (APT) between 2004 October and 2007 May, using the survey design and observing strategy laid out in Chapter 3.[1] Fields were selected using the guiding criteria outlined in Section 3-4. In brief these were: ideally within the Galactic latitude range $15° < b < 25°$; aiming for as southerly a declination as possible to maximise observing time per night and minimise airmass variations; and avoiding stars brighter than 6^{th} magnitude.

[1]During this time the rostered observers included the candidate, Michael Ashley, John Webb, Marton Hidas, Aliz Derekas, Steven Crothers, George Georgevits, Duane Hamacher, Steven Curran and Tom Young.

In total, 25 fields were observing during this time, and the results are summarised in Table 4.1. The right ascension and declinations of the centre of the each field is given, as is the Galactic latitude. Prior to 2006 September, the strategy was to obtain at least 20 nights of observations on each field; after this point as many nights as possible were obtained. The range of dates within which the fields were observed is also listed. The first 22 fields were observed in pairs and the last 3 observed singly; this modification is explained further in Section 4-3. For each field the observations spanned 2–4 months and between 1600 and 4400 data points were obtained. Fields typically contained from 1300 to 8000 stars brighter than 14^{th} magnitude, depending on the Galactic latitude. Finally the cadence, the number of images obtained on each field per hour, is shown; this is a function of the chosen exposure time and the number of fields being observed in each run. From 2006 September the range of cadences is due to an additional script[2], implemented to automatically adjust the exposure time to the sky background. Deeper exposures could then be taken during the darkest hours each night.

4-2 Initial precision

Using the initial observing strategy and the data reduction pipeline described in Section 3-3, with no additional post-processing of the light curves, we reached the photometric precision shown in the left panels of Figure 4.1. The black circles show the rms magnitude variation in the light curves down to 14^{th} magnitude for the complete data sets on a sparse field (upper panel, field R1) and a crowded field (lower panel, field Q1). The solid line in each panel is the theoretical Poisson noise limit (see Section 3-2.1), and the dashed lines are the individual contributions to the Poisson noise from the star flux (long dashed) and sky flux (short dashed). Although we are already lying quite close to the theoretical limit in the sparse field, the bulk of the stars in the crowded field are lying above this limit. This is largely because the systematic noise, as introduced in Section 1-2.6.5, is considerably more significant

[2]Written by Marton Hidas and Michael Ashley.

Table 4.1. Details of the target fields observed with the Automated Patrol Telescope from 2004 October to 2007 May. The field name and the centres of each field are given. b° is the Galactic latitude. The number of observations obtained on each field and the number of stars brighter than $I = 14^{\text{th}}$ magnitude are shown. The cadence is the number of images observed each hour and reflects changes in exposure time and number of fields being observed at a time.

Field name	α_{J2000}	δ_{J2000}	b°	Dates observed (mm/yy)	Obs	Stars	Cadence (hr^{-1})
L1	$04^h\ 56'\ 24''$	$-30^{\circ}\ 00'\ 00''$	−36.8	10/04–12/04[a]	1791	2195	7.5
L2	$04^h\ 45'\ 00''$	$-26^{\circ}\ 18'\ 00''$	−38.3	10/04–12/04	1692	1943	7.5
N1	$09^h\ 05'\ 00''$	$-14^{\circ}\ 30'\ 00''$	21.1	12/04–02/05	1824	3271	15
N2	$09^h\ 25'\ 00''$	$-13^{\circ}\ 30'\ 00''$	25.5	12/04–02/05	1619	2495	15
O3	$12^h\ 00'\ 00''$	$-36^{\circ}\ 00'\ 00''$	25.7	02/05–05/05	2441	3066	15
O4	$12^h\ 00'\ 00''$	$-38^{\circ}\ 10'\ 00''$	23.6	02/05–05/05	2420	2008	15
Q1	$17^h\ 06'\ 00''$	$-60^{\circ}\ 00'\ 00''$	−11.4	05/05–09/05	2083	8096	15
Q2	$17^h\ 09'\ 00''$	$-57^{\circ}\ 55'\ 00''$	−10.5	05/05–09/05	1853	7559	15
R1	$00^h\ 00'\ 00''$	$-59^{\circ}\ 00'\ 00''$	−56.9	07/05–11/05[b]	3708	1401	15
R2	$00^h\ 00'\ 00''$	$-57^{\circ}\ 00'\ 00''$	−58.8	07/05–11/05	3446	1496	15
S5	$04^h\ 03'\ 00''$	$-02^{\circ}\ 55'\ 00''$	−38.3	10/05–01/06	1980	1327	15
S6	$04^h\ 06'\ 00''$	$-04^{\circ}\ 55'\ 00''$	−38.7	10/05–01/06	1944	1284	15
Jan06_1	$09^h\ 20'\ 00''$	$-24^{\circ}\ 30'\ 00''$	17.5	01/06–02/06[c]	1713	3261	15
Jan06_2	$09^h\ 15'\ 00''$	$-22^{\circ}\ 30'\ 00''$	17.9	01/06–02/06	1773	3520	15
Feb06_1	$12^h\ 55'\ 00''$	$-45^{\circ}\ 15'\ 00''$	17.6	02/06–04/06	2732	4734	15
Feb06_2	$13^h\ 15'\ 00''$	$-45^{\circ}\ 10'\ 00''$	17.5	02/06–04/06	2631	4975	15
Apr06_1	$14^h\ 48'\ 00''$	$-39^{\circ}\ 00'\ 00''$	18.5	04/06–06/06	1840	5176	15
Apr06_2	$14^h\ 48'\ 00''$	$-41^{\circ}\ 00'\ 00''$	16.7	04/06–06/06	1840	3996	15
May06_1	$18^h\ 27'\ 00''$	$-65^{\circ}\ 00'\ 00''$	−21.9	05/06–06/06	2579	4421	15
May06_2	$18^h\ 27'\ 00''$	$-67^{\circ}\ 00'\ 00''$	−22.5	05/06–06/06	2731	4269	15
Jul06_1	$21^h\ 09'\ 00''$	$-66^{\circ}\ 30'\ 00''$	−38.2	07/06–08/06	2065	2246	15
Jul06_2	$21^h\ 09'\ 00''$	$-68^{\circ}\ 30'\ 00''$	−37.5	07/06–08/06	2034	2303	15
Sep06	$23^h\ 42'\ 00''$	$-69^{\circ}\ 24'\ 00''$	−46.5	09/06–12/06	3497	1630	10–40
Dec06	$08^h\ 03'\ 00''$	$-67^{\circ}\ 24'\ 00''$	−18.4	12/06–04/07	3007	3387	10–40
Mar07	$14^h\ 15'\ 00''$	$-69^{\circ}\ 00'\ 00''$	−7.3	03/07–05/07	4450	6714	10–40

[a] 3 additional nights were obtained on field L1 in 02/05 for candidates UNSW-TR-9 and UNSW-TR-10

[b] 8 additional nights were obtained on field R1 in 08/05 and 09/05 for candidate UNSW-TR-29

[c] 1 additional night was obtained on field Jan06_1 in 12/06 for candidate UNSW-TR-46

in the crowded fields.

4-3 The effect of systematics

The majority of our light curves were affected by systematics to some extent. There are many potential astronomical, instrumental and data reduction-related sources giving rise to these systematics, including:

- FWHM variations: These may be caused by temperature and/or focus changes during the night, and possibly large seeing variations. The effects of these variations will be much larger in crowded fields due to the proximity of the photometry apertures, which are often overlapping. As the FWHM varies, more or less flux from each star will spill into the nearby photometry apertures. Since the number and distribution of neighbouring stars is typically unique to each aperture, the additional flux in each case will not be uniform and will not be adequately removed in the image-to-image calibration process.

- Transparency variations: If small unseen patches of thin cloud drift through the large field of view, they may cause transparency variations on a smaller spatial scale than can be corrected for during the image-to-image calibration.

- Sky background variations: As the moon rises and sets, the sky background in the I-band can rise and fall dramatically in a short space of time. Additionally the overall slope in the sky background is noticeably time-dependent. This has highlighted a problem with our sky background subtraction routine which is discussed further in Section 4-3.1.

Stars may be affected by one or all of the above, plus almost certainly additional sources of correlated noise that we have not identified. This gives rise to a wide variety in the morphologies of the observed systematics, although they can be loosely grouped into the following categories:

- Regular signals (peaks, troughs, or more complex patterns arising from a juxtaposition of different systematics) repeating on a timescale of ~ 1 sidereal day.

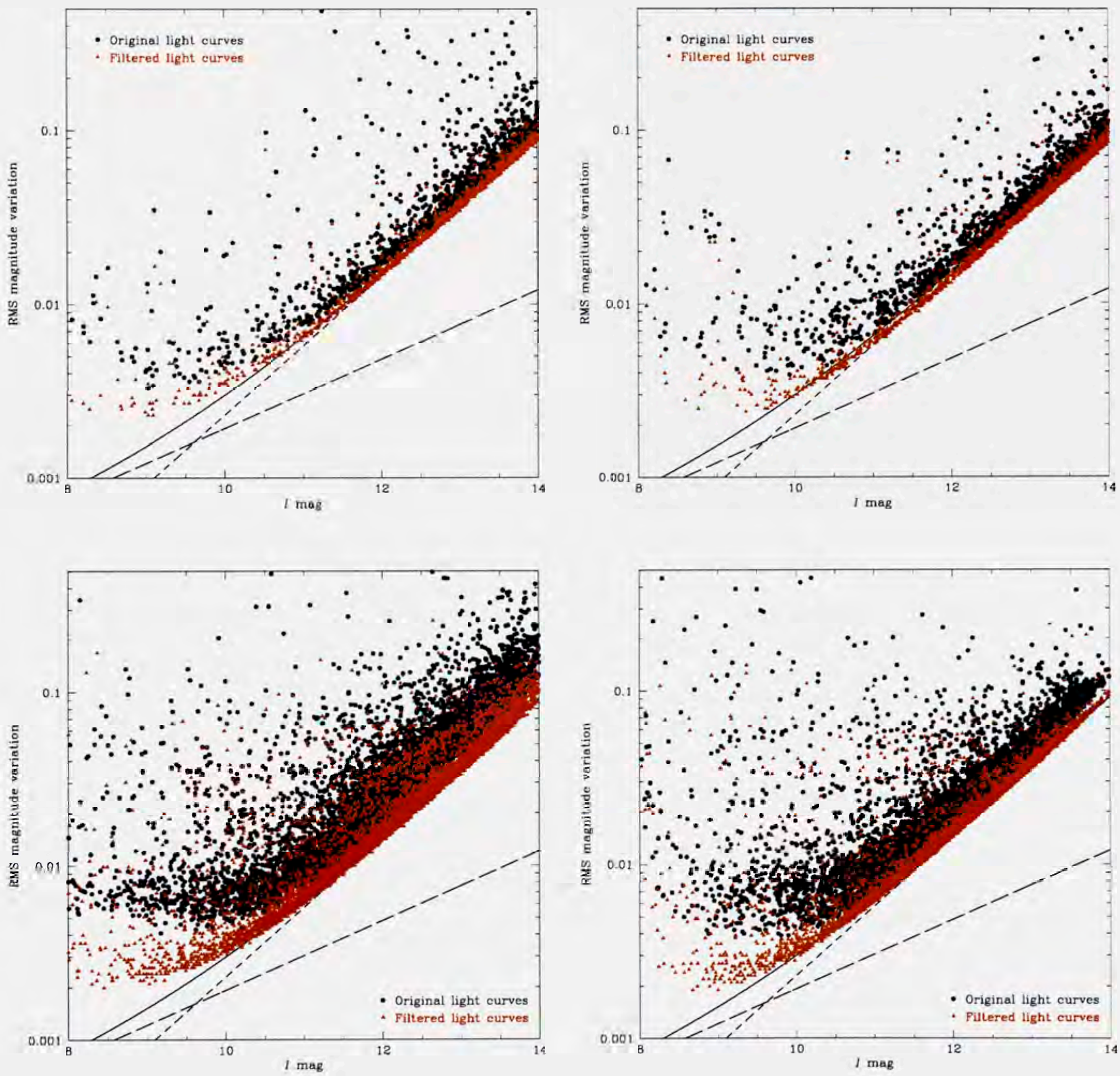

Figure 4.1. Photometric precision of our light curves. The left panels show a sparse field (upper panel) and a crowded field (lower panel), observing with the original observing strategy. The right panels show a different sparse field (upper panel) and a different crowded field (lower panel) using the modified observing strategy. The black circles are the initial photometric precision, and the red triangles are the final precision after filtering of the systematics. In all cases the line is the theoretical Poisson noise limit, with the long dashed and short dashed lines representing the star and sky flux respectively.

See, for example, the top panel of Figure 4.2, a light curve from the Q1 field. These are potentially correlated with hour angle, airmass and/or sky background variations.

- Sudden peaks or troughs that are not repetitive, possibly due to transparency variations.

- Linear slopes over the course of the night. An example light curve, also from field Q1, is shown in the middle panel of Figure 4.2. These may be due to image distortion due to differential refraction and rotation of the image during the night (as described in Section 3-2.2), since the slopes were previously found during investigations in the period 2001–2004 to be correlated somewhat with star's location along the y axis.

- Step functions/sudden jumps brighter or fainter in magnitude, as demonstrated in the bottom panel of Figure 4.2. This feature was well correlated with the rising and setting of the moon, and this problem was addressed and significantly reduced with the addition of a baffle around the telescope lens in 2006 November to reduce the moonlight impinging on the front of the lens and scattering into the telescope.

As detailed in Section 1-2.6.5, in two light curves with the same photometric precision, one with purely white noise and one with a combination of white noise and systematics, it is harder to recover transit signals to the same level of significance in the light curve with systematics as without. One solution is to increase the number of transits detected and the number of in-transit points observed—when phase folded, this then increases the S/N of the transit signal to a significant level. This led to the modification of our observing strategy in 2006 September from alternating between fields and acquiring only 20 nights of data, to observing a single field continuously for as long as possible. The photometric precision obtained using the new strategy is shown in the right hand panels of Figure 4.1 as the black circles, again with the sparse field in the top panel and the crowded field in the bottom panel. We do not expect an improvement in the initial photometric precision with the newer observing

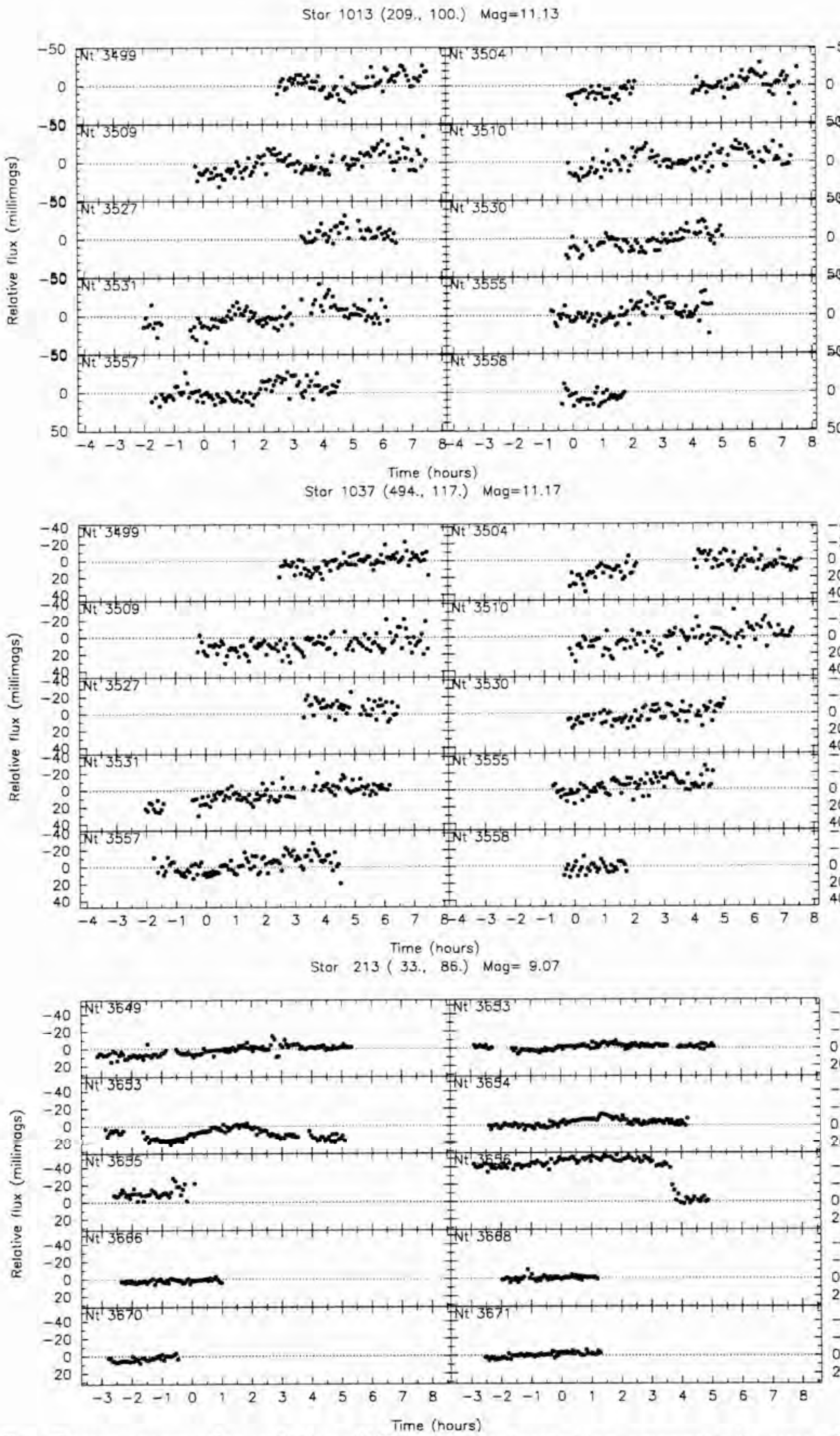

Figure 4.2. Some examples of the different systematics present in our data. The top panel shows a simple repetitive signal, with a period of ~ 1 sidereal day. The middle panel shows a linear gradient over the night. The bottom panel shows a jump in magnitude in the 6^{th} panel coincident with the rising moon.

strategy, the purpose was simply to increase in the number of data points with which to reconstruct the transit signals. Besides modifying the observing strategy, we also attempted to correct for the systematics at both the pre- and post-processing stages, as detailed below.

4-3.1 Variable sky background

One area that was identified as a possible source of systematics was the variation in the sky background and how it is handled by the data reduction pipeline. We noticed that in the data we were obtaining the overall slope of the sky background could vary significantly over the course of the night, and even from image to image, most likely due to the relatively milky lens of the APT scattering moonlight inside the telescope. The lens is made of hygroscopic glass, and the transparency has been steadily reducing after years of exposure to humidity. An example of this variation is shown in Figure 4.3. These are processed (up to and including flat-field correction) images of the Sep06 field, from a single night in 2006 September. They are evenly spaced over the night, separated by $\sim$ 35 minutes. The variation in the background slope is more pronounced towards the end of the night as dawn approaches.

The current sky background subtraction procedure is described in Section 3-3.4: an array of median values of boxes of size 64$\times$64 pixels is created and interpolated onto the original image to give the local sky background at any point. In order to assess if the current method was correctly removing the observed background variation, we decided to introduce a simple linear slope to the data. A single processed image was chosen from a sparse field (Sep06). Twenty copies of this image were made, each with a different background slope added of the form:

$$f'(x, y) = f(x, y) + ay \tag{4.1}$$

where $f(x, y)$ and $f'(x, y)$ are the original and new fluxes in ADU at the pixel coordinate x, y, a is a constant, varying from $-0.1b, -0.09b, \ldots, +0.09b, +0.1b$, and b is some factor to modify the maximum added slope to be $\sim$ 1% of the existing sky background level. The observation times were modified to allow light curves to

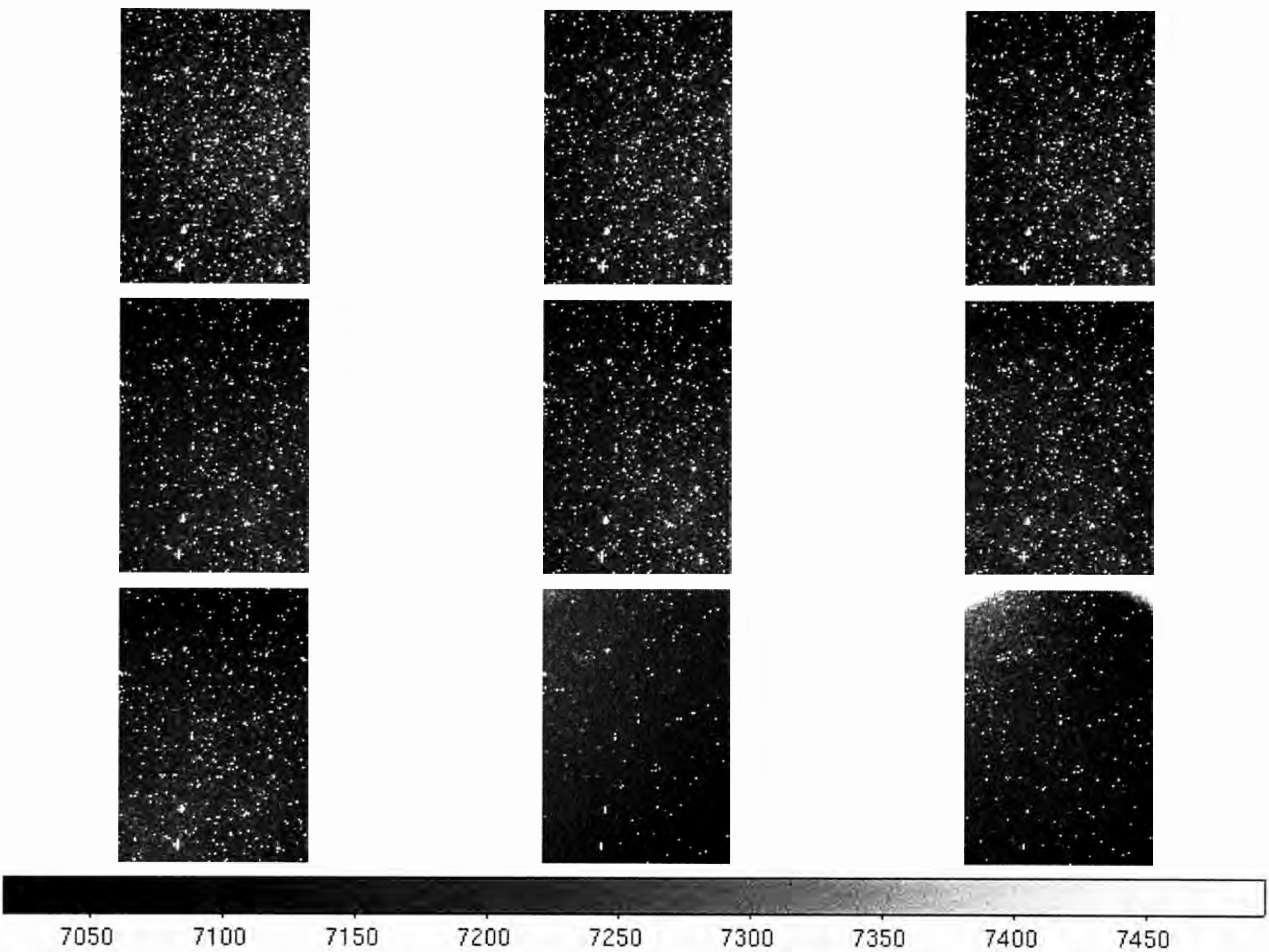

Figure 4.3. Examples of the varying sky background over the course of a night. The images are spaced by approximately 35 minutes, and the field is the Sep06 field.

be produced in the normal manner, with the images being spaced in time by ~ 2 minutes from most negative slope to most positive slope. The images were then run through the remainder of the reduction pipeline and light curves produced. This process was then repeated for an image from a more crowded field (Dec06).

Figure 4.4 shows the rms magnitude variations present in the light curves of the two fields solely as a result of the addition of the linear slopes (tests with the same set of images without the added slopes showed no rms magnitude variations). The set of light curves from the more crowded field extends deeper in magnitude due to the brighter sky background in the original sparse field image swamping the faintest stars.

The varying slope is, as suspected, not exactly removed by the data reduction pipeline, and in fact leaves considerable residual errors. The level of crowding does not seem to affect the level of additional noise to any great extent, the same scatter is seen in both sets of rms and magnitude. For stars brighter than $10^{\rm th}$ magnitude, the additional rms due to the varying background is less than 1 mmag. For stars from $10^{\rm th}$–$13^{\rm th}$ magnitude, this rises to 1–10 mmag, and for the faintest stars we are considering, $13^{\rm th}$–$14^{\rm th}$ magnitude, it reaches an unacceptable 10–50 mmag. Some example light curves from the less crowded Sep06 data set produced by adding the linear slopes are shown in Figure 4.5, in decreasing magnitude from top to bottom.

A possible solution to this is to fit and remove a slope from the real images after they have been flat-fielded, but before the sky background calculation stage, hopefully removing a large element of the time-varying nature of the background. This step was implemented using the routine `imsurfit` in IRAF, fitting a 2-dimensional surface with $2^{\rm nd}$ order polynomials in both dimensions to each image. This surface was removed and the median value of the surface added back in, to avoid negative pixel values.

To test the improvement, if any, with this additional step, two copies of a full night of data from the Sep06 field (the same night as shown in Figure 4.3) were reduced in parallel; one had the slopes fitted and removed, and one did not. Light curves were then generated and the rms magnitude variations assessed. The results

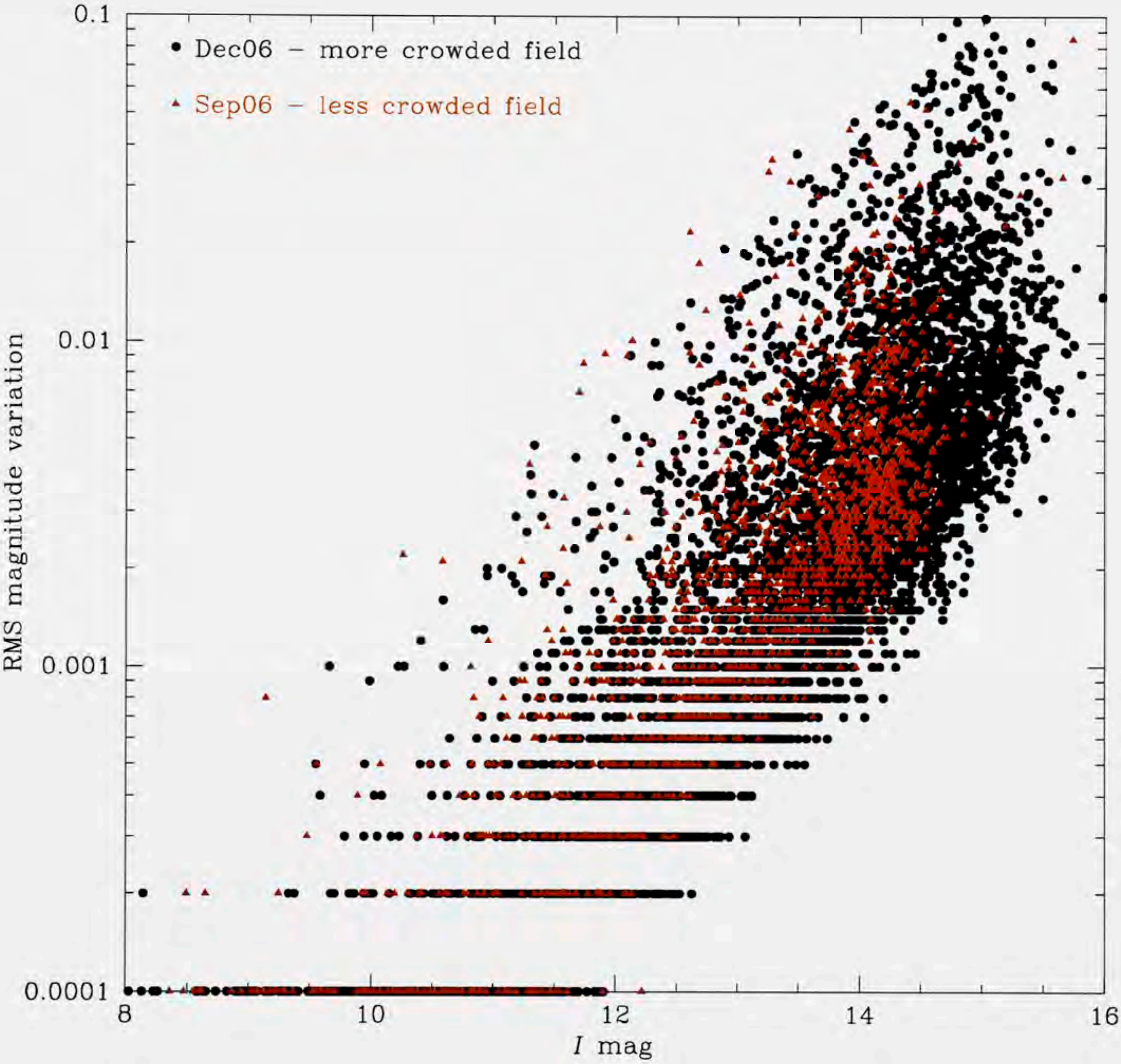

Figure 4.4. The rms noise introduced to the light curves by the addition of linear slopes to the sky background on the order of $\pm1\%$. The black circles are the results for the more crowded field (Dec06) and the red triangles are the sparse field (Sep06). The quantisation at the lowest rms is an artefact of the floating-point precision used.

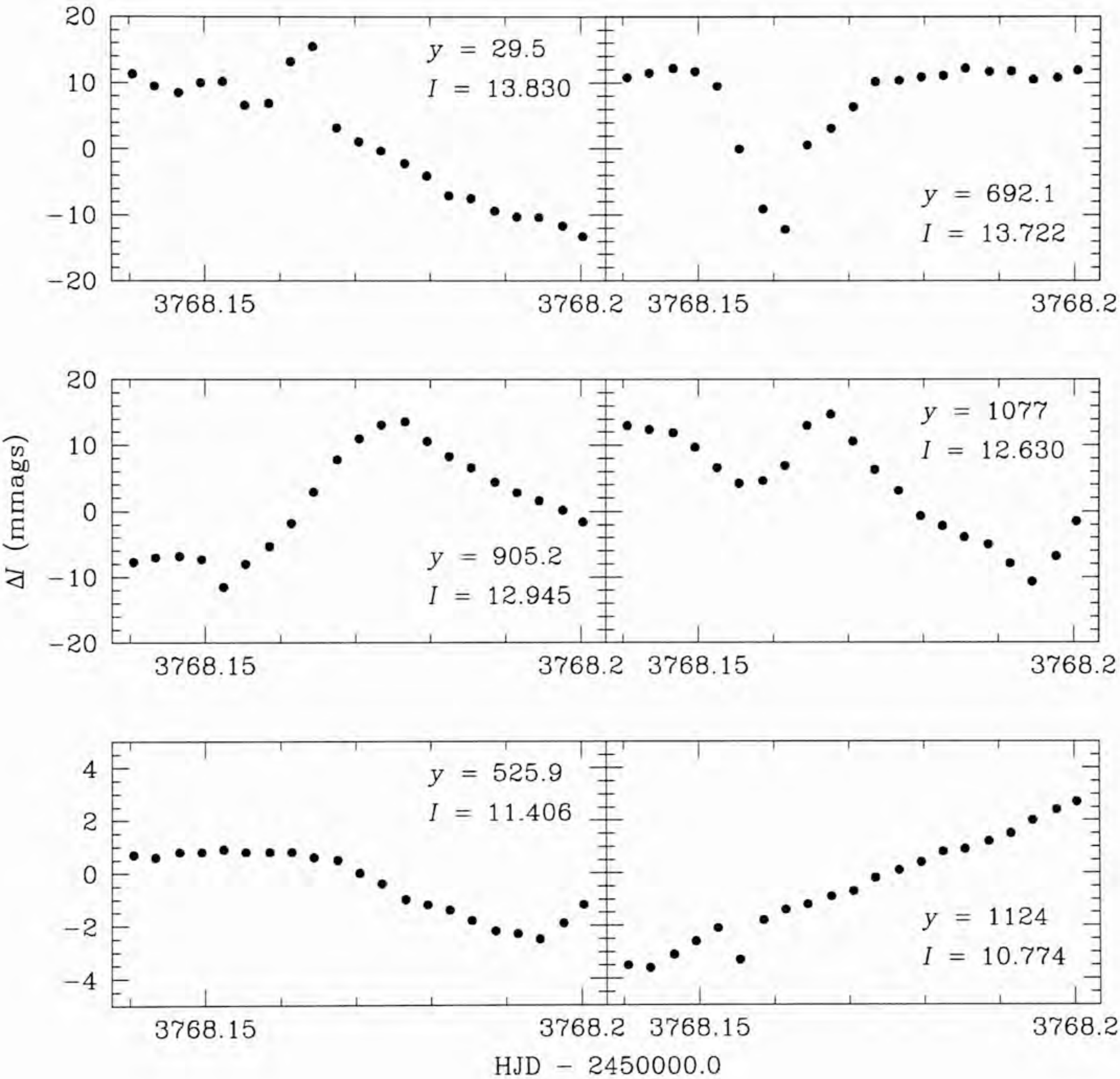

Figure 4.5. Some sample light curves from the less crowded Sep06 artificial data set. The variations are due to the residual error from the sky background subtraction process. The y pixel coordinate and mean I-band magnitude are shown for each light curve.

are shown in Figure 4.6.

There is only a slight overall improvement in the rms noise in the light curves with the additional slope correction. Similar fractions of stars have an rms of better than 10 mmag (15% for the uncorrected light curves and 17% for the corrected light curves). This process was repeated for a night of data from the more crowded Dec06 field with the same results.

This step is currently in the process of being added to the data reduction pipeline, but has not been used for the final results presented here. Another possible solution slated for future testing is to mask out the stars and fit a much higher order surface to the background, directly interpolating the local sky background value from this topographical map.

4-3.2 Aperture positioning

The more crowded the field, the shorter the typical distance from the centre of a star to its nearest neighbour. Eventually, the light from the nearest neighbour will begin to contribute to the star's photometry aperture. The current method of aperture placement is via centroiding of the deeper master reference image—the centre of the circular aperture is placed over the derived centre of the source. However, it is possible that some precision could be gained if the position of the aperture was not centred on the star, but was allowed to be shifted slightly away from the nearest neighbour. This would reduce the amount of additional light from the nearest neighbour, which we expect to be time-dependent and a source of systematic noise, whilst not significantly decreasing the amount of light in the aperture from the target star.

We tested this possibility with a night of data from the Feb06_2 field. Using the master reference image, we found the brightest pixel on the boundary of a 3-pixel radius aperture centred on each source, and recorded the direction from the centre of the aperture to the centre of that pixel. The data were then processed to the point of image transformation with the original master catalogue. The aperture photometry step was then performed on the transformed images 11 times: once

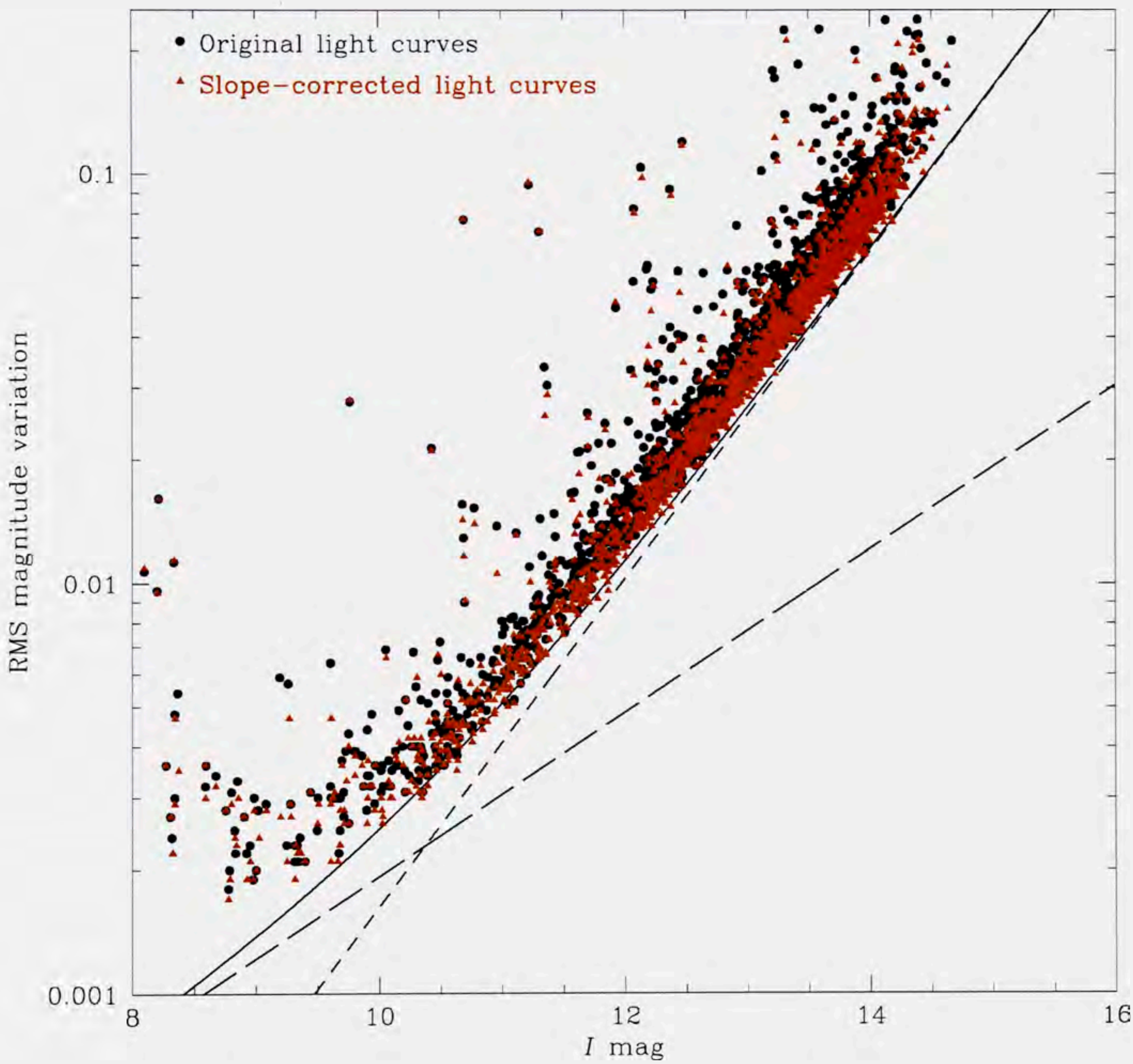

Figure 4.6. The rms noise for a single night of data on the Sep06 field. The black circles are the light curves with no slope correction, and the red triangles are light curves with slope correction.

with no shifts applied, then once each for shifts of 0.1, 0.2,..., 0.9, 1.0 pixels for each aperture in the opposite direction to the direction recorded for the brightest pixel on the boundary.

As a result, 11 light curves were generated for each source. Only those sources where a reliable measurement was made at all 11 aperture positions were considered, which decreased the total number by $\sim$ 30%. The remaining light curves were assessed to determine which shift resulted in the lowest rms magnitude variation over the night. Sources were rejected from the analysis if the measured magnitude at the position returning the lowest rms differed by more than 1 magnitude from the initial magnitude measured for that source with no shift. This limit was selected because when there was a disparity in the measurements, it was typically significantly higher than this (3–4 magnitudes); otherwise the difference was $\ll$1 magnitude.

The results are shown in Figure 4.7. The upper panel shows the rms magnitude variations for the light curves at the original positions (black circles) and at the position giving the lowest rms (red triangles). For the brighter stars ($I > 12^{\rm th}$ magnitude) the best position is typically the original position—this is unsurprising since the few brighter stars would be less affected by the proximity of numerous fainter neighbours. Some $\sim$ 20% of stars, mostly those fainter than $I = 12^{\rm th}$ magnitude, have the lowest rms when shifted by 0.1–0.2 pixels; an additional 9% benefit from a shift of > 0.3 pixels. The lower panel of Figure 4.7 shows this distribution of the number of stars and the shifts giving the lowest rms. The distributions were approximately the same in the x- and y-directions.

The next step in this process is to allow the aperture size to vary in tandem with the position, again to minimise the amount of additional flux from neighbouring stars. Preliminary tests[3] have indicated that for the brightest stars there may indeed be some gain in precision with optimisation of aperture sizes. Once these two degrees of freedom—aperture size and position—are calculated simultaneously, we expect a precision improvement across the full range of our targeted magnitudes, and this step will be integrated into our data reduction pipeline.

[3]Carried out by Duane Hamacher

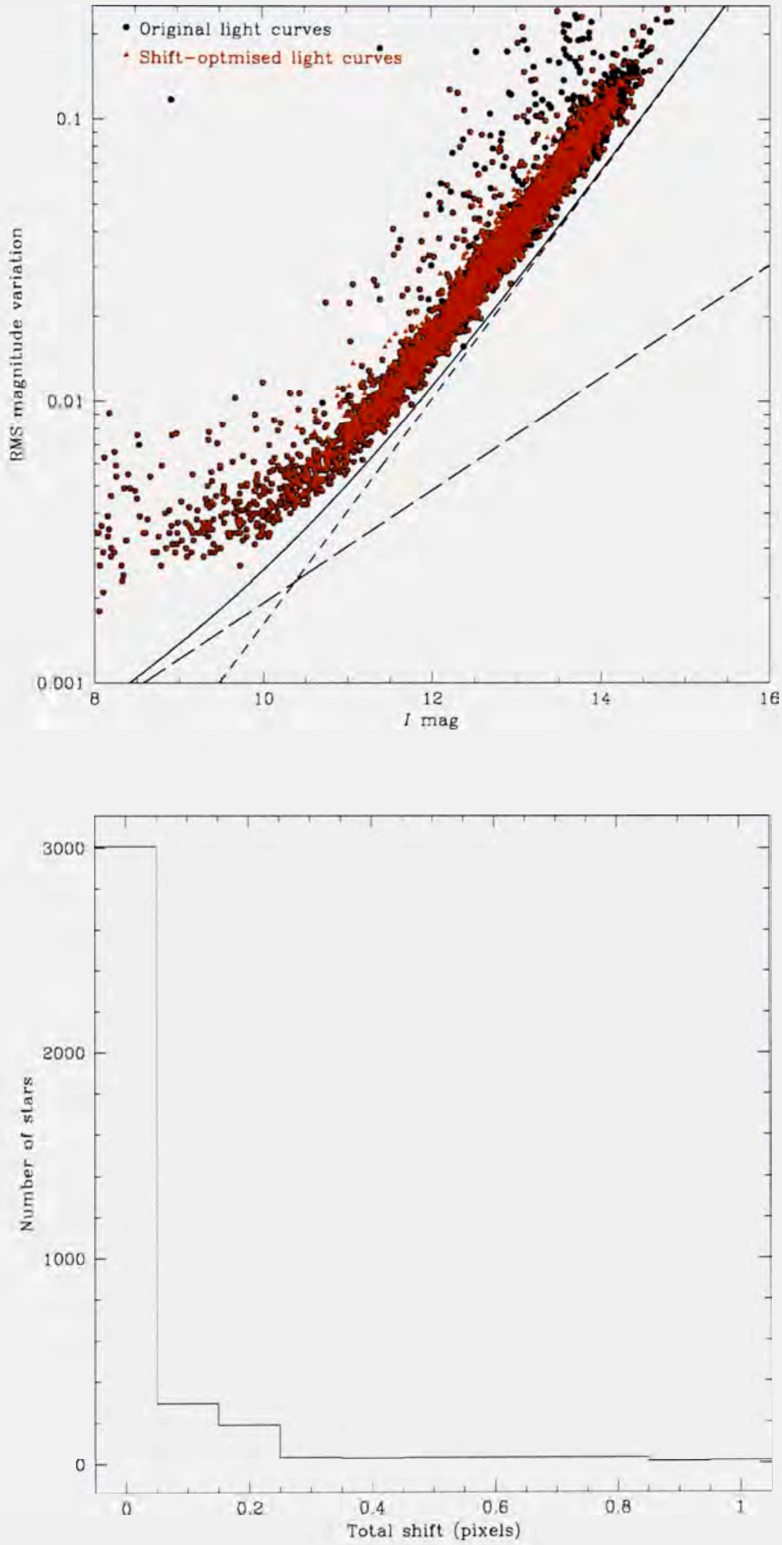

Figure 4.7. Upper panel: The rms noise for a single night of data on the Feb06_1 field. The black circles are the light curves with the original aperture positioning, and the red triangles are the light curves resulting from the aperture shift returning the lowest rms magnitude variations. Lower panel: the distribution of the numbers of stars and the shift in the aperture centre that returns the lowest rms magnitude variations.

4-3.3 Trend-filtering algorithm

We then attempted to correct for the systematics at the post-processing stage, using a trend-filtering algorithm proposed by Kovács et al. (2005) for wide-field time series photometry[4]. The basic premise of the algorithm relies on the fact that within the large set of light curves compiled on each field, there will be many light curves exhibiting similar systematics. Therefore it is possible to select a subset of the light curves which, if large enough, will contain a representative sample of the different systematics. We can then reconstruct and subtract the systematic signals in the remaining light curves, where the true light curve is assumed to be constant, using a linear combination filter of the template light curves. This fit is performed using a simple least-squares criterion. Any signals that are unique to the remaining light curves will not be removed. The template light curves can also be filtered by individually excluding them from the template set before fitting.

After some initial experimentation, a subset size of 300 light curves was chosen as giving the most robust results. The subset was randomly chosen from those light curves between 8^{th} and 14^{th} magnitude which were further than 20 pixels from the edge of the chip. Some examples of the effect of the trend-filtering algorithm on our light curves are shown in Figure 4.8. The systematic trends are removed, at the cost of a slight increase in the white noise. The overall effect on the photometric precision is shown in Figure 4.1, where the rms magnitude variations in the filtered light curves are shown as red triangles. Although there is a slight improvement for the sparse fields in the top panels, the most marked improvement is seen in the crowded fields in the bottom panels. This is to be expected since, as mentioned previously, the systematics which the algorithm is filtering out are most significant in crowded fields. Encouragingly, the trend-filtering algorithm has brought the majority of the rms magnitude variations down to the theoretical limit. There is also a significant improvement with the change in observing strategy—the increased time-sampling and total number of data points lead to a more accurate characterisation of the systematics and therefore a more accurate filtering.

[4] Our implementation was written by Marton Hidas

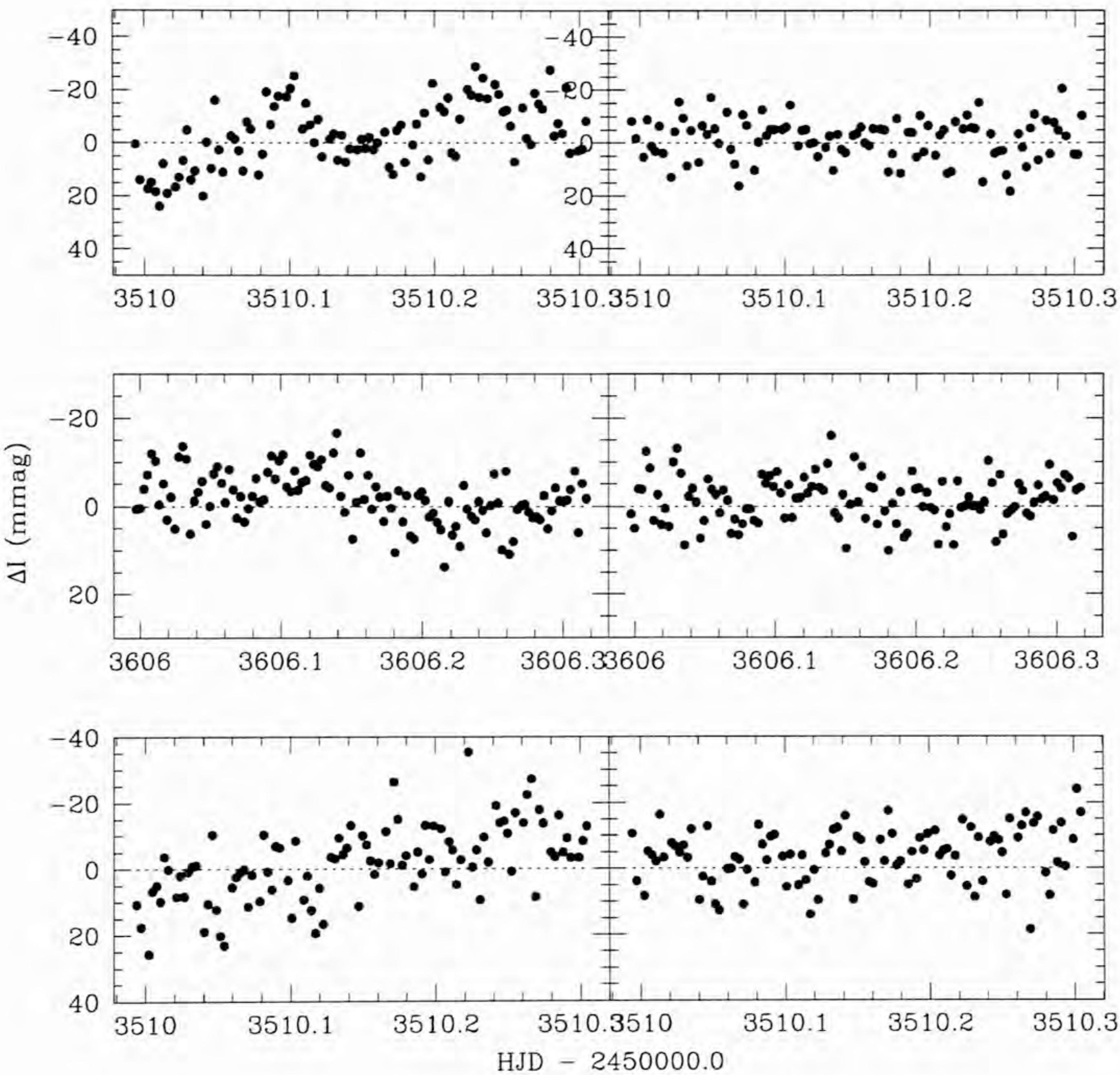

Figure 4.8. The effect of the trend-filtering algorithm on some of the systematics in our light curves. The left panels show the original light curves, and the right panels the filtered light curves.

However, there is a disadvantage of the trend-filtering algorithm: although unique signals will remain in the light curves, they will typically be distorted and the depth of the signal reduced, especially if there is a common systematic in the same time period as the signal. This is a result of the initial assumption in the fit that the true light curve will be constant. An example of this is shown in Figure 4.9, showing a transit candidate (UNSW-TR-29) before and after filtering, where the transit signal is shallower in the filtered light curve. Although with the change in observing strategy we hope to have observed enough transit events that phase-folding at the correct period will still give a high S/N detection even with distorted signals, this situation is obviously not ideal. As a result, we are currently exploring an alternative algorithm for post-processing systematics removal proposed by Tamuz et al. (2005). This is discussed further in Section 8-2.1.

4-4 Final precision

The final precision we have obtained can be seen in Figure 4.1 as the red triangles. The change in observing strategy and implementation of the trend-filtering algorithm have created a significant improvement in our overall photometric precision, and we are reaching the expected theoretical limits. The improvement can be quantified by measuring the fraction of stars that are measured to better than 10 mmag rms variation. These results are shown in Table 4.2. For the example sparse fields shown in Figure 4.1 (fields R1 and Sep06), this fraction was increased from $\sim 11\%$ to $\sim 17\%$. For the crowded fields (fields Q1 and Mar07) it was doubled from $\sim 12\%$ to $\sim 24\%$.

4-5 Initial selection of transit candidates

4-5.1 Transit criteria

Once we have constructed the final set of light curves for each field at the post-filtering stage, we can begin searching for planet transit candidates. Using the

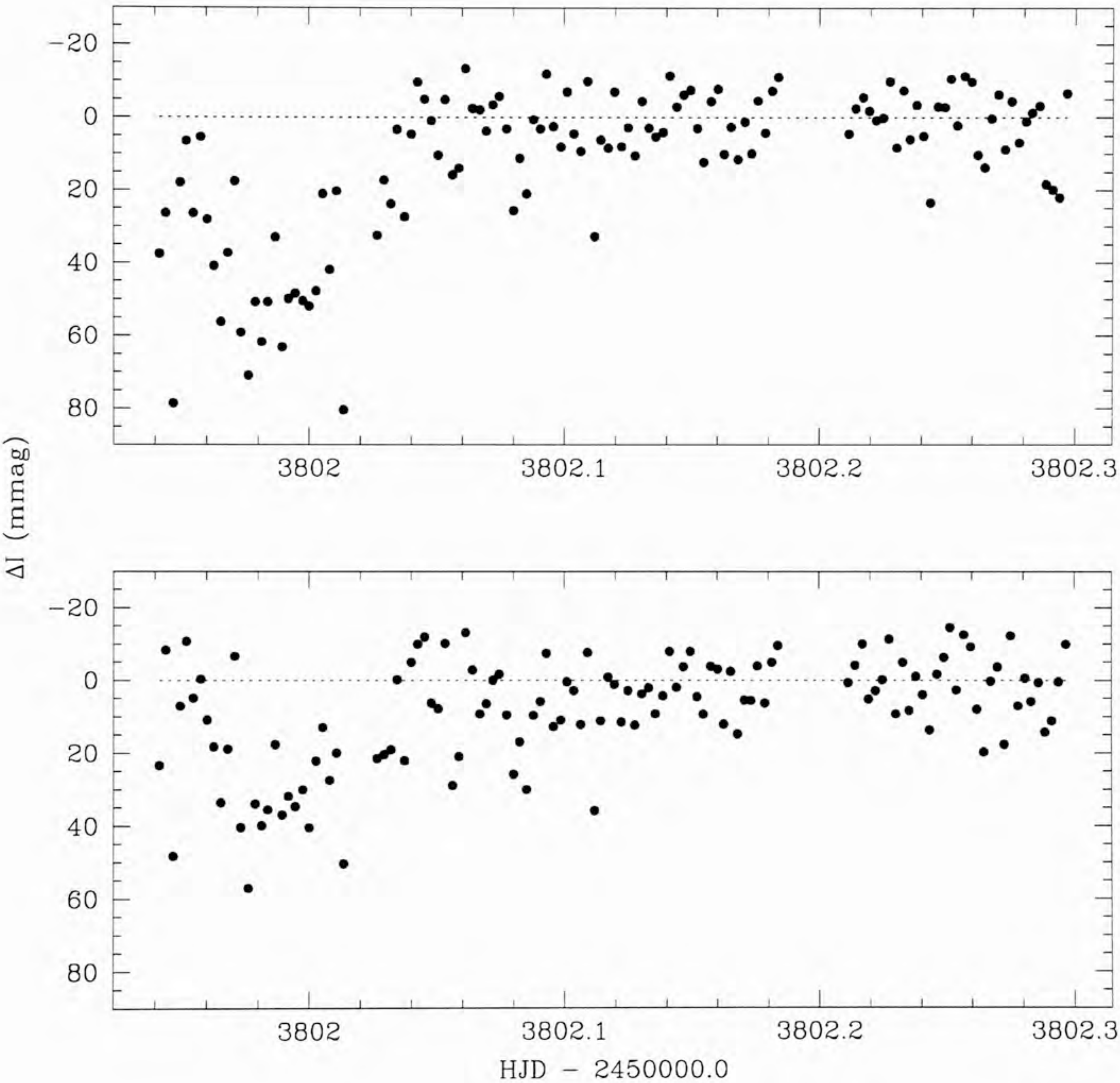

Figure 4.9. The effect of the trend-filtering algorithm on transit signals in our light curves. This signal depth is reduced from $\sim$ 60 mmag in the original light curve to $\sim$ 40 mmag in the filtered light curve.

Table 4.2. Improvement in precision: the numbers of stars in each field measured with an rms magnitude variation less than 10 mmag is given, along with the total number of stars, before and after the change in observing strategy and the implementation of the trend-filtering algorithm.

	Sparse fields		Crowded fields	
	Original	Filtered	Original	Filtered
Old observing strategy	153/1401	180/1205	931/8095	1706/7819
New observing strategy	171/1610	263/1545	908/6708	1560/6470

methods described below, we attempt to extract the light curves with signals that fall within the following criteria:

- Transit depth: Transiting hot Jupiters will produce a transit of depth up to 100 mmag around late M dwarfs, although we do not expect to observe many of these in our fields due to their density on the sky down to 14^{th} magnitude.[5] However, we are erring on the side of including more false positives than rejecting false negatives and set an upper limit on the transit depth of 100 mmag. After a future hardware upgrade described in Section 8-2.2, we expect the number of candidates per field to increase by a large factor, at which point it would be judicious to decrease the depth criterion.

- Transit shape: Due to limb-darkening and noise effects softening the edges of transit signals from the simplified transit shown in Figure 1.1, we accept flat-bottomed and rounded transits where the ingresses and egresses are quite steep, although this latter feature is not specifically characterised. V-shaped transits are excluded.

- Out-of-eclipse: The light curve must be approximately constant, with no apparent secondary eclipses, and no sinusoidal variations when wrapped to the transit period that would be indicative of a tidally distorted eclipsing binary system.

[5]The Gliese Catalog of Nearby Stars contains 1035 M dwarf stars down to 14^{th} magnitude, resulting in a rough estimate of 0.15 M dwarfs per field of view of the APT (Gliese & Jahreiß 1991).

- Number of events: At least two transits must be observed, although three are required for a proper period determination. At this stage we are still flagging light curves that display only one or two promising events, on the chance that we may obtain more data on the same field. This is a distinct possibility in the future with the hardware upgrade resulting in a much larger field of view. However, it is difficult to follow up these candidates: high spatial resolution imaging around predicted transit times is ruled out by the lack of well-determined period, which leaves only the option of spectroscopic data, which is more difficult to obtain. The highest priority candidates have at least one full and two partial events.

Other factors such as period and transit duration were taken into consideration in the parameter-fitting step used in the candidate screening process, described in Section 5-1.

4-5.2 Visual inspection

Initially, all light curves down to 13^{th} magnitude are visually inspected. This has the advantage of being reasonably immune to the effects of systematic variability in the light curves, since the brain can be quickly trained to filter out the same signals appearing in multiple light curves. However, it is less useful for light curves fainter than 13^{th} magnitude due to the increased shot noise. Significantly, it is difficult to detect shallow transits with a low S/N ratio in the unphased data, where phase-wrapping is required to increase the significance of the signal. Visual inspection also has the potential to miss light curves that exhibit only single or partial transit events, and to prevent this we attempt to have two people separately inspecting each light curve. Finally, this process is evidently very subjective and the results generally reflect this: what one person will flag as interesting, another will dismiss as insignificant. Again, we generally chose to include more false positives than reject false negatives when compiling the results at this stage.

4-5.3 Box-search algorithm

To complement the visual inspection process and to include all the data down to 14th magnitude in the transit search, the light curves were then run through a transit detection algorithm[6] (Aigrain & Irwin 2004). This algorithm searches for box-shaped transit events within specified transit duration and period windows. Each light curve has the combination of epoch, transit duration, transit depth and period within the specified range that returns the highest S/N ratio recorded. Subsequently, light curves with a S/N greater than some cut-off (typically > 8.0) are visually inspected in both raw and folded formats, using the recorded parameters. This has the advantage of providing a statistical measure and cut-off for any candidates identified in the visual inspection stage. It also has the additional advantage of flagging those light curves with only single or partial events which may have been missed during the visual inspection. We have optimised the parameter space to be investigated for hot Jupiters. The transit duration window was set as 0.04–0.25 d, with a step-size of 0.01 d ($\sim$ 15 min), considerably shorter than the shortest duration transit features expected, the ingress and egress ($\sim$ 30 min). The period window was set as 1.0–5.0 d, with a constant step-size in frequency of 0.05 d^{-1}, which was found to give the best compromise between fine sampling and long computing times. The step-size of the epoch sampling is determined by the algorithm to be the average duration between subsequent data points for ease of generating phase information (Aigrain & Irwin 2004).

We can also use the box-search algorithm to test the extent to which the trend-filtering algorithm affects the detection rate of transit signals. We expect the decrease in the S/N of the detection due to the reduction in the depth of the transit signal to be significantly outweighed by the increase due to the reduction of the out-of-eclipse systematics. To test this, we used the set of light curves from the Mar07 field. We chose ten random light curves between 9th and 11th magnitude, and to each added a fake transit signal. These signals had periods and epochs that were randomly chosen from the range 1–5 d but were forced to result in a minimum of

[6]Software kindly provided by S. Aigrain and M. Irwin.

Table 4.3. Transit recovery rates using the box-search algorithm. Results for unfiltered and filtered light curves are presented. The results for the 30–50 mmag depths are the same as for a depth of 25 mmag.

Depth (mmag)	Original (/10)	Filtered (/10)
25	8	10
20	7	9
15	7	8
10	6	8
5	2	7

three transit events. They had durations of 2 hours, and were added as discrete box shapes. The initial transit depth was 5 mmag. These modified light curves were added back into the original set, which was then run through the trend-filtering algorithm. The box-search algorithm was subsequently run on the two sets of light curves—the original set with the additional modified light curves, and the filtered set—and the recovery rates compared. A successful recovery was defined as when the box-search algorithm detected the highest signal to noise event at the same period as the inserted signal. This process was then repeated for 9 additional transit depths from 10 mmag to 50 mmag, in spacings of 5 mmag. The results are summarised in Table 4.3. For each depth, the number of light curves with the fake signal detected at the correct period with a S/N of greater than 8.0 is given, up to the total of 10 light curves. For 25 mmag and deeper, all the added transits in the filtered set and 8 of the 10 in the original set are recovered by the box-search algorithm. The two that are not recovered from the original set had significant systematics. In all cases more transits were recovered from the filtered light curves than from the original light curves, which is a positive result for both the trend-filtering algorithm and the box-search algorithm for transit detection.

4-6 Results

During the period 2004 October to 2007 May, 23 candidate light curves across the 25 fields were selected out of a total of $\sim 87,000$ light curves, using the criteria and procedures described in this chapter. Further analysis and follow up of these candidates is described in Chapter 5.

One of the aims of this thesis was to explore some of the additional science that could be performed with the compiled data set. To this end, a variable star catalogue containing 850 variable light curves was compiled; these results are presented in Chapter 6. In the course of constructing this catalogue, we discovered the first example of a high-amplitude δ Scuti star in an eclipsing binary system. This system is fully explored and analysed in Chapter 7.

Chapter 5

Transit candidates and follow up

A light curve in a single filter cannot reveal the true nature of a binary system. This is due to the degeneracy between the distance to and geometry of the system—doubling all the size parameters of the system would result in the same observed light curve. Therefore, once the best transit candidates have been identified, further analysis and more data are required to confirm or reject the hypothesis of a transiting planet. The results of this process for the 23 transit candidates identified in our data set are presented here.[1] Section 5-1 details the initial screening stages of the analysis and summarises the 10 transit candidates that were disqualified during this stage. The methods for obtaining follow up observations on a selection of the candidates are described in Section 5-2, and the results of these observations outlined in Section 5-3. The candidates which are yet to be followed up, including the most recent candidates, are summarised in Section 5-4. The results of the transit survey are summarised and assessed with respect to initial predictions in Section 5-5.

5-1 Candidate screening

As mentioned in Section 3-2.3, it is inevitable that there will be cases of blending of multiple stars in our photometry apertures, given our undersampled pixels and the

[1]Although the candidates were numbered consecutively upon discovery, there are many gaps in the final list, especially during the earlier stages. This was due to a steadily increasing understanding of the systematics and subsequent removal of objects from the final list.

Galactic latitude of our fields. Therefore, one of the first checks is a visual inspection of the placement of the photometry aperture in the field and the local environment of the target star. There are several obvious properties of the photometry aperture that decrease the level of confidence in the transit signal, including: overlap with nearby photometry apertures; multiple stars within the aperture; vertical proximity to saturated stars which may bleed by varying amounts over the night into the columns; and proximity to the edge of the chip or obvious flat-field defects.

The local environment of the target star can also be examined in more detail using high spatial resolution images from the Digitized Sky Surveys (DSS)[2]; these images typically reveal multiple stars in the photometry aperture (see Figure 5.1). Making the assumption that the source of the transit signal is the brightest star in the photometry aperture, the extent to which the signal has been diluted by additional fainter stars can be estimated. If the target star is brighter than $\sim 11^{\rm th}$ magnitude, colour information can usually be obtained from the Tycho-2 catalogue (Høg et al. 2000) via the online *VizieR* interface (Ochsenbein et al. 2000). The Tycho-2 catalogue contains the BT and VT magnitudes, from which we can obtain the $(B-V)$ colour using the relation $(B-V) = 0.85 \times (BT-VT)$. If the star is a main sequence star, which is a reasonable assumption, the colour indicates an approximate spectral type, which in turn constrains the radii of the target star and the transiting object. The proper motion of the host star, if measurable, can also provide a way to differentiate between nearby dwarfs and distant giants; the UCAC2 (Zacharias et al. 2004) catalogue was used to determine the proper motions where available.

Even without additional catalogue information, it is possible to fit the parameters of a well-sampled light curve with a known period if a few simplifying assumptions are made. Assuming a circular orbit, that all light comes from a single star and the companion is dark, that limb-darkening is negligible (a reasonable assumption in the I-band), that the stellar mass is much larger than the companion

[2]The Digitized Sky Surveys were produced at the Space Telescope Science Institute under U.S. Government grant NAG W-2166. The images of these surveys are based on photographic data obtained using the Oschin Schmidt Telescope on Palomar Mountain and the UK Schmidt Telescope.

mass and that the stellar mass-radius relation is known, we can use the equations in Seager & Mallén-Ornelas (2003) to derive values for the mass of the star, the inclination and semi-major axis of the orbit, and the radii of the star and companion. For this approximation, four of the observable parameters of the light curve—the period P, the transit depth ΔF, the total duration of the transit from the start of ingress to the end of egress t_T, and the duration of the transit contained within the ingress and egress t_F—are estimated by eye. Although this is only an rough approximation, it is a useful guide for prioritising the transit candidates for follow up. Since the trend-filtering algorithm has the known consequence of artificially reducing the depths of the transits, we use the unfiltered light curves for this analysis.

Using these additional data, the candidates listed in Table 5.1 were subsequently rejected from further analysis. The field in which the candidate was identified and the J2000.0 coordinates of the centre of the APT photometry aperture are given. The mean I-band magnitude of the APT light curve is shown; since there will typically be multiple stars in the photometry aperture, this magnitude will represent an upper limit on the true magnitude of the source hosting the transit. The epoch shown is the heliocentric Julian date of the centre of a specific transit. The four observables from the light curve that are quoted in the table are used to derive an approximation for the companion radius $R_{\rm Jup}$, using the equations of Seager & Mallén-Ornelas (2003). The $(B - V)$ colour is quoted where available, and finally the reason/s for the rejection of the candidate are noted. The proper motion is also quoted where available. In almost all cases a low proper motion consistent with either a nearby dwarf or a distant high velocity giant was found; the remainder showed no measured proper motions. The phase-folded light curves for these candidates are shown in Figure 5.1, as are the higher spatial resolution DSS images.

Table 5.1. Transit candidates rejected during the initial screening stage. See text for an explanation of the columns. The reasons for the rejection of the candidates include: (1) DSS: the higher spatial resolution imaging indicates the true transit depth is > 100 mmag. (2) Spectral type: the Tycho-2 colours indicate a spectral class with a stellar radius too large for the companion radius to be compatible with a transiting planet. (3) R_p: using the four observables and the equations of Seager & Mallén-Ornelas (2003) we find a companion radius that is too large for a transiting planet.

ID	Field	α_{J2000}	δ_{J2000}	I	Epoch	P	ΔF	t_T	t_F	R_p	$(B-V)$	μ	Notes
				(mag)	HJD - 2450000.0	(d)	(d)	(d)	($R_{\rm Jup}$)		(mas yr^{-1})		
UNSW-TR-15	Q1	17:03:25.702	-59:40:02.79	10.2	3499.515	1.4758	90	0.20	0.025	10	0.38	6.4	DSS/Spectral type
UNSW-TR-16	Q1	17:05:32.205	-60:55:11.60	11.3	3509.10	2.980	60	0.18	0.05	5.3	-	-	DSS
UNSW-TR-17	Q1	17:14:48.985	-60:33:58.68	12.3	3510.20	1.868	100	0.14	0.06	5.1	-	7.7	DSS
UNSW-TR-23	Q2	17:11:18.372	-57:40:16.12	10.5	3498.995	0.4635	35	0.09	0.02	4.6	-	4.1	DSS
UNSW-TR-24	Q2	17:15:54.378	-57:06:48.07	10.7	3504.06	1.633	60	0.17	0.04	6.9	-	-	DSS
UNSW-TR-31	R2	23:50:40.508	-57:30:21.87	10.8	3620.026	4.152	50	0.24	0.14	5.4	0.47	3.1	Spectral type
UNSW-TR-32	R2	23:51:39.790	-56:37:48.36	12.1	3578.665	3.6876	80	0.22	0.09	6.2	-	-	R_p
UNSW-TR-39	S5	03:59:31.143	-21:02:12.86	12.4	3671.10	-	90	0.16	0.03	-	-	5.6	DSS/Single event
UNSW-TR-48	Jan06_2	09:10:31.618	-21:58:20.00	11.1	3740.29	0.8431	30	0.20	0.05	13	-	4.9	R_p
UNSW-TR-64	Sep06	23:42:17.067	-69:54:23.57	11.6	4020.0867	4.251	95	0.22	0.06	6.3	-	8.2	R_p

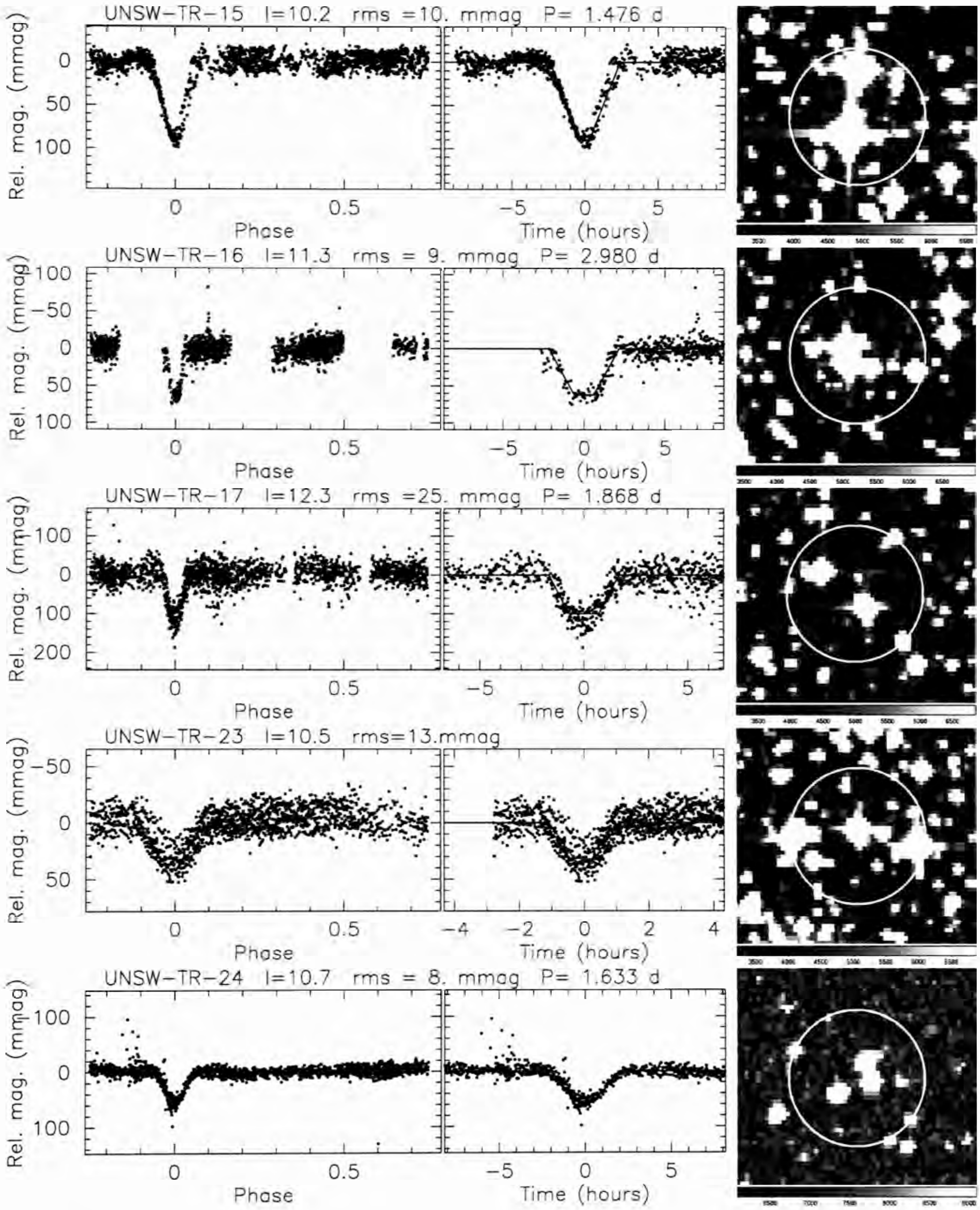

Figure 5.1. Transit candidates rejected during the initial screening stage.

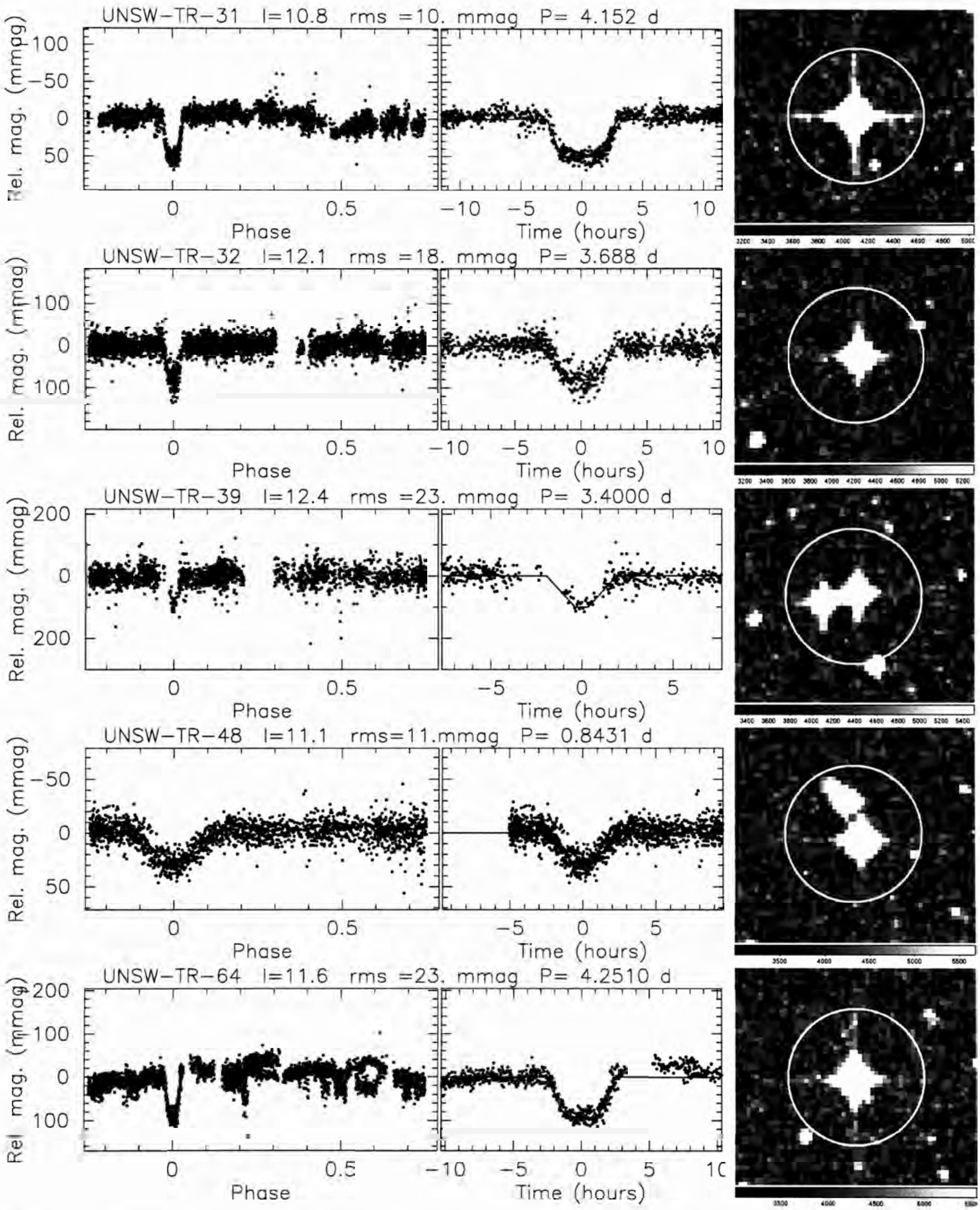

Figure. 5.1 – *continued.* Transit candidates rejected during the initial screening stage.

5-2 Follow up observations

5-2.1 Higher spatial resolution imaging

There are several different types of additional observations that can be performed at the next stage of analysis. If the photometry aperture contains more than one potential source for the transit signal, higher resolution time series photometry during predicted times of transit is required to identify which is the target of interest. If it is one of the fainter stars, the true depth of the transit will typically be much larger than the upper limit of 100 mmag.

For these observations we use the Australian National University 40-inch telescope, located on the same site as the APT at Siding Spring Observatory, with the Wide Field Imager (WFI) CCD mosaic camera. The camera has eight 4k $\times$ 2k CCDs with a spatial resolution of 0.38 arcsec pixel^{-1}, resulting in a full field of view of 52 $\times$ 52 arcmin. We do not require the full field of view for the follow up of a single candidate, therefore we minimise the amount of unused data by reading out a single CCD. We obtain the usual calibration frames (biases, twilight flats) each night, and also typically several Landolt standard stars for flux calibration where necessary (Landolt 1992). We observe 1–2 candidates each night, depending on the predicted transit times. We typically alternate observations between the Johnson V and I filters; if the depth of the transit in the higher spatial resolution imaging is still compatible with that of a planet, the colour-dependence of the transit can be used to discriminate between a planetary system and an eclipsing binary system Tingley (2004).

The data are downloaded to the same processing computer used for the APT data reduction. A modified version of the APT aperture photometry pipeline is used to produce the final light curves[3]. There are typically insufficient Tycho-2 stars in each image for the image-to-image calibration to be performed in the same manner as for the APT data, so this step is removed at the cost of a small amount of photometric

[3]The modifications were made by the candidate with the assistance of Marton Hidas. Duane Hamacher and Steven Curran performed the majority of the data reduction.

precision.

Efficiently obtaining observations of our candidates with this telescope is a challenge. Fields will generally need to be observed for up to a month before the first candidates can be detected, and typically they are observed for at least two months before a full set of candidates is established. Ideally, we want to follow these candidates up before the field sets, or additional APT observations could be required when the field rises again to re-establish the transit timing. This results in an observation-detection-follow up window of only 3–4 months. Given the quarterly time allocation schedule of the Australian National University, this inevitably means applying for time before candidates have been acquired. In order to maximise our phase coverage of these yet-to-be-discovered candidates, long blocks of time (typically 14 nights) of time have to be allocated; fortunately, the 40-inch is typically under-subscribed[4]. Even with long time allocations, weather and instrument downtime combined with an unfortunate ephemeris can mean that the most promising candidates are not observed during follow up. This is obviously not the ideal situation; given the predicted transit time it is possible to make targeted observations that would typically require only half-nights of telescope time. We are currently exploring the possibility of inserting our candidates and the predicted transit times into an automated scheduler on the Faulkes South Telescope. This option is discussed further in Section 8-2.4.

5-2.2 Medium resolution spectroscopy

Once the source of the transit has been identified, the next logical step is to obtain spectroscopic data. To obtain the very high precision spectroscopic data required to measure the radial velocity variations of a planetary companion, time on a large international facility is required. In order to compete for this time, we need to present candidates for which we have constructed a compelling case. To this end, as

[4]Time on the 40-inch was awarded in the following quarters: 2005 May–July, 2005 November–January, 2006 February–April, 2006 May–July, 2006 August–October and 2006 November–January, and the observing role was rotated between the candidate, Marton Hidas, Duane Hamacher and Tui Britton.

an intermediate step, we obtain medium resolution ($R \sim 6000$) spectroscopy on our targets. With a single spectrum, we can confirm the spectral classification of the host star, and rule out double-lined spectroscopic binaries. With additional spectra, if sufficient phase coverage is obtained, radial velocity data can be extracted and phase-folded at the calculated ephemeris of the target. Given the relatively low radial velocities we can measure with a medium resolution spectrograph $\sim 3 - 10$ km s^{-1}), any radial velocity variations that are correlated with the period will be considerably higher than the variations induced by a planetary mass companion (~ 100 m s^{-1}).

To obtain these data we use the Australian National University 2.3-m telescope, also located at Siding Spring Observatory, with the Double-Beam Spectrograph (DBS). We obtained observations in both the red and blue arms of the spectrograph, using the highest resolution gratings available for each (R1200 and B1200(1)). The grating angle and wavelength range were typically chosen to encompass the Hα and NII lines in the red, and the Hγ and Calcium H and K lines in the blue, but are listed in more detail for each individual observing run in the following section. In all cases, the D1 dichroic was used. Observations of the target stars are alternated with arc spectra for wavelength calibration, using the Fe-Ar lamp in the blue and the Ne-Ar lamp in the red. Bias frames, quartz flats and flux standards are taken each night.

The data are downloaded to the main processing computer and reduced using the standard IRAF routine `doslit`, including bias, flat-field and wavelength-response correction and wavelength calibration. We do not typically perform the flux calibration unless necessary. Where appropriate, the radial velocity data are extracted using the routine `fxcor` and fit with simple sinusoids constrained by the calculated ephemeris to measure the amplitude.[5]

Unlike the 40-inch telescope, the 2.3-m telescope is over-subscribed, and time allocation is quite competitive. Therefore we are unable to justifiably apply for time before we have identified promising candidates, which can create a significant

[5]The data were reduced by the candidate, and initial assistance from Aliz Derekas was greatly appreciated.

lag between the initial candidate detection and obtaining spectroscopic follow up, decreasing the survey efficiency.[6]

5-3 Follow up results

The candidates for which follow up observations were obtained are detailed below in chronological order of discovery. The details of each candidate are summarised in Table 5.2, which has the same format as Table 5.1. Due to the logistics of time allocation on the larger telescopes, as described previously, the final list is more a reflection of scheduling constraints than the true quality of the candidates.

5-3.1 UNSW-TR-29

UNSW-TR-29 was discovered in the R1 field, observed in 2005 July–November. The phase-folded unfiltered APT light curve is shown in Figure 5.2. This is a relatively bright candidate, with a mean I magnitude of 9.8. The depth of the transits is 18 mmag, and the period is 1.40912 d. The higher spatial resolution DSS image with the APT photometry aperture overlaid is also shown, and indicates that the transit depth is unlikely to have been diluted by any significant amount unless there is an unresolved blend. The equations of Seager & Mallén-Ornelas (2003) give an estimated companion radius of 1.3 $R_{\rm Jup}$, and the $(B-V)$ colour of 0.67 indicates a late G-type star. All of these indicators pointed to UNSW-TR-29 being a promising candidate and it was highly ranked for follow up observations.

40-inch observations of this target were obtained in 2005 November and 2006 September. Although insufficient data were obtained around the predicted time of transit to constrain the parameters of the light curve any further, it was clear in observations taken during the best $\sim 10\%$ of seeing that there was indeed an unresolved blend. The two sources are clearly separated in Figure 5.3, a single

[6] Time on the 2.3-m was awarded in the following quarters: 2005 February–April, 2005 May–July, 2007 February–April and 2007 May–July, and the observations were performed during this time by the candidate, Marton Hidas, Aliz Derekas, Laszlo Kiss, Duane Hamacher, Tui Britton and Tom Young.

Table 5.2. Transit candidates followed up with higher resolution imaging or spectroscopy. The columns have the same meanings as in Table 5.1 with the addition of μ, the proper motions from the UCAC2 (Zacharias et al. 2004) catalogue. DLSB: Double-lined spectroscopic binary; BEB: blended eclipsing binary; GEB: grazing eclipsing binary; EB: eclipsing binary.

ID	Field	α_{J2000}	δ_{J2000}	I	Epoch	P	ΔF	t_T	t_F	R_p	$(B-V)$	μ	Status
				(mag)	HJD - 2450000.0	(d)	(mmag)	(d)	(d)	($R_{\rm Jup}$)		(mas yr^{-1})	
UNSW-TR-29	R1	00:03:28.542	-58:40:25.35	9.8	3579.515	1.40912	18	0.07	0.034	1.3	0.67	32.6	DLSB
UNSW-TR-41	S5	04:01:32.329	-20:27:03.46	9.8	3726.07	2.23625	13	0.06	0.03	0.7	0.71	22.2	BEB
UNSW-TR-54	Feb06_1	12:51:38.133	-44:40:38.01	11.6	3787.573	3.6509	25	0.12	0.05	2.0	-	-	BEB
UNSW-TR-56	Feb06_2	13:13:00.321	-45:54:29.31	11.6	4254.087	0.386413	30	0.07	0.023	3.1	-0.66	12.0	GEB
UNSW-TR-60	May06_1	18:38:00.555	-65:06:07.70	10.7	3877.945	1.5087	100	0.12	0.06	3.4	0.35	7.0	EB
UNSW-TR-62	Jul06_2	21:08:04.403	-68:57:53.10	11.5	3937.805	0.9425	50	0.08	0.015	2.6	-	26.9	EB
UNSW-TR-65	Dec06	07:51:33.943	-66:48:45.95	12.3	4088.155	0.5846	40	0.065	0.025	2.1	-	15.4	DLSB
UNSW-TR-67	Dec06	08:04:04.211	-67:38:39.97	10.8	4119.995	1.3775	37	0.14	0.03	5.4	0.52	15.9	DLSB

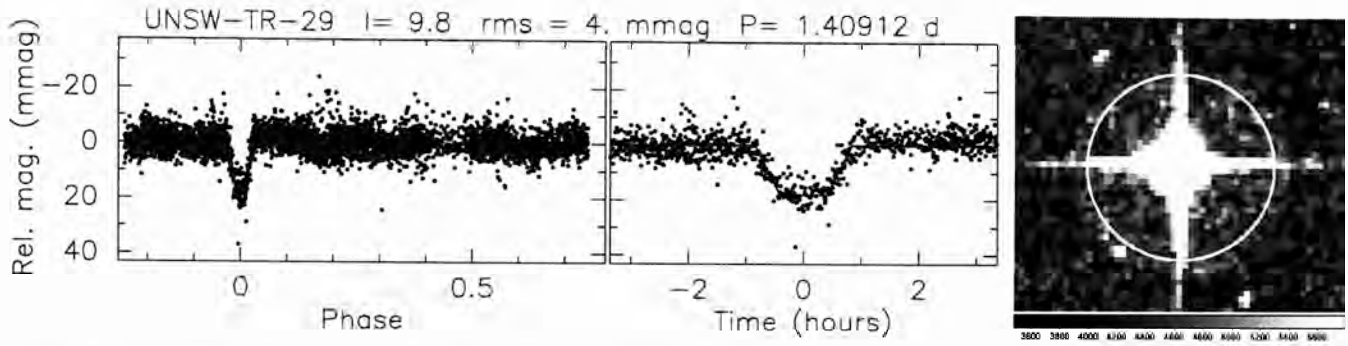

Figure 5.2. The original APT data for UNSW-TR-29 phase-folded at a period of 1.40912 d. The higher spatial resolution DSS image is also shown, with the APT photometry aperture overlaid.

observation from the 2006 September data; the overlaid circle indicates the size of the APT photometry aperture at this spatial resolution. In the majority of the remaining observations the two sources were indistinguishable. If the source of the transit signal was the brighter of the two stars, then the transit depth would still be compatible with a planet-sized companion; on the other hand, if the source was the faint star, the true depth would be much larger than that caused by a transiting planet.

We were fortunate to obtain a very high resolution spectrum ($R \sim 45000$) of the brighter component of UNSW-TR-29 using the University College London Echelle Spectrograph (UCLES) instrument on the 3.9-m Anglo-Australian Telescope at Siding Spring Observatory in 2007 August.[7] The spectrum was obtained during observations for the Anglo-Australian Planet Search, using the same instrument settings and procedures detailed in Butler et al. (1996, 2001) and Tinney et al. (2005). The spectrum was processed to the point of wavelength calibration using the standard IRAF echelle routines. The 1200 s exposure was taken in relatively poor seeing (4–5″), giving a S/N $\sim$ 24 in the region of Hα. A snapshot of the extracted spectrum in this region is shown in Figure 5.4, and the Hα line is clearly doubled, indicating the bright star is a double-lined spectroscopic binary. The lines are of approximately equal weights throughout the spectrum, indicating that the two components

[7] Many thanks to Chris Tinney for acquiring and preprocessing the spectrum.

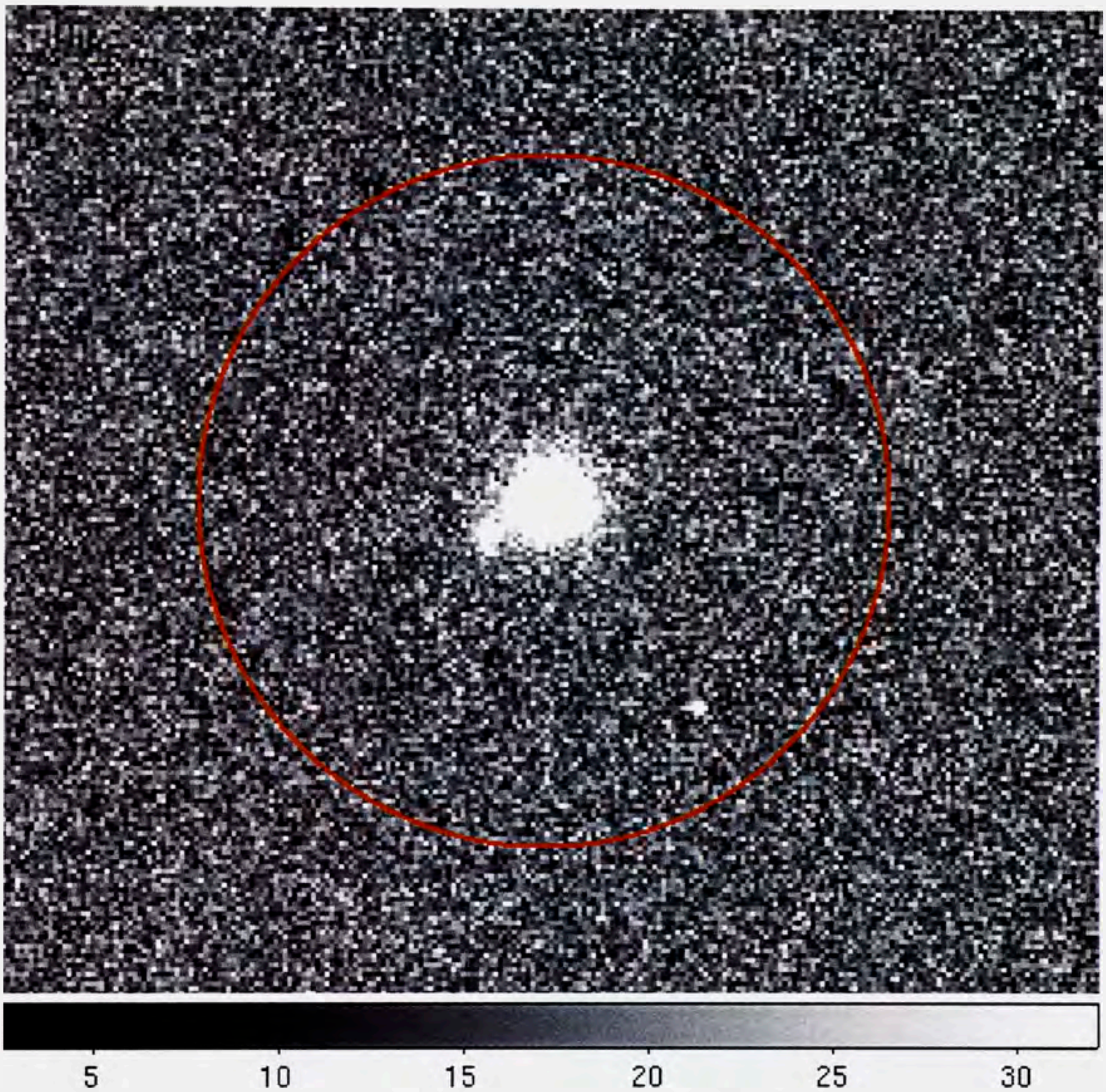

Figure 5.3. A 40-inch image of UNSW-TR-29, clearly showing that there are two resolvable sources at the centre of the original APT photometry aperture, which is overlaid. The image scale of the 40-inch is 0.38 arcsec pixel^{-1}.

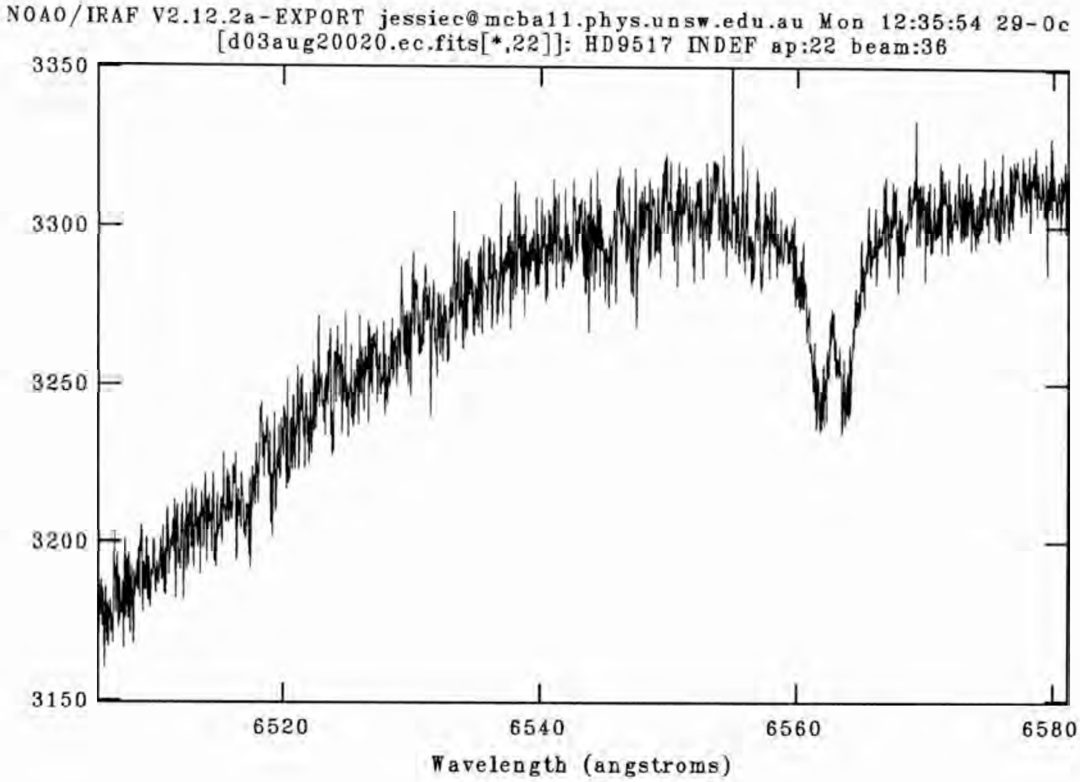

Figure 5.4. The UCLES spectrum of UNSW-TR-29 in the region of Hα. N.B.: The spectrum has not been flux calibrated.

of UNSW-TR-29 have similar spectral types.

The two obvious conclusions that can be drawn from this are: (1) that the spectroscopic binary is also a grazing eclipsing binary with a true period of twice the value quoted here, and that the brighter component is the source of the transit, or (2) the spectroscopic binary is not eclipsing and the source of the transit is the much fainter component. Both of these conclusions rule out the possibility of a hypothetical planet causing the transits. A third possibility, that the one of the components of the spectroscopic binary may contain a transiting planet, seems less likely. One of the reasons that eclipsing binary systems are considered good targets for extrasolar planet transit searches is that the planetary orbital plane is likely to be aligned with the binary orbital plane, as a result of precessionally-induced damping (Schneider & Doyle 1995). Therefore, if the transits we are observing are planetary transits, we could reasonably expect to observe eclipsing binary transits. Also, the true transit depth would be diluted to some extent by the second star,

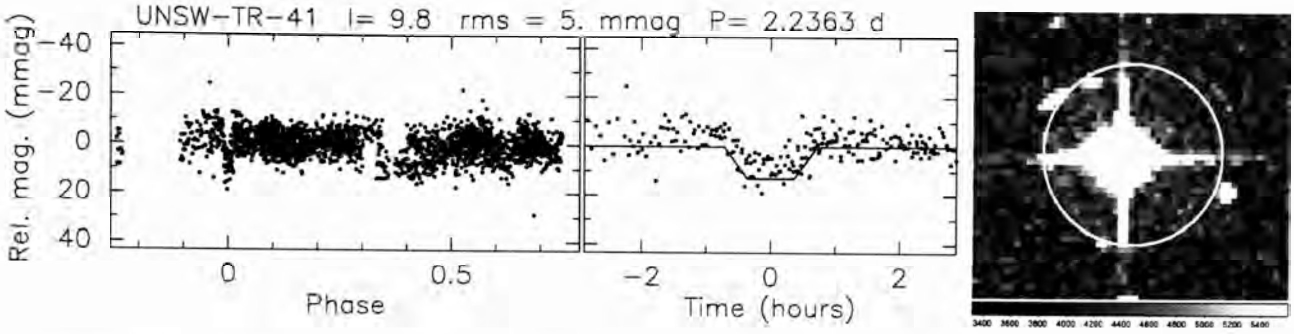

Figure 5.5. The original APT data for UNSW-TR-41 phase-folded at a period of 2.23625 d. The higher spatial resolution DSS image is also shown, with the APT photometry aperture overlaid.

inflating the estimated companion radius. One test for this possibility would be to obtain sufficient spectroscopic data to determine if the period of the radial velocity variations, if any, differs from the photometric period—if they are the same, then the transits are the result of the grazing eclipsing binary, as postulated in the first conclusion.

5-3.2 UNSW-TR-41

UNSW-TR-41 was discovered in the S5 field, observed between 2005 October and 2006 January. The phase-folded filtered light curve is shown in Figure 5.5 with the DSS image. Data from this field were significantly affected by systematics, and although the filtered light curve is shown for clarity, the parameters for the transit fit are derived from the unfiltered light curves as for the other candidates. The bright central source in the DSS image shows an asymmetry to the left, and therefore is probably a blend of two stars along the line of sight. In the APT light curve, the period is 2.23625 d and the transits are 13 mmag deep. The $(B-V)$ colour of 0.71 indicates a late G-type star, and the estimated companion radius is a low 0.7 $R_{\rm Jup}$. This candidate was also ranked highly for follow up observations.

Higher spatial resolution observations were obtained with the 40-inch telescope on 8 nights in 2007 January. The asymmetry observed in the DSS image is not resolved in the 40-inch images. There were sufficient data to create a phase-folded light curve,

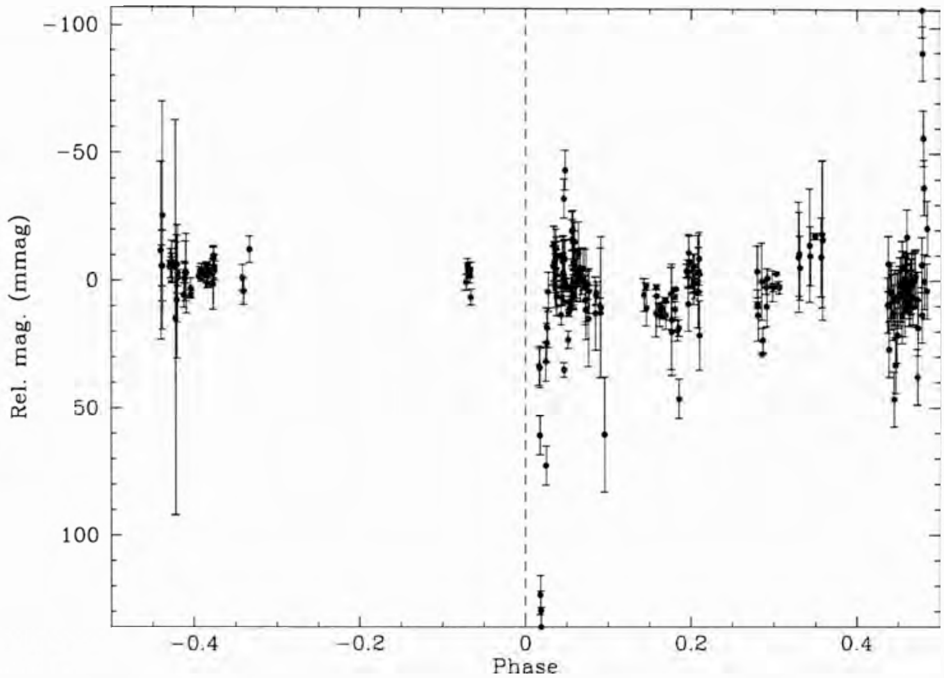

Figure 5.6. The phase-folded I-band 40-inch light curve of UNSW-TR-41, folded using the ephemeris derived from the APT light curve. The vertical dashed line indicates the expected time of transit.

which is shown in Figure 5.6. Although a full transit was not observed, data for one egress were obtained and indicate that the depth of the transit is > 100 mmag, implying the source of the transit is the fainter of the two blended stars and that this system is a blended eclipsing binary.

Several medium resolution spectra were obtained with the DBS instrument on the 2.3-m telescope in 2007 February. The central wavelength in the blue arm was 4160 Å, with a wavelength range of 3670–4650 Å and a resolution of 80 km s^{-1} pixel^{-1}. In the red arm the central wavelength was 8500 Å, with a wavelength range of 8030–8960 Å and a resolution of 37 km s^{-1} pixel^{-1}. By alternating target spectra with arc spectra, we typically achieve a wavelength calibration of better than ~ 0.1 pixels, giving us a radial velocity precision of 3–4 km s^{-1} in the red data.

There were no obvious double lines or asymmetries of the line profiles in the observed spectra; an extract from the red data around the region of the Ca II triplet is shown in Figure 5.7. This extract has been degraded to a resolution of 10 Å pixel^{-1} for comparison with the UVILIB spectral template library (Pickles

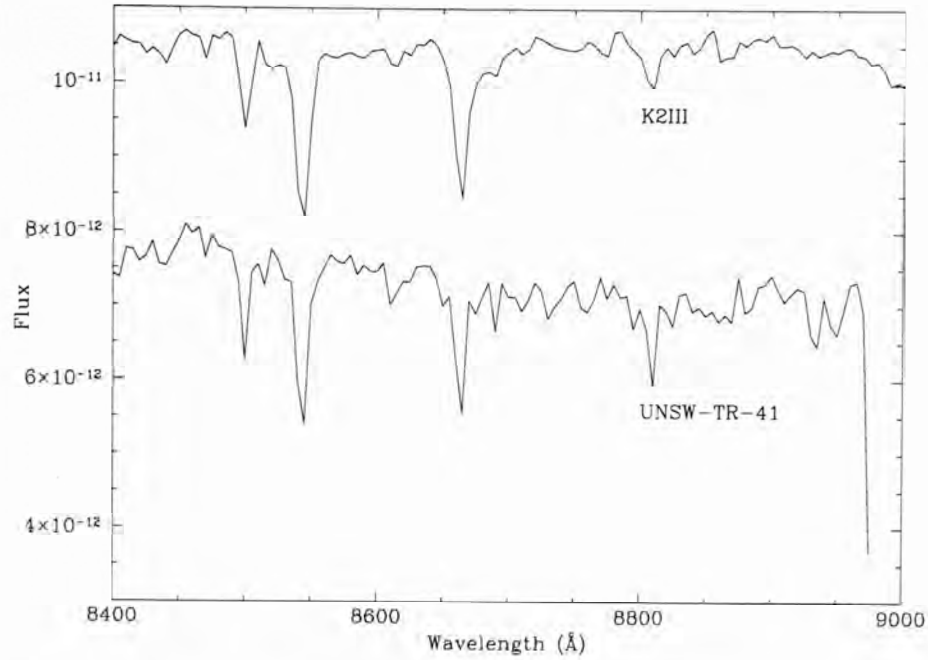

Figure 5.7. A medium resolution spectrum of UNSW-TR-41 taken with the DBS instrument on the 2.3-m telescope, degraded to a resolution of 10 Å pixel^{-1}. The closest visual UVILIB spectral template match is also shown.

1998); the closest visual match is the K2 III template spectrum. Insufficient phase coverage was obtained to measure any radial velocity variations.

In order to confirm that UNSW-TR-41 is a single-lined spectroscopic binary, more 2.3-m data would be required to increase the phase coverage, and ideally a full transit observed with the 40-inch to confirm the transit depth. However given the suspected true depth of the transit is $>$ 100 mmag, these additional observations have been given a low priority.

5-3.3 UNSW-TR-54

UNSW-TR-54 was discovered in the Feb06_1 field, observed in 2006 February–April. The original unfiltered APT light curve and DSS image are shown in Figure 5.8, phase-folded at a period of 3.6509 d. The mean magnitude of the light curve is $I =$ 11.6, and the transits are 25 mmag deep. We find a relatively high estimate for the companion radius of 2.0 $R_{\rm Jup}$. There are a few moderately bright stars in the the DSS image within the photometry aperture, however the transits are shallow enough

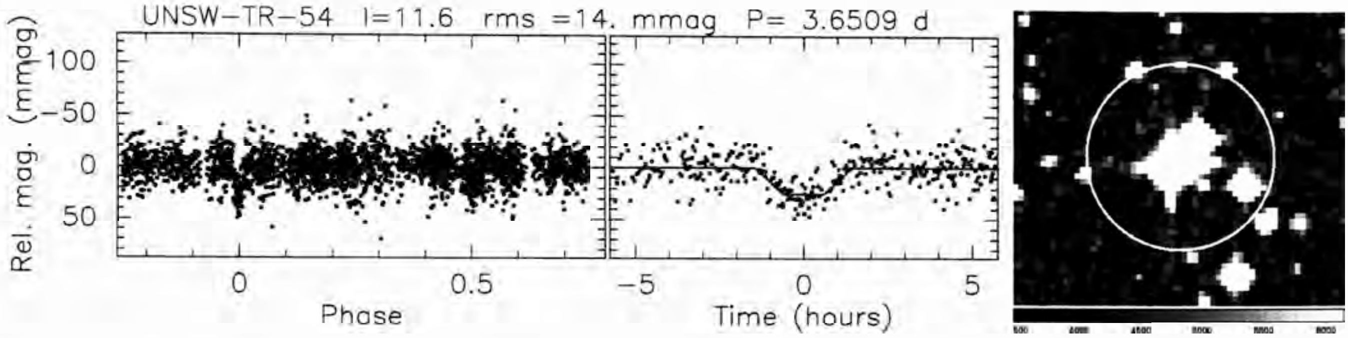

Figure 5.8. The original APT data for UNSW-TR-54 phase-folded at a period of 3.6509 d. The higher spatial resolution DSS image is also shown, with the APT photometry aperture overlaid.

to allow considerable dilution and still remain below the upper limit of 100 mmag. The star has no measurable proper motion, considerably reducing the probability that it is a nearby dwarf.

Time series photometry around a predicted transit time were obtained with the 40-inch telescope in 2006 May. The source of the transit was identified as the fainter of the two blended stars in the centre of the photometry aperture in the DSS image. The I-band light curve is shown in Figure 5.9, with the vertical dashed line indicating the centre of the predicted transit. Although only the ingress of the transit was observed, sufficient coverage was obtained to imply a transit depth greater than the 100 mmag limit, indicating that this system is a blended eclipsing binary. No further follow up data were obtained.

5-3.4 UNSW-TR-56

UNSW-TR-56 was discovered in the Feb06_2 field, observed concurrently with the Feb06_1 field in 2006 February–April. The phase-folded unfiltered light curve is shown in Figure 5.10 along with the DSS image. The light curve is folded at a period of 0.3864 d, and the transits are 30 mmag deep, resulting in a estimated companion radius of 3.1 $R_{\rm Jup}$. This period is extremely short, and combined with the very blue $(B-V)$ colour of -0.66 this points strongly towards a grazing eclipsing binary system. Although the DSS image shows several fainter stars accompanying

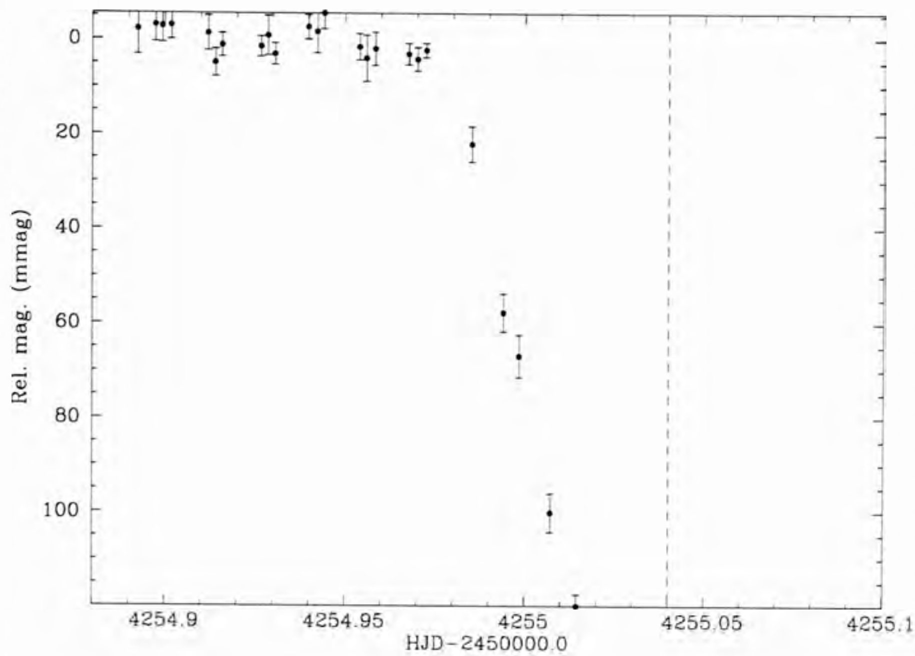

Figure 5.9. The I-band 40-inch light curve of UNSW-TR-54. The vertical dashed line indicates the centre of the predicted transit.

the bright central star in the photometry aperture, the transits are again shallow enough to allow significant dilution.

Despite the unconvincing nature of this candidate, the short period meant that it could be easily slotted into the 40-inch observing schedule as a low-ranked candidate for follow up. Data were obtained in 2007 May on three nights around three predicted transit times, and the I-band data are shown in Figure 5.11. The source of the transit signal was confirmed as the brightest star in centre of the DSS image, and the transit depth in the 40-inch light curve is therefore not noticeably increased. Again the vertical lines indicate the predicted transit times. These data were used to update the initial ephemeris to that shown in Table 5.2. Although the quality of the data from the third night is poor, the transits observed are unambiguously v-shaped, and we conclude that this candidate is a grazing eclipsing binary system.

5-3.5 UNSW-TR-60

UNSW-TR-60 was found in the May06_1 field, observed in 2006 May–June. The unfiltered APT light curve is shown in Figure 5.12, phase folded at a period of

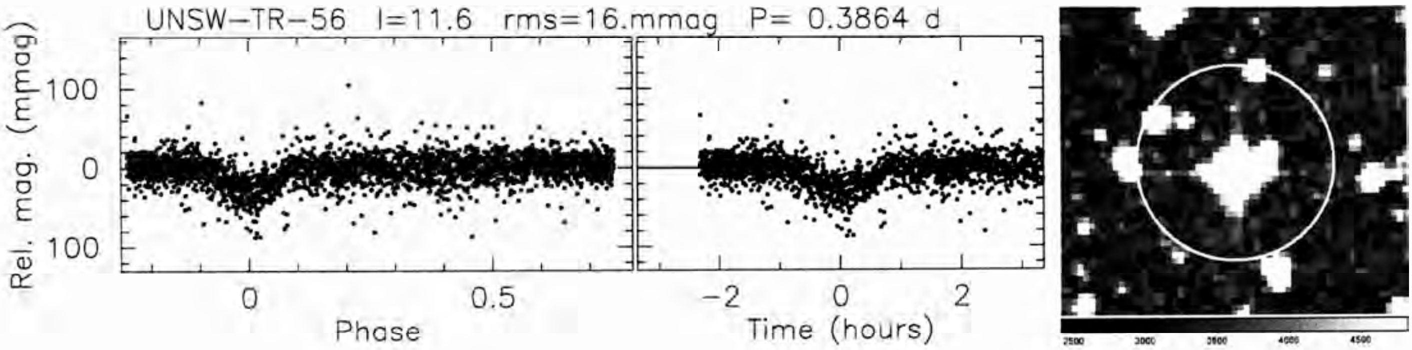

Figure 5.10. The original APT data for UNSW-TR-56 phase-folded at a period of 0.3864 d. The higher spatial resolution DSS image is also shown, with the APT photometry aperture overlaid.

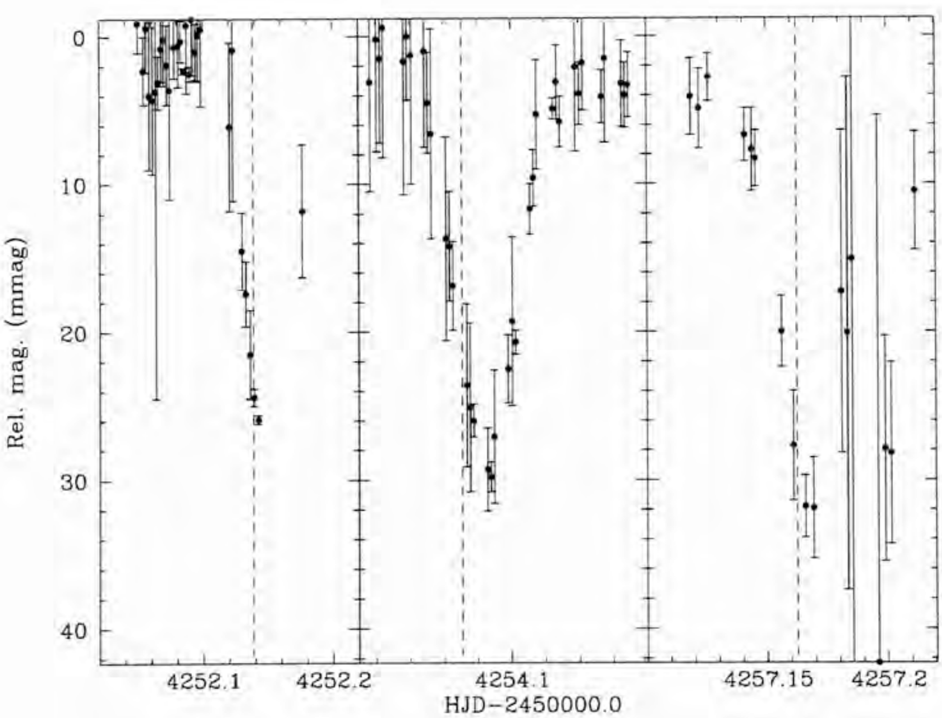

Figure 5.11. The I-band 40-inch light curve of UNSW-TR-56. The vertical dashed lines indicate the centres of the predicted transits.

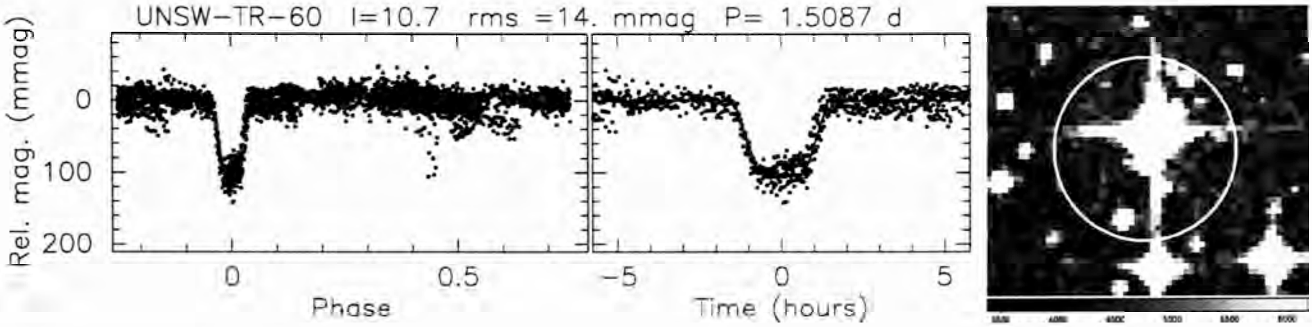

Figure 5.12. The original APT data for UNSW-TR-60 phase-folded at a period of 1.5087 d. The higher spatial resolution DSS image is also shown, with the APT photometry aperture overlaid.

1.5087 d. The DSS image shows a bright central star and several faint companions. The transit depth in the original light curve is ~ 100 mmag; combined with a $(B-V)$ colour of 0.35 and a large estimated companion radius of 3.4 $R_{\rm Jup}$, UNSW-TR-60 was not a highly ranked candidate. Additionally, the possibility of the secondary transit is not ruled out by the APT data.

Follow up observations were obtained with the 40-inch telescope in 2006 July, around the predicted times of the primary and secondary transits. The phase-folded I-band observations are shown in Figure 5.13 and confirm the presence of a secondary transit, with the central bright star identified as the source of the signal. We conclude that UNSW-TR-60 is an eclipsing binary system.

5-3.6 UNSW-TR-62

UNSW-TR-62 was discovered in the Jul06_2 field, observed between 2006 July–August. The unfiltered APT data is shown in Figure 5.14, folded at a period of 0.9425 d. There is a paucity of good quality data around a phase of 0.5, allowing for the possibility of a secondary transit. The transit depth is 50 mmag, the estimated companion radius is 2.6 $R_{\rm Jup}$, and the DSS image shows that the photometry aperture is relatively uncrowded, therefore UNSW-TR-62 was moderately highly ranked for photometric follow up to confirm the absence of a secondary transit.

40-inch photometry of UNSW-TR-62 was obtained in 2006 August, at the pre-

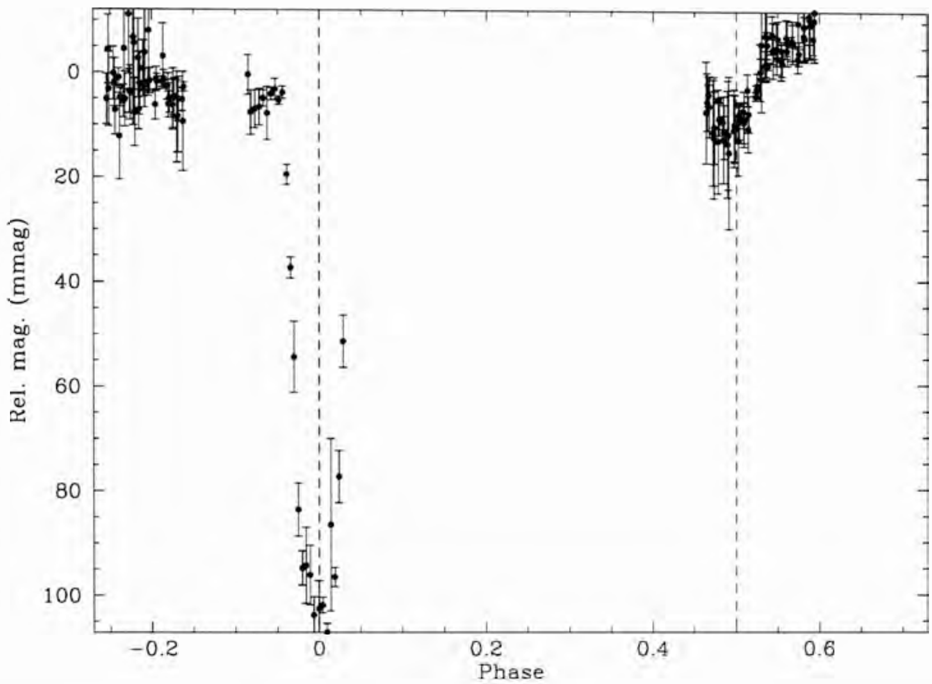

Figure 5.13. The phase-folded I-band 40-inch light curve of UNSW-TR-60, using the ephemeris derived from the APT light curve. The vertical dashed lines indicate the centre of the predicted primary and secondary transits.

dicted time of a secondary transit. The I-band data are shown in Figure 5.15 and confirm the presence of a secondary transit for the bright central star in the photometry aperture, with a depth of $\sim$ 26 mmag. It is evident that UNSW-TR-62 is an eclipsing binary system.

5-3.7 UNSW-TR-65

UNSW-TR-65 was observed in the Dec06 field between 2006 December and 2007 April. The phase-folded unfiltered APT light curve is shown in Figure 5.16. This is a fainter candidate, with a mean magnitude of $I = 12.3$, and the rms of the light curve is quite high (> 20 mmag), however, when folded at a period of 0.5846 d, a primary transit of depth 40 mmag is revealed. The DSS image shows a remarkably uncluttered photometry aperture, with one faint companion to the bright central star, and the estimated companion radius is 2.1 $R_{\rm Jup}$.

This is one of the most recent candidates, and as yet no photometric follow up has been performed to confirm the source of the signal in the photometry aperture.

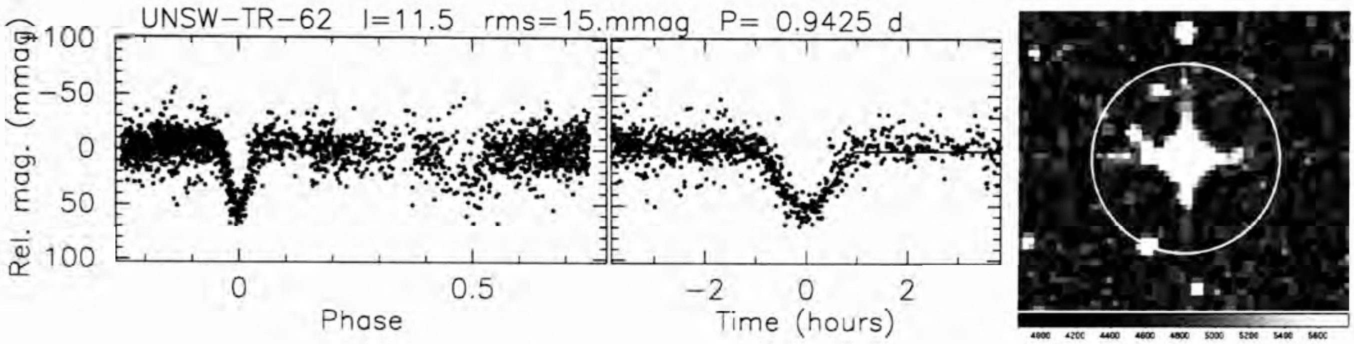

Figure 5.14. The original APT data for UNSW-TR-62 phase-folded at a period of 0.9425 d. The higher spatial resolution DSS image is also shown, with the APT photometry aperture overlaid.

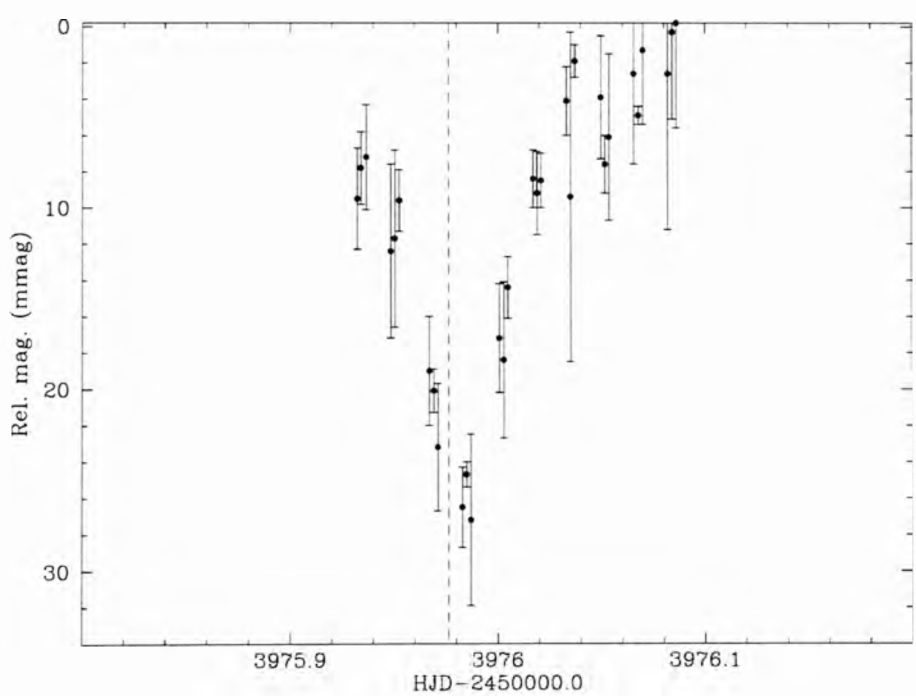

Figure 5.15. The I-band 40-inch light curve of UNSW-TR-62. The vertical dashed line indicates the centre of the predicted secondary transit.

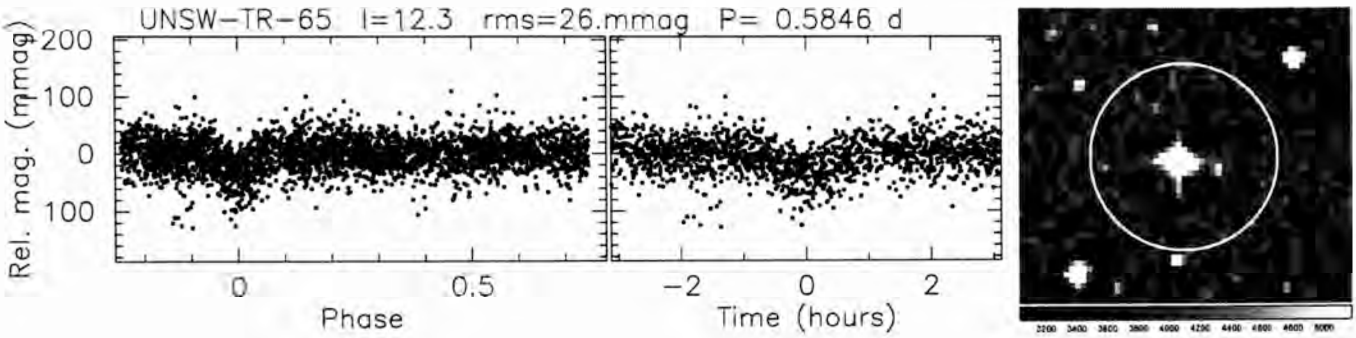

Figure 5.16. The original APT data for UNSW-TR-65 phase-folded at a period of 0.5846 d. The higher spatial resolution DSS image is also shown, with the APT photometry aperture overlaid.

However, several medium resolution spectra were obtained of the bright central star with the 2.3-m telescope in 2007 May. The central wavelength in the blue arm was 4160 Å, with a wavelength range of 3650–4670 Å and a resolution of 73 km s^{-1} pixel^{-1}. In the red arm the central wavelength was 6500 Å, with a wavelength range of 6000–7000 Å and a resolution of 45 km s^{-1} pixel^{-1}. An extract from the blue data is shown in Figure 5.17.

This spectrum has again been degraded to a lower resolution for comparison with the UVILIB stellar template spectra, the closest visual match being the G0V spectrum. There is no evident doubling or asymmetry in the lines, however, since this star not necessarily the source of the transit, at this stage we are unable to draw conclusions as to the true nature of UNSW-TR-65. The possibilities include: (1) the bright central star is the source of the transit signal; the spectrum may indicate a single-lined spectroscopic binary or a single stellar spectrum compatible with a planetary companion orbiting a single star, or (2) the fainter star is the source of the transit signal, in which case the true depth will be incompatible with that caused by a transiting planet. For confirmation we will require time series photometry to identify the source of the transit, and if required, additional spectra with sufficient phase coverage to constrain the radial velocity variations.

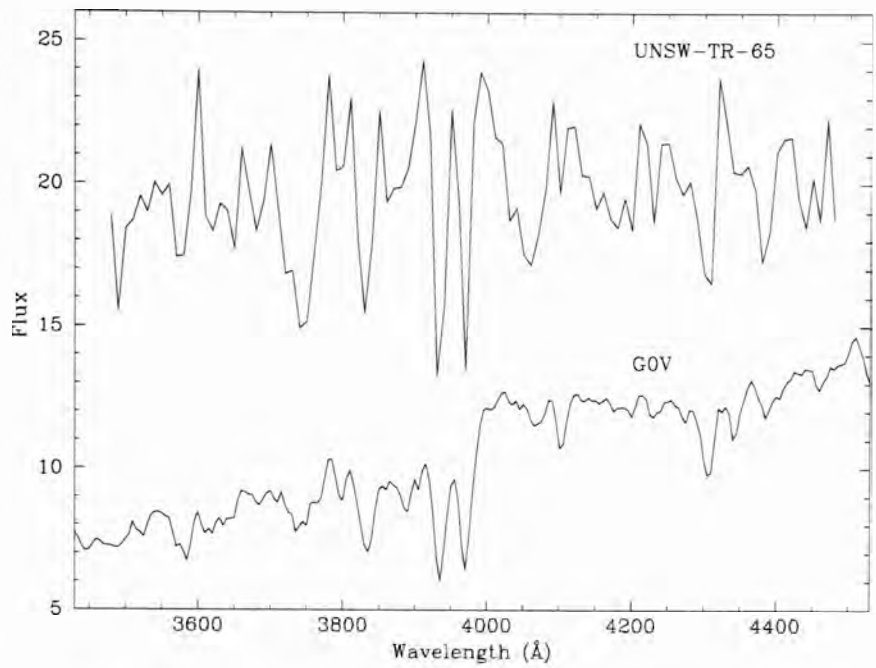

Figure 5.17. A medium resolution spectrum of UNSW-TR-65 taken with the DBS instrument on the 2.3-m telescope, degraded to a resolution of 10 Å pixel^{-1}. The closest visual UVILIB spectral template match is also shown.

5-3.8 UNSW-TR-67

UNSW-TR-67 was also found in the Dec06 field. The unfiltered APT data are shown in Figure 5.18, phase-folded at a period of 1.3775 d. The transits are 35 mmag deep, and the DSS image resolves a bright central star and several faint companions in the photometry aperture. Although the $(B-V)$ colour is a promising 0.52, indicating a G-type star, the transits are relatively v-shaped, leading to an estimated companion radius of 5.4 R_{Jup}.

As for UNSW-TR-65, we have not yet obtained higher spatial resolution follow up to ascertain the source of the transit signals within the photometry aperture. Several medium resolution spectra of the bright central star were obtained with the 2.3-m telescope on the same observing run as UNSW-TR-65, with the same instrument settings. These spectra immediately revealed the presence of doubled lines; an extract from the red data around the Hα wavelength region is shown in Figure 5.19 at the original resolution. Since we have not confirmed the source of the transit but have determined that the bright central star is a double-lined spectroscopic binary,

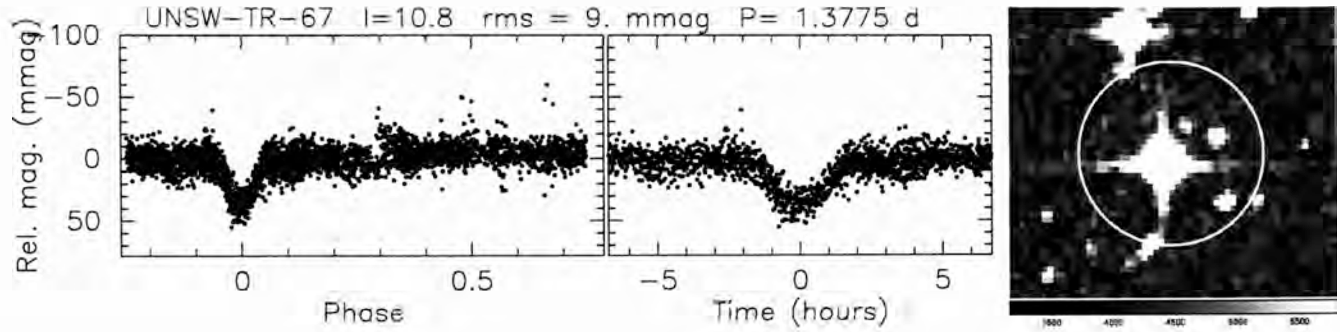

Figure 5.18. The original APT data for UNSW-TR-67 phase-folded at a period of 1.3775 d. The higher spatial resolution DSS image is also shown, with the APT photometry aperture overlaid.

the possible conclusions are the same as those outlined for UNSW-TR-29 in Section 5-3.1: a blended eclipsing binary and an unassociated double-lined spectroscopic binary within the photometry aperture, a eclipsing double-lined spectroscopic binary, or a double-lined spectroscopic binary containing a transiting planet.

5-4 Candidates requiring follow up

The transit candidates that were identified but have yet to be followed up are summarised below, in chronological order of discovery. These are typically lowly rated candidates that have not been given priority during previous observing runs, or have been found in the most recent fields and are awaiting observation. The details of these candidates are summarised in Table 5.3.

5-4.1 UNSW-TR-45

UNSW-TR-45 was observed in the Jan06_1 field in 2006 January–February. Only a single transit event was observed, of depth $\sim$ 30 mmag. The unfiltered APT data are shown in Figure 5.20, phase-folded at a trial period of 4.57 d for clarity. The DSS image shows a bright central star and a few faint background stars, and combined with the red $(B - V)$ colour of 0.66 indicates a promising candidate. However, the lack of period determination rules out targeted higher spatial resolution

Table 5.3. The transit candidates that were lowly ranked for follow up and have undetermined status. The columns have the same meanings as in Table 5.2. The observations required to determine the status of the candidates are listed as P (photometric follow up) or S (spectroscopic follow up).

ID Notes	Field	α_{J2000}	δ_{J2000}	I	Epoch	P	ΔF	t_T	t_F	R_p	$(B-V)$	μ
				(mag)	HJD - 2450000.0	(d)	(mmag)	(d)	(d)	($R_{\rm Jup}$)		(mas yr^{-1})
UNSW-TR-45	Jan06_1	09:14:35.741	-23:50:35.65	10.7	3742.015	-	30	0.17	0.02	-	0.66	8.6
Single event, S?												
UNSW-TR-46	Jan06_1	09:17:15.059	-24:35:53.69	11.4	3740.090	0.5830	20	0.08	0.03	2.9	-	26.6
P												
UNSW-TR-57	Feb06_2	13:16:37.220	-45:32:07.15	10.3	3790.085	1.7438	23	0.11	0.02	3.0	-	128.8
P												
UNSW-TR-66	Dec06	07:56:18.304	-66:37:46.24	12.2	4115.100	3.6974	50	0.13	0.065	2.2	-	4.9
P												
UNSW-TR-68	Mar07	14:34:48.816	-68:21:48.76	12.4	4175.095	1.480	30	0.06	0.03	1.0	-	17.4
P/S												

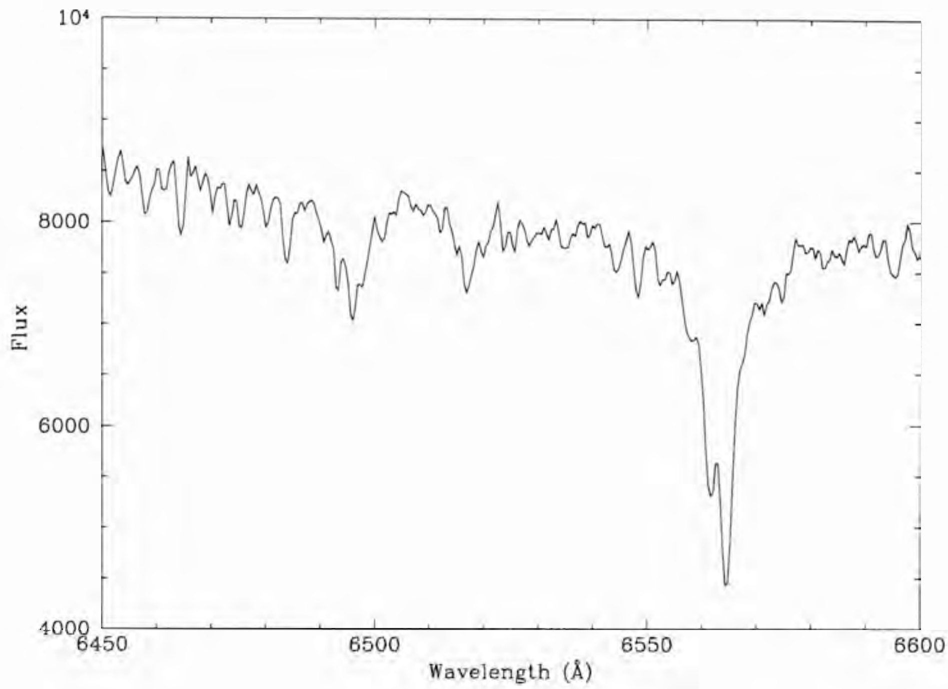

Figure 5.19. A medium resolution spectrum of UNSW-TR-67 taken with the DBS instrument on the 2.3-m telescope, at the original resolution to show the doubled lines at $\sim$ 6495Åand $\sim$ 6564Å.

follow up to determine the source of the transit within the photometry aperture. Medium resolution spectra of the central star could rule out the possibility of a planet by revealing doubled lines or large radial velocity variations, but the absence of these obvious indicators would not advance our case for this candidate significantly. UNSW-TR-45 is maintained on the active candidate list in the event of additional APT observations being acquired at these coordinates with the new camera.

5-4.2 UNSW-TR-46

UNSW-TR-46 was also observed in the Jan06_1 field. The unfiltered APT data are shown in Figure 5.21, phase-folded at a period of 0.5830 d. The transits are 20 mmag deep, and the DSS image shows a single bright star at the centre of the photometry aperture. The light curve of the bright star bordering the upper left of the photometry was phase-folded at the same period and it was confirmed that the signal was unique to UNSW-TR-46, and not some deeper eclipsing binary signal in the neighbouring star affecting the candidate light curve. The relatively high

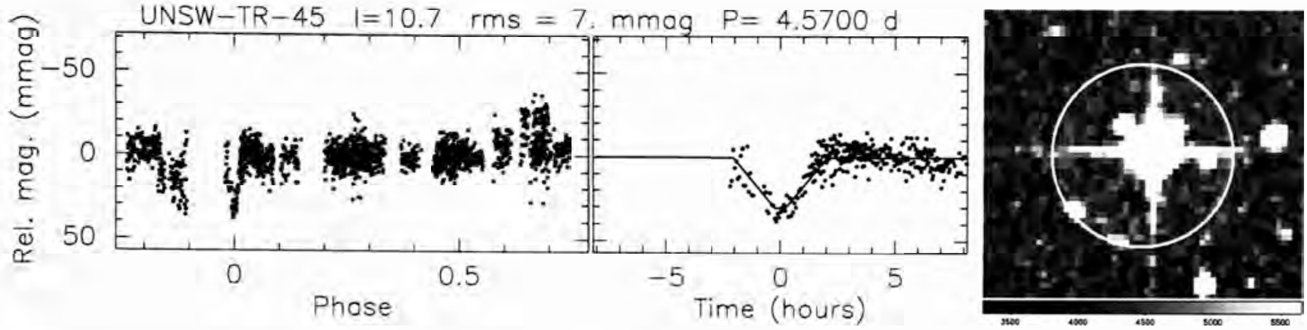

Figure 5.20. The original APT data for UNSW-TR-45 phase-folded at a trial period of 4.57 d; the original light curve contained only a single transit event. The higher spatial resolution DSS image is also shown, with the APT photometry aperture overlaid.

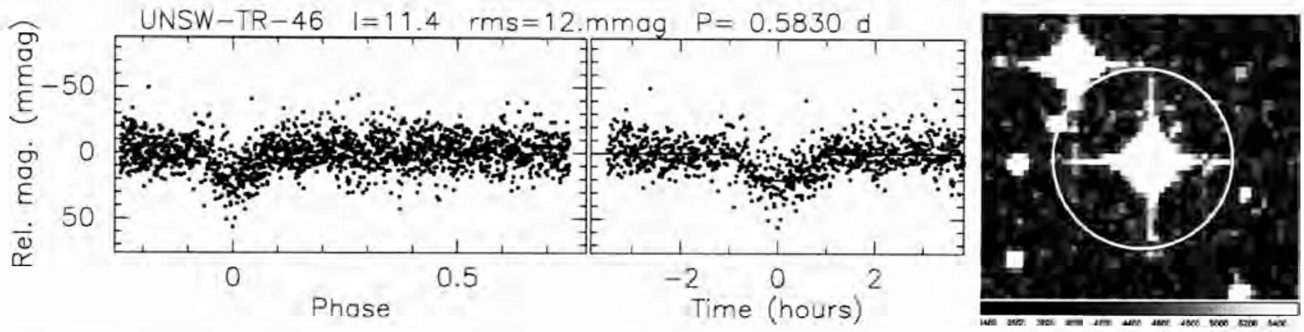

Figure 5.21. The original APT data for UNSW-TR-46 phase-folded at a period of 0.5830 d. The higher spatial resolution DSS image is also shown, with the APT photometry aperture overlaid.

estimated companion radius 2.9 $R_{\rm Jup}$ and short period qualify UNSW-TR-46 for a relatively low ranking for follow up. However, higher precision time series photometry around predicted transit times would result in an improved characterisation of the transit shape, which is fairly loosely constrained in the APT data, and increase our understanding of this candidate.

5-4.3 UNSW-TR-57

UNSW-TR-57 was discovered in the Feb06_2 field, observed in 2006 February–April. The phase-folded unfiltered APT data are shown in Figure 5.22, with a period of 1.7438 d. The DSS image shows two relatively bright stars in the centre of the photometry aperture, however in the original data the transits are 23 mmag deep, allow-

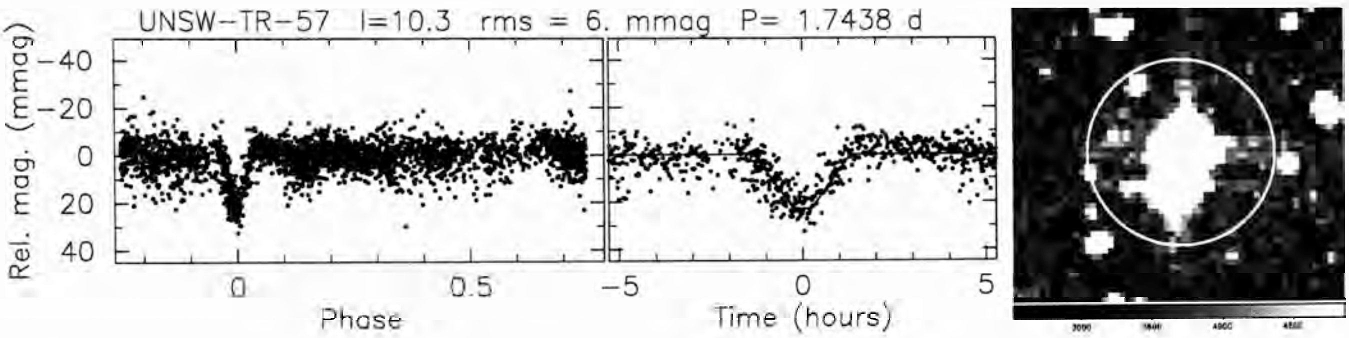

Figure 5.22. The original APT data for UNSW-TR-57 phase-folded at a period of 1.7438 d. The higher spatial resolution DSS image is also shown, with the APT photometry aperture overlaid.

ing substantial dilution. The measured proper motion a moderate 128.8 mas yr^{-1}, indicating this star is more likely a nearby dwarf than a distant giant. The estimated companion radius is 3.0 $R_{\rm Jup}$, due to the relatively v-shaped transits, and as a result UNSW-TR-57 was not a high priority candidate. At this stage, higher spatial resolution photometry around predicted transit times is required to identify the source of the transit and confirm the absence of a secondary transit.

5-4.4 UNSW-TR-66

UNSW-TR-66 was observed in the Dec06 field with UNSW-TR-65. A single transit event was observed in the APT light curve; the unfiltered data are shown in Figure 5.23, phase-folded at a trial period of 3.6974 d. The transit is 50 mmag deep, and the DSS image reveals the presence of two stars of approximately equal brightness in the photometry aperture, indicating that the true depth is $\sim$ 100 mmag and that UNSW-TR-66 is only a borderline candidate. Again, this candidate remains on the active list in the event of additional observations being obtained.

5-4.5 UNSW-TR-68

UNSW-TR-68 was detected in the most recently observed field, Mar07. Only two transit events were observed, therefore the period is somewhat uncertain. The unfiltered APT light curve is shown in Figure 5.24, phase-folded at the trial period

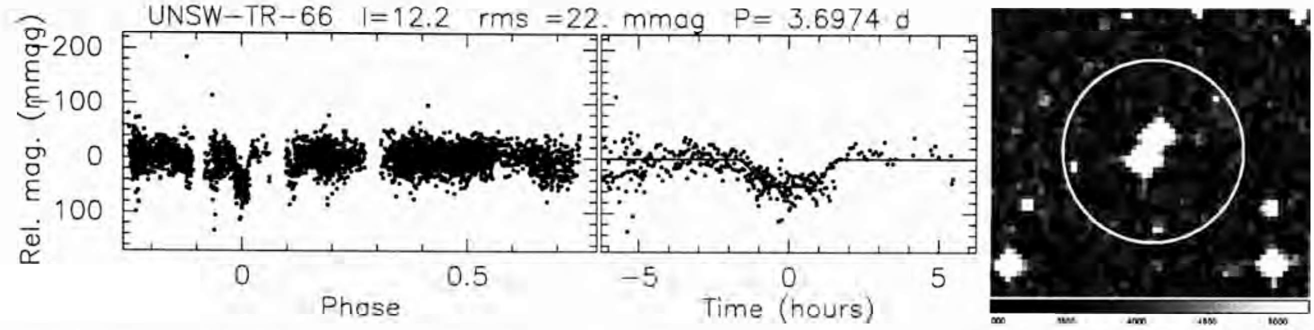

Figure 5.23. The original APT data for UNSW-TR-66 phase-folded at a trial period of 3.6974 d; the original light curve contained only a single transit event. The higher spatial resolution DSS image is also shown, with the APT photometry aperture overlaid.

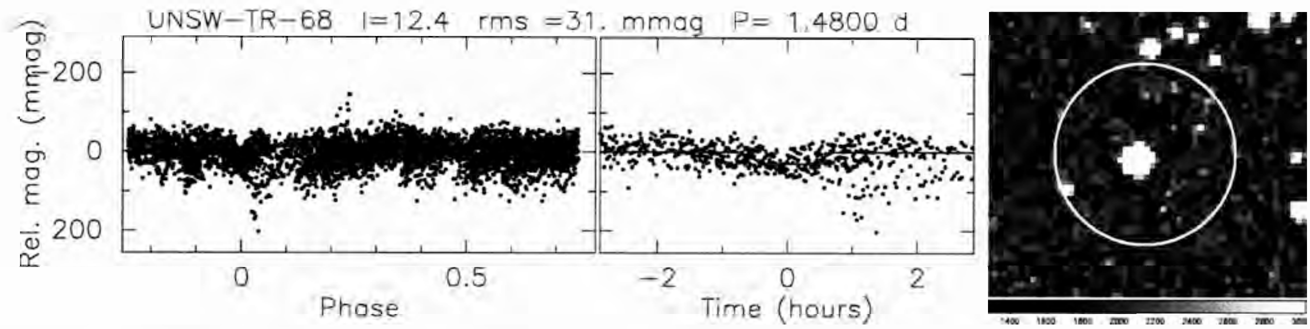

Figure 5.24. The original APT data for UNSW-TR-68 phase-folded at a period of 1.48 d. There are only two events observed in the light curve, hence the loose constraints on the period. The higher spatial resolution DSS image is also shown, with the APT photometry aperture overlaid.

of 1.48 d. This field was another significantly affected by systematics, however the two transits remain in the filtered data. The DSS image shows an isolated central star and an additional faint star on the boundary of the aperture. The transit depth of 30 mmag and the trial period give a promising companion radius estimate of 1.0 $R_{\rm Jup}$. Additional photometry is required to confirm the period, and spectroscopy would be useful to determine the spectral type and to check for the obvious indicators of a spectroscopic binary.

5-5 Summary and assessment

In the period 2004 October to 2007 May, we identified 23 potential planet candidates from $\sim 87,000$ light curves. After further analysis, ten candidates were rejected, typically on the basis that the true transit depth was indicated to be greater than our upper limit of 100 mmag. Eight candidates were followed up with either higher spatial resolution time series photometry or spectroscopy, and were identified as eclipsing binaries. The remaining five candidates still require follow up observations to determine their status.

The simulations performed in the period 2001–2004, discussed in Section 1-5.2, predicted a planet yield of 2–3 planets a year using the initial observing strategy adopted in this current work. The most significant reason for our lack of progress to this goal has been the effect of systematics in our data, and the modifications that were required to be made to the observing strategy as a result, described in Section 4-3. The ~ 20 nights that were initially obtained on each field contained too few data points for phase-folding of shallow transits to increase the S/N enough to overcome the systematics, and our likelihood of detecting potential planet candidates was therefore considerably degraded. To counteract these systematics, the number of nights obtained had to be increased, and the number of fields observed at a time decreased from two to one. This reduced the number of fields observable per year by a factor of 3–4. While this change hopefully increased the planet yield within each field back to the original predicted rate, it represented a significant reduction in the overall potential yield compared to the original simulations.

This underwhelming result is echoed in the results of other wide-field transit surveys. Although the discoveries are now trickling in at an increasing rate, as discussed in Section 1-2.6.4, the overall affect of systematics has been to reduce the total number of detections to be far lower than predicted (Pont et al. 2006; Smith et al. 2007). As an example for perspective, the SuperWASP project obtained 1.1×10^6 light curves in a magnitude range of $8 > V > 13$ for a return of two transiting planet discoveries (Collier Cameron et al. 2007). It is therefore perhaps unsurprising that our 87,000 light curves have not yielded a confirmed planet.

The results of the transit survey to date indicate that we are reaching the photometric precision required to detect transiting planets, and that the procedures we have in place are capable of extracting promising transit candidates. Our significant handicaps are currently the removal of systematics without increasing the white noise or distorting the real signals, and increasing the number of targets we are observing in line with the statistics that are emerging from successful wide-field transit surveys. Both of these issues are in the process of being addressed for the next phase of the survey, and are discussed in Chapter 8.

Chapter 6

Variable star catalogue

6-1 Abstract

We present a new catalogue of variable stars compiled from data taken for the University of New South Wales Extrasolar Planet Search. From 2004 October to 2007 May, 25 target fields were each observed for 1–4 months, resulting in $\sim$ 87000 high precision light curves with 1700–4400 data points. We have extracted a total of 850 variable light curves, 659 of which do not have a counterpart in either the General Catalog of Variable Stars, the New Suspected Variables catalogue or the All Sky Automated Survey southern variable star catalogue. The catalogue is detailed here, and includes 142 Algol-type eclipsing binaries, 23 β Lyrae-type eclipsing binaries, 218 contact eclipsing binaries, 53 RR Lyrae stars, 26 Cepheid stars, 153 uncategorised pulsating stars with periods $<$ 10 d, including δ Scuti stars, and 222 long period variables with periods $>$ 10 d. As a general application of variable stars discovered by extrasolar planet transit search projects, we discuss several astrophysical problems which could benefit from carefully selected samples of bright variables. These include: *(i)* the quest for contact binaries with the smallest mass ratio, which could be used to test theories of binary mergers; *(ii)* detached eclipsing binaries with pre-main-sequence components, which are important test objects for calibrating stellar evolutionary models; and *(iii)* RR Lyrae-type pulsating stars exhibiting the Blazhko-effect, which is one of the last great mysteries of pulsating star research.

6-2 Introduction

The University of New South Wales (UNSW) is conducting a wide-field survey for transiting extrasolar planets, and is one of an increasing number teams around the world using this method. The nature of wide-field surveys has resulted in an enormous number of high-precision light curves being produced, numbering in the millions for some teams (e.g. Collier Cameron et al. (2007)).

In order to maximise the output efficiency from wide-field surveys, it is important to make the data available for use in other studies once planet candidates have been identified. The most extensive results produced by these projects to date have been long lists of newly discovered variable stars, inevitably with very limited information apart from the period and amplitude in a single band (Hartman et al. 2004; Pepper & Burke 2006). Therefore, one can imagine the main use of these variable star catalogues is to define starting samples for astrophysically interesting follow-up studies that benefit from large samples of carefully selected stars. A recent example is the list of variable stars coincident with x-ray sources presented by Norton et al. (2007).

The UNSW Extrasolar Planet Search is performed with the largest clear aperture telescope of the wide-field transit surveys. With a diameter of 0.5-m, this project occupies the niche between the typical wide-field transit surveys observing brighter targets with 0.1–0.2-m diameter telescopes, and the deeper surveys with narrower fields of view using > 1-m diameter telescopes. The larger collecting area in this project has been exploited to increase the acquisition rate for the observations, as compared to observing deeper targets, since brighter targets have a higher potential for interesting follow-up studies. The large data set of light curves we have obtained is therefore the ideal starting point from which to compile a bright variable star catalogue of particularly well-sampled light curves with high precision photometry and moderately long observing baselines (1–4 months).

The paper is organised as follows. Section 6-3 describes the observations and reduction pipeline. Section 6-4 describes the methods by which the variable light curves were selected. The final catalogue is presented in Section 6-5, while three possible applications of the sample are discussed in Section 6-6. The data are publicly available at the University of New South Wales Virtual Observatory (VO) facility, which is described in Section 6-7. We close the main body of the paper with a short summary of the project in Section 6-8. Cross-references to the General Catalogue of Variable Stars (GCVS) and the All Sky Automated Survey (ASAS) database are given in the A.

6-3 Observations and Reduction

6-3.1 Photometry

The data were obtained using the dedicated 0.5-m Automated Patrol Telescope at Siding Spring Observatory, Australia. Observing is performed remotely on every clear night when the Moon is not full and is almost entirely automated; the observer initiates the observing script and monitors the weather conditions. The CCD camera used for these observations consists of an EEV CCD05-20 chip, with 770×1150 pixels. The pixel size of 22.5 μm produces a relatively low spatial resolution of 9.4 arcsec pixel^{-1}, and the field of view of each image is 2×3 deg^2. The observations were taken through a Johnson I filter, a decision designed to maximise the contribution to the photometry of later spectral type dwarf stars, around which it is easier to detect transiting planets. A new CCD camera covering 7×7 deg^2 with a higher spatial resolution of 4.19 arcsec pixel^{-1} has been constructed for this project and will be installed on the telescope in 2008.

Observations were obtained for 32 months from 2004 October to 2007 May on 25 target fields, listed in Table 4.1, resulting in a total sky coverage of $\sim$ 150 deg^2. The equatorial coordinates of the centre of each field is given, as are the Galactic coordinates. The strategy employed for field selection was again motivated by transit detection. The most southerly fields were chosen in order to reduce the airmass variations over the course of the night, with a maximum allowable declination of 70° due to building constraints. At the same time, the Galactic latitude was constrained to $b > 10°$ to alleviate crowding effects in the field, which led to several more northern fields being selected. This latter constraint was relaxed for the final field in order to observe a more crowded stellar field.

Most of the fields were observed in pairs in order to increase the number of target stars, with observations alternating between the two fields over the course of the night. For the majority of the fields the rate of acquisition is 15 images per hour, however for the first pair of fields it is half as often as this. For the final three fields we implemented an automated script that adjusted the exposure times according to the sky brightness levels, and the rate of acquisition ranges from 10–40 images per hour. These fields were also observed singly instead of pairwise, which accounts for the higher rates achieved. Each field was observed for a minimum of 20 nights for at least $\sim 4-5$ hours per night, resulting in $1600-4400$ observed data points for each star. Each field contained $\sim 1200-8000$ stars with $8.0 \geq I \geq 14.0$, depending on the Galactic coordinates. The numbers of stars observed down to 14^{th} magnitude in each field are included in Table 4.1, with ~ 87000 light curves being generated.

6-3.2 Reduction pipeline

In order to achieve the extremely precise photometry required for transit detection, we have developed a simple, robust, automated aperture photometry reduction pipeline. A detailed description can be found in Hidas et al. (2005); a summary is included here for completeness, and there have been no modifications.

Using the tools developed by Irwin & Lewis (2001), each image is processed in the standard manner, including bias subtraction, flat-field correction and catalogue generation. For each field, a master image is generated by combining ~ 10 consecutive, low airmass images with small image-to-image shifts, and a master coordinate list is produced. Each image frame is then transformed into the master reference frame with a positional accuracy of less than 0.01 pixels. Aperture photometry is performed on the transformed images, with a fixed aperture radius of 3 pixels, which equals $30''$ on the sky. At the typical Galactic latitude of our fields, this results in multiple stars falling within the same photometry aperture more than 80% of the time; these stars can only be resolved in higher spatial resolution images. As a result, the magnitudes listed in this catalogue should be taken as upper limits on the true magnitude, and the variability amplitudes as lower limits. Magnitude variations from image to image are calibrated by using a subset of the brightest stars. The magnitude residuals Δm for each star are fit iteratively with a position-dependent function of the form

$$\Delta m = a + bx + cy + dxy + ey^2 \tag{6.1}$$

where x and y are the pixel coordinates of the star on the CCD, and $a - e$ are a set of constants for each image. With each iteration, the stars with the highest rms residuals are removed.

After the light curves are generated by the reduction pipeline, they are processed to remove the significant systematic signals using an implementation of the trend-filtering algorithm described by Kovács et al. (2005). A random subset of several hundred stars are chosen as template light curves. For each of the remaining light curves, the closest matching synthetic light curve that can be reconstructed from a linear combination of the template light curves is subtracted. Signals that are common to the template and original light curve will be removed, and signals that are unique to the original light curve remain. Figure 4.1 shows an example of the precision achievable in typical fields of data, before and after being processed with the trend-filtering algorithm. For the stars brighter than $I \sim 11.5$ the rms precision of the filtered light curves is typically less than 10 mmag.

6-4 Selection of variable candidates

Three methods were used to extract the variable light curves from the full data set: *(i)* visual inspection of the filtered light curves down to 13$^{\text{th}}$ magnitude, *(ii)* implementation of a box-search algorithm on all filtered light curves (down to 14$^{\text{th}}$ magnitude), and *(iii)* implementation of the Stetson Variability Index on the entire set of filtered and unfiltered light curves. The first two methods formed part of the search for transiting extrasolar planets, the main science driver of this project

(Hidas et al. 2005). The third was implemented to improve the completeness of the catalogue.

6-4.1 Visual inspection

As a first pass, all light curves down to 13th magnitude are visually inspected, as described in Section 4-5.2. Similarly to when searching for transit events, visual inspection can fail for fainter stars with increased shot noise, and brighter stars where the variable signal is of low significance, and will not be evident until the light curve is phased with the correct period. Importantly, this method is not successful for the detection of variable light curves with periods greater than ~ 5 d. In these cases, the light curve for each night appears essentially flat, especially to someone specifically searching for transit events on the order of a few hours. Also, visual inspection has the potential to miss light curves that exhibit only single or partial events on a single pass through.

6-4.2 Box-search algorithm

The light curves are subsequently processed with a transit detection algorithm, as described in Section 4-5.3. The algorithm will detect the variable light curves with parameters that fall within the specified period and transit duration windows: both the shallow transit events that are flagged as potential transiting planet candidates and the deeper events produced by detached eclipsing binary systems. Additionally, it returns many variable light curves which can be approximated to some extent by a box-shaped model lying within the required period range, including: grazing eclipsing binaries exhibiting V-shaped transits; continuously varying light curves that give a significant result when folded to an optimum period; and variable light curves with periods outside the specified window but where an integer number of periods is located within the window. It also has the additional advantage of detecting those light curves with only single or partial events and providing a potential period. However, it is not useful for detecting variable light curves with periods much shorter (< 0.5 d) or much longer (> 10 d) than the specified period window.

6-4.3 Stetson Variability Index

Neither of the preceding methods will rigorously detect the longest period variables in our light curves. In order to increase the completeness of this variable star catalogue it was essential to correct this bias. An additional method of detecting variability in light curves is the Stetson Variability Index (Stetson 1996), a measure of the correlated signal in a light curve.

Using the notation of Stetson (1996), the index J is given by

$$J = \frac{\sum_{k=1}^{n} w_k \mathrm{sgn}(P_k)\sqrt{|P_k|}}{\sum_{k=1}^{n} w_k} \tag{6.2}$$

where n pairs of observations have been defined. For the kth pair, with a weighting of w_k, the magnitude residuals are $\delta_{i(k)}$ and $\delta_{j(k)}$, where i and j are the observations forming the pair. We can therefore define the product of the magnitude residuals as $P_k = \delta_{i(k)}\delta_{j(k)}$, or $P_k = \delta^2_{i(k)} - 1$ for single observations (where $i = j$). The term $\mathrm{sgn}(P_k)$ is the sign (positive or negative) of P_k. We have calculated the magnitude residuals in the same manner as Stetson (1996), scaling by the individual observational errors and correcting for the statistical bias to the mean, giving

$$\delta = \sqrt{\frac{n}{n-1}}\left(\frac{v - \bar{v}}{\sigma_v}\right) \tag{6.3}$$

where v is the measured magnitude of the observation, $\bar{v}$ is the mean magnitude over all observations, and σ_v is the individual error on the observed magnitude. To form the pairs of observations we chose a timescale of 10 minutes; all observations that lie within 10 minutes of each other are paired. All pairs with $i \neq j$ are assigned a weight of 1.0, and those with $i = j$ a weight of 0.1. We found the best results in terms of detecting longer period variables (> 1 d) when the data were binned on a similar timescale of $\sim$ 10 minutes, although this was at the cost of lowering the detection of the very shortest period variables. The solid squares in Figure 6.1 show a typical distribution of this variability index for a single field, in this case the Dec06 field, prior to the trend-filtering stage.

One problem we encountered was the tendency for our implementation of the trend-filtering algorithm to suppress or entirely remove the night-to-night magnitude jumps present in the long-period variable light curves, resulting in a smaller than expected variability index. This was solved by running the variability index on both the filtered light curves to detect the shorter period variables and the unfiltered light curves to detect the longer period variables. The caveat to this is that long period trends in the systematic signals in the data, for instance signals correlated with moon phase, are not removed from the long period light curves. In an effort to overcome this, we have removed those long period light curves where multiple light curves in the same field demonstrate the same morphology and are described well by the same period and epoch. In the future we plan to resolve this problem by replacing the trend-filtering algorithm with an implementation of SYSREM (Tamuz et al. 2005). Preliminary tests indicate this will not affect the longer period variable light curves in the same manner. The hollow triangles in Figure 6.1 show the distribution of the variability index after trend-filtering. For the unfiltered light curves, we set a cut-off of $J = 1.0$, and for the filtered light curves we set $J = 0.4$. We found these limits recovered 90–97% of the variables previously identified by visual inspection and the box-search algorithm, as well as over 150 long-period variables that had previously been undetected. The variables that were not recovered were generally the shallower longer period eclipsing binary light curves where the occasional small excursion from the mean magnitude was not sufficient to increase the variability index above the cut-off. Also missing were the shortest period variables with periods less than 1 hr, where the timescales for pairing and binning of 10 minutes were long enough to reduce the effectiveness of the variability index as a true measure of variability.

6-5 The light curve catalogue of variable stars

Using these methods, we find a total of 850 variable light curves in our data set. These have been analysed in a similar iterative fashion to Derekas et al. (2007) as follows. Initial periods have been determined with either the transit detection algorithm (for eclipsing light curves) or χ^2 fitting of sine waves using discrete Fourier transforms (for continuously varying light curves). Each of the resulting phased

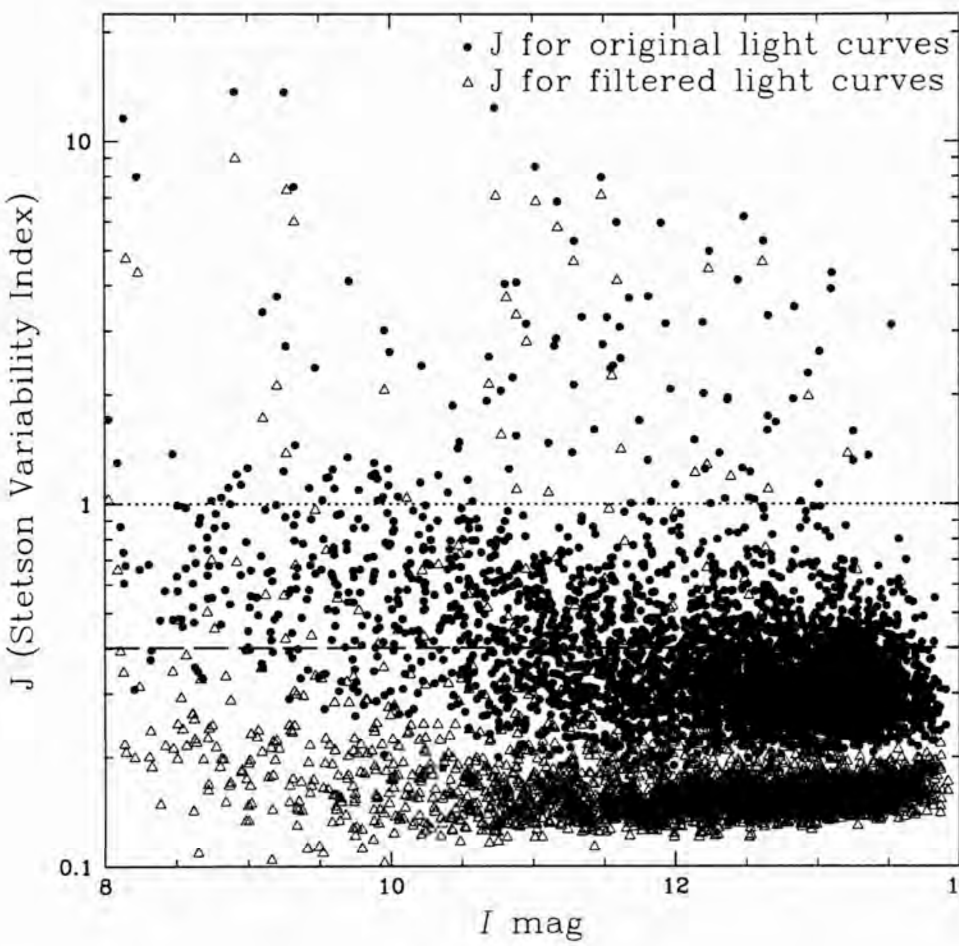

Figure 6.1. The Stetson Variability Index J as a function of magnitude for the Dec06 field. The solid circles are the original light curves, and the solid triangles are the filtered light curves. During the variable selection process unfiltered light curves with $J > 1.0$ (the dotted line) and filtered light curves with $J > 0.4$ (the dashed line) were flagged.

curves was then visually inspected to assign a type of variability, and also to confirm that the automatically determined period was not half or an integer multiple of the real period, a common occurrence for light curves of eclipsing binaries. A visual inspection of every phase diagram was usually sufficient to show whether the determined period was an alias or was slightly inaccurate. In the case of an alias, we multiplied the initial period by different constants (in most cases by 2) until the shape of the curve was consistent with that of an eclipsing binary.

We next used the string-length method (Lafler & Kinman 1965; Clarke 2002) to improve the period determination (see also Derekas et al. (2007) for further details). We applied the method for 500 periods within ±1% of the best initial period guess. The typical period improvement resulted in a change in the 3rd-4th decimal place, consistent with the limited frequency resolution of the data (which scales with $1/T_{obs}$, where T_{obs} is the time-span of the observations).

During the individual inspection of the phase diagrams, we made a visual classification of all 850 variables. Based on the light curve shapes alone, phased with the final adopted periods, we placed each star into one of the following categories: Algol-type (EA), β Lyrae-type (EB), W Ursae Majoris-type (EW), RR Lyrae stars (RRL), Cepheids (DCEP), long period variables with periods > 10 d (LPV), and pulsating variables with periods < 10 d (including δ Scuti and other multiply periodic variables, referred to as PUL). We follow the convention of using a colon to indicate a loose classification (for example, EB:). In several cases we used the "spotted variable" type, which refers to singly periodic variables with periods of several days, light curve amplitudes of a few hundredths of a magnitude and light curve shapes characteristic of known rotationally variable active stars. These can be binaries or single stars, and have multi-periodic light variations on time scales of years and decades (see for example Oláh et al. (2000). If there is an ambiguity between two categories they are listed as, for example, EW/PUL. If there are two types of variability present they are listed as, for example, EA+PUL. If there is additional information it is given as, for example, RRL-Blazhko.

The detection limits of the catalogue are shown in Figure 6.2, with the mean *I*-

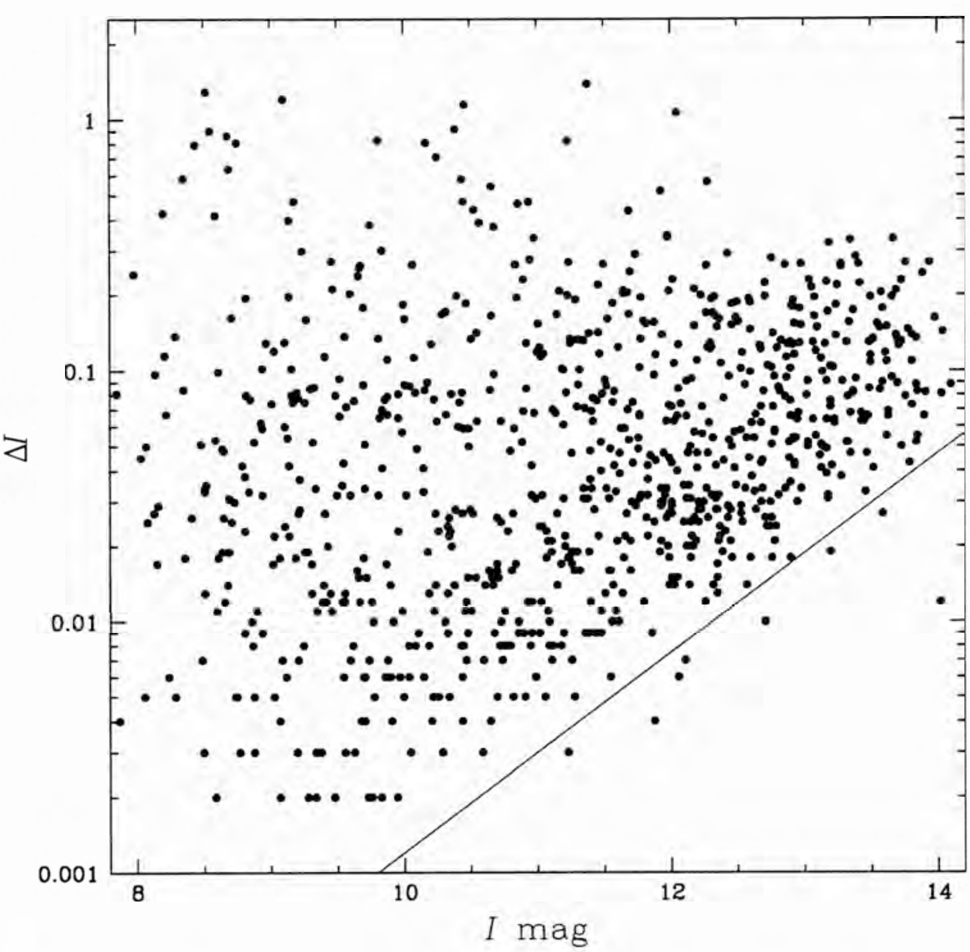

Figure 6.2. The variability amplitude detection limits for this catalogue. The mean I-band magnitude and the variability amplitude are plotted for the entire data set of variable light curves. The solid line is an empirical estimate of the detection limits to guide the reader.

band magnitude and variability amplitude plotted for all 850 variable light curves. For the detached eclipsing binaries the amplitude was the best-fitting transit depth as recorded by the box-search algorithm; for the continuously varying light curves we have used the amplitude from the sinusoid-fitting. For the multi-periodic light curves this will represent an approximate amplitude of the dominant frequency. As discussed in Section 6-3.2, due to dilution of the signal in crowded photometry apertures, the variability amplitudes presented here are lower limits on the true amplitudes. From Figure 6.2 it is apparent that around $I \approx 12$ mag we lose sensitivity to the lowest amplitude variables (such as the multi-periodic δ Scuti stars or pulsating red giants), while for $I > 13$ mag only the highest amplitude pulsators (RR Lyrae stars) and eclipsing binaries remain.

The last step in the variable star analysis was cross-correlation with existing databases to supplement the catalogue with as much additional information as possible. Namely, we queried the most recent update of the General Catalogue of Variable Stars (GCVS, Samus & Durlevich (2007)), including the New Suspected Variables catalogue, to identify already known variable stars. In addition, we checked the ASAS-3 database of southern variables (Pojmanski 2002). This revealed that 191 out of 850 variables are positionally coincident with previously published variable stars, leaving the total number of our new discoveries at 659. This corresponds to 78%, which is a lower fraction than, for instance, the 90% new discoveries found by Hartman et al. (2004) in the HATNet observations of the Kepler field. However, it is still surprisingly large, given the fact that the ASAS-3 project had previously observed each of our fields, whereas the Kepler field had not been targeted with variability surveys prior to the Hartman et al. study. We also performed a cross-correlation with the 2MASS Point Source Catalog (Skrutskie et al. 2006) to provide JHK magnitudes, and the ROSAT X-Ray Source Catalog (Voges et al. 1999, 2000) to determine which sources, if any, might be active stars with hot coronae.

A histogram of the $J - K$ colour indices (Figure 6.3) for the LPV and non-LPV variables (the latter including all eclipsing binaries and classical pulsators) demonstrates the expected dichotomy, with LPVs mostly having $J - K > 0.6$ mag,

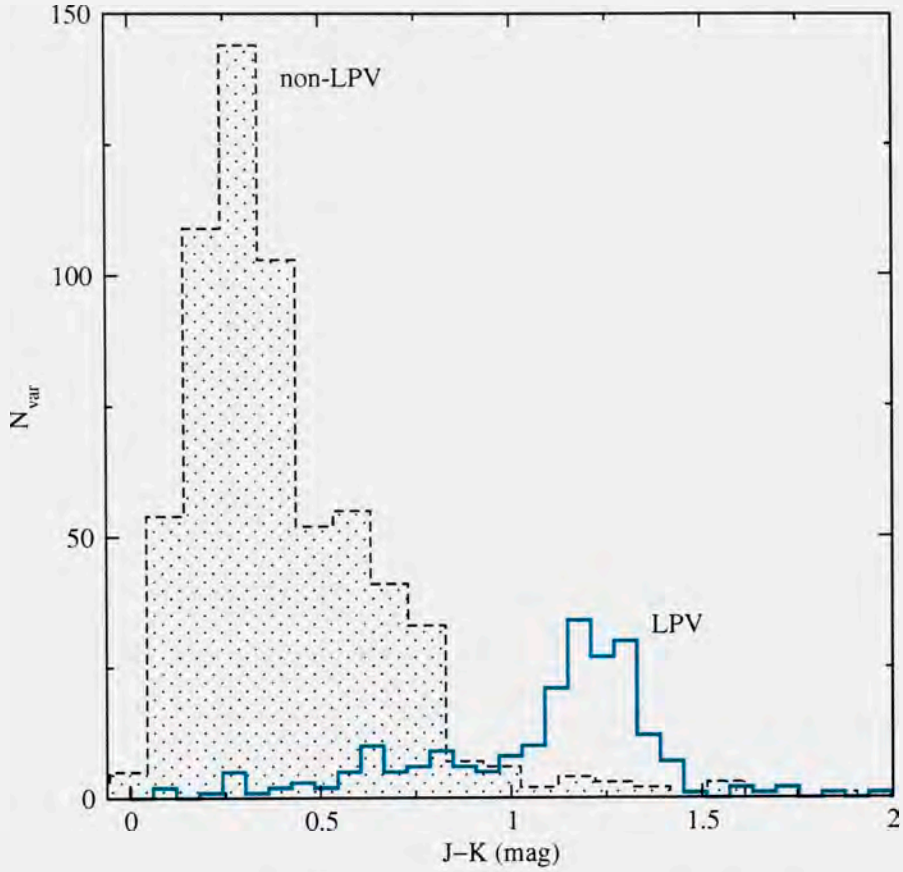

Figure 6.3. A comparison of the colour histograms for LPV and non-LPV variables.

i.e. being red giant stars. A few LPVs have bluer colours, which might indicate early-type stars with longer periods unrelated to red giant pulsations (e.g. ellipsoidal variability in binaries, rotational modulation due to starspots). Conversely, most of the non-LPVs have $J - K < 0.7$ mag, corresponding to spectral types A–K. The few redder non-LPVs are all located at lower galactic latitudes, suggesting strong interstellar reddening in their cases.

We also tested the consistency between the assigned variability types and their expected stellar types via the $J - H$ vs. $H - K$ colour-colour diagram. Using the intrinsic stellar loci determined for dwarfs and giants by Bessell & Brett (1988) and transformed into the 2MASS system (Carpenter 2001), we plot the locations of stars in three broad categories (eclipsing, pulsating, LPV) in Figure 6.4. Here we find a good agreement: almost all LPVs follow the intrinsic location of red giant stars, even showing hints of the separate carbon-rich LPV sequence for $J - K > 1.0$ mag and $H - K > 0.4$ mag. There are several outliers towards both bluer and redder

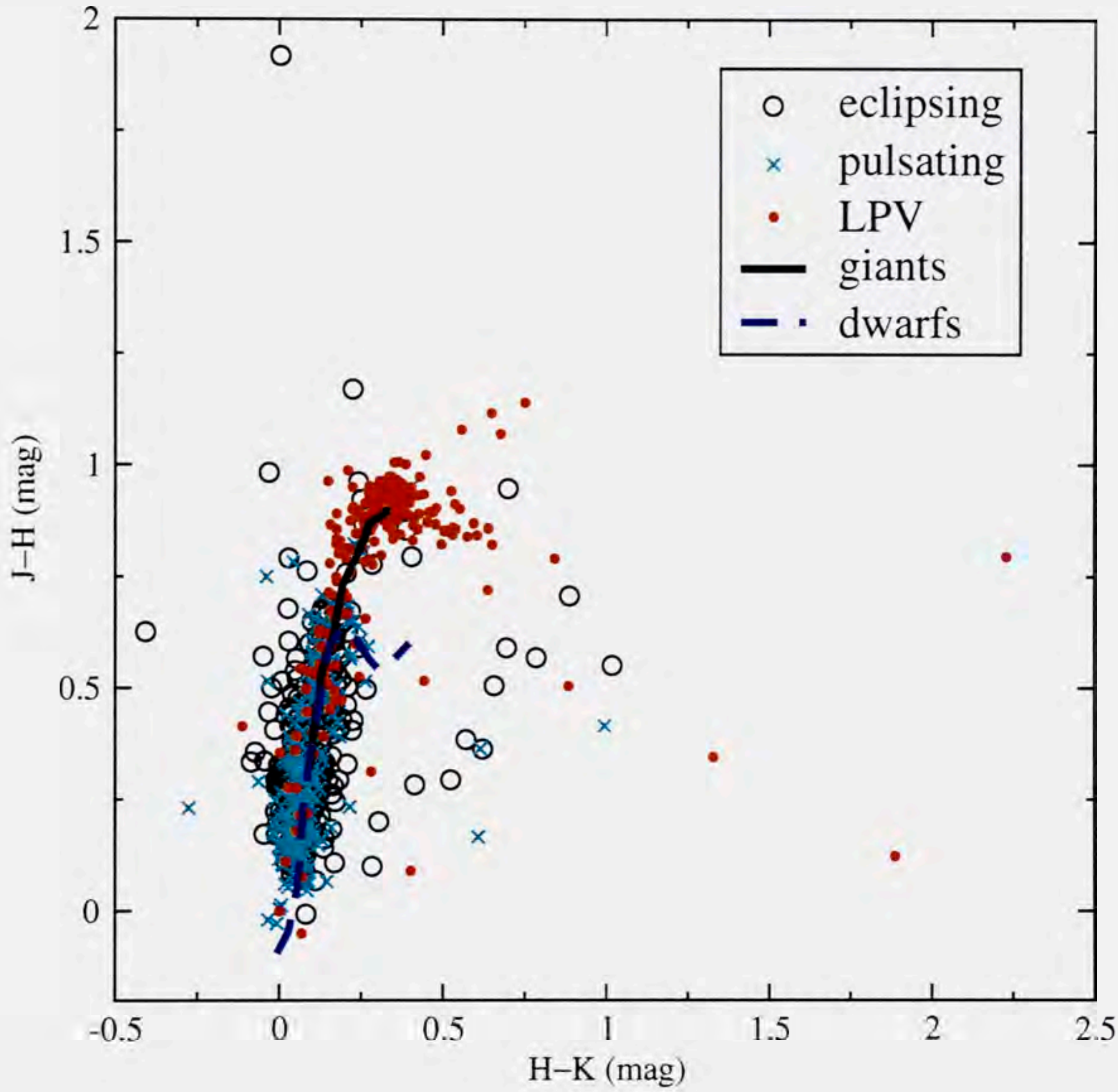

Figure 6.4. The $J-H$ vs. $H-K$ colour-colour diagram with the three broad categories and the stellar loci taken from Bessell & Brett (1988).

$H - K$ colours, almost exclusively eclipsing binaries, where we may suspect high reddening, composite colours or large photometric errors in the 2MASS magnitudes.

As an indication of the quality of the light curves in this catalogue, we plot a representative sample of eclipsing binaries, pulsating variables and LPVs (Figure 6.5). All data are publicly available at the University of New South Wales Virtual Observatory facility (see Section 6-7). Table 6.1 contains an extract of the complete summary table available in the electronic version of this paper. For each star the ID, J2000 coordinates, galactic coordinates, 2MASS JHK magnitudes, mean I-band magnitude, I-band amplitude, period, epoch of minimum light, previous identifier where appropriate and classification in this catalogue are shown.

6-6 Discussion

An extensive collection of variable stars always leads to some unexpected results: in the course of analysing transit candidates, the University of New South Wales Extrasolar Planet Search has identified a low-mass K7 Ve detached eclipsing binary ($M_{tot} = 1.04 \pm 0.06\ M_{\odot}$, (Young et al. 2006) and the first high-amplitude δ Scuti star in an eclipsing binary system (Christiansen et al. 2007). While these alone are interesting, the full breadth of the data is much more extensive. Below we discuss several possible applications, making no attempt at completeness.

6-6.1 Close eclipsing binaries with extreme properties

Contact binaries (or W UMa-type eclipsing variables) are among the most common types of variable stars, occurring at a rate of roughly 1 in every 500 FGK dwarfs (Rucinski 2006), which explains their large occurrence rate in variable star catalogues (e.g. 218 out of 850 in this catalogue). One intriguing problem related to these stars is that of binary mergers. When the total angular momentum of a binary system is at a certain critical (minimum) value, a secular tidal instability occurs which eventually forces the stars to merge into a single, rapidly rotating object (Arbutina (2007) and references therein). In the case of contact binaries, the instability occurs

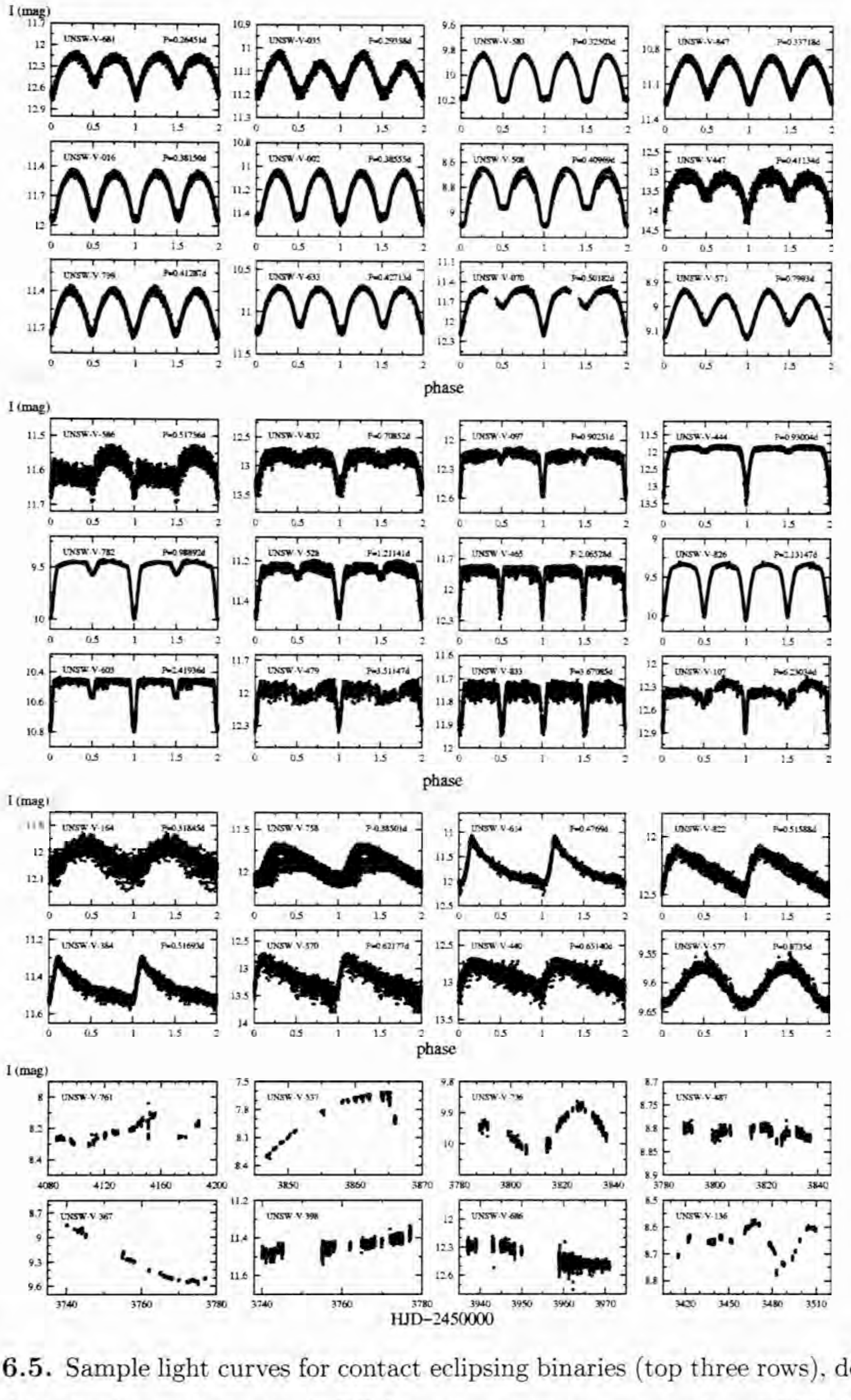

Figure 6.5. Sample light curves for contact eclipsing binaries (top three rows), detached eclipsing binaries (next three rows), RR Lyrae stars (next two rows) and LPV (bottom two rows). These light curves have not been processed with the trend-filtering algorithm.

Table 6.1. Extract from the complete catalogue. See text for an explanation of the columns.

ID	RA (J2000.0)	Dec (J2000.0)	$l°$	$b°$	J (mag)	H (mag)	K (mag)	I (mag)	A (mag)	Period (d)	Epoch HJD-2450000.0	Alternate ID	Type
UNSW-V-001	04:52:56.7	−29:48:14.3	231.0476	−37.4715	8.258	7.805	7.650	8.66	0.012	-	-		LPV
UNSW-V-002	04:53:38.1	−29:06:38.0	230.2417	−37.1672	11.228	10.933	10.821	11.23	0.200	0.38555	3289.1020	ASAS 045338-2906.6	EW
UNSW-V-003	04:53:48.2	−29:53:49.2	231.2140	−37.3108	12.475	12.078	11.969	12.71	0.026	0.69570	3289.0900		EA
UNSW-V-004	04:54:43.8	−29:34:07.0	230.8696	−37.0407	12.388	12.111	12.083	12.46	0.018	-	-		LPV
UNSW-V-005	04:57:28.8	−29:09:48.3	230.5523	−36.3636	8.540	8.235	8.160	8.75	0.005	3.2684	3289.1200		EB
UNSW-V-006	04:57:45.4	−30:14:05.8	231.8658	−36.5529	9.342	9.162	9.109	9.38	0.003	-	-		LPV
UNSW-V-007	04:58:03.5	−29:55:59.1	231.5185	−36.4208	10.068	9.823	9.745	10.21	0.128	3.0683	3324.2200	ASAS 045804-2956.0	EA
UNSW-V-008	04:58:18.2	−29:04:54.7	230.5073	−36.1695	13.720	13.279	13.238	13.73	0.050	0.31036	3288.9700		EW
UNSW-V-009	04:50:06.9	−30:39:50.7	231.9448	−38.2536	13.548	13.424	13.386	13.69	0.139	1.0641	3351.9800		EA
UNSW-V-010	04:50:18.7	−30:21:29.1	231.5754	−38.1480	11.697	11.139	10.976	12.31	0.032	1.9175	3290.4200		PUL

at a minimum mass-ratio of $q_{\rm min} \sim 0.071 - 0.076$ (Rasio 1995; Li & Zhang 2006), which has been the explanation for the very few contact systems with $q < 0.1$ (see Arbutina (2007) for the updated lists of ten contact systems in the range of 0.065-0.13). The exact limit depends on assumptions on the stellar structure and dynamical stability (Li & Zhang 2006). Since it is likely that at least a fraction of blue straggler stars in star clusters formed via binary mergers (Mapelli et al. 2004), there is an exciting opportunity to constrain binary merger theories by increasing the number of known contact binaries with extremely low mass-ratios, and probing the limits of the observed $q_{\rm min}$.

Examining the published light curves of the lowest mass-ratio systems (examples include AW UMa: Pribulla et al. (1999); V870 Ara: Szalai et al. (2007)), a single flat-bottomed minimum is always present, which corresponds to the full eclipse of the much smaller component that occurs within a certain range of inclinations. In our sample we find about five binaries with very similar periods (0.3–0.4 d) and light curve shapes (three are shown Figure 6.6), which might therefore be low mass-ratio systems deserving further attention. This could include obtaining and modelling multi-colour light curves in several bands (see, for example, Qian et al. (2005)).

Similarly to the mass-ratio, contact binary periods also have a very well-defined cut-off, which occurs at $P \approx 0.215 - 0.22$ d, just 0.05 d shorter than the maximum of the volume-corrected period distribution (Rucinski 2007). Stepien (2006) attempted to explain the period cut-off via the magnetic-wind driven angular momentum loss, the rate of which shows a progressive decay with the shortening of the period so that the period evolution takes progressively longer time. The period cut-off would then be due to a finite age of the binary population of several Gyr. Using the ASAS sample of binaries, Rucinski (2007) concluded that while no evidence exists for angular momentum evolution, the drop in numbers towards the cut-off still suffers from small number statistics and the cut-off itself remains unexplained. Hence, improving the statistics at the short-period end of contact binaries is important, where high-cadence transit search programs could play an important role. In our sample, there are four contact binaries out of 218 in the range of $P = 0.246 - 0.250$ d, which fall

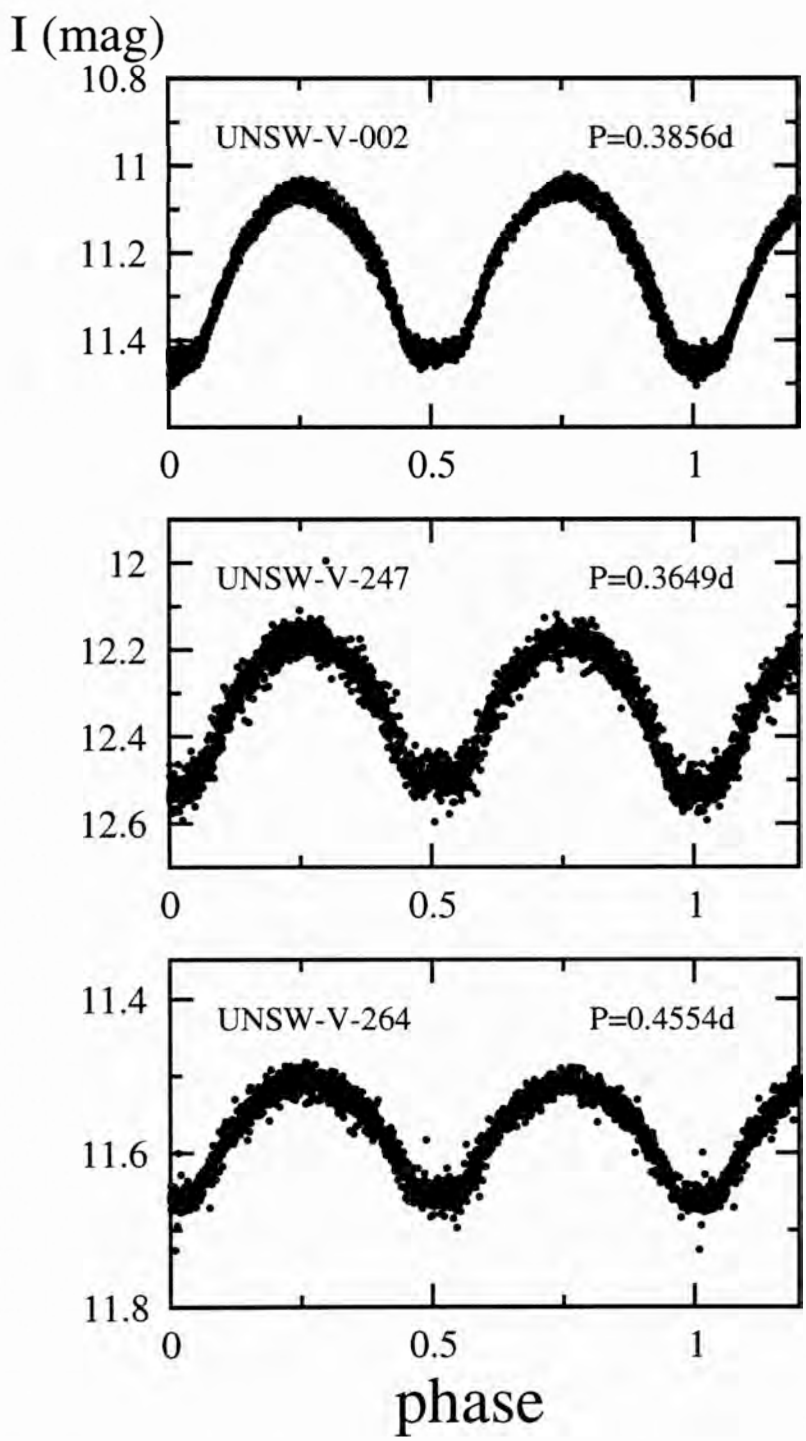

Figure 6.6. Possible candidates for low mass-ratio contact binaries.

on the short-period end of the distribution but do not improve the statistics near the cut-off (the present record holder in the Galactic field has a period of 0.2178 d; Rucinski (2007).

It is also possible to use the periods and light curve morphologies to identify close eclipsing binaries that are potentially composed of low-mass components. Identifying low-mass stars in eclipsing binaries is extremely important for accurately deriving the fundamental stellar parameters of mass and radius that are crucial for constraining low-mass stellar formation and evolution models. Following the method of Weldrake et al. (2007), we select those contact binaries with periods < 0.25 d, and Algol-type detached eclipsing binaries with no obvious out-of-eclipse variations and periods < 1.6 d as good candidates for low-mass eclipsing binary systems. We find four contact binaries (the same four located near the period cut-off) and 31 detached binaries matching these criteria, listed in Table 6.2. There are quite a few bright ($I > 12$) objects in this list which would make excellent targets for spectroscopic follow up.

6-6.2 Pre-main-sequence eclipsing binaries

Detached eclipsing binaries provide one of the most accurate (largely model-independent) sources of fundamental stellar parameters, notably masses and radii. These can be used to put the strongest constraints on stellar evolutionary models, which in turn can improve our understanding of the formation and evolution of individual stellar populations. On the pre-main-sequence, the calibration of stellar parameters is presently extremely scarce below 1 $M_{\odot}$ where only six eclipsing binaries are known, all located in the Taurus-Orion region (Irwin et al. 2007). Comparison of these systems to different stellar models have indicated difficulties in fitting both components of the binaries simultaneously, which shows our current models of low-mass stars are seriously challenged by the known systems (see also Aigrain et al. (2007b)).

One possibility for identifying pre-main-sequence binaries is by using colour-colour diagrams, such as the one depicted in Figure 6.7. Here we plot the location of the detached binaries in our sample, using 2MASS JHK magnitudes, the intrin-

Table 6.2. Eclipsing binary systems potentially composed of low-mass components.

ID	RA(J2000.0)	Dec(J2000.0)	I (mag)	P (d)
Contact eclipsing binaries				
UNSW-V-077	09 30 05.4	−14 02 17.9	12.64	0.2480
UNSW-V-219	16 55 48.1	−60 19 08.7	13.50	0.2456
UNSW-V-659	21 07 03.6	−65 56 42.0	11.08	0.2472
UNSW-V-662	21 10 21.6	−66 54 53.3	12.37	0.2492
Detached eclipsing binaries				
UNSW-V-003	04 53 48.2	−29 53 49.2	12.71	0.6956
UNSW-V-090	11 56 40.6	−35 43 43.8	12.53	1.1870
UNSW-V-097	11 59 53.9	−36 13 26.1	12.18	0.9025
UNSW-V-143	16 57 00.6	−60 29 51.9	12.17	0.8117
UNSW-V-156	17 00 06.2	−60 17 02.4	13.43	1.5618
UNSW-V-192	17 09 18.1	−60 01 43.5	13.45	1.4877
UNSW-V-198	17 10 18.2	−59 46 08.9	13.20	1.2275
UNSW-V-205	17 13 55.3	−60 12 15.3	11.83	0.9610
UNSW-V-301	17 16 37.3	−58 09 40.4	11.04	1.4828
UNSW-V-312	00 00 06.0	−59 44 48.3	13.63	1.0574
UNSW-V-353	04 04 51.2	−24 11 30.4	13.73	0.7065
UNSW-V-379	09 22 49.7	−25 12 40.8	13.35	0.4975
UNSW-V-386	09 14 14.5	−24 53 31.6	11.43	1.2956
UNSW-V-410	09 13 47.8	−22 48 23.5	13.07	0.9690
UNSW-V-472	13 08 49.2	−44 47 55.2	12.46	0.5484
UNSW-V-527	14 45 10.0	−39 25 47.3	10.99	1.363
UNSW-V-528	14 45 19.4	−38 08 48.0	11.26	1.211
UNSW-V-536	14 47 27.5	−38 31 36.7	11.56	0.2303
UNSW-V-540	14 49 09.1	−38 38 10.1	12.92	0.5216
UNSW-V-598	18 21 14.1	−64 30 03.1	11.77	0.8492
UNSW-V-617	18 38 00.5	−65 06 07.7	10.66	1.5092
UNSW-V-621	18 11 49.9	−67 06 13.8	13.76	1.0194
UNSW-V-624	18 18 48.4	−67 27 54.1	12.76	1.482
UNSW-V-644	18 34 50.6	−67 24 09.9	12.96	1.4238
UNSW-V-683	20 58 55.7	−67 02 12.8	13.21	1.0740
UNSW-V-696	21 08 04.4	−68 57 53.1	11.55	0.9428
UNSW-V-706	20 58 35.9	−69 04 01.4	12.03	1.025
UNSW-V-722	23 25 23.1	−70 01 48.5	12.20	1.3523
UNSW-V-740	08 04 02.0	−66 28 02.6	13.63	1.2634
UNSW-V-746	08 08 27.0	−68 19 07.5	12.68	1.0324
UNSW-V-846	15 03 44.5	−68 40 02.6	12.13	1.5804

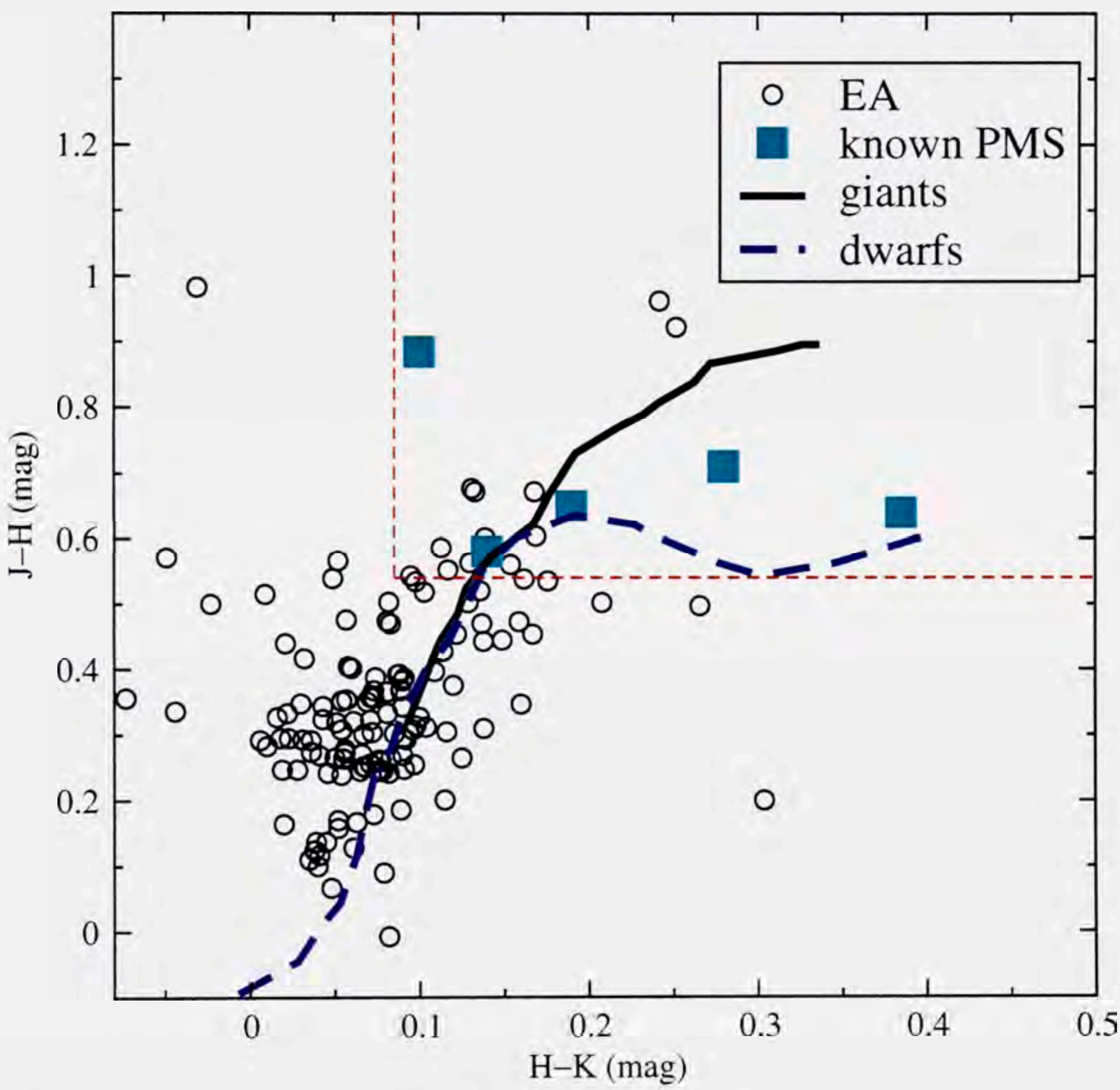

Figure 6.7. Detached binaries and the location of five known pre-main-sequence eclipsing systems (data taken from Stassun et al. (2004); Covino et al. (2004); Hebb et al. (2006); Stassun et al. (2007); Irwin et al. (2007).

Table 6.3. Candidate PMS detached binaries

ID	RA(J2000.0)	Dec(J2000.0)	I (mag)	P (d)
UNSW-V-097	11 59 53.9	−36 13 26.1	12.18	0.90251
UNSW-V-107	12 03 06.8	−35 37 47.5	12.40	6.23034
UNSW-V-153	16 59 02.4	−60 17 46.7	12.15	3.13850
UNSW-V-273	17 11 18.4	−57 40 16.1	10.46	0.92733
UNSW-V-299	17 16 10.8	−57 20 37.5	12.33	5.97542
UNSW-V-312	00 00 06.0	−59 44 48.3	13.63	1.05762
UNSW-V-491	13 12 31.5	−46 04 08.8	12.76	3.83246
UNSW-V-518	13 07 31.8	−45 12 42.0	12.59	2.75743
UNSW-V-540	14 49 09.1	−38 38 10.1	12.92	0.52173
UNSW-V-617	18 38 00.5	−65 06 07.7	10.66	1.50906
UNSW-V-676	21 20 45.9	−66 22 18.5	13.50	3.28503
UNSW-V-722	23 25 23.1	−70 01 48.5	12.20	1.01274
UNSW-V-746	08 08 27.0	−68 19 07.5	12.68	1.03214
UNSW-V-790	14 45 02.8	−68 21 09.9	10.84	2.70009
UNSW-V-791	14 45 44.6	−69 10 17.4	12.98	3.66266
UNSW-V-808	14 50 14.3	−68 18 04.7	12.90	1.64343
UNSW-V-841	15 02 41.3	−69 23 06.3	12.54	1.82850

sic stellar loci from Bessell & Brett (1988) and the position of five PMS binaries with published *JHK* photometry (mostly from 2MASS). We use two dashed lines as boundaries for defining a PMS candidate: the vertical and horizontal lines are at $H - K = 0.085$ mag and $J - H = 0.54$ mag, respectively. In total we extract 17 Algol-type systems from our sample that have redder colours than the boundary lines (i.e. located around the known PMS systems in Figure 6.7). These are listed in Table 6.3: some could be heavily reddened main-sequence stars, but since the majority of our fields are located above a Galactic altitude of 15°, there is the distinct possibility of genuine PMS binaries in the sample. One method of confirmation would be obtaining high-resolution spectroscopy to look for PMS signatures, such as strong Li absorption (Irwin et al. 2007)

6-6.3 The Blazhko-effect in RR Lyrae stars

RR Lyrae stars are horizontal branch stars showing high-amplitude pulsations driven by the κ-mechanism, with typical periods of about 0.5 days. It is known that a large fraction of RR Lyrae stars (20–30% of the fundamental mode RRabs and 2% of the first-overtone RRcs, Kovács (2001)) exhibit periodic amplitude and/or phase modulations, the so-called Blazhko-effect, which is one the greatest mysteries in classical pulsating star research. Currently, two classes of models are usually put forward as possible explanations, both assuming the presence of non-radial oscillations (note, that RR Lyrae stars have long been considered as the prototypes of purely radially pulsating stars): the resonance models, in which resonance effects excite non-radial modes in addition to the main radial mode, and the magnetic models, which are essentially oblique rotating pulsator models (see Kolenberg et al. (2006) and references for more details). Recently, Stothers (2006) published a new explanation, in which turbulent convection inside the hydrogen and helium ionization zones becomes cyclically weakened and strengthened owing to the presence of a transient magnetic field that is generated by some kind of a dynamo mechanism.

With a variety of competing models, theory is in desperate need for further empirical constraints, most notably ones that are capable of detecting non-radial oscil-

Table 6.4. RR Lyrae stars with detected Blazhko-effect and double-mode pulsation.

ID	RA(J2000.0)	Dec(J2000.0)	I (mag)	P (d)
Blazhko-effect				
UNSW-V-101	12 00 49.6	−36 11 59.2	14.26	0.6264
UNSW-V-203	17 12 35.0	−60 29 32.1	11.99	0.4933
UNSW-V-384	09 24 25.5	−24 05 03.4	11.45	0.5169
UNSW-V-442	12 50 44.3	−44 41 20.3	13.08	0.5853
UNSW-V-614	18 34 41.2	−65 27 08.1	11.74	0.4769
UNSW-V-773	14 40 40.8	−68 23 16.8	11.03	0.5518
Double-mode				
UNSW-V-358	09 16 04.3	-23 36 08.0	13.49	0.3602
				0.4840
UNSW-V-532	14 46 35.8	-39 33 31.7	12.86	0.6540
				0.5012
UNSW-V-577	14 52 42.1	-41 41 55.3	9.60	0.8735
				0.6682
UNSW-V-758	08 16 09.3	-66 44 46.3	11.94	0.3850
				0.5170
UNSW-V-810	14 50 13.3	-69 45 18.5	11.70	0.7372
				1.0576

lations and/or magnetic fields, for example high-resolution spectroscopy. Hence, the discovery of bright to moderately faint RR Lyrae stars with well-expressed Blazhko-effect could be of great interest. In our sample we find six RR Lyrae stars out of 52, listed in Table 6.4, that demonstrate the Blazhko-effect. Four were previously known variables, and two are new discoveries. Unfortunately, we could not determine the Blazhko-period for any of the stars, but the four objects brighter than $I \sim 12$ mag, one of which is a new discovery, are good candidates for further studies. We also find five double-mode RR Lyrae stars, for which the period ratios suggest the well-known mixture of fundamental+first radial overtone pulsation. Three of these are new discoveries, with two previous published in the ASAS-3 catalogue, thus raising the total number of field double-mode RR Lyrae stars known in the Galaxy to 30; see Szczygieł & Fabrycky (2007).

6-7 Online access to light curves

All APT images from 2002 July until present day, including those used in the creation of this catalogue, are stored in a publicly available archive. This archive can be accessed using a web browser and the conventional web interface located at:

`http://astro.ac3.edu.au`

Alternatively, the archive can be accessed via the Simple Image Access Protocol (SIAP) (Tody & Plante 2004) as defined by the International Virtual Observatory Alliance (IVOA). The SIAP defines a standard for retrieving images from a repository using simple URL-based queries. For example, a request made to the following URL will return a list of APT images that intersect with the 1 degree square region centred on (75,-30) with RA and Dec expressed in decimal degrees:

`http://astro.ac3.edu.au/unsw/siap?POS=75,-30&SIZE=1&TEL=APT`

The POS parameter is mandatory and defines the centre of the search region. The SIZE parameter is optional (default is SIZE=1) and determines the size of the search region. The TEL parameter distinguishes between images from different telescopes, and is specific to the UNSW implementation of the SIAP service.

The list of images returned by the SIAP query is in VOTable format (Ochsenbein 2004). Each item in the list contains a set of attributes describing a particular image that satisfies the search criteria. Also included is a URL which can be used to download the associated image.

The catalogue of light curves discussed in this paper is available from the UNSW archive via the Simple Spectral Access Protocol (SSAP) (Tody et al. 2007). The SSAP is an IVOA standard for accessing archives of one dimensional spectra, including time series data such as light curves. The format of an SSAP query is very similar to the format of an SIAP query. For example, the query specified in the following URL will search for light curves of stars within a circle of diameter 1 degree centred at the point (75,-30).

`http://astro.ac3.edu.au/unsw/ssap?REQUEST=queryData&POS=75,-30&SIZE=1`

The REQUEST parameter is the only mandatory parameter. The optional parameters include POS, SIZE, BAND and TIME, which are used to constrain the search by region (degrees), bandpass (metres) and time of observation (ISO 8601).

The list of light curves returned by the SSAP query is in VOTable format, and each item in the list contains a set of metadata describing a particular light curve, including a URL for downloading the data. The light curve data itself is also presented in VOTable format and follows the structure of the Spectrum Data Model (McDowell 2007). Consequently, these light curve VOTables may be examined with any VO-compliant tool, such as TOPCAT (Taylor 2005).

6-8 Summary

We have presented a catalogue of 850 variable stars, compiled from 32 months of observations obtained for the University of New South Wales Extrasolar Planet Search. Of these stars, 659 are new discoveries that have not been previously reported in the GCVS, NSV or ASAS-3 catalogues. This catalogue of well-sampled high precision light curves, each spanning 1–4 months, has significant potential for astrophysically interesting data mining. We have nominated several possibilities, including eclipsing binary systems with low mass-ratios, low-mass components or pre-main sequence components, and RR Lyrae stars demonstrating the curious Blazhko-effect. The data have been made publicly available on the University of New South Wales VO server in a standard format for retrieval and for analysis with standard VO tools.

Chapter 7

First high-amplitude δ Scuti star in an eclipsing binary system

7-1 Abstract

We report the discovery of the first high-amplitude δ Scuti star in an eclipsing binary, which we have designated UNSW-V-500. The system is an Algol-type semi-detached eclipsing binary of maximum brightness $V = 12.52$ mag. A best-fitting solution to the binary light curve and two radial velocity curves is derived using the Wilson-Devinney code. We identify a late A spectral type primary component of mass 1.49 ± 0.02 $M_{\odot}$ and a late K spectral type secondary of mass 0.33 ± 0.02 $M_{\odot}$, with an inclination of $86.5 \pm 1.0°$, and a period of 5.3504751 ± 0.0000006 d. A Fourier analysis of the residuals from this solution is performed using PERIOD04 to investigate the δ Scuti pulsations. We detect a single pulsation frequency of $f_1 = 13.621 \pm 0.015$ cd^{-1}, and it appears this is the first overtone radial mode frequency. This system provides the first opportunity to measure the dynamical mass for a star of this variable type; previously, masses have been derived from stellar evolution and pulsation models.

7-2 Introduction

The serendipitous arrangement of a pulsating star in an eclipsing binary system represents a unique laboratory for astrophysical measurements. The binarity constrains the physical and geometrical parameters of the system, and can also assist in mode identification in the pulsations. Since the pulsating star and non-pulsating companion can reasonably be assumed to have formed from the same parent cloud, we can utilise information from the non-pulsating companion in identifying stellar evolution models for pulsating stars. We present here the first known example of a high-amplitude δ Scuti (HADS) star in an eclipsing binary system, designated UNSW-V-500.

δ Scuti stars are the main-sequence analogues of Cepheid variables. They are late A to early F spectral type, and pulsate with periods of between 1–6 hours. They are typically on or slightly above the main-sequence. Low-amplitude δ Scuti stars typically pulsate in many higher, non-radial modes simultaneously with amplitudes of less than 0.05 mag. High-amplitude δ Scuti pulsate primarily in the radial modes and have higher amplitudes, with the conventional cut-off given as $A_{\mathrm{V}} \geq 0.30$ mag. Fig. 7.1 shows the δ Scuti region of the HR diagram; high-amplitude δ Scuti stars are constrained to a narrower range in T_{eff} of width $\sim$ 300 K within this region. The subset of low metallicity Population II HADS stars are designated as SX Phe stars. Prior to the discovery of UNSW-V-500, all bright field HADS stars were identified as pulsating in the fundamental radial mode. A significant fraction ($\sim$ 40 per cent) are double-mode pulsators, additionally pulsating in the radial first overtone mode (McNamara 2000a). However, SX Phe stars have been identified in globular clusters as pulsating in the first overtone rather than the fundamental mode (McNamara 2000b; Nemec et al. 1994).

Soydugan et al. (2006) present a list of 25 confirmed eclipsing binary systems with pulsating components in the δ Scuti region of the instability strip. All of these have low pulsation amplitudes, ranging from $A_{\mathrm{V}} = 0.007$–0.02 mag and up to $A_{\mathrm{B}} = 0.06$ mag. Three systems that have been studied in detail are Y Cam (Kim et al. 2002a), AS Eri (Mkrtichian et al. 2004) and AB Cas (Rodríguez et al. 2004). Parameters of

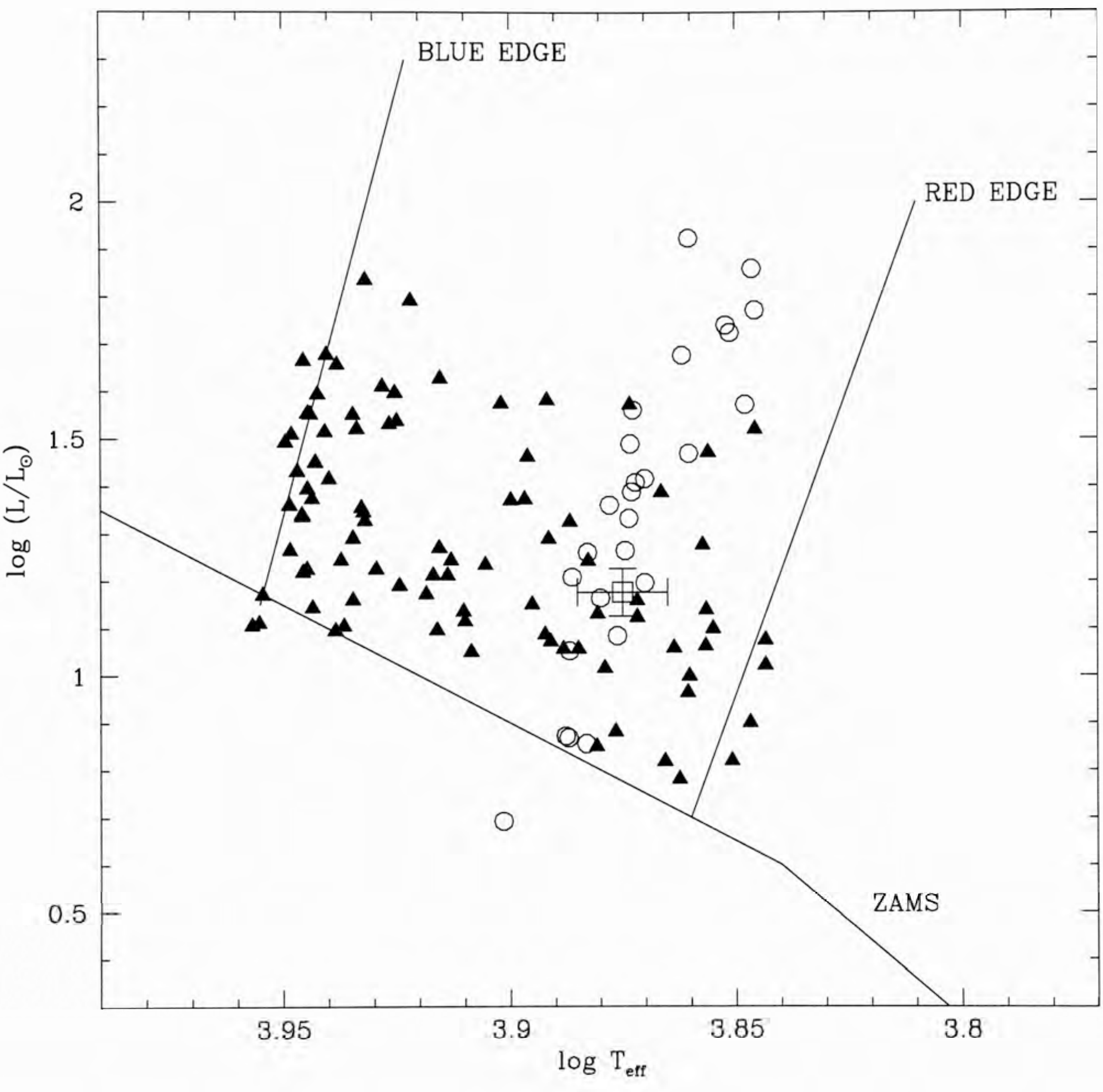

Figure 7.1. A HR diagram showing the positions of δ Scuti stars in eclipsing binaries. The solid triangles are data from Table 4 of Soydugan et al. (2006). The open circles are high-amplitude δ Scuti stars from Table 2 of McNamara (2000b). UNSW-V-500 is shown as an open square. The observational red and blue edges of the classical instability strip are shown, as well as the theoretical zero-age main sequence.

Table 7.1. A sample of δ Scuti stars in eclipsing binary systems. A_V is the amplitude of the δ Scuti pulsations. $^a V_{max}$ from the ASAS catalogue.

Name	V	A_V	Spectral Type	P_{puls}	P_{orb}	Inclination
	mag	mag		(d)	(d)	°
Y Cam	10.56	0.04	A7V	0.063	3.3055	86
AB Cas	10.16	0.05	A3V	0.058	1.3669	87.5
AS Eri	8.31	0.0068	A3V	0.016	2.6642	–
UNSW-V-500	12.52^a	$\sim$0.35$\pm$0.5	A7V	0.0734$\pm$0.0001	5.3504751$\pm$0.0000006	86.5$\pm$1.0

these systems are shown in Table 7.1, with the parameters of UNSW-V-500 shown for comparison.

We note that although 35 δ Scuti stars in eclipsing binary systems have been identified (25 in Soydugan et al. (2006); 9 recently in Pigulski & Michalski (2007); and the subject of this paper), UNSW-V-500 is the first HADS star. This is a curious statistic, since with larger amplitudes, surveys might be expected to be observationally biased towards finding HADS stars in these systems. A census of the Rodríguez et al. (2000) catalogue shows that the detected fraction of HADS stars is $\sim$ 25 per cent of the total δ Scuti population. One assumes that this fraction is influenced by the same observational selection bias affecting the detection of HADS stars in eclipsing binary systems; we are seeing a detection rate nearly an order of magnitude below this. However, it is difficult to draw conclusions from the small numbers of binary systems that have been found.

7-3 Observations

7-3.1 Photometry

UNSW-V-500 was initially observed over 29 nights from February 2006 to April 2006. The photometric I-band observations were performed with the 0.5-m Automated Patrol Telescope at Siding Spring Observatory, Australia. The observations formed part of an extrasolar planet transit search being undertaken by the University of New

South Wales. The CCD has 770 × 1150 pixels and images a 2 × 3 deg^2 field with a relatively low spatial resolution of 9.4 arcsec per pixel. We have used a customised aperture photometry data reduction pipeline to construct our target light curves. A full explanation of the transit search and the data reduction process can be found in Hidas et al. (2005). The results of the project include the discovery of a new eclipsing system of K7 dwarf components (Young et al. 2006).

Identification of UNSW-V-500 as demonstrating both eclipsing and pulsating variations was made during routine cataloguing of the variable light curves detected in the transit search, to be published separately. The photometry aperture used in the reduction process, which is nearly 1 arcmin in diameter, can usually be expected to contain more than one star due to crowding effects in the target fields (typically chosen to have a Galactic latitude of 10–20°). Higher resolution images from the Digitized Sky Survey catalogue showed that in the case of UNSW-V-500 the photometry aperture contained one bright central star and 6 additional stars at least 3.5 magnitudes fainter. Due to the large amplitude of the δ Scuti pulsations (diluted to ~ 0.1 mag in the original photometry aperture) the system was identified with the bright central star, $\alpha_{J2000} = 13^{\mathrm{h}}\ 10'\ 18''.7$, $\delta_{J2000} = -45°\ 9'\ 13''$. A catalogue search revealed that this system had been previously observed and identified in the All Sky Automated Survey Catalog of Variable Stars III (Pojmanski & Maciejewski 2004) as an eclipsing binary system, designated ASAS131018-4509.2. From their data they measured an initial epoch of T_0 = JD2451892.6 and a period of P = 5.350479 d. However, their precision was insufficient for detection of the δ Scuti pulsation.

In the original run of 29 nights one secondary minimum and two partial secondary eclipses were observed, but only two primary eclipse egresses. In order to improve coverage of this part of the light curve, UNSW-V-500 was observed again in the same configuration as described previously on two nights in February 2007 and March 2007 at the predicted times of primary eclipse. These two nights and the 22 best nights of the 2006 data are shown in Fig. 7.2, phased at a period of 5.3504751 d. The primary eclipse data conclusively confirmed that the light curve was not the result of a δ Scuti star blended with a background eclipsing binary: the flat-bottomed eclipses show no sign of the pulsations that are evident in the remainder of the light curve. Therefore, the δ Scuti star must be fully eclipsed by the secondary component of the binary during primary eclipse. The inset in Fig. 7.2 shows the flat primary eclipse in more detail.

In order to confirm the identification of the bright central star in the original photometry aperture as the eclipsing binary, higher spatial resolution observations were obtained with the 40-inch telescope at Siding Spring Observatory. The WFI CCD mosaic was used, with an image scale of 0.38 arcsec per pixel. Observations were taken on a single night in January 2007, in the Johnson V filter. These data were reduced using a modified version of our aperture photometry pipeline. The identification of the pulsating star was confirmed and the data are shown in Fig. 7.3 as solid circles. For comparison, the light curve of a nearby star of similar magnitude, GSC0824700373, is shown as open squares. The lower limit on the amplitude of the δ Scuti pulsation, diluted in these data by light from the secondary, is $A_{\rm V} = 0.21 \pm 0.02$ mag. Combined with a primary eclipse depth in the I band of ~ 60 per cent, the final lower limit is $A_{\rm V} = 0.35 \pm 0.05$ mag, confirming this star as a high-amplitude δ Scuti star.

7-3.2 Spectroscopy

Several medium resolution spectra (R $\sim$ 6000) were obtained over two nights in February 2007 with the Double-Beam Spectrograph on the 2.3-m telescope at Siding Spring Observatory. The wavelength range covered was 3900–4400 Å in the blue arm and 8000–8900 Å in the red. The spectra were reduced using standard IRAF[1] spectroscopy routines. The observations were alternated with arc spectra of Fe-Ar in the blue and Ne-Ar in the red. The flux calibration of the system was performed using the standard stars HR4469 and HR4963. The spectra were rebinned to a resolution of 10 Å using the IRAF routine `rebin` and compared with UVILIB template

[1]IRAF is distributed by the National Optical Astronomy Observatories, which are operated by the Association of Universities for Research in Astronomy, Inc., under cooperative agreement with the National Science Foundation.

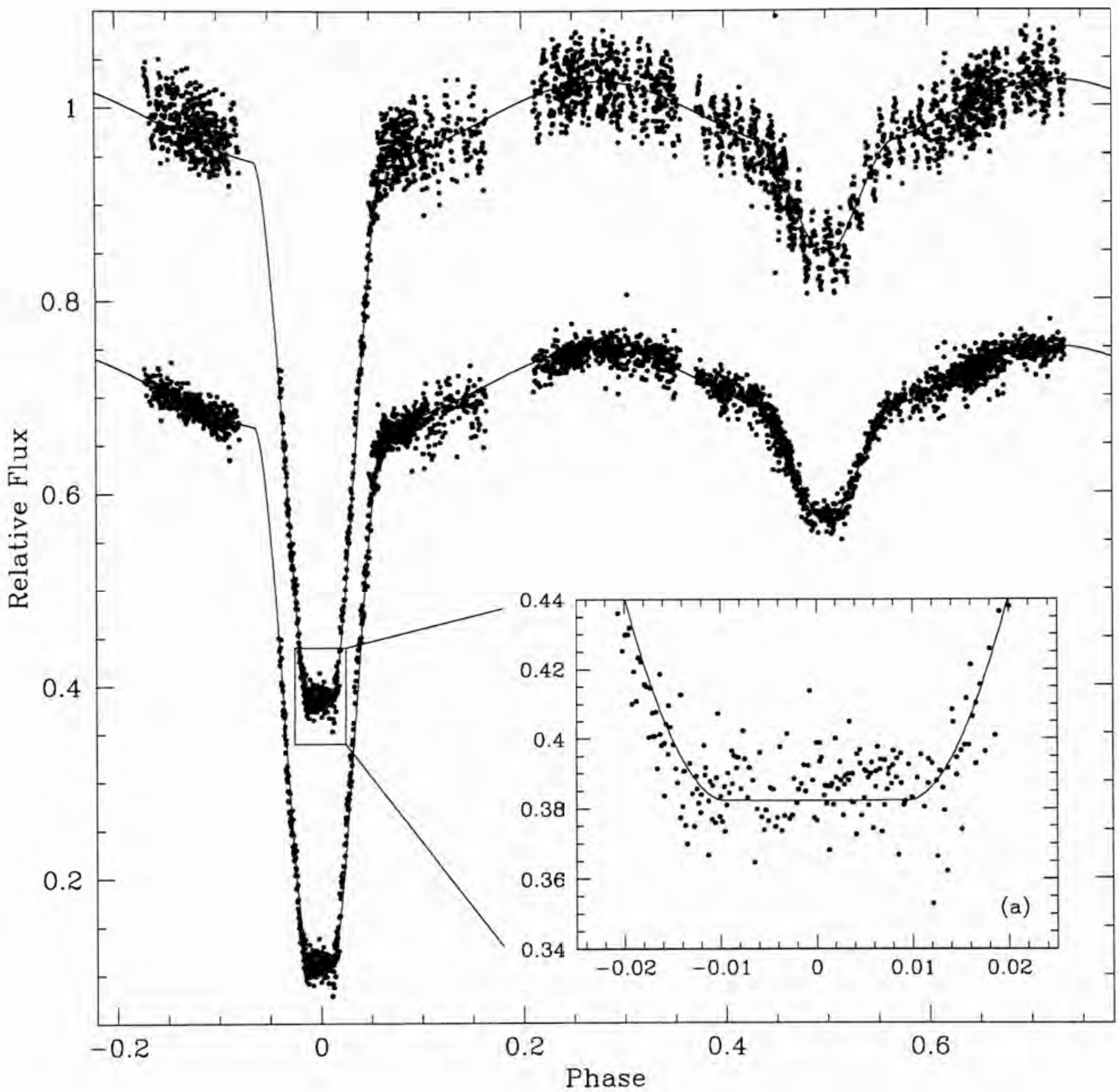

Figure 7.2. The phased light curve of 24 nights of data taken with the Automated Patrol Telescope in the I band. The upper curve is the original data, with the scatter outside the primary eclipse due to the δ Scuti pulsation. The lower curve is the same data with the δ Scuti pulsation reconstructed from the frequency analysis and removed. In both cases, the solid line is the fit to the original curve using the Wilson-Devinney code. Panel (a) shows the primary eclipse in more detail—there is no evidence of δ Scuti variations in this region.

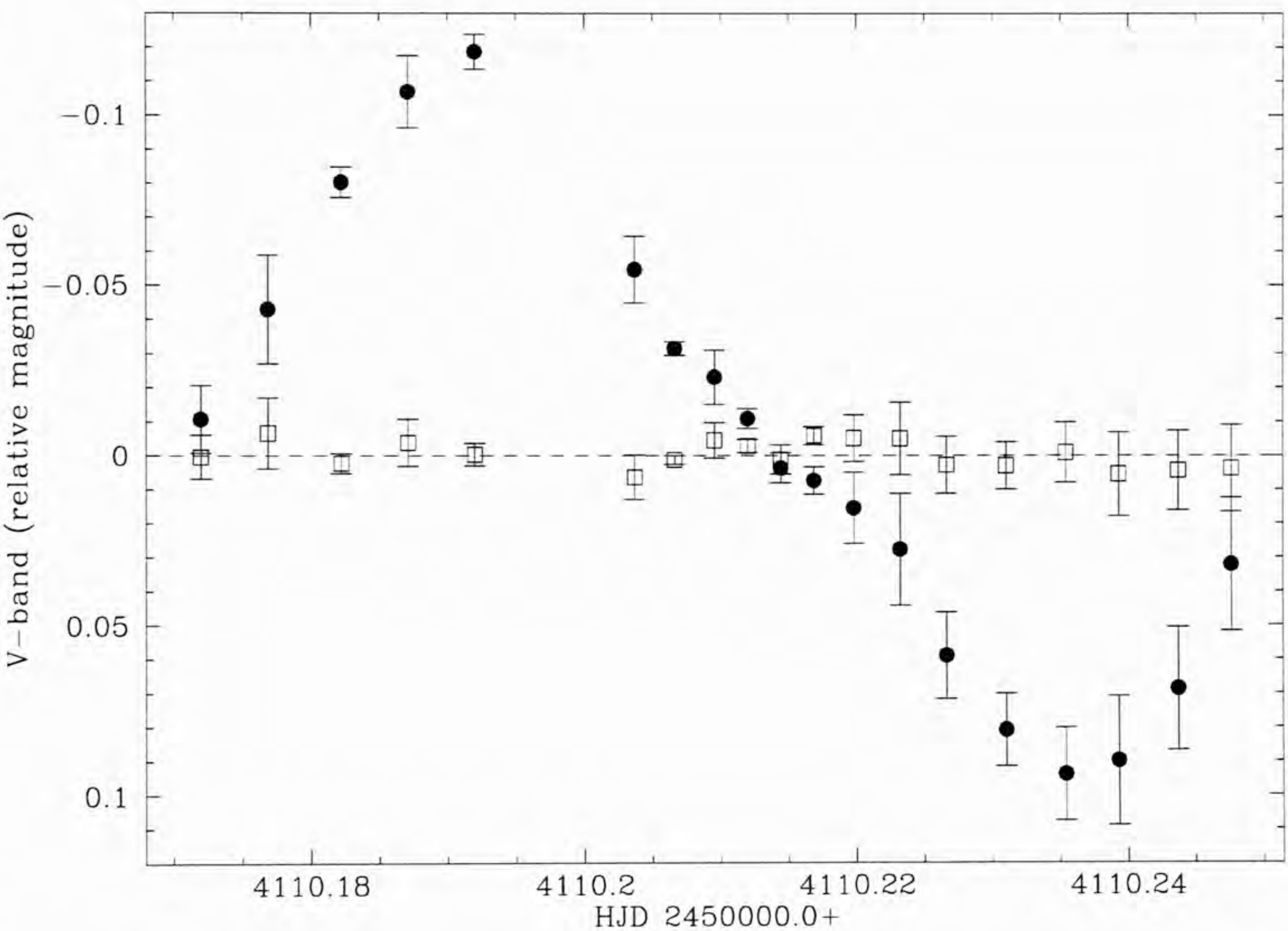

Figure 7.3. Light curves observed with the higher spatial resolution of the 40-inch telescope. The solid circles show the δ Scuti pulsation of our target, and the open squares show the light curve of the nearby star GSC0824700373 for comparison.

spectra (Pickles 1998). Visual inspection resulted in the classification of the spectra as an A7V star. The phase coverage was insufficient to measure the dynamical mass.

To obtain sufficient phase coverage, we obtained additional spectra with the same instrument on five nights in May 2007. The gratings and grating angle were set to give a wavelength coverage of 3600–4700 Å in the blue arm and 6000–7000 Å in the red. The same procedure of alternating observations with arc spectra for wavelength calibration was followed. However, we encountered significant shifts in the position of the arc spectra on the CCD between adjacent calibration frames. Therefore we used the night sky lines present in each spectrum in the red half of the data for additional calibration. The data were then continuum normalised. The red data clearly show spectral features of both the primary and secondary components, and also a significant component of $H\alpha$ emission. Given the semi-detached nature of UNSW-V-500 (see Sec. 7-4) this may indicate the existence of a gas stream between the two components (see for instance the set of well observed Algol-type eclipsing binaries in Richards & Albright (1999); Vesper et al. (2001)). The blue data show only single-lined spectral features, and are entirely dominated by the spectrum of the primary component. Therefore the blue data were used to identify the spectral type of the primary, by using the preliminary identification from the earlier data and the synthetic stellar template library released by Munari et al. (2005), rebinned as previously. We performed a least-squares fit and identified the $T_{\rm eff}$ = 7500 K, log g = 4.0, [Fe/H]= −0.5 template as the best fit. From the residuals to this fit, we attempted to match the spectrum of the secondary component. A preliminary light curve analysis had indicated a secondary component with a temperature of $\sim$ 4200 K; hence the least-squares fit to the residuals was restricted to the ATLAS9 models with $T_{\rm eff}$ = 4250 K and [Fe/H]= −0.5, since we can assume the binary system will have a common origin and thus metallicity. The best fit was achieved with the log g = 3.0 template.

We note again that the pulsating primary component is essentially fully eclipsed by the secondary star at primary eclipse. Therefore, a high resolution spectrum during the time of primary eclipse would necessarily be a spectrum of the secondary star, and would be useful for constraining the stellar spectral type and physical parameters derived via light curve-fitting in Section 7-4.

7-3.3 Radial velocity analysis

In order to extract the radial velocities of the two binary components, we used the program TODCOR (Zucker & Mazeh 1994), which performs a two-dimensional correlation between two supplied template spectra and an object spectrum of a binary system. Using the two stellar templates identified previously, radial velocities were extracted for the majority of the spectra we had obtained. The correlation was limited to the wavelength region 6200–6530 Å to avoid the $H\alpha$ emission noted previously. The flux ratio of the secondary to the primary template spectra was left as a free parameter for TODCOR, and was found to vary from 0.2–0.4 with phase.

The radial velocities are shown in Fig. 7.4, with the primary component shown as triangles and the secondary component as circles. The lines are the best-fitting sine curves, with velocity amplitudes of $K_1 = 27.0 \pm 1.8$ km s^{-1} and $K_2 = 121.2 \pm 1.4$ km s^{-1}, indicating a mass ratio of 0.22±0.02, and a systemic velocity of 43.6 ± 0.9 km s^{-1}.

The large scatter in the primary component data of ~ 20 km s^{-1} is due to the δ Scuti radial velocity pulsations, and is similar to the radial velocity amplitude of other HADS stars we have measured with the same instrument (Derekas et al. 2006). The frequency spectrum of these data were analysed in the same manner described in Sec. 7-5 and two peaks corresponding to the orbital and pulsational periods (5.36 d and 0.073 d) were identified, a second confirmation that this is not a blended system.

7-4 Binary System

In order to fit the orbital parameters of UNSW-V-500, we applied the Wilson-Devinney code (Wilson & Devinney 1971; Wilson 1979, 1990) to the APT light curve and the two radial velocity curves simultaneously. This system is an Algol-type semi-

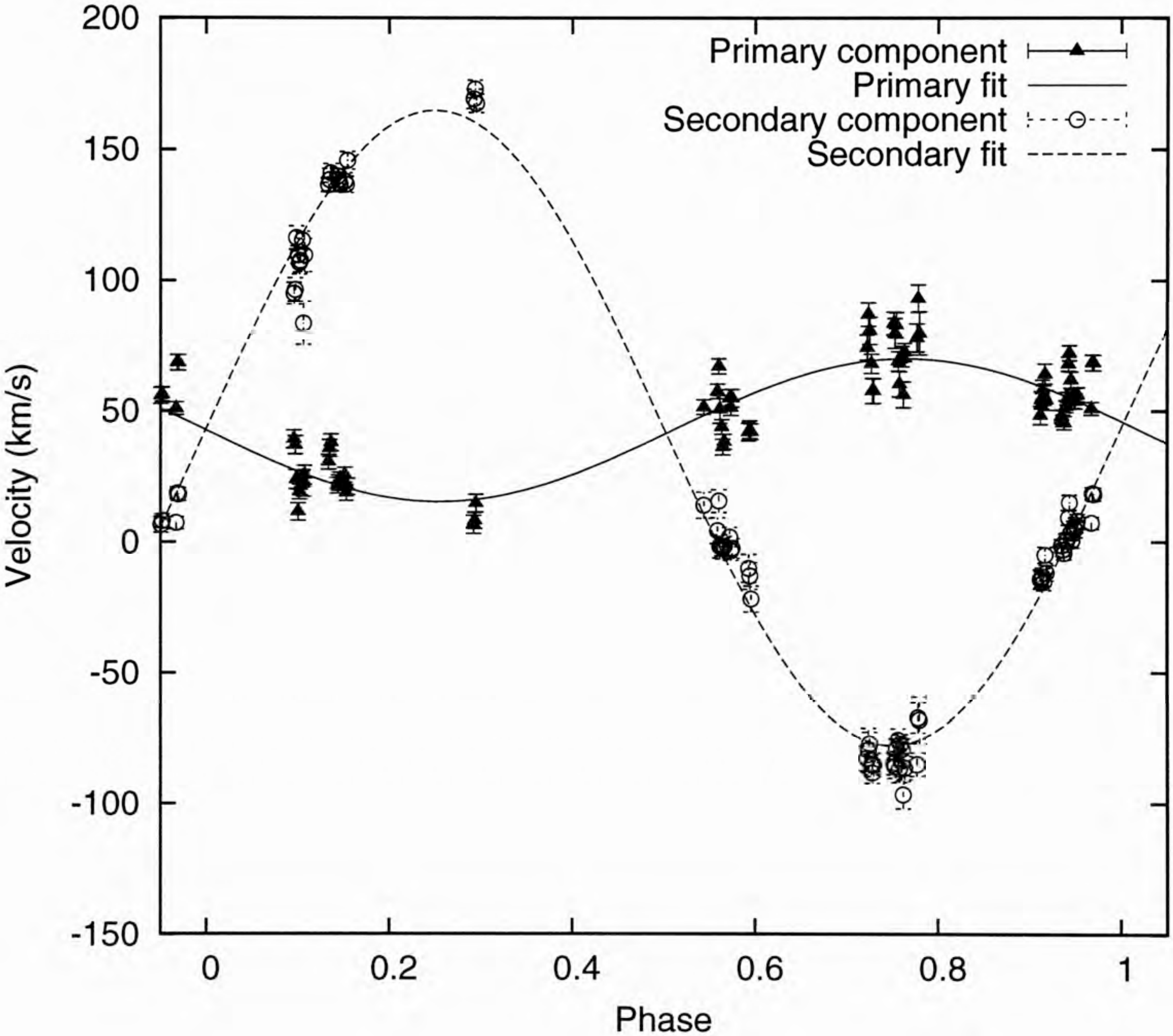

Figure 7.4. The radial velocities of the primary (solid triangles) and secondary (open circles) components. The lines are the best fitting sine curves.

detached eclipsing binary system, with the secondary star filling its Roche lobe, and consequently the code was operated in mode 5. The effective temperature of the primary was fixed at T_1 = 7500K from the template fit. The gravity brightening coefficients were set to 1.00 for the radiative primary component and 0.32 for the convective secondary component. The albedos were set to the standard theoretical value of 1.00. The bolometric and bandpass-specific limb darkening coefficients were adopted from values for the closest models in van Hamme (1993). The third light l_3 was assumed to be non-zero due to the crowded photometry aperture, and was allowed to vary as a free parameter. It was given an initial value of $l_3 = 0.2$ from an estimate of the maximum total contribution to the normalised flux at phase 0.25. The eccentricity was assumed to be ~ 0 due to the secondary eclipse occurring at a phase of 0.5. To confirm this, the eccentricity was allowed to vary and did not result in any significant improvement in the fit, so was fixed at 0 for the subsequent fitting. The semi-major axis was fixed at 15.69 $R_\odot$ from the total mass and period of the system, and the systemic velocity was fixed at 43.6 km s^{-1}. The mass ratio was fixed at 0.22 from the radial velocity data. The free parameters were thus the third light l_3, the inclination i, the effective temperature of the secondary T_2, the potential (as defined by Kopal (1954)) of the primary Ω_1 and the luminosity of the primary L_1. The values of these parameters used in the final solution are shown in Table 7.2, as are the derived quantities for the two components of mass, radius, log g and M_{bol}.

The solid line in Fig. 7.2 shows the best-fitting solution. The high inclination ($i = 86.5 \pm 1.0°$) is indicated by the flat bottom of the primary eclipse. In fact this is the first eclipsing binary system containing a pulsating component to demonstrate a flat-bottomed eclipse, with the possible exception of the recent discovery of the pulsating component of HD 99612 (Pigulski & Michalski 2007). The normalised third light contribution is found to be 0.096 at the reference phase of 0.25.

We note that the log g values that have been derived in the Wilson-Devinney fit (3.87 ± 0.01 and 2.74 ± 0.01 for the primary and secondary components respectively) confirm the estimated values from the synthetic template fitting (4.0 ± 0.5 and

Table 7.2. The parameters for the binary system solution. Starred quantities indicate the free parameters in the Wilson-Devinney code. Quoted errors for the starred quantities and the calculated quantities (L_2 and Ω_2) are standard deviations produced by the Wilson-Devinney code. [a] These are the bandpass luminosities in the I-band. [b] This is the corrected value of the third light for reference phase 0.25.

Parameter	Value
e	0.0000
q*	0.22±0.02
T_1 (K)	7500
T_2* (K)	3850±20
L_1* $(L_\odot)^a$	6.96±0.03
L_2 $(L_\odot)^a$	3.89±0.03
Ω_1*	6.9±0.1
Ω_2	2.3±0.1
i* (°)	86.5±1.0
$l_3{}^{*b}$	0.096±0.005
M_1 $(M_\odot)$	1.49±0.02
M_2 $(M_\odot)$	0.33±0.02
R_1 $(R_\odot)$	2.35±0.02
R_2 $(R_\odot)$	4.04±0.01
$M_{bol,1}$	1.80±0.02
$M_{bol,2}$	3.53±0.02
log g_1	3.87±0.01
log g_2	2.74±0.01

3.0 ± 0.5) in Sec. 7-3.2.

From the $T_{\rm eff}$ and derived mass we have identified the two components as a late A spectral type primary, confirming the A7V classification, and a late K spectral type secondary. Using the derived parameters, we attempted to fit the positions of the two components in the HR diagram with the Y^2 isochrones (Yi et al. 2001; Kim et al. 2002) in order to find an age estimate for the system. However, we found that the isochrones and evolutionary tracks were unable to reproduce the current positions of the components; hence we conclude that there has been significant mass transfer to the pulsating primary component from the secondary component. This component appears in a much more evolved state despite its lower mass, a well-recognized phenomenon known as the Algol paradox. We caution that standard evolution and pulsation models for HADS stars may not apply to UNSW-V-500 due to its binary evolution. However, we do note that it is well described by the ML3 mass-luminosity relation for HADS stars shown in fig. 1 of Petersen & Christensen-Dalsgaard (1996), which is based on models with a metal content of $Z = 0.02$.

7-5 Pulsation

Once the binary solution has been subtracted, an analysis of the δ Scuti pulsation can be performed. We have used data from phase 0.1 to 0.9 for this analysis, discarding those data around the primary eclipse where the HADS star is completely eclipsed. This reduces the total number of data points by 700, or $\sim$ 25 per cent. The residuals from the binary subtraction between phase 0.1 to 0.9 are shown in Fig. 7.5.

Fig. 7.6 shows the frequency analysis, as performed with the program PERIOD04 (Lenz & Breger 2005). The spectral window is shown in panel (a). Panel (b) shows the initial periodogram. The dominant frequency is identified as $f_1 = 13.621 \pm 0.015$ cd^{-1}, i.e. a period of 0.0734 ± 0.0001 d, which is typical for δ Scuti stars. The four additional frequencies identified with a S/N > 4.0, as suggested by Breger et al. (1993), are shown in panel (c), after removal of f_1. These can be identified as low-power frequencies, probably due to artefacts of the binary subtraction ($f_2 =$

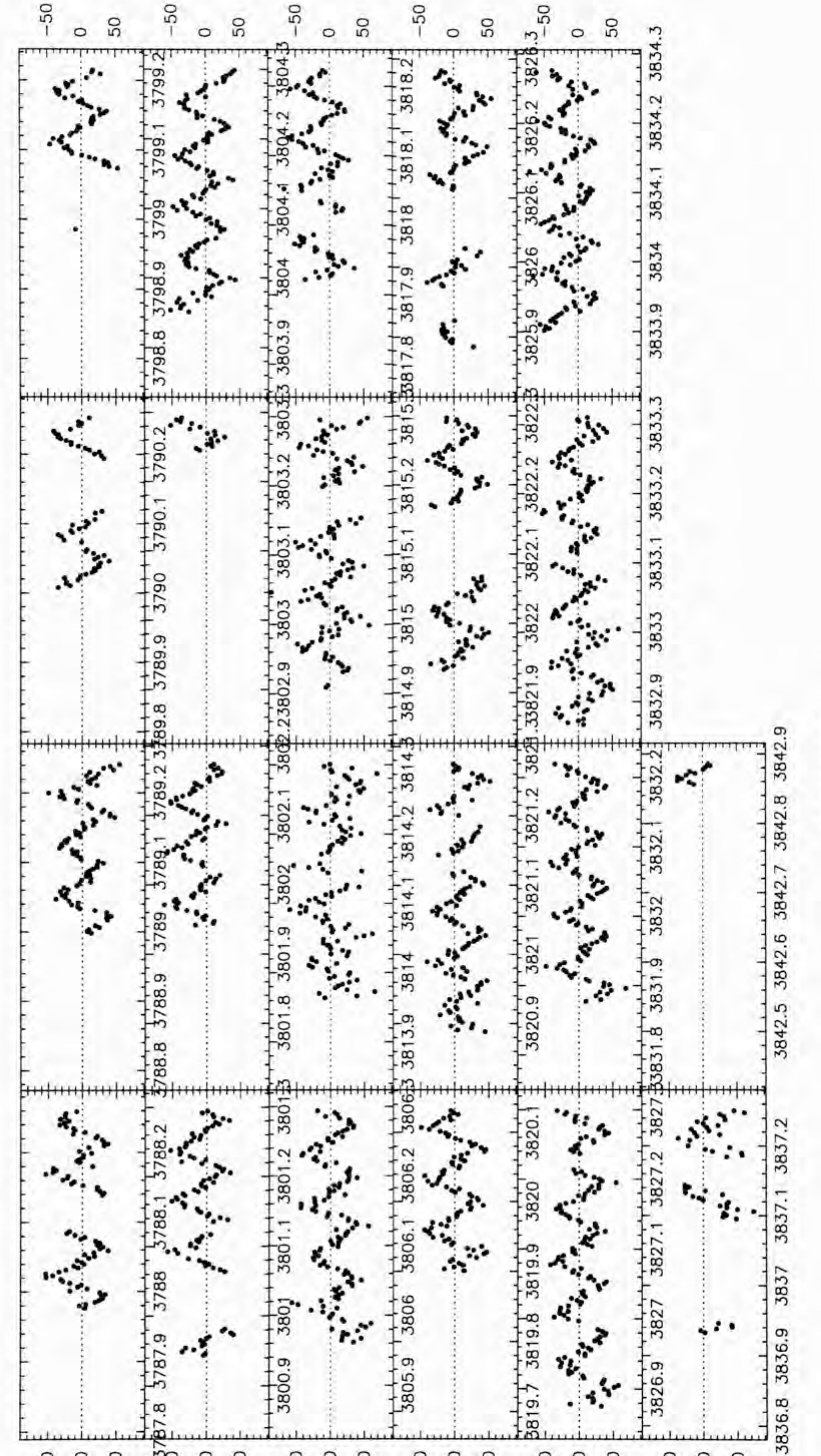

Figure 7.5. The residuals in the original data after the subtraction of the best-fitting binary solution, between phases 0.1 and 0.9.

0.187 ± 0.033 cd^{-1} and $f_4 = 0.255 \pm 0.084$ cd^{-1}), or harmonics of f_1 ($f_3 = 2f_1 = 27.242 \pm 0.084$ cd^{-1} and $f_5 = 3f_1 = 40.86 \pm 0.14$ cd^{-1}). The absence of any additional frequencies in the δ Scuti range supports the identification of a HADS star oscillating in a single radial mode to the limits of our detection.

As an additional check, these frequencies were removed from the original data. The resulting light curve is shown in Fig. 7.2, offset below the original data. The Wilson-Devinney code was re-run using this second light curve, with no significant change in the derived parameters.

Using the relation from Breger et al. (1993), we can calculate the pulsation constant Q_{obs}.

$$\log Q_{obs} = -6.456 + \log P + 0.5 \log g + 0.1 M_{bol} + \log T_e \tag{7.1}$$

We find a Q_{obs} of 0.025±0.001. Petersen & Jørgensen (1972) derived theoretical pulsation constants of $Q_0 = 0.0333$ for the fundamental radial mode, $Q_1 = 0.0252$ for the first overtone radial mode, and $Q_2 = 0.0201$ for the second overtone radial mode. Inspection of the HADS stars catalogued in McNamara (2000a) reveals that of the 26 well studied field stars, all have observed pulsation constants in the range 0.0309–0.331, indicating they are pulsating in the fundamental mode. UNSW-V-500 appears to be the first identified to be pulsating primarily in the first overtone radial mode, joining a number of SX Phe stars in globular clusters to have been identified in this mode (McNamara 2000b).

7-6 Summary

We have presented here the detection of the first example of a high-amplitude δ Scuti star in an eclipsing binary system, and the probable first detection of a field HADS star pulsating in the single first overtone radial mode. Several HADS stars have been detected in binary systems previously (including SZ Lyn (Derekas et al. 2003) with a period of 1190 d; and RS Gru (Joner & Laney 2004) with a period of approximately 2 weeks), however these are much wider systems. This new fully

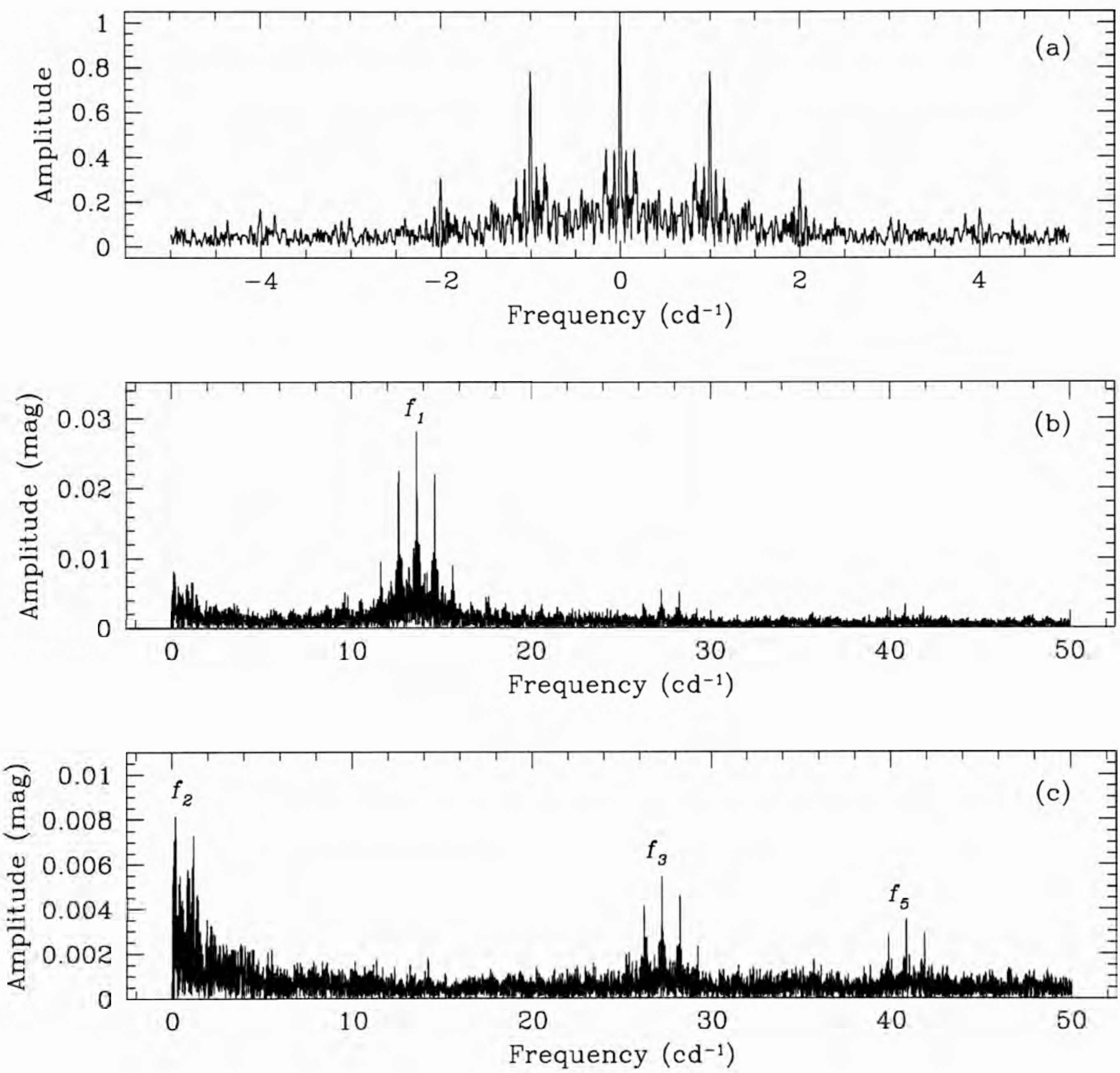

Figure 7.6. The frequency analysis of the pulsation. Panel (a) shows the spectral window. Panel (b) shows the strongest frequency f_1 at 13.621 cd^{-1}. Panel (c) shows the frequency spectrum with f_1 removed. On this scale, f_4 is coincident with f_2.

eclipsing binary opens up many further opportunities for studies of HADS stars and pulsating stars in binary systems. Many of the poorly understood processes governing the effects of mass transfer, tidal interactions, rotation, convection and magnetism on δ Scuti pulsations may be explored with this system.

7-7 Supplementary material

This section contains additional data and figures used in the analysis of UNSW-V-500 that were not included in the paper.

7-7.1 Spectral classification

Spectroscopic data were obtained in both the red and blue wavelength regions, as described in Section 7-3.2. For clarity in identifying the main features, Figure 7.7 shows the mean of 6 contiguous spectra observed in the wavelength region 6500-6600 Å around phase 0.75, when the spectral features of the two components should be at maximum separation. The double-lined absorption features and the Hα emission are marked.

In the blue wavelength region, the spectral features of the primary A star component entirely dominate the spectra, and only single-lined spectral features are seen. Therefore we use the blue data for the spectral type classification of the primary component. Figure 7.8 shows a spectrum of UNSW-V-500 in the wavelength region 3800–4400 Å below the closest matching template from the Munari et al. (2005) synthetic stellar template library.

Figure 7.9 shows the two synthetic stellar templates in the wavelength region 6200–6530 Å that were used in the TODCOR cross-correlation, identified as per Section 7-3.2.

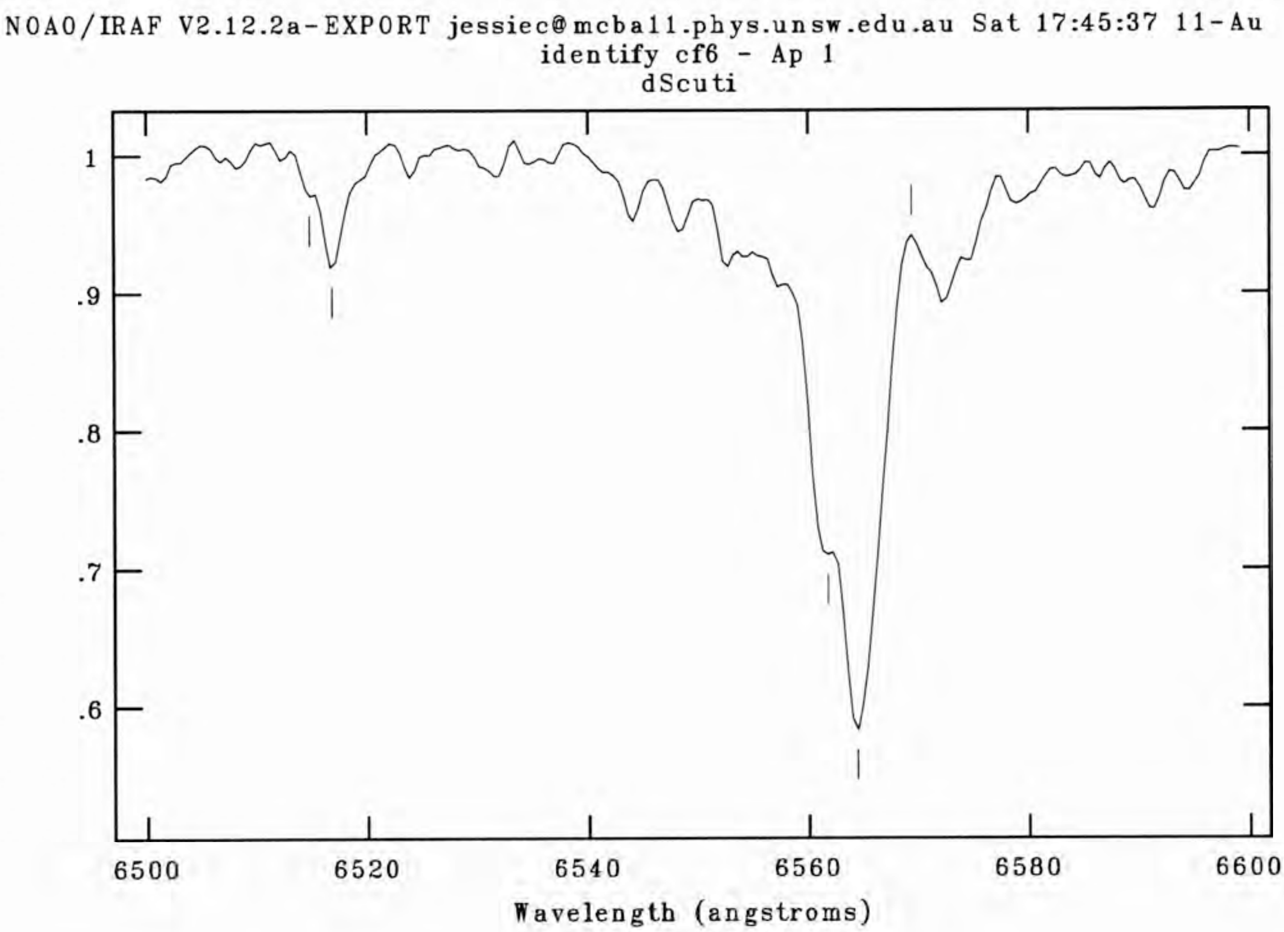

Figure 7.7. Average of 6 spectra in the region 6500–6600 Å around phase 0.75, showing the double-lined spectral features (e.g. the lines at 6515 Å and the Hα line at 6563 Å). The secondary, non-pulsating component of the binary system has the weaker Hα absorption feature and is blue-shifted relative to the primary δ Scuti component. The component of Hα emission that could be the result of a hypothetical gas stream between the two components is visible at 6569 Å. This is not unexpected since the secondary component has filled its Roche lobe and there is ongoing mass-transfer to the primary component.

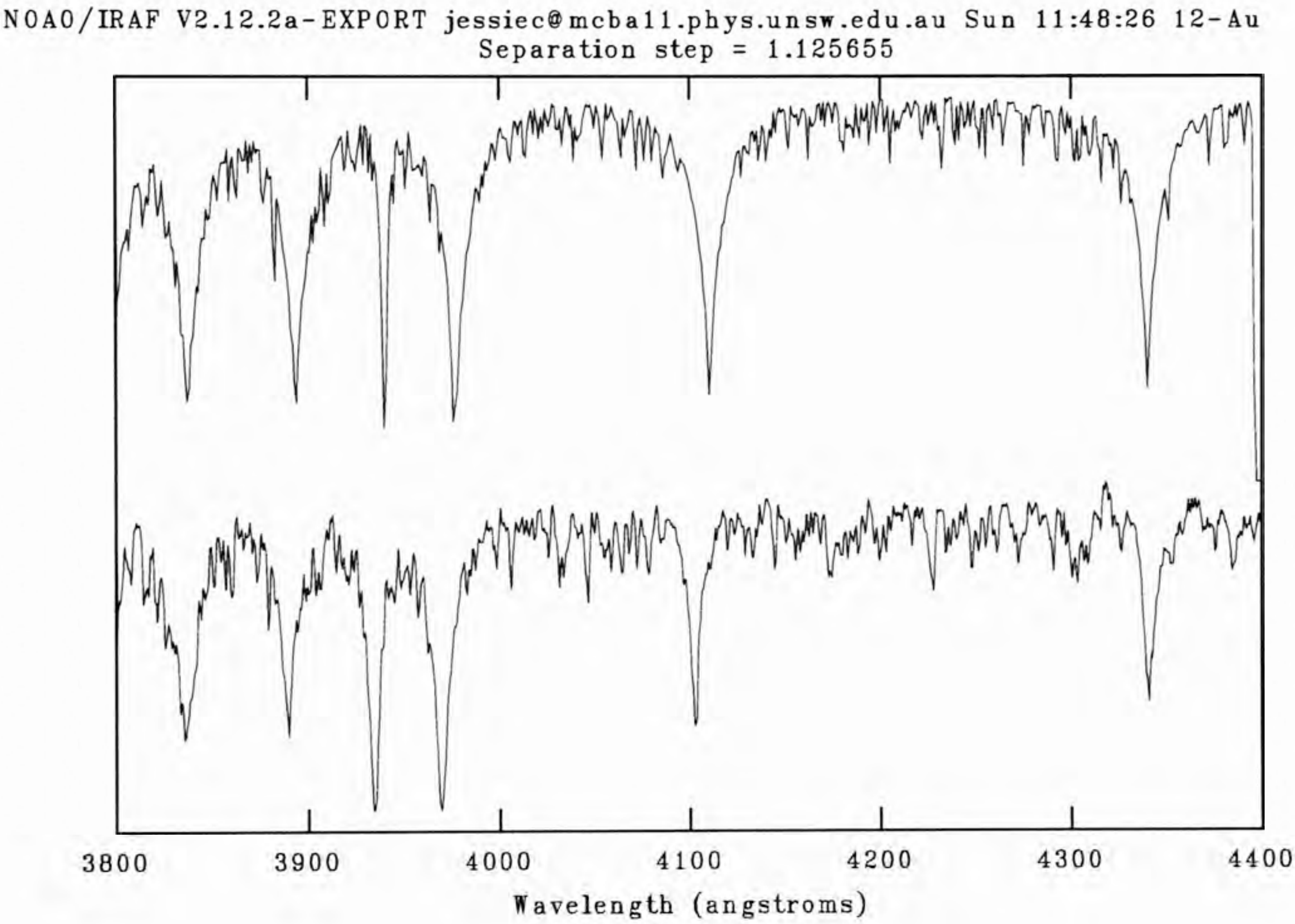

Figure 7.8. A comparison of the T_{eff} = 7500K, log g = 4.0, [Fe/H] = -0.5, V_{rot} = 30kms^{-1} synthetic template spectrum (top) from the Munari et al. (2005) template library with a spectrum of UNSW-V-500 (bottom) observed with the blue arm of the DBS instrument on the 2.3-m telescope.

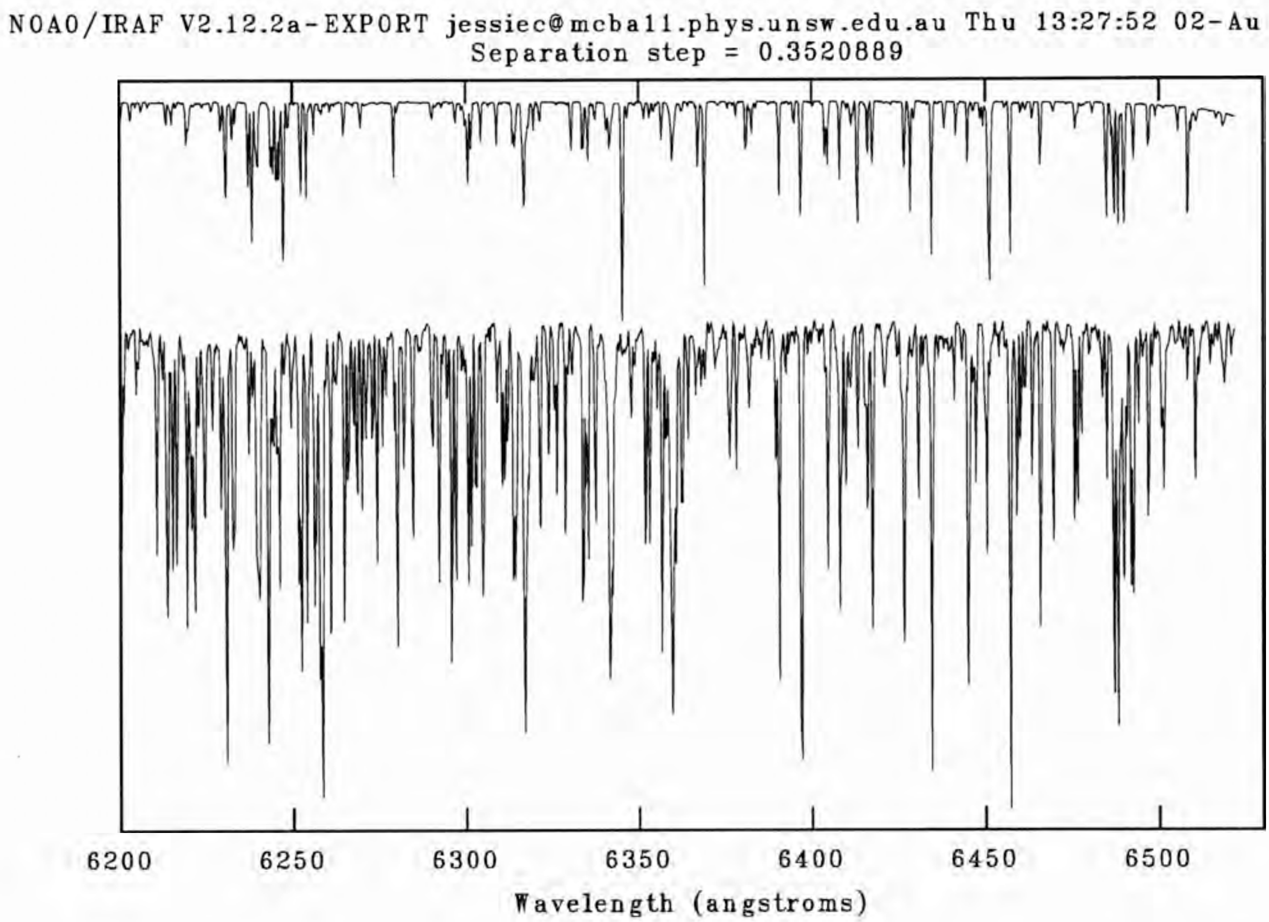

Figure 7.9. The two synthetic template spectra from the Munari et al. (2005) template library used in the TODCOR analysis. The top spectrum is the $T_{\text{eff}} = 7500K$, $\log g = 4.0$, [Fe/H]$= -0.5$ template, and the bottom spectra is the $T_{\text{eff}} = 4250K$, $\log g = 3.0$, [Fe/H]$= -0.5$ template. For the purposes of cross-correlation in TODCOR, we have used templates with no rotational broadening (i.e. the sharpest spectral features) in order to give the clearest correlation. TODCOR automatically rebins the template spectra to the resolution of the supplied object spectrum.

7-7.2 TODCOR cross-correlation program

In order to obtain Doppler shifts from observed spectra, the usual method is to perform a cross-correlation with a template spectrum. The position which gives the correlation maximum can then be converted to a radial velocity shift. However, in the case of spectroscopic binaries with small relative velocities and blended line profiles, this results in poorly-resolved double peaks in the correlation function. It is for this reason that the TwO-Dimensional CORrelation algorithm, TODCOR, was designed (Mazeh & Zucker 1992; Zucker & Mazeh 1994). Given two template spectra, the algorithm produces a set of combinations of the spectra with all possible shifts, and calculates the two-dimensional correlation of this set with the observed spectrum.

The flux ratio α of the secondary component to the primary component can either be set as a fixed parameter or allowed to vary. We performed the cross-correlation analysis with α as both a fixed and free parameter and found no significant difference in the results.

Table 7.3 contains the radial velocity data as fitted to the two components of UNSW-V-500 using TODCOR.

Table 7.3. The radial velocity data extracted for the two components with TODCOR. The columns are Heliocentric Julian Date (HJD), the radial velocity of the primary component (V_1) and the error (σ_1), the radial velocity of the secondary component (V_2) and the error (σ_2), α is the flux ratio as fit by TODCOR, and V_{HELIO} are the heliocentric corrections to the radial velocities to compensate for the motion of the Earth, calculated with the IRAF routine `RVCORRECT`.

HJD	V_1 (kms^{-1})	σ_1	V_2 (kms^{-1})	σ_2	α	V_{HELIO} (kms^{-1})
4222.925781	51.3	2.8	13.8	5.0	0.22	-2.12
4223.005371	57.4	2.8	4.0	4.9	0.23	-2.28
4223.012207	66.9	2.9	15.4	4.4	0.23	-2.30
4223.019531	50.5	5.3	-1.9	4.5	0.29	-2.32
4223.029785	43.8	2.8	-2.0	3.6	0.24	-2.34
4223.036621	36.1	3.0	-2.7	4.0	0.21	-2.35
4223.043945	38.1	2.8	-1.9	3.7	0.25	-2.37
4223.076172	54.8	3.3	1.7	3.7	0.27	-2.44
4223.083496	51.1	2.9	-3.6	3.7	0.25	-2.45
4223.090332	54.7	3.4	-2.7	3.8	0.27	-2.47
4223.187500	41.9	3.4	-10.4	5.3	0.24	-2.64
4223.194336	42.8	3.4	-13.3	5.2	0.24	-2.65
4223.201660	42.0	3.0	-22.1	5.0	0.22	-2.66
4223.880859	74.2	4.8	-82.8	4.6	0.48	-2.47
4223.887695	86.8	4.5	-79.7	8.3	0.22	-2.48
4223.895020	80.6	5.2	-77.4	4.5	0.44	-2.49
4223.905273	68.0	3.7	-85.2	3.8	0.39	-2.50
4223.912109	57.5	4.9	-88.3	4.1	0.51	-2.52
4223.918945	57.6	4.7	-85.3	4.4	0.47	-2.53
4224.036133	83.3	4.3	-84.8	4.2	0.47	-2.77
4224.043457	79.6	5.7	-85.9	4.5	0.47	-2.78
4224.050781	82.7	4.8	-79.4	3.9	0.47	-2.80
4224.062500	68.9	3.7	-75.9	4.3	0.41	-2.82

Table. 7.3 – *continued.* Radial velocity data.

HJD	V_1 (kms^{-1})	σ_1	V_2 (kms^{-1})	σ_2	α	V_{HELIO} (kms^{-1})
4224.069336	60.1	4.9	-86.7	5.3	0.45	-2.84
4224.076172	69.7	2.9	-77.4	3.7	0.35	-2.85
4224.085938	70.7	3.9	-79.5	4.2	0.44	-2.87
4224.092773	56.1	5.0	-96.8	5.4	0.25	-2.89
4224.100098	72.3	3.4	-86.5	4.4	0.30	-2.90
4224.172363	77.8	5.4	-85.2	4.4	0.44	-3.03
4224.179199	92.9	5.3	-67.4	5.8	0.53	-3.04
4224.186523	79.6	8.3	-68.3	9.0	0.47	-3.05
4224.892578	48.2	3.4	-14.5	3.7	0.43	-2.90
4224.899414	54.2	3.2	-14.5	3.1	0.41	-2.91
4224.906738	57.9	3.8	-13.6	3.4	0.44	-2.92
4224.913574	55.9	3.8	-15.6	3.2	0.43	-2.93
4224.920898	64.1	3.8	-5.2	3.1	0.46	-2.94
4224.927734	54.1	3.7	-12.0	3.0	0.48	-2.96
4225.017090	47.9	2.4	-1.6	2.4	0.38	-3.14
4225.024414	46.3	2.2	-3.2	2.3	0.38	-3.16
4225.031250	45.4	2.5	-4.5	2.5	0.42	-3.17
4225.042969	51.6	2.3	0.4	2.6	0.38	-3.20
4225.049805	54.6	2.5	0.8	2.5	0.39	-3.21
4225.056641	67.9	2.7	9.1	2.9	0.43	-3.23
4225.063965	72.0	2.8	14.8	2.9	0.45	-3.24
4225.071289	61.8	3.1	3.4	2.8	0.41	-3.26
4225.078125	55.3	2.9	0.2	2.7	0.44	-3.27
4225.088379	53.5	2.6	5.3	2.5	0.44	-3.29
4225.095215	53.7	3.0	4.7	3.1	0.44	-3.31
4225.102539	55.6	3.0	6.4	3.0	0.46	-3.32
4225.109375	56.1	2.7	7.8	2.6	0.45	-3.33
4225.190918	50.8	2.4	7.1	2.3	0.43	-3.47
4225.197754	68.3	3.0	18.3	2.4	0.51	-3.48
4225.205078	68.2	3.0	17.9	2.5	0.50	-3.49

Table. 7.3 – *continued.* Radial velocity data.

HJD	V_1 (kms^{-1})	σ_1	V_2 (kms^{-1})	σ_2	α	V_{HELIO} (kms^{-1})
4225.878906	39.1	3.4	94.8	4.2	0.41	-3.29
4225.886230	36.9	3.5	96.2	4.5	0.37	-3.30
4225.893066	23.7	3.6	116.1	4.4	0.36	-3.31
4225.902832	11.4	3.3	109.5	3.3	0.37	-3.32
4225.909668	19.1	2.9	106.5	4.4	0.27	-3.34
4225.916504	21.2	3.4	107.3	4.4	0.36	-3.35
4225.926758	23.7	3.1	115.1	3.4	0.35	-3.37
4225.933594	22.3	5.1	83.4	8.3	0.39	-3.38
4225.940918	25.4	3.6	109.4	6.3	0.31	-3.39
4226.080566	30.4	2.9	136.2	2.6	0.37	-3.69
4226.087402	35.6	3.2	138.2	4.3	0.29	-3.70
4226.094238	37.8	3.2	140.8	3.6	0.31	-3.72
4226.132812	21.4	3.0	139.6	3.1	0.37	-3.79
4226.139648	22.4	3.0	138.2	3.1	0.38	-3.80
4226.146973	23.9	2.4	136.5	2.9	0.30	-3.81
4226.175781	25.4	2.8	137.6	3.3	0.35	-3.86
4226.183594	18.6	3.0	136.4	3.1	0.35	-3.87
4226.190430	21.0	3.1	145.6	3.4	0.34	-3.88
4226.930176	6.4	3.5	169.1	3.7	0.35	-3.79
4226.937012	8.0	3.0	172.9	3.4	0.31	-3.80
4226.944336	14.6	3.4	167.4	3.5	0.30	-3.81

7-7.3 The Wilson-Devinney program

The Wilson-Devinney code is a general purpose program for modelling observables of binary systems. It contains two main modules—the first computes observables such as light curves and radial velocity curves from a given set of input parameters, and the second performs the inverse problem of fitting parameters to observed data via differential correction. Several versions have been released since the original in 1971, and the program now takes into account rotational and tidal distortions, detailed reflection and re-radiation effects, limb- and gravity-darkening, arbitrary rotation rates and orbital eccentricity, and allows for the addition of spots and circumstellar clouds. It can be run in various modes relating to the configuration of the binary system, including modes for detached, semi-detached, contact, double-contact and compact x-ray binaries.

Following is a sample of the input to the Wilson-Devinney differential correction module. In this example, the program is being run in mode 5, which is appropriate for a semi-detached eclipsing binary system with the secondary component overflowing its Roche lobe. The free parameters in this run are the orbital inclination i, the secondary component effective temperature T_2, the primary component potential Ω_2, the primary component bandpass luminosity L_1, and the third light l_3, as indicated by the zeroes in the fourth line of code. The input data expected by the program for this run are radial velocity curves for each of the components and an I-band light curve. The ellipses indicate clipped data for clarity. The limb-darkening law coefficients used in this input are listed in Table 7.4.

```
+2.0d-2 +2.0d-2 +2.0d-2 +2.0d-2 +2.0d-2 +2.0d-2 +2.0d-2 +2.0d-2
+1.0d-2 +1.0d-2 +1.0d-1 +1.0d-1 +2.0d-3 +1.0d-3 +1.0d-2 +1.0d-2 +1.0d-2 +3.0d-3
+1.0d-2 +1.0d-2 +3.0d-2 +3.0d-2 +1.0d-3 +1.0d-2 +1.0d-2 +1.0d-2 +1.0d-2
1111 1111 1111111 01110 11011 11111 01110 1 1 1 1.000d-05
 1  0  2  0
1 1 01 2 0 0 1
1 1 1 1 1 1 3
2 0044145.079000 0.535047510D+01 -0.000000D-08 0000.0051
05 0 1 1 30 30 15 15 +0007.050000 0.60354D-05 0.00000  100.000
.00001 1.569000d+01 +001.0000 +001.0000   +0.4492 +086.678 01.000 00.320 +00.00
00.7500 00.3847 +1.000 +0.500 0.693400D+01 0.236639D+01 0.22000d+00 +0.248 +0.078 +0.488 +0.556
```

```
 9 005.50000 005.31319 +0.097 +0.823 +0.583 -0.089 0.000D+00 0.97500D-01  0.640000
 9 005.50000 005.31319 +0.097 +0.823 +0.583 -0.089 0.000D+00 0.97500D-01  0.640000
10 006.97040 003.68943 +0.025 +0.425 +0.539 +0.274  0.1016 0.000D+00 1 0.13500D-01 00.900000
300.00000
300.00000
150.
       0.54370  0.5134  1.00
       0.55858  0.5735  1.00
       ...      ...     ...
       0.29477  0.1461  1.00
  -10001.
       0.54370  0.1380  1.00
       0.55857  0.0404  1.00
       ...      ...     ...
       0.29476  1.6740  1.00
  -10001.
       0.25230  0.9976  1.00
       0.25320  0.9743  1.00
       ...      ...     ...
       0.01544  0.3624  1.20
  -10001.
 1111 1111 0001110 01110 11000 00101 01110 0 1 0 1.000d-05
 1111 1111 0001110 01110 11000 00101 01111 0 1 0 1.000d-05
 1111 1111 1111111 11111 11111 11111 11110 0 1 0 1.000d-05
 2
```

Table 7.4. The coefficients for the square-root cosine law of limb darkening used in the Wilson-Devinney code. The x and y terms for the both the bolometric and bandpass-specific limb darkening laws are shown. These coefficients are taken from the two closest models in van Hamme (1993), models number 176 for the primary component and number 40 for the secondary.

Model no.	$T_{\rm eff}$	log$g$	$x_{\rm bol}$	$y_{\rm bol}$	$x_{\rm I}$	$y_{\rm I}$	$x_{\rm R}$	$y_{\rm R}$
176	7500	4.0	0.248	0.488	0.025	0.539	0.097	0.583
40	3750	3.0	0.078	0.556	0.425	0.274	0.823	-0.089

7-7.4 PERIOD04 frequency analysis package

The software package PERIOD04 is specifically designed for analysis of astronomical time series data containing gaps (Lenz & Breger 2005). Using discrete Fourier transformations and least-squares fitting, one can extract individual or multiple frequencies from the data. Additionally, one can measure amplitude and/or phase variations in the data. This package was used to investigate the δ Scuti pulsations in the residuals from the binary solution fit. Data from phases 0.1–0.9 were used, since the δ Scuti pulsations are not detected during primary eclipse. Table 7.5 contains the frequency, frequency error, amplitude and phase information extracted for the frequencies detected above the signal-to-noise threshold of 4.

Table 7.5. PERIOD04 frequency analysis of the δ Scuti pulsations.

	Frequency (cd^{-1})	σ_f	Amplitude	Phase
f_1	13.6208	0.0129	0.0285	0.1256
f_2	0.186752	0.0292	0.0126	0.1613
$f_3 = 2 \times f_1$	27.2423	0.0669	0.0055	0.7331
f_4	0.255093	0.0683	0.0054	0.8583
$f_5 = 3 \times f_1$	40.8628	0.1068	0.0034	0.7981

7-7.5 Binary Maker 3

Binary Maker 3[2] is a 3D visualisation software package for binary systems. Given the input parameters of mass ratio, Ω potentials from the Wilson-Devinney code and temperatures for each of the two components, limb- and gravity-darkening coefficients, albedos, third light component, angle of inclination, eccentricity and rotation rates, the package renders the appropriate 3D models, and also light curves and radial velocity curves. The user is able to animate the models throughout an entire orbital cycle. Figure 7.10 shows three still frames from the animation of UNSW-V-500 at phases 0.25, 0.96 and 0.00.

[2]http://www.binarymaker.com/

Figure 7.10. 3D visualisations of the binary system using Binary Maker 3. The top panel shows the side-on view of two stars at phase 0.25. The primary δ Scuti component is the smaller star on the left, the secondary component is the larger star on the right, with the distinctive shape indicating it has filled its Roche lobe. The middle panel shows the δ Scuti star being partially eclipsed by the secondary component at phase 0.96, and the bottom panel shows to the total eclipse of the δ Scuti star at phase 0.00. This corresponds to the flat-bottomed eclipse seen in the light curve where the δ Scuti pulsations are absent. The red dots and lines trace out the positions of the centres of mass of the two components.

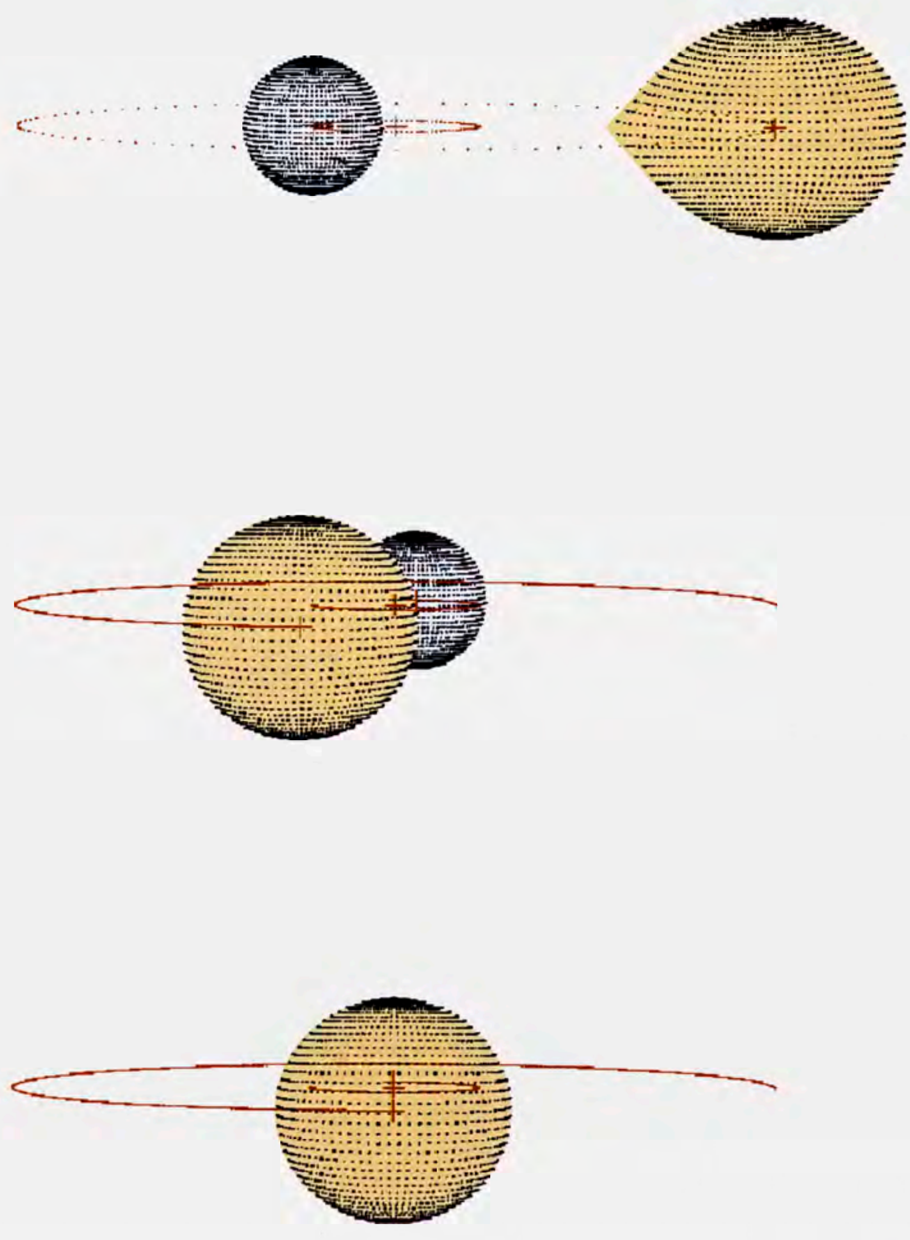

7-8 Future work

UNSW-V-500 represents an exciting system for further investigation. One possibility is a measurement of the Rossiter-McLaughlin effect. In an eclipsing binary system, different regions of the projected surface area of the background star will be covered as the foreground star passes in front of it. This causes the centres of gravity of the spectral lines of the background star to vary during the eclipse. This effect can typically be hard to measure, since the spectral lines of the foreground star will blend with those of the background star in the eclipse. However, UNSW-V-500 is composed of two quite different stars, and as noted previously the blue wavelength region of the spectrum is entirely dominated by the δ Scuti star. A high resolution spectrometer on a moderately-sized telescope is sufficient for measuring this effect in a stellar binary system once the problem of foreground spectral lines can be controlled (Albrecht et al. 2007); the University College London Echelle Spectrograph (UCLES) on the 3.9-m Anglo Australian Telescope would suffice.

These data could provide the first low spatial resolution map of the surface velocity fields of a δ Scuti star. Additionally, the Rossiter-McLaughlin effect can also indicate the orientation of the stellar rotation axes, using the method described by Albrecht et al. (2007). The alignment between the spin and orbital axes may provide information about the possible binary formation and evolution scenarios. Since it is evident that the δ Scuti star in this system has undertaken an unusual evolutionary path compared to single δ Scuti stars, any information that can constrain this path would be interesting.

Chapter 8

Conclusions

8-1 Summary

Part II of this work described the University of New South Wales Extrasolar Planet Search, a wide-field transit survey using the 0.5-m Automated Patrol Telescope located at Siding Spring Observatory, Australia, in the period 2004 October to 2007 May.

Using the initial observing strategy developed in an earlier phase of the survey, 11 pairs of fields were observed for a minimum of ~ 20 nights, and the data obtained analysed for transiting planet candidates. The presence of significant systematics in the data necessitated a modification to the observing strategy, and three additional single fields were observed for a minimum of ~ 3 months. In total, 25 fields were observed, and a total of $\sim 87,000$ light curves were constructed with magnitudes $8 < I < 14$.

Attempts to reduce the effects of the various sources of systematics on the data included the addition of a hood around the lens of the telescope to minimise scattered moonlight, and an attempt to optimise the photometry aperture positioning to minimise blending with neighbouring stars. The remaining systematics in the light curves were largely removed in the post-processing stages using the trend-filtering algorithm of Kovács et al. (2005).

Using both visual inspection and a box-search algorithm (Aigrain & Irwin 2004), light curves which displayed a minimum number of transits matching a set of criteria defining the transit depth, shape, and out-of-eclipse variations were extracted; 23 promising candidates were obtained from this analysis. Further analysis using archived high spatial resolution Digitized Sky Survey images, colour information extracted from online catalogues and the equations of Seager & Mallén-Ornelas (2003) for characterisation the light curves allowed us to eliminate 10 of these candidates.

Additional observations were obtained for eight of the remaining candidates. These included higher spatial resolution imaging with the Wide Field Imager on the 40-inch telescope at Siding Spring Observatory, Australia, and medium resolution spectroscopy with the Double-Beam Spectrograph on the 2.3-m telescope at the same site. The majority were conclusively shown to be either grazing or blended eclipsing binaries; for the remainder where the results were inconclusive the most likely interpretation is that of some configuration of an eclipsing binary. The final five candidates have not yet received additional observations but are slated for 40-inch follow up in the next few months.

Although initial predictions were that the University of New South Wales Extrasolar Planet Search would discover 2–3 planets per year, analysis of the observations failed to yield any confirmed planet detections. This disparity can be attributed to the effect of systematics on the detection threshold used in the predictions; in the presences of systematics, many more in-transit data points are required to achieve a significant detection than was originally expected.

In order to maximise the scientific output of the large data set of light curves, an additional variability analysis was performed using the Stetson Variability Index (Stetson 1996). A final catalogue of 850 variable light curves was produced, with a preliminary classification and catalogue cross-identification performed. Several astrophysically interesting subsets of the full catalogue were identified as potential starting points for further analysis.

During the analysis of the variable star catalogue, the first high-amplitude δ Scuti star in an eclipsing binary was discovered and designated UNSW-V-500. Stars in eclipsing binaries provide a wealth of additional information that cannot be accurately measured for single stars, including radii and masses. UNSW-V-500 represented to first opportunity for these parameters to be measured for a high-amplitude δ Scuti star. Medium resolution spectroscopy with the Double-Beam Spectrograph on the 2.3-m telescope was obtained with sufficient phase coverage to construct a radial velocity curve. The radial velocity curve the and light curve were solved simultaneously using the Wilson-Devinney code (Wilson & Devinney 1971; Wilson 1979, 1990) and the orbital and stellar parameters derived. The system is an Algol-type eclipsing binary, where the secondary star has filled its Roche lobe and thereafter transferred significant mass to the primary star. This additional mass appears to have pushed the primary star into the high-amplitude δ Scuti region of the HR diagram.

8-2 Future work

During the course of this work, several areas of improvement were identified. Some potential solutions are outlined below.

8-2.1 SYSREM

An alternative method of removing systematics in the post-processing stage to the trend-filtering algorithm implemented in this work was proposed by Tamuz et al. (2005). The systematics removal (SYSREM) algorithm can be best explained using the example for which it was initially developed—colour-dependent atmospheric extinction correction. Over the course of the night, each star will be observed at a series of airmasses. The residuals on each measurement will be linearly correlated with the airmass in a way that depends on the colour of the star. The coefficient of this correlation c_i for the ith star can be found by minimising

$$S_i^2 = \sum_j \frac{(r_{ij} - c_i a_j)^2}{\sigma_{ij}^2} \tag{8.1}$$

where r_{ij} is the residual on the jth measurement of the ith star, a_j is the airmass of the jth observation, and σ_{ij}^2 is the error on the jth measurement of the ith star.

This approach can be generalised to any effect which varies linearly with some property of the star. Once the set of coefficients c_i has been derived, they can be held and the set of a_j that minimises equation 8.1 can be derived. This process can be iterated, solving for a_j and c_i, until a user-specified number of solutions have been found.

This method has two clear advantages over the trend-filtering algorithm. The first is that the user gains actual information about the form of the systematics. After each iteration the set of correlations can be analysed for the potential source of the systematics, for example the a_j may be found to correlate to temperature variations, or moon phase, and the set of c_i may be found to correlate to stellar magnitude or position on the chip. Once the significant sources of systematics are identified, steps can be taken to minimise their effect on the light curves.

The second advantage is the mitigation of the major fault of the trend-filtering algorithm: when the reconstructed light curve, with some inherent noise, is subtracted from the original light curve, with a different inherent noise, the final result is a filtered light curve with an increased intrinsic level of white noise, even though a significant component of the low frequency red noise has been removed. In SYSREM, because linear trends are fitted and removed, the white noise in the final result is not increased over the initial noise in the light curve.

Due to these advantages, we are currently in the process of implementing a version of SYSREM for analysis of our light curves. Once this is operating satisfactorily we will re-analyse the existing data set of $\sim 87,000$ light curves for shallow transit candidates that may have been hidden by systematics.

8-2.2 New camera

Observations have been suspended since 2007 May due to the removal of the old camera and preparation for the installation of a new camera, built by the Anglo Australian Observatory. The observing strategy and data analysis will need to be assessed and modified given the characteristics of the new camera.

- The new camera is a mosaic of two MITLL 6k×3k chips, giving a total of 6k×6k pixels. The pixels, at 9 μm each, are significantly smaller than the pixels in the old camera, giving a correspondingly better spatial resolution of 3.77″ pixel^{-1} (compared to the 9.43″ pixel^{-1}). Across the two chips the field of view will be 7°×7°, although the usable field of view will be constrained by the current flat-field optics to a diameter of $\sim$ 5°. Given the larger field of view and the smaller pixels, the field selection strategy of choosing fields in the Galactic latitude range $15° < |b| < 45°$ may not be ideal. Additionally, with better sampled pixels, the three methods of extracting high precision photometry (aperture photometry, PSF-fitting and image subtraction, described below) should be reassessed to determine which will produce the best results.

- The quantum efficiency of the new camera will be twice that of the old camera, and the read-out time will be considerably shorter. This could be exploited in several ways: either the time-sampling on a single field could be improved, or two fields could be alternately observed in pairs. Although the latter method was rejected when the observing strategy was updated in this work, this was due to the presence of systematics. With improved time-sampling and the expected success of SYSREM, it may be worthwhile to return to the practice of observing pairs of fields.

- One disadvantage of the new camera is that it will be affected by fringing due to atmospheric emission lines. This might reduce the photometric accuracy in the I-band. However, a new rapid filter changer will be installed with the new camera, including the Johnson VRI filters and a set of Sloan $griz$ filters. Changing filters will take on the order of a few seconds, and the new observing strategy will have to be designed to exploit this capability. Tingley (2004) shows that by observing transits in two filters, transits due to planets and transits due to grazing or blended eclipsing binaries can be differentiated to some extent, reducing the rate of false positives. Whether this additional information is worth the sacrifice in time-sampling in a single filter needs to be assessed. Alternatively, at the start of each observing run on a new field, master frames in a selection of filters could be generated to characterise the colours of the target stars.

8-2.3 Image subtraction

A third technique for extracting high precision photometry that was not considered in this work is image subtraction. This method is being used increasingly for long photometric surveys and was recently shown to significantly out-perform both aperture photometry and PSF-fitting for a wide range of spatial resolutions (Montalto et al. 2007).

In this method, a reference image is typically created from an aligned stack of the best seeing images. The kernel that convolves the PSF of the reference image to the PSF of each individual image is then modeled using a simple least-squares fit to the pixels in both images, and the convolved reference image is then subtracted from the individual images. Aperture photometry can then be performed on the subtracted image, which has had the majority of the signal removed. The only flux that remains is from the variable objects in the frame which are relatively brighter or fainter with respect to the rest of the stars than they were in the reference frame.

Image subtraction can be used for lower spatial resolution data than PSF-fitting since it does not assume or require a well-defined functional form for the PSF, modeling the kernel anew for each image. It can also be used for extremely crowded fields such as globular clusters (Corwin et al. 2006) due to the fact that the stars that are not variable are largely erased in the subtracted images.

Due to the success of this method, we will be testing image subtraction on the data from the new camera using the ISIS2.2 package (Alard & Lupton 1998), and comparing the results to those of the existing aperture photometry pipeline. We anticipate increasing the precision of our data and additionally, to potentially be able to probe more crowded fields, increasing the number of target stars.

8-2.4 Follow up observations

The current process for obtaining follow up observations was noted to be relatively inefficient, in terms of the amount of time required to be allocated in order to ensure a conclusive result. A much more effective proposition would be if targeted blocks of time of several hours were allocated for each candidate in amongst other observations. An opportunity has arisen through a collaboration with Marton Hidas at the Las Cumbres Observatory Global Telescope network for access to the Faulkes Telescope South (FTS) for our follow up observations.

The FTS is a 2.0-m optical imaging telescope located at Siding Spring Observatory, Australia. The current CCD camera is not ideal for obtaining high precision time series photometry: the field of view is only $4.6' \times 4.6'$, meaning there are very few, if any, comparison stars to confirm the photometry; and the camera suffers from a significant residual charge problem, which degrades the achievable precision. However, a new CCD camera is scheduled to be installed in 2008 February with a $10.5' \times 10.5'$ which should be sufficient for useful follow up observations.

Observations on the FTS are automated and scheduled in advance. By supplying the ephemerides and a ranking of our transit candidates, they would be added to the schedule and observed at the appropriate times. This would be a significant reduction in both telescope and personnel time, and a dramatic improvement in the lag time between initial identification of candidates and acquiring follow up observations.

Appendix A

Variable star catalogue cross-identification

The positions of the stars in this catalogue were correlated with the General Catalog of Variable Stars (GCVS) and All Sky Automated Survey (ASAS) variable star catalogues, using the *Vizier* online database (Ochsenbein et al. 2000). The photometry aperture used in our data reduction pipeline has a radius of $28.2''$, and so a simple cone search with a radius of $30''$ was performed. The results of the correlation are shown in Table A.1. 191 of the 850 stars presented in this catalogue are positionally coincident with previously published variable stars. The columns in the table are the UNSW identifier from this catalogue, the right ascension and declination (J2000.0), the mean I-band magnitude, I-band amplitude of variation, period, epoch, the identifier from either the GCVS, NSV or ASAS catalogues, and our classification, which was found to be in good agreement with the published classification in more than 90% of the cases with a few exceptions, like V717 Ara (EB), which is listed as an RR Lyr in the GCVS or V500 Ara (EW), also RR Lyr in the GCVS. However, these are the classes with highly sinusoidal, i.e. indistinguishable light curve shapes, and it is therefore not surprising that single-filtered light curves are not enough in doubtful cases.

The positions were also correlated with x-ray sources in the ROSAT 1RXS

(Voges et al. 1999, 2000) and 2RXP (ROSAT 2000) catalogues, similarly to Norton et al. (2007). The search was again performed through *Vizier* using a 30″ cone search, and the results are shown in Table A.2. The columns are as for Table A.1, although in this case the second identifier column contains the ROSAT source identifier. 22 of the 850 stars were found to be spatially coincident with ROSAT sources, although we note that since the majority have been classified as pulsating variables, which are not expected to be strong X-ray sources (Makarov 2003), it is doubtful how much of the coincidence is real.

Table A.1. UNSW variable stars coincident with GCVS/ASAS records.

ID	RA (J2000.0)	Dec (J2000.0)	I (mag)	A (mag)	Period (d)	Epoch HJD-2450000.0	Alternate ID	Type
UNSW-V-002	04 53 38.1	−29 06 38.0	11.23	0.200	0.38555	3289.1020	ASAS 045338-2906.6	EW
UNSW-V-007	04 58 03.5	−29 55 59.1	10.21	0.128	3.06827	3324.2200	ASAS 045804-2956.0	EA
UNSW-V-011	05 00 55.6	−30 07 54.1	12.06	0.127	0.84183	3291.1200	ASAS 050056-3007.9	EW
UNSW-V-013	05 02 46.6	−29 44 04.2	8.41	0.026	-	-	ASAS 050247-2944.1	LPV
UNSW-V-016	04 51 51.6	−29 34 22.4	11.65	0.209	0.38150	3289.3880	ASAS 045151-2934.3	EW
UNSW-V-018	04 42 00.0	−25 28 45.5	13.52	0.134	0.58747	3289.1000	ASAS 044200-2528.8	RRL
UNSW-V-019	04 42 16.3	−25 49 32.1	11.46	0.220	0.25489	3285.3350	ASAS 044216-2549.5	EW
UNSW-V-021	04 42 25.4	−26 17 31.3	11.52	0.087	0.45552	3285.2000	ASAS 044225-2617.5	EW
UNSW-V-026	04 48 00.9	−25 31 23.1	12.23	0.200	0.54883	3285.1700	ASAS 044801-2531.4	RRL
UNSW-V-035	09 03 32.6	−14 52 45.5	11.12	0.070	0.29358	3376.9850	ASAS 090333-1452.8	EW
UNSW-V-043	09 05 55.6	−14 51 23.4	10.90	0.069	0.56636	3377.1500	ASAS 090556-1451.4	EW
UNSW-V-046	09 07 07.5	−14 07 37.7	9.84	0.041	-	-	ASAS 090708-1407.7	LPV
UNSW-V-050	09 08 20.6	−13 35 43.2	11.14	0.068	15.44279	3389.0400	ASAS 090821-1335.8	EA
UNSW-V-055	08 59 54.2	−15 15 22.9	11.57	0.186	0.39362	3371.1350	ASAS 085954-1515.4	EW
UNSW-V-057	09 22 21.2	−13 38 50.4	12.50	0.188	0.53220	3377.9800	IV HYA/ASAS 092220-1338.8	RRL
UNSW-V-061	09 23 55.7	−14 20 22.1	8.65	0.026	35.06803	3393.0000	ASAS 092356-1420.4	LPV
UNSW-V-062	09 24 55.9	−13 11 58.2	12.92	0.180	0.61124	3382.1500	ASAS 092456-1312.0	RRL
UNSW-V-066	09 26 41.0	−13 45 06.5	9.66	0.239	0.44976	3377.2500	EZ HYA/ASAS 092641-1345.1	EW
UNSW-V-070	09 28 20.1	−12 50 51.2	11.70	0.248	0.50182	3377.0970	ASAS 092820-1250.9	EB
UNSW-V-071	09 28 28.7	−13 26 33.2	11.68	0.205	0.73146	3378.4340	ASAS 092829-1326.5	EB
UNSW-V-074	09 28 57.5	−13 07 12.4	8.16	0.029	45.49365	3402.0000	ASAS 092857-1307.2	LPV
UNSW-V-075	09 29 15.3	−14 05 57.2	12.27	0.263	0.33259	3377.2450	ASAS 092915-1405.9	EW
UNSW-V-081	09 20 17.4	−14 05 09.7	8.61	0.099	-	-	ASAS 092018-1405.1	LPV
UNSW-V-084	11 55 44.0	−36 26 19.8	11.78	0.134	0.53132	3415.1900	ASAS 115544-3626.3	EW
UNSW-V-086	11 56 12.9	−35 59 29.9	11.50	0.266	0.37801	3415.1180	V0576 CEN/ASAS 115613-3559.5	EW
UNSW-V-087	11 56 20.4	−35 28 45.5	11.39	0.141	0.29374	3415.3250	ASAS 115620-3528.8	EW

ID	RA (J2000.0)	Dec (J2000.0)	I (mag)	A (mag)	Period (d)	Epoch HJD-2450000.0	Alternate ID	Type
UNSW-V-090	11 56 40.6	−35 43 43.8	12.53	0.102	1.18713	3415.1300	V577 CEN	EA
UNSW-V-091	11 57 20.2	−36 40 23.3	13.52	0.133	0.58688	3422.9900	V0580 CEN	RRL
UNSW-V-092	11 57 57.2	−36 06 10.3	13.41	0.266	0.34622	3415.1670	V0581 CEN	EW
UNSW-V-097	11 59 53.9	−36 13 26.1	12.18	0.057	0.90251	3422.1700	NSV 05410	EA
UNSW-V-101	12 00 49.6	−36 11 59.2	14.26	0.170	0.62644	3423.0900	V0582 CEN	RRL
UNSW-V-105	12 02 27.6	−35 26 39.3	14.04	0.143	0.67441	3423.0800	EF HYA	RRL
UNSW-V-107	12 03 06.8	−35 37 47.5	12.40	0.078	6.23034	3415.0100	NSV 05437	EA
UNSW-V-115	11 53 52.2	−35 26 55.4	13.57	0.084	0.58367	3415.1200	DS HYA	RRL
UNSW-V-116	11 54 06.9	−35 14 54.8	11.22	0.082	3.30294	3423.1900	ASAS 115407-3514.9	EA
UNSW-V-122	11 56 27.7	−38 08 51.3	8.85	0.077	84.16663	-	ASAS 115628-3808.9	LPV
UNSW-V-131	12 01 25.6	−37 24 52.6	8.35	0.583	135.44203	-	V0583 CEN/ASAS 120125-3724.9	LPV
UNSW-V-132	12 02 19.3	−38 46 22.3	12.86	0.264	0.45906	3415.0900	V0584 CEN/ASAS 120219-3846.4	RRL
UNSW-V-137	12 06 53.6	−37 37 36.0	12.51	0.157	0.39816	3415.3260	ASAS 120654-3737.7	EW
UNSW-V-138	11 53 40.7	−38 22 00.5	10.55	0.063	0.82146	3423.5700	ASAS 115341-3822.1	EW
UNSW-V-140	16 56 35.0	−59 04 41.2	10.44	0.580	184.16278	-	CG ARA	LPV
UNSW-V-143	16 57 00.6	−60 29 51.9	12.17	0.020	0.81166	3510.1600	V0805 ARA	EA
UNSW-V-144	16 57 15.2	−60 08 05.3	12.71	0.224	0.92708	3499.5400	V0705 ARA	EW
UNSW-V-145	16 57 50.6	−59 07 20.0	12.60	0.187	0.57442	3509.1100	V0414 ARA	RRL
UNSW-V-147	16 57 43.8	−60 41 16.4	9.33	0.086	1.20159	3499.8030	ASAS 165744-6041.3	EW
UNSW-V-154	16 59 07.2	−60 05 25.4	8.55	0.903	174.95479	-	LS ARA/ASAS 165907-6005.4	LPV
UNSW-V-171	17 02 35.4	−59 30 48.7	9.84	0.302	118.49562	-	V0810 ARA	LPV
UNSW-V-178	16 54 36.1	−60 09 04.8	10.68	0.375	-	-	V0696 ARA	LPV
UNSW-V-184	17 05 59.3	−59 40 34.1	12.63	0.033	0.51838	3499.1100	V0464 ARA	RRL
UNSW-V-186	17 06 48.2	−59 03 20.0	8.68	0.864	152.13318	-	CH ARA/ASAS 170648-5903.3	LPV
UNSW-V-187	17 07 32.4	−60 58 45.6	11.47	0.117	2.32845	3504.1400	ASAS 170732-6058.8	EA
UNSW-V-194	17 09 43.0	−60 31 14.9	12.27	0.170	0.35894	3499.2330	ASAS 170944-6031.2	EW

ID	RA (J2000.0)	Dec (J2000.0)	I (mag)	A (mag)	Period (d)	Epoch HJD-2450000.0	Alternate ID	Type
UNSW-V-195	17 10 07.8	−60 39 45.7	10.51	0.134	2.52195	3499.2000	V0617 ARA/ASAS 171008-6039.8	CEP
UNSW-V-198	17 10 18.2	−59 46 08.9	13.20	0.072	1.22754	3555.2400	V0485 ARA	EA
UNSW-V-199	17 11 16.1	−60 20 42.8	8.69	0.637	184.16278	-	CN ARA	LPV
UNSW-V-200	17 11 32.5	−60 14 35.9	9.46	0.273	152.13318	-	NSV 08245	LPV
UNSW-V-203	17 12 35.0	−60 29 32.1	11.99	0.045	0.49332	3504.2800	CS ARA	RRL
UNSW-V-207	17 13 52.6	−59 05 16.1	9.56	0.137	75.56063	-	V0733 ARA/ASAS 171352-5905.2	LPV
UNSW-V-214	17 15 58.6	−60 04 06.2	11.25	0.129	0.40006	3499.1600	ASAS 171559-6004.1	EW
UNSW-V-215	17 16 19.3	−59 55 07.2	12.77	0.072	0.77541	3504.2500	DG ARA	RRL
UNSW-V-217	17 16 35.5	−60 21 01.4	11.65	0.204	0.36364	3499.1060	V0791 ARA/ASAS 171636-6021.1	EW
UNSW-V-218	17 17 40.0	−60 31 19.1	11.77	0.066	0.59981	3499.1400	MT ARA	EB
UNSW-V-229	17 01 00.5	−58 35 18.1	12.12	0.066	1.28635	3504.2500	V717 ARA	EW
UNSW-V-231	17 01 23.8	−58 16 46.1	12.90	0.036	0.58292	3504.1000	V0441 ARA	RRL
UNSW-V-232	17 01 33.8	−58 18 35.1	13.47	0.047	2.04759	3558.1000	V0442 ARA	EA
UNSW-V-233	17 01 49.3	−57 59 33.5	10.25	0.712	166.85367	-	V0779 ARA	LPV
UNSW-V-238	17 02 59.7	−57 06 42.8	9.49	0.080	0.98892	3510.2800	V0722 ARA	EA
UNSW-V-248	16 57 56.7	−57 52 46.4	10.94	0.471	-	-	V0776 ARA	LPV
UNSW-V-252	17 06 37.5	−58 07 40.2	11.02	0.124	0.89702	3504.2500	ASAS 170637-5807.7	EW
UNSW-V-254	17 06 33.9	−57 42 51.4	8.71	0.163	129.34859	-	NSV 08172/ASAS 170634-5742.9	LPV
UNSW-V-255	17 06 46.4	−58 31 15.2	12.05	1.066	175.19339	-	V0780 ARA	LPV
UNSW-V-259	16 58 20.3	−57 19 38.9	11.20	0.031	0.11082	3504.2200	V0709 ARA	PULS
UNSW-V-262	17 09 25.7	−57 44 43.4	12.60	0.099	0.66760	3504.5700	V0817 ARA	EB
UNSW-V-264	17 09 44.2	−57 53 42.2	11.57	0.075	0.45536	3504.0700	ASAS 170944-5753.7	EW
UNSW-V-265	17 09 55.7	−58 43 14.5	12.32	0.014	0.90689	3504.2800	V0783 ARA	EA
UNSW-V-267	17 10 00.8	−58 10 08.9	11.82	0.154	0.41460	3504.0800	CL ARA/ASAS 171000-5810.2	EW
UNSW-V-268	17 10 01.4	−57 58 26.0	9.87	0.017	8.56234	3581.5000	ASAS 171002-5758.4	EA
UNSW-V-269	17 10 15.8	−57 26 47.2	10.05	0.087	58.40231	-	V0731 ARA/ASAS 171016-5726.7	LPV

ID	RA (J2000.0)	Dec (J2000.0)	I (mag)	A (mag)	Period (d)	Epoch HJD-2450000.0	Alternate ID	Type
UNSW-V-271	17 11 13.0	−57 14 03.1	13.04	0.230	0.96374	3504.1900	V0785 ARA	EB
UNSW-V-274	17 11 24.2	−57 00 47.6	12.30	0.129	0.49237	3503.9700	V0492 ARA	EW
UNSW-V-277	17 11 58.9	−57 36 53.2	10.39	0.918	166.85367	-	V0493 ARA/ASAS 171200-5737.2	LPV
UNSW-V-278	17 12 09.1	−58 34 15.1	10.66	0.543	166.85367	-	CQ ARA/ASAS 171209-5834.2	LPV
UNSW-V-280	17 12 34.4	−57 24 11.1	11.23	0.823	122.58292	-	CT ARA	LPV
UNSW-V-285	17 13 33.5	−57 55 15.3	10.57	0.389	119.22419	-	V0732 ARA/ASAS 171334-5755.2	LPV
UNSW-V-287	17 14 24.3	−58 46 39.6	10.39	0.918	140.15567	-	V0498 ARA	LPV
UNSW-V-289	17 14 28.1	−57 26 15.9	12.97	0.177	0.39302	3504.2300	V0500 ARA	EW
UNSW-V-295	17 15 33.2	−57 05 15.1	10.46	1.149	175.19339	-	DE ARA	LPV
UNSW-V-301	17 16 37.3	−58 09 40.4	11.04	0.032	1.48306	3531.2800	ASAS 171638-5809.7	EA
UNSW-V-307	17 18 45.7	−57 46 29.7	11.17	0.208	0.79384	3510.2070	NSV 08452/ASAS 171846-5746.5	EB
UNSW-V-308	17 18 45.1	−57 26 20.8	8.03	0.045	1.80572	3499.6000	V0858 ARA	PUL
UNSW-V-310	23 57 02.7	−58 26 01.3	13.42	0.223	0.68809	3582.2300	ASAS 235702-5826.0	RRL
UNSW-V-317	00 04 15.9	−58 15 53.5	9.11	0.060	143.47872	-	ASAS 000416-5815.9	LPV
UNSW-V-327	00 01 47.5	−57 14 30.4	10.09	0.082	0.47036	3579.1760	ASAS 000147-5714.5	EW
UNSW-V-329	00 02 29.3	−56 53 49.9	8.79	0.042	13.21167	3591.5000	ASAS 000229-5653.9	CEP
UNSW-V-336	23 51 57.4	−57 25 20.8	10.01	0.088	0.39260	3577.1370	ASAS 235157-5725.4	EW
UNSW-V-337	23 54 23.7	−57 56 27.6	10.40	0.199	0.58423	3577.5100	ASAS 235424-5756.5	EW
UNSW-V-352	04 13 38.9	−24 33 32.5	12.05	0.066	-	-	ASAS 041339-2433.5	EW
UNSW-V-367	09 18 55.4	−25 16 44.1	9.14	0.398	59.06429	-	Z PYX/ASAS 091855-2516.7	LPV
UNSW-V-369	09 19 41.8	−24 18 38.5	9.96	0.081	36.01291	-	ASAS 091942-2418.6	LPV
UNSW-V-370	09 20 00.7	−23 38 42.9	8.51	0.034	52.60413	-	ASAS 092000-2338.7	LPV
UNSW-V-377	09 22 37.7	−25 27 06.4	12.18	0.212	0.48368	3740.2300	SS PYX/ASAS 092238-2527.1 1	EW
UNSW-V-384	09 24 25.5	−24 05 03.4	11.45	0.076	0.51693	3742.0900	ASAS 092425-2405.1	RRL
UNSW-V-390	09 25 51.5	−24 00 39.4	7.98	0.242	59.06429	-	LP HYA	LPV

ID	RA (J2000.0)	Dec (J2000.0)	I (mag)	A (mag)	Period (d)	Epoch HJD-2450000.0	Alternate ID	Type
UNSW-V-396	09 10 29.0	−22 44 34.4	8.71	0.025	35.67026	-	ASAS 091029-2244.6	LPV
UNSW-V-400	09 11 03.1	−23 27 16.3	11.69	0.168	0.62330	3743.0300	ASAS 091103-2327.3	EW
UNSW-V-421	09 17 26.3	−22 48 10.7	9.03	0.120	59.06429	-	ASAS 091726-2248.2	LPV
UNSW-V-450	12 54 31.3	−46 07 36.5	8.68	0.014	1.04272	3805.1500	NSV 06020	CEP
UNSW-V-461	12 47 23.7	−45 35 03.3	9.26	0.075	-	-	ASAS 124724-4535.1	LPV
UNSW-V-473	13 08 47.6	−45 56 58.3	8.35	0.084	67.33070	-	ASAS 130848-4557.3	LPV
UNSW-V-477	13 10 17.1	−44 25 59.7	8.08	0.025	48.60485	-	ASAS 131017-4426.2	LPV
UNSW-V-480	13 10 31.5	−45 19 31.4	9.30	0.085	49.98603	-	NSV 06118	LPV
UNSW-V-494	13 13 20.7	−45 38 13.4	8.21	0.115	48.60485	-	ASAS 131321-4538.5	LPV
UNSW-V-495	13 13 33.0	−44 49 31.8	9.10	1.206	57.39314	-	ASAS 131333-4449.8	LPV
UNSW-V-500	13 10 18.5	−45 08 59.8	11.38	0.031	5.35927	3787.9950	ASAS 131018-4509.2	EA+DSCT
UNSW-V-503	13 15 39.9	−45 51 14.9	12.18	0.151	0.33926	3788.1100	ASAS 131540-4551.5	EW
UNSW-V-508	13 16 49.0	−45 48 47.2	8.82	0.195	0.40969	3788.1050	ASAS 131649-4549.0	EW
UNSW-V-516	13 18 21.8	−44 43 28.1	12.08	0.074	0.30021	3788.0000	ASAS 131823-4443.9	RRL
UNSW-V-520	13 21 15.1	−45 13 21.9	8.36	0.018	29.35691	4000.0000	ASAS 132115-4513.6	LPV
UNSW-V-524	14 43 52.6	−39 54 40.2	10.07	0.265	31.46413	-	V0549 CEN	LPV
UNSW-V-535	14 47 23.2	−39 06 22.6	11.80	0.158	0.31378	3846.9350	ASAS 144723-3906.4	EW
UNSW-V-537	14 48 14.5	−38 18 32.7	8.44	0.795	29.14202	-	V0557 CEN/ASAS 144815-3818.6	LPV
UNSW-V-551	14 52 30.1	−38 24 33.2	10.44	0.082	30.28946	-	ASAS 145230-3824.6	LPV
UNSW-V-556	14 54 44.7	−38 56 47.8	9.81	0.135	31.77751	-	V0566 CEN	LPV
UNSW-V-557	14 42 20.5	−38 40 32.9	12.76	0.103	3.09517	3848.9600	V0544 CEN	EA
UNSW-V-558	14 43 27.3	−41 02 05.7	8.07	0.050	-	-	V0642 CEN	LPV
UNSW-V-562	14 45 49.0	−41 26 12.4	8.51	0.013	-	-	V0551 CEN	LPV
UNSW-V-564	14 46 58.5	−41 17 50.6	12.82	0.083	0.69187	3847.2000	NSV 06795	RRL
UNSW-V-567	14 48 05.4	−41 45 23.6	10.47	0.186	-	-	V0555 CEN/ASAS 144805-4145.4	LPV
UNSW-V-570	14 49 00.4	−41 26 55.0	13.17	0.226	0.62177	3847.1400	V0558 CEN	RRL

ID	RA (J2000.0)	Dec (J2000.0)	I (mag)	A (mag)	Period (d)	Epoch HJD-2450000.0	Alternate ID	Type
UNSW-V-571	14 49 31.6	−40 06 29.1	9.01	0.074	0.79930	3847.1250	ASAS 144932-4006.4	EW
UNSW-V-572	14 49 24.8	−40 04 27.9	9.14	0.042	-	-	V0560 CEN	LPV
UNSW-V-574	14 50 28.2	−40 56 15.0	11.99	0.208	0.47623	3847.1100	ASAS 145028-4056.3	EW
UNSW-V-577	14 52 42.1	−41 41 55.3	9.60	0.032	0.87351	3847.0400	ASAS 145242-4141.9	RRL
UNSW-V-583	14 42 34.7	−40 27 17.4	10.00	0.184	0.32503	3846.9750	V0677 CEN/ASAS 144235-4027.2	EW
UNSW-V-584	14 42 55.3	−41 18 47.4	9.70	0.088	-	-	V0545 CEN	LPV
UNSW-V-591	18 18 43.6	−64 37 59.6	9.55	0.043	-	-	ASAS 181843-6437.9	LPV
UNSW-V-592	18 19 04.5	−65 35 35.3	9.18	0.473	-	-	DF PAV/ASAS 181904-6535.6	LPV
UNSW-V-595	18 20 32.2	−64 17 23.7	8.51	0.033	-	-	ASAS 182031-6417.3	LPV
UNSW-V-599	18 21 32.3	−64 15 58.1	8.59	0.416	-	-	NSV 10616	LPV
UNSW-V-601	18 22 36.6	−65 30 18.4	9.63	0.076	-	-	ASAS 182236-6530.3	LPV
UNSW-V-603	18 24 38.7	−65 11 02.0	10.49	0.059	2.41936	3879.1400	ASAS 182438-6511.0	EA
UNSW-V-606	18 26 23.7	−64 57 45.9	12.68	0.072	2.49162	3872.8300	DP PAV	EA
UNSW-V-607	18 29 37.0	−64 54 43.1	7.39	1.814	-	-	NSV 10827/ASAS 182937-6454.7	LPV
UNSW-V-609	18 13 35.1	−65 14 13.1	10.86	0.463	-	-	NW PAV/ASAS 181335-6514.2	CEP
UNSW-V-610	18 30 35.7	−64 51 33.7	8.69	0.031	-	-	ASAS 183034-6451.5	LPV
UNSW-V-614	18 34 41.2	−65 27 08.1	11.74	0.291	0.47690	3874.1000	BH PAV/ASAS 183441-6527.0	RRL
UNSW-V-615	18 35 24.0	−64 57 04.4	9.24	0.300	-	-	ASAS 183523-6457.0	LPV
UNSW-V-623	18 18 32.0	−67 19 48.5	9.21	0.078	-	-	ASAS 181833-6719.9	LPV
UNSW-V-627	18 21 15.4	−66 38 47.7	11.42	0.078	2.32625	3879.1100	ASAS 182117-6638.8	EA
UNSW-V-633	18 25 26.2	−67 34 42.4	10.90	0.231	0.42713	3866.2150	ASAS 182528-6734.8	EW
UNSW-V-639	18 30 46.4	−67 08 15.2	12.43	0.293	1.85125	3886.2200	NSV 10858	EA
UNSW-V-641	18 33 32.9	−66 54 00.5	9.35	0.011	1.92981	3867.2800	ASAS 183333-6654.0	PUL
UNSW-V-643	18 34 13.5	−66 07 10.0	11.98	0.340	-	-	ASAS 183414-6607.2	LPV
UNSW-V-645	18 35 38.8	−66 55 52.6	8.94	0.032	0.84381	3866.2300	ASAS 183540-6656.0	EB
UNSW-V-646	18 36 25.9	−67 56 03.1	8.52	1.293	-	-	DG PAV/ASAS 183627-6756.0	LPV

ID	RA (J2000.0)	Dec (J2000.0)	I (mag)	A (mag)	Period (d)	Epoch HJD-2450000.0	Alternate ID	Type
UNSW-V-656	21 04 47.3	−66 46 16.6	10.02	0.032	0.42922	3937.2050	ASAS 210447-6646.3	EW
UNSW-V-658	21 06 49.1	−66 33 51.0	11.00	0.119	3.02652	3937.8800	ASAS 210649-6633.8	EA
UNSW-V-665	21 11 35.9	−66 12 49.8	12.46	0.152	0.37251	3937.1700	ASAS 211136-6612.8	EW
UNSW-V-672	21 17 04.8	−67 01 47.3	8.97	0.129	45.25221	-	ASAS 211705-6701.8	LPV
UNSW-V-674	21 18 53.4	−67 16 14.8	8.48	0.051	41.88170	-	ASAS 211855-6716.2	LPV
UNSW-V-675	21 20 21.8	−65 46 45.6	13.57	0.148	0.46078	3937.0900	NSV 13650	RRL
UNSW-V-677	21 20 51.0	−65 50 15.5	8.84	0.033	32.99997	3046.0000	ASAS 212051-6550.3	LPV
UNSW-V-690	21 02 58.2	−68 45 12.8	10.66	0.166	0.51007	3937.3190	ASAS 210258-6845.2	EW
UNSW-V-695	21 06 59.9	−68 21 03.5	8.88	0.052	-	-	ASAS 210700-6821.0	LPV
UNSW-V-714	23 48 48.7	−69 46 53.4	11.32	0.101	0.39326	3991.2520	ASAS 234849-6946.9	EW
UNSW-V-716	23 30 40.7	−69 53 33.5	10.68	0.097	0.63150	3991.1660	ASAS 233041-6953.5	EW
UNSW-V-719	23 33 56.1	−69 11 14.1	11.20	0.101	0.95375	3990.9800	ASAS 233356-6911.2	EW
UNSW-V-723	07 55 30.6	−66 59 44.7	11.03	0.114	1.10830	4086.7700	ASAS 075530-6659.7	EW
UNSW-V-724	07 55 14.7	−68 08 11.9	10.85	0.196	97.58038	-	ASAS 075514-6808.2	LPV
UNSW-V-726	07 57 00.3	−66 35 51.3	9.32	0.052	1.29478	4087.1300	ASAS 075700-6635.8	EB
UNSW-V-733	08 00 55.4	−66 41 11.1	9.96	0.023	46.64445	-	ASAS 080055-6641.2	LPV
UNSW-V-735	08 01 35.6	−68 19 36.3	8.14	0.097	66.31470	-	ASAS 080135-6819.6	LPV
UNSW-V-736	08 01 59.7	−68 17 39.5	9.14	0.198	94.34667	-	ASAS 080200-6817.7	LPV
UNSW-V-739	08 04 10.3	−67 54 56.5	11.53	0.161	0.41287	4085.9850	ASAS 080410-6755.0	EW
UNSW-V-741	08 04 53.8	−66 48 49.3	11.19	0.102	0.48046	4086.0050	ASAS 080454-6648.8	EW
UNSW-V-745	08 07 15.2	−67 12 17.1	9.21	0.027	28.64224	4110.0000	ASAS 080715-6712.3	LPV
UNSW-V-755	08 12 59.1	−67 14 44.3	11.61	0.124	0.34062	4085.9850	ASAS 081259-6714.7	EW
UNSW-V-756	08 14 09.5	−68 02 13.0	11.31	0.088	0.41789	4086.1350	ASAS 081409-6802.2	EW
UNSW-V-758	08 16 09.3	−66 44 46.3	11.94	0.139	0.38501	4086.1000	ASAS 081610-6644.8	RRL
UNSW-V-761	07 52 35.7	−67 15 11.1	8.22	0.067	1.01055	-	ASAS 075236-6715.2	LPV

ID	RA (J2000.0)	Dec (J2000.0)	I (mag)	A (mag)	Period (d)	Epoch HJD-2450000.0	Alternate ID	Type
UNSW-V-768	14 36 15.8	−69 51 10.3	12.34	0.165	-	-	XZ CIR	LPV
UNSW-V-770	14 39 01.4	−69 22 43.2	11.15	0.168	-	-	NSV 06732	LPV
UNSW-V-801	14 47 44.1	−68 54 05.6	9.57	0.072	7.24716	4175.8000	ASAS 144744-6854.1	CEP
UNSW-V-806	14 49 45.1	−69 35 31.7	9.16	0.080	-	-	ASAS 144945-6935.6	LPV
UNSW-V-807	14 49 56.5	−69 20 50.8	11.93	0.521	-	-	BL CIR	LPV
UNSW-V-824	14 56 41.9	−68 34 47.9	10.92	0.129	1.05497	4170.2500	ASAS 145643-6834.8	EA
UNSW-V-825	14 57 20.7	−69 45 02.2	10.45	0.473	-	-	ASAS 145720-6945.0	LPV
UNSW-V-826	14 56 33.0	−68 08 35.2	9.47	0.212	2.13147	4173.1100	EM TRA/ASAS 145633-6808.6	EA
UNSW-V-842	15 02 19.0	−68 16 01.1	11.67	0.027	1.78869	4184.2700	NSV 06882	EA
UNSW-V-844	15 03 08.6	−69 50 58.3	11.29	0.192	0.36855	4170.0500	ASAS 150308-6950.9	EW
UNSW-V-847	15 05 11.1	−68 45 56.7	11.01	0.154	0.33718	4170.1500	ASAS 150511-6845.9	EW

Table A.2. UNSW variable stars coincident with ROSAT x-ray sources.

ID	RA (J2000.0)	Dec (J2000.0)	I (mag)	A (mag)	Period (d)	Epoch HJD-2450000.0	ROSAT ID	Type
UNSW-V-005	04 57 28.8	−29 09 48.3	8.75	0.005	3.26837	3289.1200	1RXS J045728.9-290953	EB
UNSW-V-040	09 05 22.3	−15 03 42.9	9.60	0.007	0.62883	3377.0800	1RXS J090522.2-150302	PUL
UNSW-V-362	09 16 44.1	−24 47 42.9	9.56	0.012	2.59901	3744.1000	1RXS J091644.7-244735	CEP
UNSW-V-450	12 54 31.3	−46 07 36.5	8.68	0.014	1.04272	3805.1500	1RXS J125430.7-460735	CEP
UNSW-V-468	12 47 55.7	−44 57 34.1	8.94	0.059	-	-	1RXS J124757.9-445735	PUL
UNSW-V-470	12 48 07.6	−44 39 17.5	8.59	0.053	1.04962	3788.7300	1RXS J124807.6-443913	CEP
UNSW-V-493	13 13 07.4	−45 37 30.3	9.56	0.013	6.85120	3791.4000	1RXS J131306.7-453740	CEP
UNSW-V-494	13 13 20.7	−45 38 13.4	8.21	0.115	48.60485	0.0000	1RXS J131306.7-453740	LPV
UNSW-V-506	13 16 38.9	−45 46 56.0	8.88	0.003	0.08857	3788.0200	1RXS J131651.3-454905	PUL
UNSW-V-508	13 16 49.0	−45 48 47.2	8.82	0.195	0.40969	3788.1050	1RXS J131651.3-454905	EW
UNSW-V-510	13 17 24.2	−45 28 17.4	9.84	0.070	72.84351	0.0000	1RXS J131717.7-452541	LPV
UNSW-V-514	13 17 46.5	−44 56 39.3	10.19	0.013	0.48342	3788.0700	1RXS J131747.3-445707	PUL
UNSW-V-521	13 22 04.2	−45 03 10.8	9.03	0.022	1.44852	3787.8500	1RXS J132204.7-450312	CEP
UNSW-V-525	14 44 14.2	−39 10 15.9	10.29	0.003	0.09340	3847.0150	1RXS J144357.0-390847	PUL
UNSW-V-538	14 40 47.7	−38 47 05.7	9.21	0.007	0.19950	3847.1700	1RXS J144037.4-384658	PUL
UNSW-V-541	14 49 26.1	−39 50 48.4	9.67	0.012	3.74574	3847.3000	1RXS J144925.7-395042	CEP
UNSW-V-559	14 44 04.4	−40 59 23.9	8.15	0.017	0.50383	3846.9200	1RXS J144405.2-405940	EW
UNSW-V-568	14 48 13.2	−41 03 00.0	9.72	0.015	-	-	1RXS J144812.6-410310	PUL
UNSW-V-577	14 52 42.1	−41 41 55.3	9.60	0.032	0.87351	3847.0400	1RXS J145240.7-414206	RRL
UNSW-V-582	14 42 16.0	−41 00 19.0	9.43	0.020	2.57400	3848.3000	1RXS J144214.5-410026	CEP:
UNSW-V-718	23 32 37.1	−69 54 31.2	8.61	0.018	-	-	1RXS J233239.5-695432	PUL
UNSW-V-760	07 51 49.4	−68 14 04.3	10.70	0.026	0.19789	4086.0500	2RXP J075145.0-681416	PUL

References

Adams E. R., Seager S., Elkins-Tanton L., 2007, astro-ph/0710.4941

Adams F. C., Laughlin G., 2006, ApJ, 649, 992

Agol E., Steffen J., Sari R., Clarkson W., 2005, MNRAS, 359, 567

Aigrain S., Barge P., Deleuil M., Fressin F., Moutou C., Queloz D., Auvergne M., Baglin A., the CoRoT Exoplanet Science Team 2007, astro-ph/0702062

Aigrain S., Hodgkin S., Irwin J., Hebb L., Irwin M., Favata F., Moraux E., Pont F., 2007b, MNRAS, 375, 29

Aigrain S., Irwin M., 2004, MNRAS, 350, 331

Alard C., Lupton R. H., 1998, ApJ, 503, 325

Albrecht S., Reffert S., Snellen I., Quirrenbach A., Mitchell D. S., 2007, A&A, 474, 565

Alonso R., Brown T. M., Torres G., Latham D. W., Sozzetti A., Mandushev G., Belmonte J. A., Charbonneau D., Deeg H. J., Dunham E. W., O'Donovan F. T., Stefanik R. P., 2004, ApJ, 613, L153

Arbutina B., 2007, MNRAS, 377, 1635

Ashley M. C. B., Burton M. G., Lawrence J. S., Storey J. W. V., 2004, Astron. Nachr., 325, 619

Ashley M. C. B., Burton M. G., Storey J. W. V., Lloyd J. P., Bally J., Briggs J., Harper D. A., 1996, Publ. Astron. Soc. Pac., 108, 721

Bakos G., Noyes R. W., Kovács G., Stanek K. Z., Sasselov D. D., Domsa I., 2004, Publ. Astron. Soc. Pac., 116, 266

Barnes J. W., Fortney J. J., 2004, ApJ, 616, 1193

Bean J. L., McArthur B. E., Benedict G. F., Harrison T. E., Bizyaev D., Nelan E., Smith V. V., 2007, AJ, 134, 749

Beaulieu J.-P., Bennett D. P., Fouqué P., Williams A., Dominik M., Jorgensen U. G., Kubas D., Cassan A., Coutures C., Greenhill J., Hill K., Menzies J., Sackett P. D., Albrow M., et al. 2006, Nat, 439, 437

Beichman C., Lawson P., Lay O., Ahmed A., Unwin S., Johnston K., 2006, in Advances in Stellar Interferometry. Edited by Monnier, John D., Schöller, Markus, Danchi, William C., Proceedings of the SPIE, Volume 6268, pp. 62680S.

Benedict G. F., McArthur B. E., Forveille T., Delfosse X., Nelan E., Butler R. P., Spiesman W., Marcy G., Goldman B., Perrier C., Jefferys W. H., Mayor M., 2002, ApJ, 581, L115

Bennett D. P., Rhie S. H., 1996, ApJ, 472, 660

Bessell M. S., Brett J. M., 1988, Publ. Astron. Soc. Pac., 100, 1134

Biller B. A., Kasper M., Close L. M., Brandner W., Kellner S., 2006, ApJ, 641, L141

Bond I. A., Udalski A., Jaroszyński M., Rattenbury N. J., Paczyński B., Soszyński I., Wyrzykowski L., Szymański M. K., Kubiak M., Szewczyk O., Żebruń K., Pietrzyński G., et al. 2004, ApJ, 606, L155

Bonfils X., Mayor M., Delfosse X., Forveille T., Gillon M., Perrier C., Udry S., Bouchy F., Lovis C., Pepe F., Queloz D., Santos N. C., Bertaux J.-L., 2007, A&A, 474, 293

Borucki W. J., Caldwell D., Koch D. G., Webster L. D., Jenkins J. M., Ninkov Z., Showen R., 2001, Publ. Astron. Soc. Pac., 113, 439

Borucki W. J., Dunham E., Koch D., Cullers D. K., Jenkins J., Reitsema H., 1995, in Butler B. J., Muhleman D. O., eds, Bulletin of the American Astronomical Society Vol. 27, Bulletin of the American Astronomical Society. p. 1382

Borucki W. J., Summers A. L., 1984, Icarus, 58, 121

Boss A. P., Butler R. P., Hubbard W. B., Ianna P. A., Kürster M., Lissauer J. J., Mayor M., Meech K. J., Mignard F., Penny A. J., Quirrenbach A., Tarter J. C., Vidal-Madjar A., 2007, Transactions of the International Astronomical Union, Series A, 26, 183

Bouchy F., Pont F., Santos N. C., Melo C., Mayor M., Queloz D., Udry S., 2004, A&A, 421, L13

Bower G. C., Bolatto A., Ford E., Kalas P., Ulvestad J., 2007, astro-ph/0704.0238, 704

Breger M., Stich J., Garrido R., Martin B., Jiang S. Y., Li Z. P., Hube D. P., Ostermann W., Paparo M., Scheck M., 1993, A&A, 271, 482

Brown T. M., 2003, ApJ, 593, L125

Brown T. M., Charbonneau D., Gilliland R. L., Noyes R. W., Burrows A., 2001, ApJ, 552, 699

Bryden G., Beichman C. A., Rieke G. H., Stansberry J. A., Stapelfeldt K. R., Trilling D. E., Turner N. J., Wolszczan A., 2006, ApJ, 646, 1038

Burrows A., Hubeny I., Budaj J., Hubbard W. B., 2007, ApJ, 661, 502

Burton M., Aitken D. K., Allen D. A., Ashley M. C. B., Burton M. G., Cannon R. D., Carter B. D., Dacosta G. S., Dopita M. A., Duldig M. L., 1994, Proc. Astron. Soc. Austral., 11, 127

Butler R. P., Marcy G. W., Williams E., McCarthy C., Dosanjh P., Vogt S. S., 1996, Publ. Astron. Soc. Pac., 108, 500

Butler R. P., Tinney C. G., Marcy G. W., Jones H. R. A., Penny A. J., Apps K., 2001, ApJ, 555, 410

Butler R. P., Wright J. T., Marcy G. W., Fischer D. A., Vogt S. S., Tinney C. G., Jones H. R. A., Carter B. D., Johnson J. A., McCarthy C., Penny A. J., 2006, ApJ, 646, 505

Carpenter J. M., 2001, AJ, 121, 2851

Carter B. D., Ashley M. C. B., Sun Y.-S., Storey J. W. V., 1992, Proceedings of the Astronomical Society of Australia, 10, 74

Charbonneau D., Allen L. E., Megeath S. T., Torres G., Alonso R., Brown T. M., Gilliland R. L., Latham D. W., Mandushev G., O'Donovan F. T., Sozzetti A., 2005, ApJ, 626, 523

Charbonneau D., Brown T. M., Latham D. W., Mayor M., 2000, ApJ, 529, L45

Charbonneau D., Brown T. M., Noyes R. W., Gilliland R. L., 2002, ApJ, 568, 377

Chatterjee S., Ford E. B., Rasio F. A., 2007, astro-ph/0703166

Chauvin G., Lagrange A.-M., Dumas C., Zuckerman B., Mouillet D., Song I., Beuzit J.-L., Lowrance P., 2004, A&A, 425, L29

Chauvin G., Lagrange A.-M., Zuckerman B., Dumas C., Mouillet D., Song I., Beuzit J.-L., Lowrance P., Bessell M. S., 2005, A&A, 438, L29

Christiansen J. L., Ashley M. C. B., Caldwell D., 2006, Astronomy in Antarctica, 26th meeting of the IAU, Special Session 7, 22-23 August, 2006 in Prague, Czech Republic, SPS7, 27, 7

Christiansen J. L., Derekas A., Ashley M. C. B., Webb J. K., Hidas M. G., Hamacher D. W., Kiss L. L., 2007, MNRAS, 382, 239

Clarke D., 2002, A&A, 386, 763

Collier Cameron A., Bouchy F., Hébrard G., Maxted P., Pollacco D., Pont F., Skillen I., Smalley B., et al. 2007, MNRAS, 375, 951

Collier Cameron A., Wilson D. M., West R. G., Hebb L., Wang X.-B., Aigrain S., Bouchy F., Christian D. J., Clarkson W. I., Enoch B., Esposito M., Guenther E., Haswell C. A., Hébrard G., et al. 2007b, MNRAS, 380, 1230

Corwin T. M., Sumerel A. N., Pritzl B. J., Smith H. A., Catelan M., Sweigart A. V., Stetson P. B., 2006, AJ, 132, 1014

Costes V., Bodin P., Levacher P., Auvergne M., 2004, in Warmbein B., ed., ESA Special Publication Vol. 554, 5th International Conference on Space Optics. p. 281

Covino E., Frasca A., Alcalá J. M., Paladino R., Sterzik M. F., 2004, A&A, 427, 637

Cox A. N., 2000, Allen's astrophysical quantities. Allen's astrophysical quantities, 4th ed. Publisher: New York: AIP Press; Springer, 2000. Edited by Arthur N. Cox. ISBN: 0387987460

Dempsey J. T., Storey J. W. V., Ashley M. C. B., Burton M. G., Calisse P. G., Jarnyk M. A., 2004, in Moorwood A. F. M., Iye M., eds, Ground-based Instrumentation for Astronomy. Edited by Alan F. M. Moorwood and Iye Masanori. Proceedings of the SPIE, Volume 5492, pp. 811-821. p. 811

Dempsey J. T., Storey J. W. V., Phillips A., 2005, Publications of the Astronomical Society of Australia, 22, 91

Derekas A., Kiss L. L., Bedding T. R., 2007, ApJ, 663, 249

Derekas A., Kiss L. L., Csák B., Griffin J., Lindström C., Mészáros S., Székely P., Ashley M. C. B., Bedding T. R., 2006, Memorie della Societa Astronomica Italiana, 77, 517

Derekas A., Kiss L. L., Székely P., Alfaro E. J., Csák B., Mészáros S., Rodríguez E., Rolland A., Sárneczky K., Szabó G. M., Szatmáry K., Váradi M., Kiss C., 2003, A&A, 402, 733

Dopita M. A., Wood P. R., Hovey G. R., 1996, Publications of the Astronomical Society of Australia, 13, 39

Doyle L. R., Deeg H.-J., 2004, in Norris R., Stootman F., eds, IAU Symposium Vol. 213, Bioastronomy 2002: Life Among the Stars. p. 80

Fischer D. A., Valenti J., 2005, ApJ, 622, 1102

Ford E. B., Rasio F. A., 2007, astro-ph/0703163

Fowler A. M., Sharp N., Ball W., Schinckel A., Ashley M. C., Boccas M., Storey J. W., Depoy D. L., Martini P., Harper A., Marks R., 1998, in Fowler A. M., ed., Presented at the Society of Photo-Optical Instrumentation Engineers (SPIE) Conference Vol. 3354, Proc. SPIE Vol. 3354, p. 1170-1178, Infrared Astronomical Instrumentation, ed. Albert M. Fowler. p. 1170

Gaudi B. S., Seager S., Mallen-Ornelas G., 2005, ApJ, 623, 472

Gillingham P. R., 1991, Proc. Astron. Soc. Austral., 9, 55

Gillon M., Demory B.-O., Barman T., Bonfils X., Mazeh T., Pont F., Udry S., Mayor M., Queloz D., 2007, A&A, 471, L51

Gillon M., Pont F., Demory B.-O., Mallmann F., Mayor M., Mazeh T., Queloz D., Shporer A., Udry S., Vuissoz C., 2007b, A&A, 472, L13

Gliese W., Jahreiß H., 1991, in Brotzmann L. E., Gesser S. E., eds, On: The Astronomical Data Center CD-ROM: Selected Astronomical Catalogs, Vol. I; NASA/Astronomical Data Center, Goddard Space Flight Center, Greenbelt, MD.

Gould A., Dorsher S., Gaudi B. S., Udalski A., 2006, Acta Astronomica, 56, 1

Grether D., Lineweaver C. H., 2006, ApJ, 640, 1051

Halzen F., 1998, New Astronomy Review, 42, 289

Hartman J. D., Bakos G., Stanek K. Z., Noyes R. W., 2004, AJ, 128, 1761

Hartman J. D., Gaudi B. S., Holman M. J., McLeod B. A., Stanek K. Z., Barranco J., 2007, in Afonso C., Weldrake D., Henning T., eds, Astronomical Society of the Pacific Conference Series Vol. 366, Transiting Extrapolar Planets Workshop. p. 64

Hartman J. D., Stanek K. Z., Gaudi B. S., Holman M. J., McLeod B. A., 2005, AJ, 130, 2241

Hebb L., Wyse R. F. G., Gilmore G., Holtzman J., 2006, AJ, 131, 555

Henry G. W., Marcy G. W., Butler R. P., Vogt S. S., 2000, ApJ, 529, L41

Hidas M. G., Ashley M. C. B., Webb J. K., Irwin M., Phillips A., Toyozumi H., Derekas A., Christiansen J. L., Nutto C., Crothers S., 2005, MNRAS, 360, 703

Hoekstra H., Wu Y., Udalski A., 2005, ApJ, 626, 1070

Høg E., Fabricius C., Makarov V. V., Urban S., Corbin T., Wycoff G., Bastian U., Schwekendiek P., Wicenec A., 2000, A&A, 355, L27

Holman M. J., Murray N. W., 2005, Science, 307, 1288

Horne K., 2003, in Deming D., Seager S., eds, Astronomical Society of the Pacific Conference Series Vol. 294, Scientific Frontiers in Research on Extrasolar Planets. p. 361

Ida S., Lin D. N. C., 2005, ApJ, 626, 1045

Irwin J., Aigrain S., Hodgkin S., Stassun K. G., Hebb L., Irwin M., Moraux E., Bouvier J., Alapini A., Alexander R., Bramich D. M., Holtzman J., Martín

E. L., McCaughrean M. J., Pont F., Verrier P. E., Zapatero Osorio M. R., 2007, MNRAS, 380, 541

Irwin M., Lewis J., 2001, New Astronomy Review, 45, 105

Irwin M. J., 1997, in Espinosa J. M. R., ed., Instrumentation for Large Telescopes; Cambridge University Press. p. 35

Jenkins J. M., Chandrasekaran H., Caldwell D. A., Allen C., Bryson S. T., Batalha N. M., Borucki W. J., 2007. p. 83

Johnson J. A., Fischer D. A., Marcy G. W., Wright J. T., Driscoll P., Butler R. P., Hekker S., Reffert S., Vogt S. S., 2007, ApJ, 665, 785

Joner M. D., Laney C. D., 2004, in Bulletin of the American Astronomical Society. p. 1429

Kaltenegger L., Fridlund M., 2005, Advances in Space Research, 36, 1114

Kane S. R., Collier Cameron A., Horne K., James D., Lister T. A., Pollacco D. L., Street R. A., Tsapras Y., 2005, MNRAS, 364, 1091

Kenyon S., Lawrence J., Ashley M. C. B., Storey J. W. V., Tokovinin A., Fossat E., 2006, Astronomy in Antarctica, 26th meeting of the IAU, Special Session 7, 22-23 August, 2006 in Prague, Czech Republic, SPS7, 30, 7

Kim S.-L., Lee J. W., Youn J.-H., Kwon S.-G., Kim C., 2002a, A&A, 391, 213

Kim Y.-C., Demarque P., Yi S. K., Alexander D. R., 2002, ApJS, 143, 499

Kjeldsen H., Frandsen S., 1992, Publ. Astron. Soc. Pac., 104, 413

Klahr H., Brandner W., eds, 2006, Planet Formation: Theory, Observations, and Experiments. Cambridge University Press

Kolenberg K., Smith H. A., Gazeas K. D., Elmaslı A., Breger M., Guggenberger E., van Cauteren P., Lampens P., Reegen P., Niarchos P. G., Albayrak B., Selam S. O., Özavcı I., Aksu O., 2006, A&A, 459, 577

Konacki M., Torres G., Jha S., Sasselov D. D., 2003, Nat, 421, 507

Kopal Z., 1954, ApJ, 120, 159

Kovács G., 2001, in Takeuti M., Sasselov D. D., eds, Stellar pulsation - nonlinear studies. Kluwer Academic Publishers: Dordrecht

Kovács G., Bakos G., Noyes R. W., 2005, MNRAS, 356, 557

Lafler J., Kinman T. D., 1965, ApJS, 11, 216

Landolt A. U., 1992, AJ, 104, 340

Lanza A. F., De Martino C., Rodonò M., 2008, New Astronomy, 13, 77

Latham D. W., 2003, in Deming D., Seager S., eds, Astronomical Society of the Pacific Conference Series Vol. 294, Scientific Frontiers in Research on Extrasolar Planets. p. 409

Latham D. W., Stefanik R. P., Mazeh T., Mayor M., Burki G., 1989, Nat, 339, 38

Laughlin G., Butler R. P., Fischer D. A., Marcy G. W., Vogt S. S., Wolf A. S., 2005, ApJ, 622, 1182

Lawrence J. S., Ashley M. C. B., Burton M. G., Storey J. W. V., 2007, Acta Astronomica Sinica, 48, 48

Lawrence J. S., Ashley M. C. B., Tokovinin A., Travouillon T., 2004, Nat, 431, 278

Lenz P., Breger M., 2005, Communications in Asteroseismology, 146, 53

Li L., Zhang F., 2006, MNRAS, 369, 2001

Liu K., Yue Y. L., Xu R. X., 2007, MNRAS, 381, L1

Makarov V. V., 2003, AJ, 126, 2408

Mallén-Ornelas G., Seager S., Yee H. K. C., Minniti D., Gladders M. D., Mallén-Fullerton G. M., Brown T. M., 2003, ApJ, 582, 1123

Mandushev G., O'Donovan F. T., Charbonneau D., Torres G., Latham D. W., Bakos G. Á., Dunham E. W., Sozzetti A., Fernández J. M., Esquerdo G. A., Everett M. E., Brown T. M., Rabus M., Belmonte J. A., Hillenbrand L. A., 2007, ApJ, 667, L195

Mapelli M., Sigurdsson S., Colpi M., Ferraro F. R., Possenti A., Rood R. T., Sills A., Beccari G., 2004, ApJ, 605, L29

Marcy G., Butler R. P., Fischer D., Vogt S., Wright J. T., Tinney C. G., Jones H. R. A., 2005b, Progress of Theoretical Physics Supplement, 158, 24

Marks R. D., Vernin J., Azouit M., Manigault J. F., Clevelin C., 1999, A&AS, 134, 161

Mayor M., Queloz D., 1995, Nat, 378, 355

Mazeh T., Zucker S., 1992, in McAlister H. A., Hartkopf W. I., eds, Astronomical Society of the Pacific Conference Series Vol. 32, IAU Colloq. 135: Complementary Approaches to Double and Multiple Star Research. p. 164

McDowell J., 2007, IVOA Recommendation 29 October 2007

McNamara D. H., 2000a, in Breger M., Montgomery M., eds, ASP Conf. Ser. 210: Delta Scuti and Related Stars. p. 373

McNamara D. H., 2000b, Publ. Astron. Soc. Pac., 112, 1096

Mkrtichian D. E., Kusakin A. V., Rodriguez E., Gamarova A. Y., Kim C., Kim S.-L., Lee J. W., Youn J.-H., Kang Y. W., Olson E. C., Grankin K., 2004, A&A, 419, 1015

Mochejska B. J., Stanek K. Z., Sasselov D. D., Szentgyorgyi A. H., Bakos G. Á., Hradecky J., Devor V., Marrone D. P., Winn J. N., Zaldarriaga M., 2005, AJ, 129, 2856

Montalto M., Piotto G., Desidera S., de Marchi F., Bruntt H., Stetson P. B., Arellano Ferro A., Momany Y., Gratton R. G., Poretti E., Aparicio A., Barbieri M., Claudi R. U., Grundahl F., Rosenberg A., 2007, A&A, 470, 1137

Munari U., Sordo R., Castelli F., Zwitter T., 2005, A&A, 442, 1127

Naef D., Mayor M., Beuzit J.-L., Perrier C., Queloz D., Sivan J.-P., Udry S., 2005, in Favata F., et al. eds, ESA Special Publication Vol. 560, 13th Cambridge Workshop on Cool Stars, Stellar Systems and the Sun. p. 833

Nelson A. F., 2000, ApJ, 537, L65

Nemec J. M., Nemec A. F. L., Lutz T. E., 1994, AJ, 108, 222

Neuhäuser R., Guenther E. W., Wuchterl G., Mugrauer M., Bedalov A., Hauschildt P. H., 2005, A&A, 435, L13

Norton A. J., Wheatley P. J., West R. G., Haswell C. A., Street R. A., Collier Cameron A., Christian D. J., Clarkson W. I., Enoch B., Gallaway M., Hellier C., Horne K., Irwin J., et al. 2007, A&A, 467, 785

Ochsenbein F., 2004, IVOA Recommendation 11 August 2004

Ochsenbein F., Bauer P., Marcout J., 2000, A&AS, 143, 23

O'Donovan F. T., Charbonneau D., Bakos G. Á., Mandushev G., Dunham E. W., Brown T. M., Latham D. W., Torres G., Sozzetti A., Kovács G., Everett M. E., Baliber N., Hidas M. G., Esquerdo G. A., Rabus M., et al. 2007, ApJ, 663, L37

Oláh K., Kolláth Z., Strassmeier K. G., 2000, A&A, 356, 643

Ortolani, S. ed. 2003, ESPAS Site Summary Series 1.2, Mauna Kea. Garching: ESO

Osmer P. S., Wood H. J., 1984, in Ardeberg A., Woltjer L., eds, Site Testing for Future Large Telescopes. p. 95

O'Toole S. J., Butler R. P., Tinney C. G., Jones H. R. A., Marcy G. W., Carter B., McCarthy C., Bailey J., Penny A. J., Apps K., Fischer D., 2007, ApJ, 660, 1636

Patel S. G., Vogt S. S., Marcy G. W., Johnson J. A., Fischer D. A., Wright J. T., Butler R. P., 2007, ApJ, 665, 744

Patience J., White R. J., Ghez A. M., McCabe C., McLean I. S., Larkin J. E., Prato L., Kim S. S., Lloyd J. P., Liu M. C., Graham J. R., Macintosh B. A., Gavel D. T., Max C. E., Bauman B. J., Olivier S. S., et al. 2002, ApJ, 581, 654

Pepper J., Burke C. J., 2006, AJ, 132, 1177

Perryman M., Hainaut O., Dravins D., Leger A., Quirrenbach A., Rauer H., Kerber F., Fosbury R., Bouchy F., Favata F., Fridlund M., Gilmozzi R., Lagrange A. M., Mazeh T., Rouan D., Udry S., Wambsganss J., 2005, astro-ph/0506163

Perryman M. A. C., 2000, Reports of Progress in Physics, 63, 1209

Petersen J. O., Christensen-Dalsgaard J., 1996, A&A, 312, 463

Petersen J. O., Jørgensen H. E., 1972, A&A, 17, 367

Peterson J. B., Griffin G. S., Newcomb M. G., Alvarez D. L., Cantalupo C. M., Morgan D., Miller K. W., Ganga K., Pernic D., Thoma M., 2000, ApJ, 532, L83

Phillips A., Burton M. G., Ashley M. C. B., Storey J. W. V., Lloyd J. P., Harper D. A., Bally J., 1999, ApJ, 527, 1009

Pickles A. J., 1998, Publ. Astron. Soc. Pac., 110, 863

Pigulski A., Michalski G., 2007, Acta Astron.

Pojmanski G., 2002, astro-ph/0210283, 52, 397

Pojmanski G., Maciejewski G., 2004, Acta Astronomica, 54, 153

Pollacco D. L., Skillen I., Cameron A. C., Christian D. J., Hellier C., Irwin J., Lister T. A., Street R. A., et al. 2006, Publ. Astron. Soc. Pac., 118, 1407

Pont F., Bouchy F., 2006, ApSS, 304, 235

Pont F., Bouchy F., Melo C., Santos N. C., Mayor M., Queloz D., Udry S., 2005, A&A, 438, 1123

Pont F., Zucker S., Queloz D., 2006, MNRAS, 373, 231

Pribulla T., Chochol D., Rovithis-Livaniou H., Rovithis P., 1999, A&A, 345, 137

Qian S.-B., Zhu L.-Y., Soonthornthum B., Yuan J.-Z., Yang Y.-G., He J.-J., 2005, AJ, 130, 1206

Rasio F. A., 1995, ApJ, 444, L41

Raymond S. N., Quinn T., Lunine J. I., 2004, Icarus, 168, 1

Richards M. T., Albright G. E., 1999, ApJS, 123, 537

Robin A. C., Reylé C., Derrière S., Picaud S., 2003, A&A, 409, 523

Rodríguez E., García J. M., Gamarova A. Y., Costa V., Daszyńska-Daszkiewicz J., López-González M. J., Mkrtichian D. E., Rolland A., 2004, MNRAS, 353, 310

Rodríguez E., López-González M. J., López de Coca P., 2000, A&AS, 144, 469

Rosenblatt F., 1971, Icarus, 14, 71

Rucinski S. M., 2006, MNRAS, 368, 1319

Rucinski S. M., 2007, MNRAS, 382, 393

Sahu K. C., Casertano S., Bond H. E., Valenti J., Ed Smith T., Minniti D., Zoccali M., Livio M., Panagia N., Piskunov N., Brown T. M., Brown T., Renzini A., Rich R. M., Clarkson W., Lubow S., 2006, Nat, 443, 534

Samus N. N., Durlevich O. V., 2007, The combined table of General Catalogue of Variable Stars Vols. I–III, 4th ed. and Namelists of Variable Stars Nos. 67–78 with improved coordinates. Sternberg Astronomical Institute: Moscow

Sándor Z., Kley W., 2006, A&A, 451, L31

Sato B., Fischer D. A., Henry G. W., Laughlin G., Butler R. P., Marcy G. W., Vogt S. S., Bodenheimer P., Ida S., Toyota E., Wolf A., Valenti J. A., Boyd L. J., Johnson J. A., Wright J. T., Ammons M., et al. 2005, ApJ, 633, 465

Schneider J., Doyle L. R., 1995, Earth Moon and Planets, 71, 153

Seager S., Mallén-Ornelas G., 2003, ApJ, 585, 1038

Skrutskie M. F., Cutri R. M., Stiening R., Weinberg M. D., Schneider S., Carpenter J. M., Beichman C., Capps R., Chester T., Elias J., Huchra J., Liebert J., Lonsdale C., Monet D. G., et al. 2006, AJ, 131, 1163

Smith A. M. S., Collier Cameron A., Christian D. J., Clarkson W. I., Enoch B., Evans A., Haswell C. A., Hellier C., et al. 2007, in Afonso C., Weldrake D., Henning T., eds, Astronomical Society of the Pacific Conference Series Vol. 366, Transiting Extrapolar Planets Workshop. p. 152

Smith A. M. S., Collier Cameron A., Christian D. J., Clarkson W. I., Enoch B., Evans A., Haswell C. A., Hellier C., Horne K., Irwin J., Kane S. R., Lister T. A., Norton A. J., Parley N., Pollacco D. L., et al. 2006, MNRAS, 373, 1151

Soydugan E., Soydugan F., Demircan O., İbanoğlu C., 2006, MNRAS, 370, 2013

Stassun K. G., Mathieu R. D., Valenti J. A., 2007, ApJ, 664, 1154

Stassun K. G., Mathieu R. D., Vaz L. P. R., Stroud N., Vrba F. J., 2004, ApJS, 151, 357

Stepien K., 2006, Acta Astronomica, 56, 347

Stetson P. B., 1996, Publ. Astron. Soc. Pac., 108, 851

Storey J. W. V., 1998, in Novak G., Landsberg R., eds, ASP Conf. Ser. 141: Astrophysics From Antarctica. p. 313

Storey J. W. V., Ashley M. C. B., Boccas M., Phillips M. A., Schinckel A. E. T., 1999, Publ. Astron. Soc. Pac., 111, 765

Storey J. W. V., Ashley M. C. B., Burton M. G., 1996, Publications of the Astronomical Society of Australia, 13, 35

Stothers R. B., 2006, ApJ, 652, 643

Szalai T., Kiss L. L., Mészáros S., Vinkó J., Csizmadia S., 2007, A&A, 465, 943

Szczygieł D. M., Fabrycky D. C., 2007, MNRAS, 377, 1263

Tamuz O., Mazeh T., Zucker S., 2005, MNRAS, 356, 1466

Taylor M. B., 2005, in Shopbell P., Britton M., Ebert R., eds, Astronomical Society of the Pacific Conference Series Vol. 347, Astronomical Data Analysis Software and Systems XIV. p. 29

Thommes E. W., Bryden G., Wu Y., Rasio F. A., 2007, astro-ph/0706.1235, 706

Tingley B., 2004, A&A, 425, 1125

Tinney C. G., Butler R. P., Marcy G. W., Jones H. R. A., Penny A. J., McCarthy C., Carter B. D., Fischer D. A., 2005, ApJ, 623, 1171

Tody D., Dolensky M., McDowell J., Bonnarel F., Budaveri T., Busko I., Micol A., Osuna P., Salgado J., Thompson R., Valdes F., 2007, IVOA Proposed Recommendation 17 September 2007

Tody D., Plante R., 2004, IVOA Working Draft 24 May 2004

Tokovinin A., Baumont S., Vasquez J., 2003, MNRAS, 340, 52

Tokovinin A., Vernin J., Ziad A., Chun M., 2005, Publ. Astron. Soc. Pac., 117, 395

Toyozumi H., Ashley M. C. B., 2005, Publications of the Astronomical Society of Australia, 22, 257

Traub W. A., Levine M., Shaklan S., Kasting J., Angel J. R., Brown M. E., Brown R. A., Burrows C., Clampin M., Dressler A., Ferguson H. C., Hammel H. B., Heap S. R., Horner S. D., Illingworth G. D., et al. 2006, in Advances in Stellar Interferometry. Edited by Monnier, John D.; Schöller, Markus; Danchi, William C. Proceedings of the SPIE, Volume 6268, pp. 62680T.

Travouillon T., Ashley M. C. B., Burton M. G., Storey J. W. V., Loewenstein R. F., 2003, A&A, 400, 1163

Udry S., Bonfils X., Delfosse X., Forveille T., Mayor M., Perrier C., Bouchy F., Lovis C., Pepe F., Queloz D., Bertaux J.-L., 2007, A&A, 469, L43

Udry S., Mayor M., Benz W., Bertaux J.-L., Bouchy F., Lovis C., Mordasini C., Pepe F., Queloz D., Sivan J.-P., 2006, A&A, 447, 361

Udry S., Santos N. C., 2007, ARA&A, 45, 397

van Hamme W., 1993, AJ, 106, 2096

Vesper D., Honeycutt K., Hunt T., 2001, AJ, 121, 2723

Vidal-Madjar A., Désert J.-M., Lecavelier des Etangs A., Hébrard G., Ballester G. E., Ehrenreich D., Ferlet R., McConnell J. C., Mayor M., Parkinson C. D., 2004, ApJ, 604, L69

Vidal-Madjar A., Lecavelier des Etangs A., Désert J.-M., Ballester G. E., Ferlet R., Hébrard G., Mayor M., 2003, Nat, 422, 143

Voges W., Aschenbach B., Boller T., Bräuninger H., Briel U., Burkert W., Dennerl K., Englhauser J., Gruber R., Haberl F., Hartner G., Hasinger G., Kürster M., Pfeffermann E., Pietsch W., et al. 1999, å, 349, 389

Voges W., Aschenbach B., Boller T., Brauninger H., Briel U., Burkert W., Dennerl K., Englhauser J., Gruber R., Haberl F., Hartner G., Hasinger G., Pfeffermann E., Pietsch W., Predehl P., Schmitt J., et al. 2000, , 7432, 1

von Braun K., Lee B. L., Seager S., Yee H. K. C., Mallén-Ornelas G., Gladders M. D., 2005, Publ. Astron. Soc. Pac., 117, 141

Weldrake D. T. F., Sackett P. D., Bridges T. J., 2007, AJ, 133, 1447

Weldrake D. T. F., Sackett P. D., Bridges T. J., Freeman K. C., 2005, ApJ, 620, 1043

Wilson R. E., 1979, ApJ, 234, 1054

Wilson R. E., 1990, ApJ, 356, 613

Wilson R. E., Devinney E. J., 1971, ApJ, 166, 605

Winn J. N., Johnson J. A., Peek K. M. G., Marcy G. W., Bakos G. Á., Enya K., Narita N., Suto Y., Turner E. L., Vogt S. S., 2007, ApJ, 665, L167

Wolszczan A., Frail D. A., 1992, Nat, 355, 145

Wood P. R., Rodgers A. W., Russell K. S., 1995, Publications of the Astronomical Society of Australia, 12, 97

Wright J. T., Marcy G. W., Fischer D. A., Butler R. P., Vogt S. S., Tinney C. G., Jones H. R. A., Carter B. D., Johnson J. A., McCarthy C., Apps K., 2007, ApJ, 657, 533

Yi S., Demarque P., Kim Y.-C., Lee Y.-W., Lejeune T., Barnes S., 2001, ApJS, 136, 417

Young T. B., Hidas M. G., Webb J. K., Ashley M. C. B., Christiansen J. L., Derekas A., Nutto C., 2006, MNRAS, 370, 1529

Zacharias N., Urban S. E., Zacharias M. I., Wycoff G. L., Hall D. M., Monet D. G., Rafferty T. J., 2004, AJ, 127, 3043

Zucker S., Mazeh T., 1994, ApJ, 420, 806

Fin Lib.